Improved Modeling of Lidar Wind Preview for Wind Turbine Control

A thesis accepted by the Faculty of Aerospace Engineering and Geodesy
of the University of Stuttgart in fulfillment of the requirements
for the degree of Doctor of Engineering Sciences (Dr.-Ing.)

by Feng Guo

born in Kunming, China

Main referee:	Prof. Dr. Po Wen Cheng
Co-referee:	Prof. Dr. David Schlipf
	Prof. Dr. Jakob Mann
Day of defense:	February 21, 2023

Institute of Aircraft Design
University of Stuttgart
2023

Acknowledgments

First of all, I would like to express my sincere gratitude to David Schlipf, whose guidance, advice, and encouragement were indispensable for the completion of my thesis. I would also like to thank Po Wen Cheng, whose advice and encouragement have always been an inspiration to me. In addition, I would like to give special thanks to Jakob Mann, whose constructive guidance has helped me to gain a better understanding of turbulence. Of course, I am also grateful to Alfredo Peña for his help with the measured data and the analysis of the data.
Next, I would like to thank all my colleagues in the Lidar Knowledge Europe project, including the rest 14 fellow Ph.D. students and all supervisors. Every time I interacted with them, I felt like a team of people working together, which is always an inspiring feeling. Special thanks to colleagues at the Wind Energy Technology Institute of Flensburg University of Applied Science. I still remember the first day when I started working there and their warm welcome.
I would also like to express my appreciation to the Movelaser team, especially Hailong Zhu, for their invaluable help in providing the lidar, assisting with lidar testing, answering questions, and so on. Thanks to Andrew from Leosphere, colleagues from DTU Wind Energy, and colleagues from SOWENTO, the interaction with you during the secondment has been of great significance to my research. I would also like to thank a few people from Flensburg University of Applied Science: Hugo, Marcel, Nils, and Christoph. It was an exciting time working with them on the "Smart lidar" project.
I also would like to thank my friends and family members for their care and support during the Ph.D. project.
And most importantly, I owe my deepest gratitude to my wife Lijun Zhang for her daily encouragement and support.
In the end, I want to show my sincere gratitude to the funding source of my research. This research received financial support from the European Union's Horizon 2020 research and innovation program under the Marie Skłodowska-Curie grant agreement No. 858358 (LIKE – Lidar Knowledge Europe).

Contents

Abbreviations ix

List of Symbols xi

Abstract xvii

Kurzfassung xix

1 Introduction 1
- 1.1 Motivation . . . 1
- 1.2 Related Studies . . . 2
  - 1.2.1 Turbulence Evolution . . . 2
  - 1.2.2 Lidar Wind Preview for Turbine Control . . . 3
  - 1.2.3 Evaluation of Lidar-assisted Pitch Feedforward Control . . . 4
- 1.3 Research Objectives and Methodology . . . 4
- 1.4 Thesis Structure . . . 5
- 1.5 Notations and Conventions . . . 6
  - 1.5.1 Font Types . . . 6
  - 1.5.2 Subscripts . . . 6
  - 1.5.3 Einstein Summation Convention . . . 7

2 Background on Wind, Wind Lidars, and Wind Turbines 9
- 2.1 Wind . . . 9
  - 2.1.1 Origin of Wind . . . 9
  - 2.1.2 Variations in Wind . . . 10
  - 2.1.3 Statistical Representation of Wind . . . 12
  - 2.1.4 Concept of Eddies in Turbulence . . . 16
  - 2.1.5 Standard Turbulence Spectral Models . . . 18
- 2.2 Wind Lidar . . . 22
  - 2.2.1 Applications of Wind Lidar . . . 23
  - 2.2.2 Measurement Principles of Wind Lidar . . . 23
- 2.3 Wind Turbines . . . 26
  - 2.3.1 Overview of Wind Turbine Development . . . 27
  - 2.3.2 Aeroelastic Simulation: OpenFAST . . . 28
  - 2.3.3 Wind Turbine Control . . . 30
  - 2.3.4 Wind Turbine Wakes . . . 34

3 Background on Conventional Three-dimensional Turbulence Generation 35
3.1 Stochastic Turbulent Wind Field Generation . . . 35
3.1.1 Veers Method . . . 35
3.1.2 Mann Method . . . 37
3.2 Simulation of Wake-included Turbulence . . . 39
3.2.1 Wake Deficit . . . 39
3.2.2 Wake Meandering . . . 40
3.2.3 Wake-induced Turbulence . . . 41

4 Modeling of Turbulence Evolution 43
4.1 Including Longitudinal Coherence in the Kaimal Model . . . 43
4.1.1 Exponential Longitudinal Coherence Model . . . 44
4.1.2 Four-dimensional Turbulence Generation by Veers Method . . . 44
4.2 Including Longitudinal Coherence to the Mann Model . . . 48
4.2.1 Derivation of the Space-time Tensor . . . 48
4.2.2 Four-dimensional Turbulence Generation by Space-time Tensor . . . 52
4.3 Evaluation of Four-dimensional Turbulence Models . . . 56
4.3.1 Spectral Properties of the Lidar Measurements . . . 57
4.3.2 Model Validation Against Simulation . . . 63
4.3.3 Measurement Site . . . 66
4.3.4 Model Evaluation . . . 70
4.4 Chapter Summary and Outlook . . . 82

5 Lidar Wind Preview Quality under Various Turbulence Conditions 87
5.1 Turbulence Parameters of Different Atmospheric Stability Classes . . . 88
5.2 Correlations between Lidar and Turbine . . . 92
5.2.1 Rotor Effective Wind Speed . . . 92
5.2.2 Lidar-estimated Rotor Effective Wind Speed . . . 92
5.2.3 Cross-spectrum between Turbine and Lidar . . . 94
5.2.4 Lidar Wind Preview Quality . . . 95
5.3 Lidar Wind Preview Quality under Freestream Turbulence . . . 96
5.3.1 Lidar Trajectory Optimization . . . 96
5.3.2 Sensitivity of Lidar Wind Preview to Turbulence Parameters . . . 99
5.4 Lidar Wind Preview Quality under Wake Conditions . . . 103
5.4.1 Potential Impact of Turbine Wake . . . 103
5.4.2 Simulation Configurations . . . 104
5.4.3 Simulation Results . . . 106
5.5 Chapter Summary and Outlook . . . 109

6 Improving Lidar Module in Aeroelastic Simulations 111
6.1 Overview of the Updated Features . . . 112
6.2 Integrating the Evolving Turbulence . . . 113
6.3 Simulating the Blade Blockage Effect . . . 114
6.3.1 Blade Blockage Detection . . . 114
6.3.2 Verification of Implementation . . . 115
6.4 Simulating the Lidar Measurement Availability . . . 116
6.4.1 Measurement Campaign for Lidar Data Availability Model . . . 116

6.4.2 Spectral Analysis of CNR . . . 117
6.4.3 Data Availability Implementation in OpenFAST . . . 120
6.5 Assessment of Lidar Preview Quality with the Updated Lidar Simulator . . . 121
6.5.1 Lidar Data Processing Algorithm . . . 121
6.5.2 Simulation Setup . . . 122
6.5.3 Results and Discussions . . . 123
6.6 Chapter Summary and Outlook . . . 124

7 Evaluation of Lidar-assisted Control 127
7.1 Simulation Setups . . . 128
7.1.1 Lidar Simulation . . . 128
7.1.2 Turbulence Simulation . . . 128
7.1.3 Turbine Configurations . . . 129
7.2 Results and Discussions . . . 130
7.2.1 Time Series . . . 130
7.2.2 Spectral Analysis . . . 132
7.2.3 Simulation Statistic . . . 136
7.3 Chapter Summary and Outlook . . . 140

8 Conclusions and Recommendations 141
8.1 Conclusions . . . 141
8.1.1 Turbulence Evolution Phenomenon . . . 141
8.1.2 Lidar Wind Preview for Turbine Control . . . 142
8.1.3 Evaluating of Lidar-assisted Pitch Feedforward Control . . . 143
8.2 Recommendations . . . 144
8.2.1 Observing Turbulence Spectral Characteristics using Lidar . . . 144
8.2.2 Lidar Wind Preview Quality Investigations . . . 145
8.2.3 Design and Evaluation of Lidar-assisted Control . . . 145
8.3 Main Contributions . . . 146

A Appendix 147
A.1 Derivation of Veers Method for Turbulence Generation . . . 147
A.2 Derivation of the Mann Uniform Shear Model . . . 148
A.3 Code Availability . . . 152
A.4 Publications not Included in This Thesis . . . 153

Bibliography 155

Curriculum Vitae 165

Abbreviations

1p	One-per-revolution
3-D	Three-Dimensional
3p	Three-per-revolution
4-D	Four-Dimensional
AMSL	Above Mean Sea Level
CFD	Computational Fluid Dynamics
CNR	Carrier-to-Noise Ratio
CW	Continious Wave
DEL	Damage Equivalent Load
DLL	Dynamic Link Library
DOF	Degree of Freedom
DWM	Dynamic Wake Meandering
EKF	Extended Kalman Filter
EP	Energy Production
ESC	Einstein Summation Convention
FAST	Fatigue, Aerodynamics, Structures, and Turbulence
FB	Feedback
FBC	Feedback (collective pitch) Controller
FFC	Feedforward (pitch) Controller
FFFB	Feedforward+feedback
FFP	Feedforward Pitch
FFT	Fast Fourer Transform
FWHM	Full Width at Half Maximum
GTC	Generator Torque Controller
HAWC2	Horizontal Axis Wind turbine simulation Code 2nd generation
IEC	International Electrotechnical Commission
IFFT	Inverse Fast Fourier Transform
LAC	Lidar-assisted Control
LACer	Lidar-assisted Controller
LDL	Square-root-free Cholesky decomposition, named after the used matrices L and D
LDP	Lidar Data Processing
LES	Large Eddy Simulation

lidar	light detection and ranging
LOS	Line-of-sight
N-S	Navier-Stokes
PI	Proportional Integral
REWS	Rotor Effective Wind Speed
ROSCO	Reference Open-source Controller
STD	Standard Deviation
SWE	Stuttgart Wind Energy
TI	Turbulence Intensity

List of Symbols

Greek letters

α	spectral Kolmogorov constant
$\alpha\varepsilon^{2/3}$	an energy level constant valid in the inertial subrange, acting as a proportional gain to the spectral tensor
β	a non-dimensional shear distortion factor
Δf	step length of the discrete frequency vector
Δt	time difference
$\Delta x, \Delta y, \Delta z$	step lengths of the turbulence field in three directions
Δy	separation distance in the lateral direction
Δyz	separation distance in lateral-vertical plane
Δz	separation distance in the vertical direction
ϵ	rate of viscous dissipation of specific turbulent kinetic energy
γ_{ij}	coherence as a function of frequency
$\gamma_{\mathrm{los,los'}}$	frequency-based coherence of lidar line-of-sight wind speeds
γ_{RL}	frequency-based coherence between lidar estimated and turbine-based rotor effective wind speeds
γ_x	frequency coherence with separations in longitudinal direction
γ_{xyz}	frequency coherence with separations in three-dimensional space
γ_{yz}	frequency coherence with separations in lateral-vertical plane
κ	von Kármán constant
λ_{L}	laser wavelength
μ	mean value of Gaussian distribution
ν_{kv}	kinematic viscosity
ν_T	eddy viscosity
Ω_{g}	wind turbine generator speed
Ω_{gf}	filtered wind turbine generator speed
$\Omega_{\mathrm{g,ref}}$	control reference of the wind turbine generator speed
$\boldsymbol{\phi}$	uniformly distributed phase angles between 0 to 2π
ϕ_{L}	azimuth angle of lidar beam
Φ_{ij}	elements of Mann spectral velocity tensor ($\mathbf{\Phi}$)
$\Phi_{\mathrm{iso},ij}$	elements of the isotropic spectral velocity tensor
ρ	fluid density
σ	standard deviation of Gaussian distribution
σ_i	standard deviations of the fluctuating part of the velocity components
σ_u	standard deviation of longitudinal wind fluctuation

τ	time lag or time difference
τ_{e}	eddy lifetime responsible for the turbulence evolution
τ_{s}	eddy lifetime responsible for the shear distortion effect of turbulence
θ_{filter}	phase response of the filter
θ	collective blade pitch angle
θ_{L}	elevation angle of lidar beam
θ_{FB}	feedback blade pitch reference value
θ_{FF}	feedforward blade pitch reference value
Θ_{ij}	elements of space-time tensor ($\boldsymbol{\Theta}$)
θ_{ss}	steady-state blade pitch angle
θ_{v}	fluctuation part of the virtual potential temperature
θ_{pitch}	phase response of the pitch actuator
φ	the weighting function of lidar probe volume measurement
$\hat{\varphi}$	Fourier transform of the weighting function of lidar probe volume measurement

Roman letters

${}_2F_1()$	hypergeometric function
$a_{\mathrm{c}}, d_{\mathrm{c}}, e_{\mathrm{c}}$	three empirical parameters for the spectral model of Carier-to-Noise ratio
$\boldsymbol{A}(\boldsymbol{k})$	a 3 by 3 matrix of coefficients related to the spectral tensor
$\boldsymbol{A}_u$	a diagonal matrix or a vector containing the amplitude of the Fourier series at a specific frequency
A_{wake}	wake cross-section area
a_{yz}	coherence decay constant for lateral-vertical coherence
a_x	coherence decay constant for longitudinal coherence
b_1, b_2	slope parameters for the eddy lifetime formula
$\boldsymbol{k}, \boldsymbol{k'}$	wavenumber vector
$\boldsymbol{k_0}$	initial non-sheared wavenumber vector
$\boldsymbol{n}$	a unit vector in the direction of a lidar beam
$\boldsymbol{n}_{\mathrm{c}}$	orientation vector that aligns with the chord length direction
$\boldsymbol{n}_{\mathrm{r}}$	normal vector of the rotational plane
$\boldsymbol{r}$	seperation vector of the Cartesian Coordinate system
$\boldsymbol{u}$	velocity vector (fluctuating part)
$\boldsymbol{x}$	position vector of the Cartesian Coordinate system
b_x	coherence intercept constant for longitudinal coherence
b_{yz}	coherence intercept constant for lateral-vertical coherence
c_1, c_2	aerodynamic centers of the two airfoil cross-sections, whose position coordinate are $\boldsymbol{c}_1$ and $\boldsymbol{c}_2$
$\boldsymbol{C}(\boldsymbol{k})$	a 3 by 3 matrix of coefficients related to the matrix $\boldsymbol{A}(\boldsymbol{k})$
coh_{ij}	coherence as a function of wavenumber
$\mathrm{coh}_{\mathrm{los,los'}}$	wavenumber-based coherence of lidar line-of-sight wind speeds
$\mathrm{coh}_{\mathrm{RL}}$	wavenumber-based coherence between lidar estimated and turbine-based rotor effective wind speeds
$\boldsymbol{C}_{u,xyz}$	the coherence matrix containing the coherence of any two signals in three-dimensional space
$\boldsymbol{C}_{u,yz}$	the coherence matrix containing the coherence of any two signals in lateral-vertical plane
c_{wb}	scale parameter of the Weibull Distribution

D	turbine rotor diameter
d_0	origin position of lidar beam, whose position coordinate is $\boldsymbol{d}_0$
d_1	a point lies on both the lidar beam and on the turbine rotational plane, whose position coordinate is $\boldsymbol{d}_1$
d_2	measurement position of lidar beam
D_{xy}	integration area
E	von Kámán energy spectrum
f	frequency
f_e	frequency of the emitted light
f_g	probability density of the Gaussian distribution
f_i	components in the external force vector
F_{ij}	auto-spectrum or cross-spectrm as a function of wavenumber
F_LL	wavenumber-based auto-spectrum of lidar estimated rotor effective wind speed
$F_{\mathrm{los,los}'}$	wavenumber-based auto-spectrum or cross-spectrum of lidar line-of-sight wind speeds
f_r	frequency of the received light
F_RL	wavenumber-based cross-spectrum between lidar estimated and turbine-based rotor effective wind speeds
F_RR	wavenumber-based auto-spectrum of turbine rotor effective wind speed
$f_{\mathrm{rw},i}$	weighting factor of the discrete range weighting function
f_wb	probability density of the Weibull distribution
g	gravitational acceleration
$\boldsymbol{g}(\boldsymbol{k})$	a 3 by 1 vector of independent Gaussian stochastic complex variables with unit variance
G_RL	optimal transfer function gain
h_p	half the length of a rectangular pulse
$\boldsymbol{H}_{u,xyz}$	a matrix resulted from applying Cholesky factorization to the coherence matrix $\boldsymbol{C}_{u,xyz}$
$\boldsymbol{H}_{u,yz}$	a matrix resulted from applying Cholesky factorization to the coherence matrix $\boldsymbol{C}_{u,yz}$
i	imaginary unit
I_ref	reference turbulence intensity
J_1	Bessel function of the first kind
k_p	proportional gain
k_wb	shape parameter of the Weibull Distribution
k_wt	a empirical scaling factor for the wake-induced turbulence
L	turbulence length scale related to the size of the eddies containing the most energy
l_1, l_2	leading edges of the airfoils, whose position coordinate are $\boldsymbol{l}_1$ and $\boldsymbol{l}_2$
L_c	coherence scale parameter for lateral-vertical coherence
L_i	integral length scales of velocity components
L_O	Obukhov length
L_x, L_y, L_z	sizes of the turbulence field in three directions
m_1, m_2	trailing edges of the airfoils, whose position coordinate are $\boldsymbol{m}_1$ and $\boldsymbol{m}_2$
M_g	wind turbine generator torque
M_LSS	low-speed shaft torsional moment

$M_{\mathrm{y,root}}$	blade out-of-plane bending moment
M_{yT}	tower base fore-aft bending moment
N_x, N_y, N_z	discrete steps of the turbulence field in three directions
p	pressure
P	probability
P_{el}	electrical power
r	radial displacement from wake center
R_{ij}	covariance of data sets i and j
R_{wake}	radius of the wake
s, s_i	(discrete) displacement along the lidar beam direction from the measured position or the complex frequency $2\pi f\mathrm{i}$
S	power spectrum density
U_0, A_b, B_a	constants of second-order polynomial fit for wind profile approximation
S_{ij}	auto-spectrum or cross-spectrm as a function of frequency
S_{LL}	frequency-based auto-spectrum of lidar estimated rotor effective wind speed
$S_{\mathrm{los,los'}}$	frequency-based auto-spectrum or cross-spectrum of lidar line-of-sight wind speeds
S_{RL}	frequency-based cross-spectrum between lidar estimated and turbine-based rotor effective wind speeds
S_{RR}	frequency-based auto-spectrum of turbine rotor effective wind speed
$S_{\mathrm{so},ii}$	spectra estimated from the sonic cup data
$S_{u,i}$	one-sided power spectrum of the simulated signal at i position
t	time
T	reference temperature
T_{buffer}	buffer time of pitch forward controller
T_{filter}	time lag introduced by signal filtering
T_{I}	integrator time constant
$\tilde{u}_i$	velocity components
T_{lead}	leading time of the lidar range gate
T_{lidar}	half of the lidar full scan time
T_{pitch}	pitch actuator time delay
u	longitudinal (stream-wise) wind speed
U	mean longitudinal wind speed
$\hat{\boldsymbol{u}}_{yz}$	a vector of frequency domain Fourier series of turbulence fluctuation in lateral-vertical plane
$\hat{\boldsymbol{u}}_{xyz}$	a vector of frequency domain Fourier series of turbulence fluctuation in three-dimensional space
$\boldsymbol{u}_{e_i}$	velocity field composed of specific waves
$\boldsymbol{u}_{\mathrm{turb}}$	velocity field composed of simple waves
u_{f}	friction velocity
u_{ind}	wake-induced turbulence
u_{LL}	lidar estimated rotor effective wind speed
U_{ref}	reference mean wind speed
u_{RR}	turbine rotor effective wind speed
u_{ss}	steady wind speed
u_{wake}	wake-included turbulence (fluctuating part)
U_x	mean wake velocity in longitudinal direction

v	lateral (cross-wind) wind speed
$v_\mathrm{c}, w_\mathrm{c}$	wake center speeds in lateral and vertical directions
V_hub	hub-height mean wind speed
v_los	line-of-sight wind speed
$\hat{v}_\mathrm{los}$	Fourier transform of line-of-sight wind speed
$v_{\mathrm{losP},i}$	single point line-of-sight wind speed at discrete position i
V_r	mean wake velocity in radial direction
w	vertical wind speed
x_i	components in the position vector of the Cartesian Coordinate system
$\boldsymbol{X}_{u,xyz}$	a vector of complex random numbers for turbulence fluctuations in three-dimensional space
$\boldsymbol{X}_{u,yz}$	a vector of complex random numbers for turbulence fluctuations in lateral-vertical plane
$y_\mathrm{c}, z_\mathrm{c}$	wake center coordinate in lateral and vertical directions

Operators

$\overline{(\cdot)}$	average
$\mathcal{F}\{\cdot\}$	one-dimensional Fourier transform
$\mathcal{F}^*\{\cdot\}$	complex conjugate of one-dimensional Fourier transform
chol	Cholesky decomposition
$(\cdot)^*$	conjugate transpose
$\delta(\cdot)$	Dirac delta function
$\langle\cdot\rangle$	ensemble average
$\otimes$	Kronecker product
$\propto$	proportional to
$\Re$	real number operator
$\sim$	similar to
$(\cdot)^\top$	matrix transpose

Abstract

Lidar has been used in the wind energy field for decades. Most of the time, it was mainly used for wind resource assessments of potential wind farms. In recent years, the cost of lidar systems has decreased significantly, and the applications of lidar have become increasingly diverse. In some cases where it is more expensive to erect meteorological mast towers, such as offshore wind farm development, lidar has become the preferred resource assessment choice. In addition to resource assessment, lidar has attracted extensive research interest in wind turbine control, power performance characterization, wind power prediction, and wind farm control. In terms of lidar-assisted control, this technology has been proven to reduce wind turbine loads, rotor speed variations, and power fluctuations. In recent years, lidar-assisted wind turbine control has been applied to commercial projects.

Wind turbines operate mainly in atmospheric turbulence, where wind speeds are highly random and fluctuating. The wind rotates the turbine to generate electricity while also imposing fatigue loads. Traditional wind turbine control only relies on feedback control, which adjusts the blade pitch angles and the generator torque by measuring changes in the rotational speed of the turbine. This control effect is achieved after the turbulent wind disturbance has already acted on the wind turbine and it is lagging. Differently, lidar-assisted control uses the wind preview provided by nacelle- or spinner-lidars to achieve feedforward control. For example, when the wind speed changes, the lidar can sense that and inform the pitch control system to achieve an earlier pitch adjustment.

Some key features of nacelle lidar measurements make it necessary to process the lidar measurement before it can be used for turbine control. For instance, the lidar measurement is the projection of the three-dimensional wind velocity vector onto the lidar beam direction, but the turbine rotor is mainly interacting with the axial component in the velocity vector. In addition, the lidar system provides only limited measurements of the upstream position while the turbine rotor interacts with the downstream turbulence through its three blades. Usually, differences in turbulence at upstream and rotor positions are described as wind evolution. Further, the lidar measurement can be unavailable due to blade blockage or special weather patterns. Therefore, a lidar preview quality study needs to be performed to determine the usable part of the wind

preview provided by the lidar. A filter design is necessary to filter out uncorrelated information in the lidar wind preview. In actual operation, wind turbines suffer from different atmospheric stability conditions. In different atmospheric stability conditions, the spectrum and coherence of the turbulent wind can vary. Because of the limited measurement at upstream positions, lidar preview is highly linked to the spatial coherence of turbulence. Thus far, it is still unclear whether the variation of the turbulence characteristics will have an impact on the lidar preview quality and the benefits of lidar-assisted control.

Although there are already commercial use cases for lidar-assisted control, the existing lidar-assisted control simulation environment does not fully cover the characteristics of lidar measurements discussed above. Therefore, the main objective of this thesis is to improve the lidar wind preview modeling and assess the benefits of lidar-assisted control using the improved modeling. First, the improvement is achieved by incorporating the wind evolution phenomenon into conventional three-dimensional turbulence models: the Mann and Kaimal models, resulting in four-dimensional turbulence models. The performances of these two extended models in predicting turbulence spectra and spatial coherences are evaluated using measurements from a pulsed lidar and a meteorology mast.

Furthermore, the analytical models which represent the correlation between the lidar-previewed rotor effective wind speed and the rotor effective wind speed at the rotor position, are derived based on the extended turbulence models. Spectra and coherences of turbulence in different atmospheric stabilities are summarized, and their impacts on lidar preview qualities are investigated. A preliminary study on whether the upstream wind turbine wake affects the lidar preview of a downwind wind turbine is also conducted.

Moreover, a realistic lidar module is updated in the aeroelastic simulation tool, which allows for studying the impact of unavailable lidar data on lidar wind preview quality. Through simulations using realistic data availability, this study indicates that the blade blockage and low data availability event have negligible impacts on the lidar preview quality.

Finally, this thesis evaluates the benefits of lidar-assisted control under various turbulence characteristics representative of different atmospheric stabilities using the updated aeroelastic simulation tool. This study exhibits that the benefits of lidar-assisted control are related to the mean wind speed, turbulence spectrum, turbulence spatial coherence, and used turbulence models. For the NREL 5.0 MW turbine and a four-beam lidar, the benefits of lidar-assisted control are primarily reductions in rotor speed variation, power fluctuation, and tower-base bending load. The benefits are observed in all three investigated stabilities: unstable, neutral, and stable.

Kurzfassung

Lidar wird seit Jahrzehnten im Bereich der Windenergie eingesetzt. Die meiste Zeit wurde Lidar hauptsächlich zur Bewertung der Windressourcen potenzieller Windparks eingesetzt. In den letzten Jahren sind die Preise für Lidar gesunken, und die Einsatzmöglichkeiten werden immer vielfältiger. In einigen Fällen, in denen es teurer ist, meteorologische Masten zu errichten, wie z.B. bei der Entwicklung von Offshore-Windparks, ist Lidar die bevorzugte Wahl für die Ressourcenbewertung geworden. Neben der Ressourcenbewertung hat Lidar ein großes Forschungsinteresse bei der Regelung von Windturbinen, der Charakterisierung der Leistungsmerkmale, der Vorhersage der Windleistung und der Regelung von Windparks geweckt. Was die Lidar-gestützte Regelung betrifft, so hat sich diese Technologie als geeignet erwiesen, die Belastung der Windkraftanlagen, die Schwankungen der Rotordrehzahl und die Leistungsschwankungen zu reduzieren. In den letzten Jahren wurde sie auch bei kommerziellen Projekten eingesetzt.

Windturbinen arbeiten hauptsächlich in atmosphärischen Turbulenzen, wo die Windgeschwindigkeiten sehr zufällig und schwankend sind. Turbulente Winde ermöglichen die Stromerzeugung durch Windenergie, stellen aber auch eine Ermüdungsbelastung dar. Die herkömmliche Regelung von Windkraftanlagen beruht auf einer Rückkopplungsregelung, bei der die Blattanstellwinkel und das Drehmoment des Generators durch Messung von Änderungen der Rotordrehzahl der Anlage angepasst werden. Dieser Regeleffekt wird erzielt, nachdem die turbulente Windstörung bereits auf die Windturbine eingewirkt hat und regiert dadurch immer mit einem Zeitversatz. Die Lidar-gestützte Regelung hingegen nutzt die Windvorhersage durch Gondel- oder Spinner-Lidar-Systeme, um eine Vorsteuerung zu erreichen. Wenn sich beispielsweise die Windgeschwindigkeit ändert, kann das Lidar dies erkennen und dem Pitch-Steuerungssystem mitteilen, um eine frühere Pitch-Anpassung zu erreichen.

Einige Hauptmerkmale der Gondel-Lidarmessungen machen es notwendig, die Lidarmessung zu verarbeiten, bevor sie für die Turbinensteuerung verwendet werden kann. Zum Beispiel ist die Lidar-Messung die Projektion des dreidimensionalen Windgeschwindigkeitsvektors auf die Lidar-Strahlrichtung, aber der Turbinenrotor interagiert hauptsächlich mit der Windkomponente in Strömungsrichtung. Darüber hinaus liefert das Lidar-System nur begrenzte Messungen an stromaufwärts gelegenen Positionen, während der Turbinenrotor durch seine drei

Flügel mit der stromabwärts gelegenen Turbulenz interagiert. Normalerweise werden die Unterschiede in der Turbulenz an der Anström- und Rotorposition als Windevolution beschrieben. Darüber hinaus kann die Lidar-Messung durch die Abschattung von Rotorblättern oder durch spezielle Wettermuster nicht verfügbar sein. Daher muss eine Studie zur Qualität der Lidar-Windvorhersage durchgeführt werden, um den nutzbaren Teil der vom Lidar gelieferten Windvorhersage zu bestimmen. Ein Filterdesign ist notwendig, um unkorrelierte Informationen in der Lidar-Windvorhersage herauszufiltern. Im Betrieb sind Windkraftanlagen unterschiedlichen atmosphärischen Stabilitätsbedingungen ausgesetzt. Bei unterschiedlichen atmosphärischen Stabilitätsbedingungen können das Spektrum und die Kohärenz des turbulenten Windes variieren. Aufgrund der begrenzten Messmöglichkeiten an stromaufwärts gelegenen Positionen ist die Lidar-Windvorhersage stark von der räumlichen Kohärenz der Turbulenz abhängig. Bisher ist noch unklar, ob die Variation der Turbulenzcharakteristika einen Einfluss auf die Qualität der Lidar-Windvorhersage und die Vorteile der Lidar-gestützten Regelung hat.
Obwohl es bereits kommerzielle Anwendungsfälle für die Lidar-gestützte Regelung gibt, deckt die bestehende Simulationsumgebung für die Lidar-gestützte Regelung die oben beschriebenen Eigenschaften der Lidar-Messungen nicht vollständig ab. Daher ist das Hauptziel dieser Arbeit die Verbesserung der Lidar-Windvorhersagemodellierung und die Bewertung der Vorteile der Lidar-gestützten Regelung unter Verwendung dieser verbesserten Modellierung.
Zunächst wird die Verbesserung dadurch erreicht, dass das Phänomen der Windevolution in konventionelle dreidimensionale Turbulenzmodelle integriert wird: in das Mann- und in das Kaimal-Modell. Dies führt zu vierdimensionalen Turbulenzmodellen. Die Genauigkeit dieser beiden erweiterten Modelle bei der Vorhersage von Turbulenzspektren und räumlichen Kohärenzen wird anhand von Messungen mit einem gepulsten Lidar und einem meteorologischen Meßmast bewertet.
Darüber hinaus werden - auf der Grundlage der erweiterten Turbulenzmodelle - analytische Modelle abgeleitet, die die Korrelation zwischen der mit den Lidarmessungen geschätzen rotoreffektiven Windgeschwindigkeit und der rotoreffektiven Windgeschwindigkeit selbst darstellen. Spektren und Kohärenzen von Turbulenzen in verschiedenen atmosphärischen Stabilitätszuständen werden zusammengefasst und ihre Auswirkungen auf die Qualität der Lidar-Windvorhersage werden untersucht. Ebenfalls wird eine vorläufige Studie zur Frage durchgeführt, ob der Nachlauf einer Windkraftanlage die Lidar-Windvorhersage einer windabwärts gelegenen Windenergieanlage beeinflusst.
Auch wurde in dieser Arbeit ein realistisches Lidar-Modul in ein aeroelastisches Simulationsprogramm integriert, mit dem die Auswirkungen nicht verfügbarer Lidar-Daten auf die Qualität der Lidar-Windvorhersage untersucht werden können. Durch Simulationen mit realistischer Datenverfügbarkeit zeigt diese Studie, dass die Abschattung durch die Rotorblätter und die geringe Datenverfügbarkeit vernachlässigbare Auswirkungen auf die Qualität der Lidar-Windvorhersage haben.

Schließlich werden in dieser Arbeit mit Hilfe des aktualisierten aeroelastischen Simulationsprogramm die Vorteile der Lidar-gestützten Regelung unter verschiedenen Turbulenzcharakteristiken bewertet, die für unterschiedliche atmosphärische Stabilitätszuständen repräsentativ sind. Diese Studie zeigt, dass die Verbesserungen durch die Lidar-gestützten Regelung mit der mittleren Windgeschwindigkeit, dem Turbulenzspektrum, der räumlichen Kohärenz der Turbulenz und den verwendeten Turbulenzmodellen zusammenhängen. Für die NREL 5.0 MW Referenzwindenergieanlage und ein Vierstrahl-Lidar liegen die Vorteile der Lidar-gestützten Regelung vor allem in der Verringerung der Rotordrehzahlschwankungen, der Leistungsfluktuation und der Biegebelastung am Turmfuß. Die Vorteile sind in allen drei untersuchten atmosphärischen Stabilitätszuständen zu beobachten: instabil, neutral und stabil.

1

Introduction

1.1 Motivation

Light detection and ranging (lidar) technology has been adopted in the wind energy industry for decades. In the past, the prominent role of lidar systems in wind energy applications was wind resource and site assessment. However, the reduced cost of lidar systems in recent years has resulted in more interest from the wind energy community in more research topics. As a result, many studies have focused on the use of lidar for wind turbine control, turbulence characterization, power performance assessment, wind farm control, wake measurement, and power prediction.

Conventionally, wind turbines are controlled through feedback control. The rotor rotational speed is typically measured and fed into a feedback controller. The feedback controller then determines the blade pitch angle and generator torque. With a feedback control algorithm, the turbine reacts to the turbulent disturbance after the aerodynamic effects of turbulence have happened to the turbine. Nacelle- or spinner-based lidar can provide a preview of the incoming turbulence; therefore, it enables the turbine to react to the incoming disturbance prior to its impact on the turbine rotor. This has been reported to be beneficial for turbine load reductions. At the end of 2019, lidar technology was first deployed by the turbine manufacturer Goldwind to assist the control system, meaning it was the first commercial application of lidar-assisted wind turbine control. By 2020, 1000 wind turbines from Goldwind were equipped with lidar-assisted control (LAC) systems [1].

Although LAC systems have been used in industrial applications, the existing open-source LAC simulation environment still relies on some assumptions and cannot reflect certain phenomena

that occur in practice. The avoidance of these assumptions in simulations and whether these assumptions have an impact on LAC are still unexplored. This thesis focuses on improving lidar wind preview modeling and assessing the benefits of LAC using an improved lidar wind preview modeling approach.

1.2 Related Studies

Thus far, several studies have investigated lidar wind preview for turbine control and the benefits of lidar-assisted turbine control. Additionally, turbulence evolution, which is a critical phenomenon in lidar wind preview modeling, has been studied by several researchers. The highlights of these studies are summarized in this section.

1.2.1 Turbulence Evolution

Turbulence evolution is defined as the physical phenomenon that the turbulent wind field evolves as it propagates from upstream to downstream. Because lidar systems measure turbulence at upstream positions while the turbine rotor is interacting with turbulence at the downstream rotor position, the evolution of turbulence is an inherent phenomenon in LAC. In practice, turbulence evolution is often quantified by the coherence between the velocity fluctuations at two longitudinally separated positions. Moreover, the longitudinal direction is the direction of turbulence propagation. On the other hand, Taylor's frozen theory [2] assumes that the turbulence field propagates without any change, meaning that turbulence evolution is ignored, and the longitudinal coherence is always 1. When turbulence evolution is considered, a 4-dimensional (4-D) turbulence field is required to describe the temporal velocity fluctuations over a 3-dimensional (3-D) spatial field. With Taylor's frozen theory, a 3-D turbulence field is sufficient because we can simply convert between the longitudinal direction and the time dimension.

The early research on turbulence evolution can be traced to the study by Pielke and Panofsky [3]. They suggested using the exponential coherence model by Davenport [4], originally proposed to describe coherence with vertical separations, to describe the longitudinal coherence. Moreover, Kristensen [5] proposed another expression for longitudinal coherence, which differs from that of Pielke and Panofsky.

More recently, the concept of LAC [6] has spurred research interest in turbulence evolution. Simley and Pao used large eddy simulation (LES), which solves the large-scale fluid motion described by the Navier-Stokes (N-S) equations, to study the longitudinal coherence. Through LES data, Simley and Pao [7] observed that neither Pielke and Panofsky's nor Kristensen's expressions can always correctly represent the longitudinal coherence. However, by incorporating additional parameters to Pielke and Panofsky's expression, they observed that the modified

exponential coherence model has better agreement with the coherence calculated from LES data. Davoust and von Terzi [8] further validate Simley and Pao's model. Through lidar measurements from a beam staring into the longitudinal direction, they found good agreements between the data-based coherence and that based on Simley and Pao's model. After that, Chen et al. [9] parameterized Simley and Pao's model using Gaussian process regression. The parameterized model can provide parameters for the longitudinal coherence based on other observed variables [9]. Except for the empirical exponential coherence-based models, De Maré and Mann [10] extended the 3-D Mann spectral tensor [11] to four dimensions by incorporating Kristensen's model [5]. De Maré and Mann's model has more physical considerations and has thus far been validated using LES simulations.

1.2.2 Lidar Wind Preview for Turbine Control

Currently, the most promising and industrially applied LAC algorithm is the collective pitch feedforward control proposed by [6], which is also the focus of this thesis. With this control strategy, a filter must be designed based on the correlation between the lidar-estimated rotor effective wind speed (REWS) and turbine REWS. A correlation study determines the lidar wind preview quality and can be performed using an analytical turbulence spectral model or by field testing.

Several studies have analyzed the coherence between the lidar- and turbine-based REWSs, using the two turbulence models provided by the International Electrotechnical Commission (IEC) 61400-1 standard [12]. The two turbulence spectral models are the Mann uniform shear model [11], hereafter referred to as the Mann model, and the Kaimal spectra [13] with an exponential coherence model, hereafter referred to as the Kaimal model. The studies on lidar-rotor coherence using the Kaimal model include [14, 6, 15, 16, 17]. These studies considered turbulence evolution using exponential longitudinal coherence models. Held and Mann [18] compared the performance of the two IEC turbulence spectral models in predicting lidar-turbine coherence using measurements from a field experiment that used two commercial lidars and a small-size wind turbine. Liang et al. [19] compared the lidar-rotor coherence, considering both turbulence models and different rotor sizes. Taylor's frozen theory was applied in [18, 19]. Before [20], which was published during this Ph.D. project, no study had analyzed lidar wind preview using the Mann model and considering turbulence evolution.

1.2.3 Evaluation of Lidar-assisted Pitch Feedforward Control

Several studies have evaluated the benefits of lidar-assisted pitch feedforward control using aeroelastic simulations. Early research on lidar-assisted pitch feedforward control includes studies in [21, 22], using the aeroelastic design tool Bladed. In [6], FAST (Fatigue, Aerodynamics, Structures, and Turbulence) was used for the evaluation of LAC. In these studies, the Kaimal model was used. More recent studies by [23, 24] use HAWC2 (Horizontal Axis Wind turbine simulation Code 2nd generation) and the Mann model to assess the LAC benefits. All these studies used the turbulence parameters suggested by the IEC 61400-1 standard [12]. Therefore, the variation in turbulence parameters owing to changes in external atmospheric conditions was not considered.

1.3 Research Objectives and Methodology

The main objective of this thesis is to improve lidar systems' wind preview modeling and evaluate lidar-assisted wind turbine control using improved lidar preview modeling. The improvement is achieved by investigating the following topics:

(a) The turbulence evolution phenomenon is included in the Mann model and the Kaimal model. For both models, 4-D turbulence field generation methods are explored to enable simulating lidar measurements with turbulence evolution. The performance of the evolution-included models in predicting the spatial coherence of turbulence is then validated using site measurements from a pulsed lidar.

(b) The variations in turbulence spectra and spatial coherence (including longitudinal coherence) by different atmospheric stability conditions are investigated using measurements from a meteorological mast and a pulsed lidar.

(c) The lidar wind preview quality in different atmospheric stability conditions is investigated using the improved turbulence models. Here, both free-stream and wake-included turbulent wind fields are investigated. The free-stream turbulence is represented by the spectral turbulence models, and the wake-included turbulence is generated using the dynamic wake meandering (DWM) model.

(d) The impact of lidar measurement unavailability owing to blade blockage and the low carrier-to-noise ratio (CNR) is investigated using the updated lidar module in an aeroelastic simulation tool. A stochastic analysis of the lidar CNR signals is performed using measurements from a pulsed lidar, and the method of generating stochastic CNR time series is studied.

(e) With the updated lidar module in the aeroelastic code OpenFAST, the benefits of lidar-assisted pitch feedforward control are evaluated using both Mann and Kaimal turbulence models, considering different atmospheric stability conditions.

1.4 Thesis Structure

After this introduction (Chapter 1), Chapter 2 provides the background on wind, wind turbines, and wind lidars. Chapter 3, describes details about current 3-D turbulence generation methods for both free-stream and wake-included scenarios, providing some fundamentals for Chapters 4 and 5.

Subsequently, Chapter 4 presents the first primary research outcomes of this thesis. This chapter discusses the methods that extend the Kaimal and Mann models to include turbulence evolution (longitudinal coherence). For the Kaimal model, the exponential longitudinal coherence is considered. A method that uses a two-step Cholesky decomposition is introduced, which can efficiently generate 4-D turbulence fields at multiple parallel lateral-vertical planes. In terms of the Mann model, the turbulence evolution is included using the "eddy lifetime" approach. A novel mathematical expression of eddy lifetime, which can be flexibly adjusted and provides a good estimation of turbulence spectral properties, is presented. Based on both turbulence models, the spectral properties of lidar measurements are derived. With the derived lidar spectral properties, the performances of the two models in predicting turbulence spectra and spatial coherence under various atmosphere stability conditions are evaluated.

For lidar-assisted feedforward control, the lidar preview quality is defined by how correctly the lidar predicts the rotor-effective disturbance or, in other words, the REWS. The control-oriented nacelle- or spinner- lidar system is typically designed to measure several upstream positions. A wind turbine interacts with turbulence through its three blades. Therefore, the spatial coherence of any two points is not sufficient to reflect the preview quality of a lidar system. Instead, the turbine- and lidar-based REWSs should be defined and derived from the turbulence models. Moreover, the correlation between these two REWSs must be investigated. The lidar preview quality is related to the filter design of the feedforward pitch controller. It defines the amount of frequency-domain content in the lidar-estimated REWS that can be used for control. These contents are analyzed in Chapter 5. The turbulence spectral characteristics representative of different atmospheric stability classes are summarized, and the lidar preview quality is analyzed by considering and not considering the upstream turbine wake. A four-beam pulsed lidar system, whose measurement trajectories are optimized for assisting the control system of the 5.0 MW reference wind turbine by the National Renewable Energy Laboratory (NREL), is considered in the preview quality analysis.

To further assess the benefits of LAC in aeroelastic simulations, Chapter 6, describes the updating of the lidar simulation module in OpenFAST. Three new features are integrated to make

the coupled simulation more realistic: turbulence evolution, blade blockage, and adjustable lidar measurement availability. The statistical properties of lidar CNR signals are analyzed with the measurement from a pulsed lidar. The methods that can generate CNR time series, which provide data availability similar to measured data, are proposed. The impact of these three new features on the lidar preview quality is also analyzed.
In Chapter 7, the benefits of LAC are evaluated using the new lidar-integrated OpenFAST. The evaluation is performed considering a typical four-beam pulsed lidar and the NREL 5.0 MW turbine. Three atmospheric stability conditions are considered: unstable, neutral, and stable. The evaluation is performed using both the Kaimal model and the Mann model for the above-rated wind speed operations.
Chapter 8 concludes the thesis and presents recommendations for further research.

1.5 Notations and Conventions

This section explains the notations and conventions used in this thesis to facilitate the reader's understanding of the formulas and derivations.

1.5.1 Font Types

In this thesis, scalars are denoted in standard fonts. Vectors or matrices are represented by **bold fonts**. For example, the wind velocity vector described by three scalars u,v, and w is simply denoted as $\boldsymbol{u} = (u, v, w)$ and the two-dimensional matrix is expressed as

$$\boldsymbol{R} = \begin{bmatrix} R_{11} & R_{12} & R_{13} \\ R_{21} & R_{22} & R_{23} \\ R_{31} & R_{32} & R_{33} \end{bmatrix}. \tag{1.1}$$

1.5.2 Subscripts

The subscripts, written as specific index letters or numbers in standard font, are used to indicate the elements in a vector or matrix. For instance, R_{ij}, with i and j being the indexes, is used to point at an unspecified element in the matrix $\boldsymbol{R}$. R_{11} is the element in the first row and first column. The letters i, j, l, m, and n are used exclusively as *subscript index-letters*.
Frequently, when the subscripts are written as non-numeric standard fonts or letters not included in the *subscript index-letters*, they are used to indicate the information related to the variable. For example, Ω_r is the rotor rotational speed, where "r" is used to indicate "rotor", and a_x is a parameter indicating the longitudinal (x direction) coherence decay.
If a subscript is required to indicate both the element position in a matrix and the information related to the variable, the subscript is separated by a comma; for example, $C_{u,x,ij}$ is an element

with indexes i and j in the two-dimensional matrix $\boldsymbol{C}_{u,x}$. Moreover, the subscripts u and x indicate that the matrix is related to the u velocity component and the x direction, respectively.

1.5.3 Einstein Summation Convention

The Einstein summation convention (ESC) [25] is convenient to avoid lengthy equations. It dictates that when a sub-index (e.g., i or j) is repeated in the same equation twice or more, one sum is used across all the dimensions. Using the incompressible N-S equations as an example, the continuity equation of fluid is expressed as

$$\frac{\partial \tilde{u}_i}{\partial x_i} = 0 \quad \text{(ESC)}, \tag{1.2}$$

which is equivalent to

$$\frac{\partial \tilde{u}_1}{\partial x_1} + \frac{\partial \tilde{u}_2}{\partial x_2} + \frac{\partial \tilde{u}_3}{\partial x_3} = 0. \tag{1.3}$$

Moreover, the conservation of momentum

$$\frac{\partial \tilde{u}_i}{\partial t} + \tilde{u}_j \frac{\partial \tilde{u}_i}{\partial x_j} = -\frac{1}{\rho}\frac{\partial p}{\partial x_i} + \nu_{\text{kv}} \frac{\partial^2 \tilde{u}_i}{\partial x_j^2} + f_i \quad \text{(ESC)}, \tag{1.4}$$

is equivalent to

$$\frac{\partial \tilde{u}_1}{\partial t} + \tilde{u}_1 \frac{\partial \tilde{u}_1}{\partial x_1} + \tilde{u}_2 \frac{\partial \tilde{u}_1}{\partial x_2} + \tilde{u}_3 \frac{\partial \tilde{u}_1}{\partial x_3} = -\frac{1}{\rho}\frac{\partial p}{\partial x_1} + \nu_{\text{kv}} \left(\frac{\partial^2 \tilde{u}_1}{\partial x_1^2} + \frac{\partial^2 \tilde{u}_1}{\partial x_2^2} + \frac{\partial^2 \tilde{u}_1}{\partial x_3^2} \right) + f_1, \tag{1.5}$$

$$\frac{\partial \tilde{u}_2}{\partial t} + \tilde{u}_1 \frac{\partial \tilde{u}_2}{\partial x_1} + \tilde{u}_2 \frac{\partial \tilde{u}_2}{\partial x_2} + \tilde{u}_3 \frac{\partial \tilde{u}_2}{\partial x_3} = -\frac{1}{\rho}\frac{\partial p}{\partial x_2} + \nu_{\text{kv}} \left(\frac{\partial^2 \tilde{u}_2}{\partial x_1^2} + \frac{\partial^2 \tilde{u}_2}{\partial x_2^2} + \frac{\partial^2 \tilde{u}_2}{\partial x_3^2} \right) + f_2, \tag{1.6}$$

$$\frac{\partial \tilde{u}_3}{\partial t} + \tilde{u}_1 \frac{\partial \tilde{u}_3}{\partial x_1} + \tilde{u}_2 \frac{\partial \tilde{u}_3}{\partial x_2} + \tilde{u}_3 \frac{\partial \tilde{u}_3}{\partial x_3} = -\frac{1}{\rho}\frac{\partial p}{\partial x_3} + \nu_{\text{kv}} \left(\frac{\partial^2 \tilde{u}_3}{\partial x_1^2} + \frac{\partial^2 \tilde{u}_3}{\partial x_2^2} + \frac{\partial^2 \tilde{u}_3}{\partial x_3^2} \right) + f_3. \tag{1.7}$$

In the context of N-S equations, because there are three spatial dimensions, i and j are repeated three times. The momentum equations are simply expressed as three lines, and each line corresponds to one i. For the equations in which the ESC applies, "(ESC)" is placed at the end of the equations.

2

Background on Wind, Wind Lidars, and Wind Turbines

This section gives some background knowledge about wind, wind lidars, and wind turbines. This background knowledge will set the stage for the subsequent chapters and guide the reader through the relevant literature.

2.1 Wind

Wind turbines generate renewable electricity by extracting the kinetic energy of wind flow. At the same time, turbulent wind results in turbine structure loads. Therefore, we must understand wind before defining the role of wind lidar in wind energy. This section begins with a general introduction to wind and then outlines the characteristics of turbulence.

2.1.1 Origin of Wind

On a global scale, the wind is a product of the redistribution of heat in the atmosphere. Owing to the curvature of our planet, regions near the equator absorb more solar heat than regions at the poles. Because only one side of the earth is heated by the sun and the distribution of land and ocean is unequal, the unbalanced heating becomes even more complicated. Because of the heat imbalance, the warmer air tends to ascend, whereas the cooler air tends to sink, resulting in different pressure zones. In addition to the pressure system, the earth's rotation causes the Coriolis effect, by which the prevailing wind direction can be observed at a specific place on the

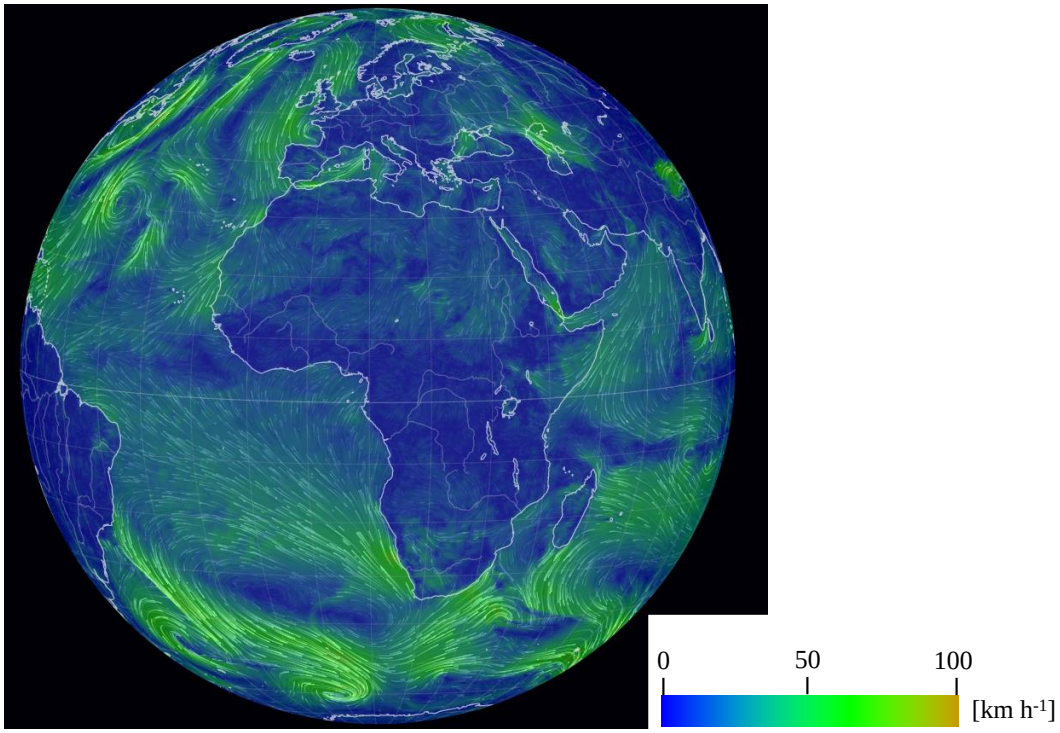

Figure 2.1: An snapshot of the global wind flow on Jan 1, 2021 at the height associated with an atmosphere pressure of 1000 hPa. Source: `https://earth.nullschool.net/`.

planet. All these phenomena can be summarized as the global atmospheric circulation [26]. A snapshot of the semi-global wind flow is shown in Figure 2.1. Close to the equator, the wind in the Atlantic Ocean (west of Africa) tends to converge and flow towards the west. This specific trend is caused by the global atmospheric circulation.

On a smaller scale, winds can result from monsoon circulations caused by thermal low circulations over terrains or high plateaus; they can be produced by sea or land breeze cycles in coastal areas and may occur in the form of canyon winds in highly variable terrains.

2.1.2 Variations in Wind

Winds occur over a wide range across the globe and vary over different spatial and temporal scales. Therefore, we must understand the wind variability at a given site for wind turbine operation.

Frequently, anemometers are mounted on meteorology masts to record the wind time series. The horizontal wind speed over a small volume is recorded using a cup anemometer. An example of an actual horizontal wind speed measurement from a measurement campaign in Bremerhaven, Germany, over the winter of 2009 is shown in Figure 2.2 (see [27] for more details). The total wind speed is the raw measurement recorded by a cup anemometer at a height of 44 m. The 10 min mean value is the average horizontal wind speed over each 10 min interval, and the

fluctuation part is the total wind speed extracted using the 10 min mean. We can observe that the variation in the 10 min mean value is slower and diurnal, whereas each 10 min interval has high-frequency fluctuations.

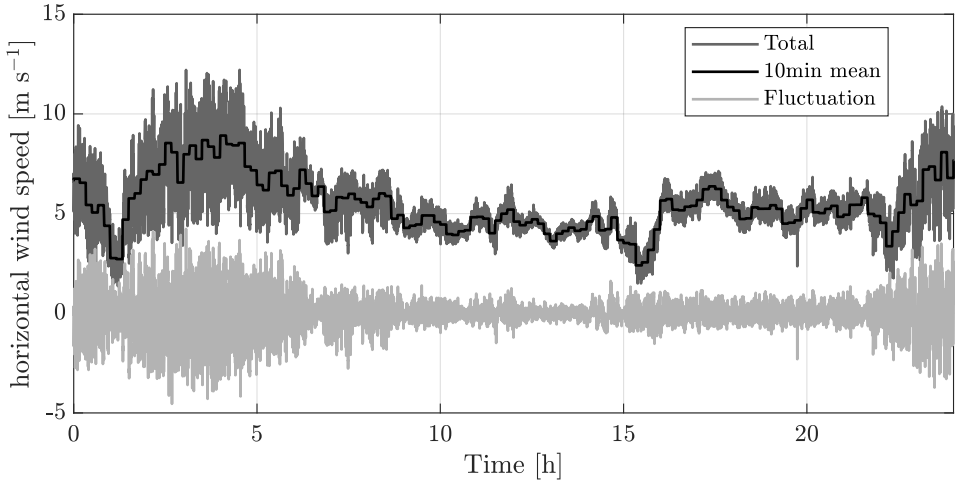

Figure 2.2: The Horizontal wind speed time series from Bremerhaven measurement campaign measured by a cup anemometer at a height of 44m.

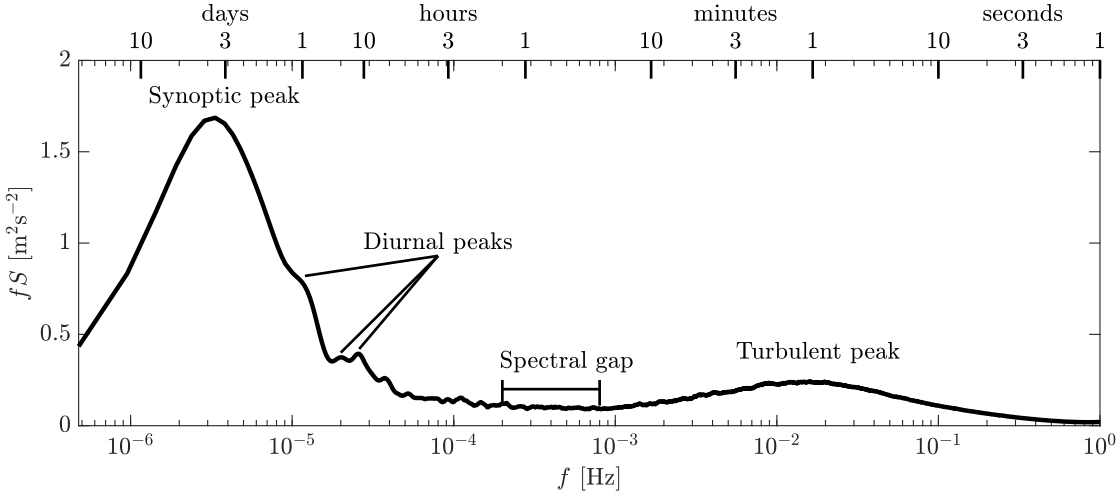

Figure 2.3: The Horizontal wind speed spectrum from Bremerhaven measured by a cup anemometer at the height of 44 m, redrawn based on [6].

To better present the energy of the variations in the frequency (f) domain, Figure 2.3 shows the horizontal wind speed spectrum. Large-scale weather patterns primarily influence the synoptic peak. The diurnal peaks are related to the day-night cycle and the imbalanced heat over land and sea. From 10 min to 1 h, the wind variation is frequently weaker under normal conditions; therefore, this range is often labeled as the spectral gap. Above the frequency associated with the minute scale, another peak is associated with turbulence.

For modern wind turbines, the higher frequency part of wind fluctuation is more important because most of the structure's natural frequencies are in this range in which fatigue loads are excited. The lower frequency part of the spectrum is more important for the power production variation and grid balancing [28]. Owing to the existence of the spectral gap, for wind turbine design, the turbulent and the mean parts of the wind are often characterized by 10 to 30 min intervals. If we characterize them by a longer time interval, we might include some variations contributed by diurnal peaks, which do not have an essential role in the turbine load.

2.1.3 Statistical Representation of Wind

As discussed earlier, the wind variation is typically characterized in 10 min intervals. For wind resource assessment and turbine lifetime load calculation, the probability distribution of the 10 min is important. Moreover, the probability distribution of turbulent fluctuation is vital for turbine load simulation.

Weibull Distribution

Usually, the 10 min mean horizontal wind speed is equivalent to the mean stream-wise wind speed, and the mean cross-wind (lateral) wind speeds are zero. The mean stream-wise wind speed U is observed to follow the Weibull distribution:

$$f_{\mathrm{wb}}(U) = \frac{k_{\mathrm{wb}}}{c_{\mathrm{wb}}} \left(\frac{U}{c_{\mathrm{wb}}} \right)^{k_{\mathrm{wb}}-1} \exp\left(- \left(\frac{U}{c_{\mathrm{wb}}} \right)^{k_{\mathrm{wb}}} \right), \tag{2.1}$$

where k_{wb} and c_{wb} are the shape and scale parameters, respectively. These parameters can vary by site, and they are important for estimating the annual energy production of the turbines. For the same site, they can also vary by height above ground; typically, the parameters fitted from hub-height measurements are used as the reference for resource assessment.

Gaussian Distribution

The fluctuation part of horizontal wind speed can be projected onto the stream-wise (longitudinal) and cross-wind (lateral) directions using the 10 min mean wind direction. Both the stream-wise and cross-wind fluctuations with higher frequencies (denoted as u), namely, the turbulence, are often characterized by the Gaussian distribution (also called the normal distribution):

$$f_{\mathrm{g}}(u) = \frac{1}{\sigma\sqrt{2\pi}} \exp\left(-\frac{(u-\mu)^2}{2\sigma^2} \right), \tag{2.2}$$

where μ is the mean value equivalent to zero because the mean value U is extracted in our specific application, and σ is the standard deviation. When analyzing the probability distribution

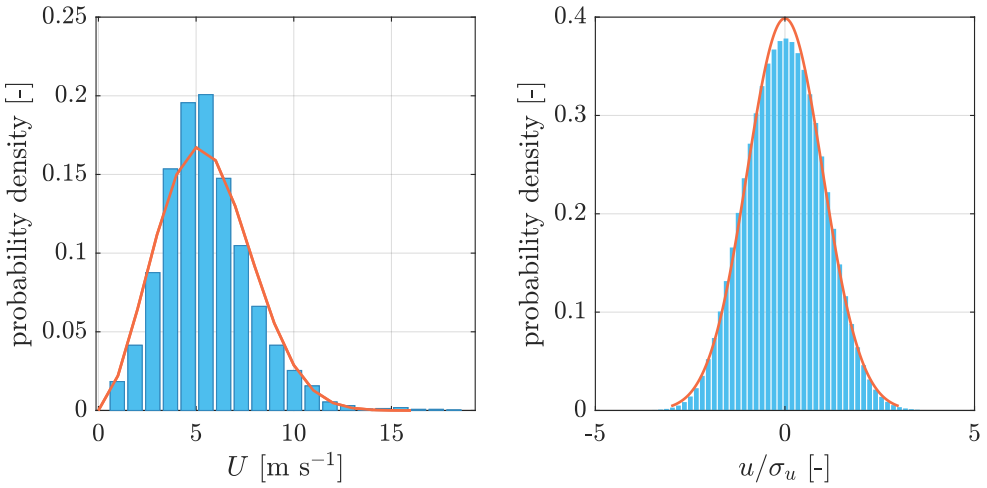

Figure 2.4: Left: probability distribution of the 10 min mean stream-wise wind speed and the fitted Weibull distribution with $k_{\mathrm{wb}} = 2.60$ and $c_{\mathrm{wb}} = 6.23$. Right: probability distribution of the normalized 10 min stream-wise wind speed fluctuation and the fitted Gaussian distribution with $\mu = 0$ and $\sigma = 1$. Both datasets are based on the Bremerhaven measurement campaign using a cup anemometer at a height of 44 m.

of turbulence, the fluctuation u is frequently normalized by its standard deviation σ_u, resulting in a unit standard deviation. This Gaussian distribution of turbulence is an important characteristic as it enables us to generate a stochastic turbulence field using a simple and well-known stochastic process. More details are provided in Chapter 3.

The probability densities of the mean and turbulent winds calculated from the mast anemometer data are compared with the mathematical distribution in Figure 2.4, which shows that the data are in good agreement with the theoretical distributions.

Covariances, Autocorrelations, and Spectra

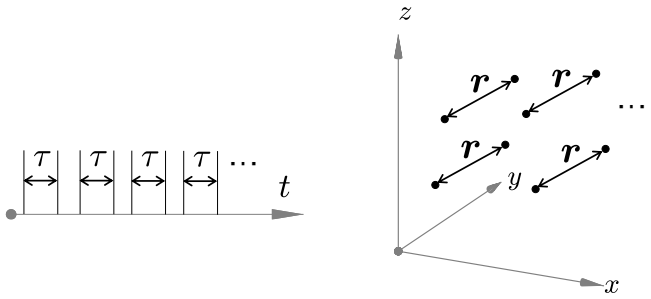

Figure 2.5: Illustrations of the data pairs for covariance calculation. Left: one-dimensional time-dependent data. Right: 3-D spatially distributed data.

The covariance, by definition, is the second-order moment of any two time series u_i and u_j shifted by a time lag τ [28]:

$$R_{ij}(\tau) = \langle u_i(t) u_j(t+\tau) \rangle, \tag{2.3}$$

where $\langle\,\rangle$ denotes the ensemble average. Depending on the time axis, we have many pairs of data that are shifted by τ (Figure 2.5). The ensemble average is applied to these pairs to obtain $R_{ij}(\tau)$. In particular, when the two time series are identical, the covariance becomes an autocorrelation function:

$$R_{ii}(\tau) = \langle u_i(t) u_i(t+\tau) \rangle. \tag{2.4}$$

Assuming the fluctuation part of the turbulence at a certain position is periodic and integrable, by applying the Fourier transform to the covariance, we obtain the cross-spectrum of the two time series:

$$S_{ij}(f) = \int_{-\infty}^{\infty} R_{ij}(\tau) \exp(-2\pi \mathrm{i} f \tau) \mathrm{d}\tau, \tag{2.5}$$

where i is the imaginary unit. When the two time series are equal, we obtain the auto-spectrum S_{ii}. The correlation of two signals in the frequency domain is frequently defined using the magnitude squared coherence:

$$\gamma_{ij}^2(f) = \frac{|S_{ij}(f)|^2}{S_{ii}(f) S_{jj}(f)}. \tag{2.6}$$

A turbulent wind field has significantly more points than two positions. At each position, using the Cartesian coordinate, we can describe the speed vector using three velocity components: the longitudinal u (stream-wise), lateral v (cross-wind), and vertical w components. We take a snapshot of the 3-D velocity field at a particular time and may express the fluctuating part of the velocity field as

$$\boldsymbol{u}(\boldsymbol{x}) = [u(\boldsymbol{x})\, v(\boldsymbol{x})\, w(\boldsymbol{x})] = [u_1(\boldsymbol{x})\, u_2(\boldsymbol{x})\, u_3(\boldsymbol{x})], \tag{2.7}$$

where $\boldsymbol{x} = (x, y, z)$ are the spatial position vectors defined using the Cartesian coordinate system. Similar to the time shift introduced earlier, the covariance of any two turbulence fluctuations in the space can be expressed as

$$R_{ij}(\boldsymbol{r}) = \langle u_i(\boldsymbol{x}) u_j(\boldsymbol{x} + \boldsymbol{r}) \rangle, \tag{2.8}$$

where the indexes i, $j = 1, 2, 3$ now represent the velocity components, and $\boldsymbol{r} = (r_1, r_2, r_3)$ are the separation vectors. Figure 2.5 shows the pairs of turbulence fluctuations with a separation of $\boldsymbol{r}$ in the Cartesian coordinate system. Theoretically, if the field size is infinite, we have an endless number of pairs to obtain the ensemble average for $R_{ij}(\boldsymbol{r})$. A 3-D Fourier transform of the covariance tensor R_{ij} yields the spectral velocity tensor (or spectral tensor in brief) [11]:

$$\Phi_{ij}(\boldsymbol{k}) = \frac{1}{(2\pi)^3} \int R_{ij} \exp(-\mathrm{i}\boldsymbol{k} \cdot \boldsymbol{r}) \mathrm{d}\boldsymbol{r}, \tag{2.9}$$

where $\boldsymbol{k} = (k_1, k_2, k_3)$ are the wavenumber vectors, and $\int \mathrm{d}\boldsymbol{r} \equiv \int_{-\infty}^{\infty} \int_{-\infty}^{\infty} \int_{-\infty}^{\infty} \mathrm{d}r_1 \mathrm{d}r_2 \mathrm{d}r_3$. Subsequently, the one-dimensional (along the longitudinal wavenumber) cross-spectra of any two velocity components with separations Δy and Δz in the y-z plane can be obtained using

$$F_{ij}(k_1, \Delta y, \Delta z) = \int_{-\infty}^{\infty} \int_{-\infty}^{\infty} \Phi_{ij}(\boldsymbol{k}) \exp(\mathrm{i}(k_2 \Delta y + k_3 \Delta z)) \mathrm{d}k_2 \mathrm{d}k_3. \tag{2.10}$$

In particular, the auto-spectrum of one velocity component at one point, usually expressed as $F_{ii}(k_1)$, is obtained by considering $i = j$ and $\Delta y = \Delta z = 0$. The magnitude squared coherence between two velocity components in the same y-z plane is also interested, which can be calculated using [11]

$$\mathrm{coh}_{ij}^2(k_1, \Delta y, \Delta z) = \frac{|F_{ij}(k_1, \Delta y, \Delta z)|^2}{F_{ii}(k_1) F_{jj}(k_1)}. \tag{2.11}$$

Here, we use coh_{ij} for the wavenumber coherence to distinguish it from the frequency coherence γ_{ij}.

2.1.4 Concept of Eddies in Turbulence

This section clarifies the definition of "eddy" in this thesis to explain the terminology "eddy" that appears several times later. In fluid dynamics, an eddy may be explained as a violent swirling motion caused by the position and direction of turbulent flow [29]. In atmospheric turbulence studies, "eddy" does not refer to any specific local distribution of velocity but to an arbitrary local flow pattern that is characterized only by its length scale [30, 31]. The energies of eddies of different sizes are described by a spectrum. The turbulent motion can be superimposed by sinusoidal waves of different wavelengths [30].

To better illustrate this concept, Figure 2.6 shows an example of two-dimensional turbulent flow superimposed by sinusoidal waves. The first velocity field $\boldsymbol{u}_{e_1}$ is composed of two waves that both have a wavelength of 4π but propagate in two perpendicular directions. The velocity field has four half-swirling motions that merge in the center of the field, resulting in a near-zero flow in the center.

The second velocity field $\boldsymbol{u}_{e_2}$ is represented by waves that both have a length scale of $\sqrt{2}\pi$. The waves of the two velocity components propagate in the same direction but have a phase shift of $\pi/2$. Swirling motions are not very clearly observable in the velocity field.

The last velocity field $\boldsymbol{u}_{e_3}$ has perpendicular waves with a size of π, and they are phase-shifted by π. We can observe that the velocity field has many swirling motions, and each of them has a size of π.

Finally, the turbulent flow $\boldsymbol{u}_{\text{turb}}$ is superimposed by the three velocity fields mentioned earlier, for which we can still observe some swirling motions but not as much as in $\boldsymbol{u}_{e_3}$. This example shows that the "eddies" defined as swirling motions in some fluid dynamic literature can be superimposed from sinusoidal waves. In turbulence studies, the term "eddy" is not limited to swirling motion but is generally recognized as waves of different lengths.

However, the turbulent flow in the atmosphere is much more complicated than the example here. Here, the identical amplitude is assumed for all waves. In practice, the amplitudes follow an energy spectrum (e.g., the von Kámán energy spectrum), and their energies are determined by the wavelengths, which are discussed further in the next section.

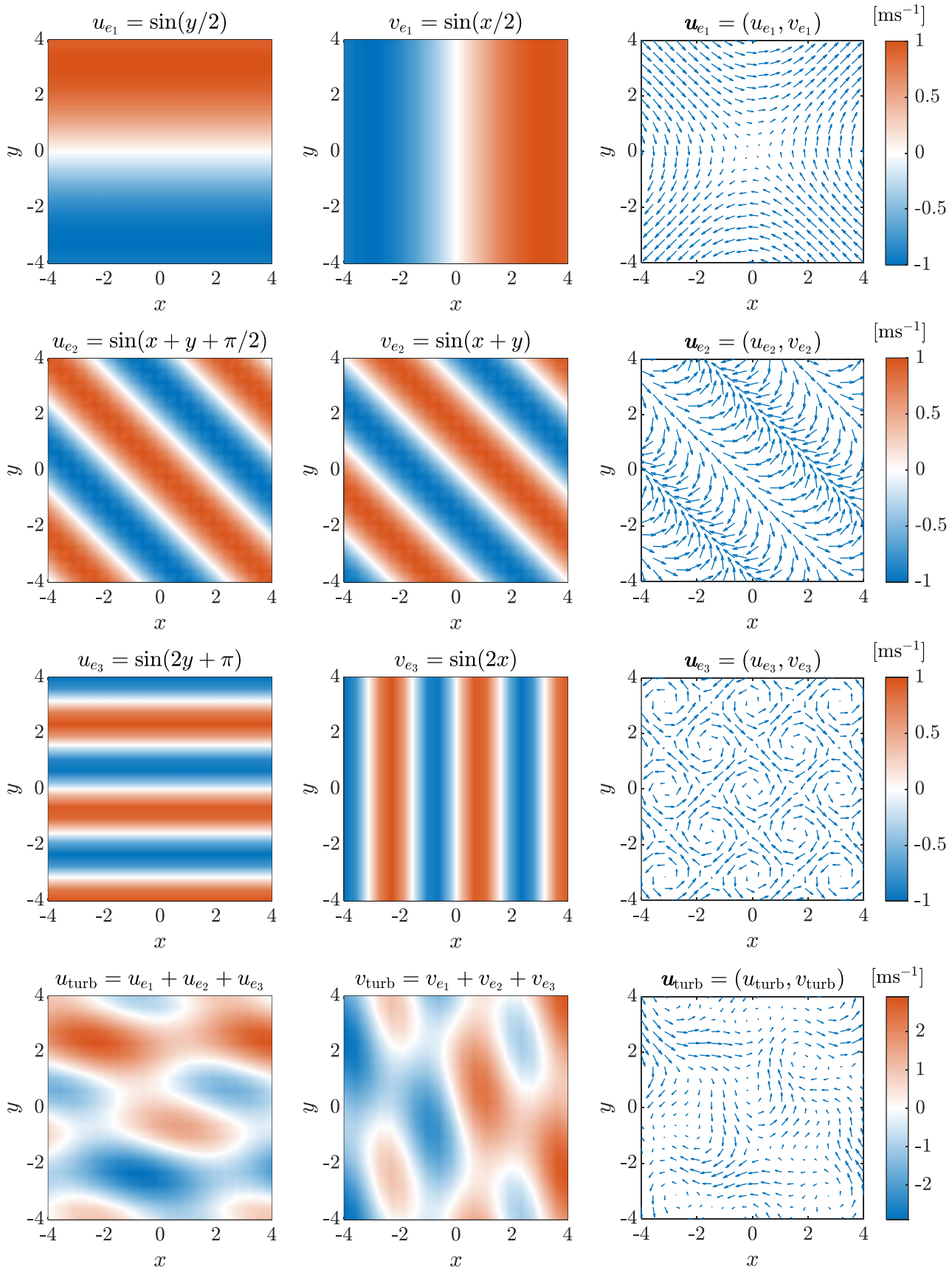

Figure 2.6: An example of eddy superimposition for the turbulent flow $\boldsymbol{u}_{\text{turb}}$. The field is superimposed by eddies with different wavelengths.

2.1.5 Standard Turbulence Spectral Models

In the wind turbine design phase, the turbine performance and load are evaluated using aeroelastic simulations (more details in Section 2.3.2). The function of the turbulence spectral model is to represent the statistical characteristic of the wind variation at a higher frequency for its lifetime (20 to 25 years). Additionally, the turbine blades interact with wind flow over the rotor-swept area; therefore, the turbulence field that covers the rotor area is required for aeroelastic simulation. This section provides an introductory description of the two turbulence models provided by the IEC 61400-1 standard [12].

Kaimal Spectra and Exponential Coherence Model

The Kaimal spectral model [12, 13] is an empirical model that describes the spectra of wind velocity components as

$$S_{ii}(f) = \frac{4\sigma_i^2 \frac{L_i}{U_{\text{ref}}}}{(1 + 6f\frac{L_i}{U_{\text{ref}}})^{5/3}} \tag{2.12}$$

where L_i is the integral length scale, σ_i is the standard deviation, and U_{ref} is the reference wind speed equivalent to hub-height mean wind speed V_{hub}. The indexes i=1,2 ,and 3 represent the u, v, and w components, respectively. The standard deviation is defined from the reference turbulence intensity (TI) I_{ref} as

$$\sigma_1 = \sigma_u = I_{\text{ref}}(0.75U_{\text{ref}} + 5.6), \quad \sigma_2 = 0.8\sigma_1, \quad \sigma_3 = 0.5\sigma_1. \tag{2.13}$$

The reference TI is an indicator for the turbulence class or turbine class with values of 18%, 16% 14%, and 12%, corresponding to Classes A^+, A, B, and C, respectively [12]. The integral length L_i suggested by the IEC 61400-1 standard is

$$L_1 = 8.1\Lambda_1, \quad L_2 = 2.7\Lambda_1, \quad L_3 = 0.66\Lambda_1, \tag{2.14}$$

where Λ_1 is a turbulence scale parameter defined as the wavelength where $fS_{11}(f)/\sigma_1^2 = 0.05$. Note that the Kaimal spectra parameters suggested by the IEC 61400-1 standard are representative of neutral atmospheric stability only. Section 5.1 describes how these parameters can vary by atmospheric stability class. Additionally, the Kaimal spectra expressed by Equation 2.12 are one-sided, such that the variance becomes

$$\sigma_i^2 = \int_0^\infty S_{ii}(f)\mathrm{d}f. \tag{2.15}$$

In addition to the Kaimal spectra, the exponential coherence model (extended from the model proposed by Davenport [4]) is provided to describe the correlation of longitudinal component

fluctuation, i.e.

$$\gamma_{yz}^2(\Delta yz, f) = \exp\left(-2a_{yz}\Delta yz\sqrt{\left(\frac{f}{U_{\text{ref}}}\right)^2 + b_{yz}^2}\right), \quad \text{with} \quad b_{yz} = \frac{0.12}{L_{\text{c}}}, \tag{2.16}$$

where $\Delta yz = \sqrt{\Delta y^2 + \Delta z^2}$ is the separation distance in the lateral-vertical plane separated by Δy in the lateral direction and Δz in the vertical direction, a_{yz} is the coherence decay constant, and L_{c} is the coherence scale parameter. Note that the coherence without a square is used in the IEC standard [12]. However, the y-z plane coherence of v and w components are not provided by the IEC 61400-1 standard. For simplicity, the Kaimal spectra and exponential coherence model are collectively referred to as the Kaimal model in the remainder of this thesis.

Mann Uniform Shear Model

Unlike the empirical Kaimal model, the Mann uniform shear model [11] (hereinafter referred to as the Mann model) is derived from linearized N-S equations and therefore includes more physical aspects. A more detailed derivation of the Mann model is provided in Appendix A.2. Overall, Mann [11, 32] derived the uniform shear model based on the rapid distortion theory and assumed that the turbulence is stretched from the initial isotropic condition by a linear shear profile. Subsequently, an eddy lifetime solution was applied to model the second-order spatial statistics (variance) of the turbulence affected by the shear stretching [11]. For isotropic turbulence, the turbulence statistics are unchanged under rotations and reflections, and the spectra of different velocity components are identical [33, 34].
The von Kámán isotropic spectral tensor is used for the initial non-sheared condition and is expressed as

$$\Phi_{\text{iso},ij}(\boldsymbol{k_0}) = \frac{E(k_0)}{4\pi k_0^4}(\delta_{ij}k_0^2 - k_i k_j), \tag{2.17}$$

where $\boldsymbol{k_0} = (k_1, k_2, k_{30})$ is the initial and non-sheared wavenumber vector that has a magnitude of $|\boldsymbol{k_0}| = k_0$, and the indexes $i, j = 1, 2$, and 30. $E(k_0)$ is the von Kámán energy spectrum:

$$E(k_0) = \alpha\epsilon^{\frac{2}{3}}L^{\frac{5}{3}}\frac{(Lk_0)^4}{(1+(Lk_0)^2)^{\frac{17}{6}}}, \tag{2.18}$$

where ϵ is the rate of viscous dissipation of specific turbulent kinetic energy [11], L is the turbulence length scale related to the size of the eddies containing the most energy [18], and α is the spectral Kolmogorov constant. $\alpha\varepsilon^{2/3}$ formulates an energy level constant valid in the inertial subrange, functioning as a proportional gain to the spectral tensor, and is often adjusted to obtain a specific TI level.
The final shear distorted wavenumber vector is denoted as $\boldsymbol{k} = (k_1, k_2, k_3)$, in which the third

scalar k_3 is related to k_{30} by $k_{30} = k_3 + \beta k_1$. Here, $\beta = \frac{\mathrm{d}U}{\mathrm{d}z}\tau_\mathrm{s}$ is a non-dimensional distortion factor that depends on the "eddy lifetime":

$$\tau_\mathrm{s}(\boldsymbol{k}) = \Gamma\left(\frac{\mathrm{d}U}{\mathrm{d}z}\right)^{-1}(|\boldsymbol{k}|L)^{-\frac{2}{3}}\left[{}_2F_1\left(\frac{1}{3},\frac{17}{6};\frac{4}{3};-(|\boldsymbol{k}|L)^{-2}\right)\right]^{-\frac{1}{2}}, \tag{2.19}$$

where ${}_2F_1()$ is a hypergeometric function, and $\frac{\mathrm{d}U}{\mathrm{d}z}$ is the mean vertical shear profile. The subscript "s" in τ_s means shear. Except for the wavenumber vector, energy level constant $\alpha\varepsilon^{2/3}$ and length scale L, Γ is the last parameter describing the Mann model, which is often described as the anisotropy caused by the shear effect in a near-surface boundary layer [18]. When $\Gamma = 0$, $k_3 = k_{30}$, the turbulence is isotropic [35]. The impact of Γ on the wavenumber magnitude is shown in Figure 2.7. For isotropic turbulence, the wavenumber magnitude is simply a ball. In the distorted scenario (Γ=3.4), the distorted wavenumber magnitude becomes an ellipsoid tilting towards the positive k_1 direction.

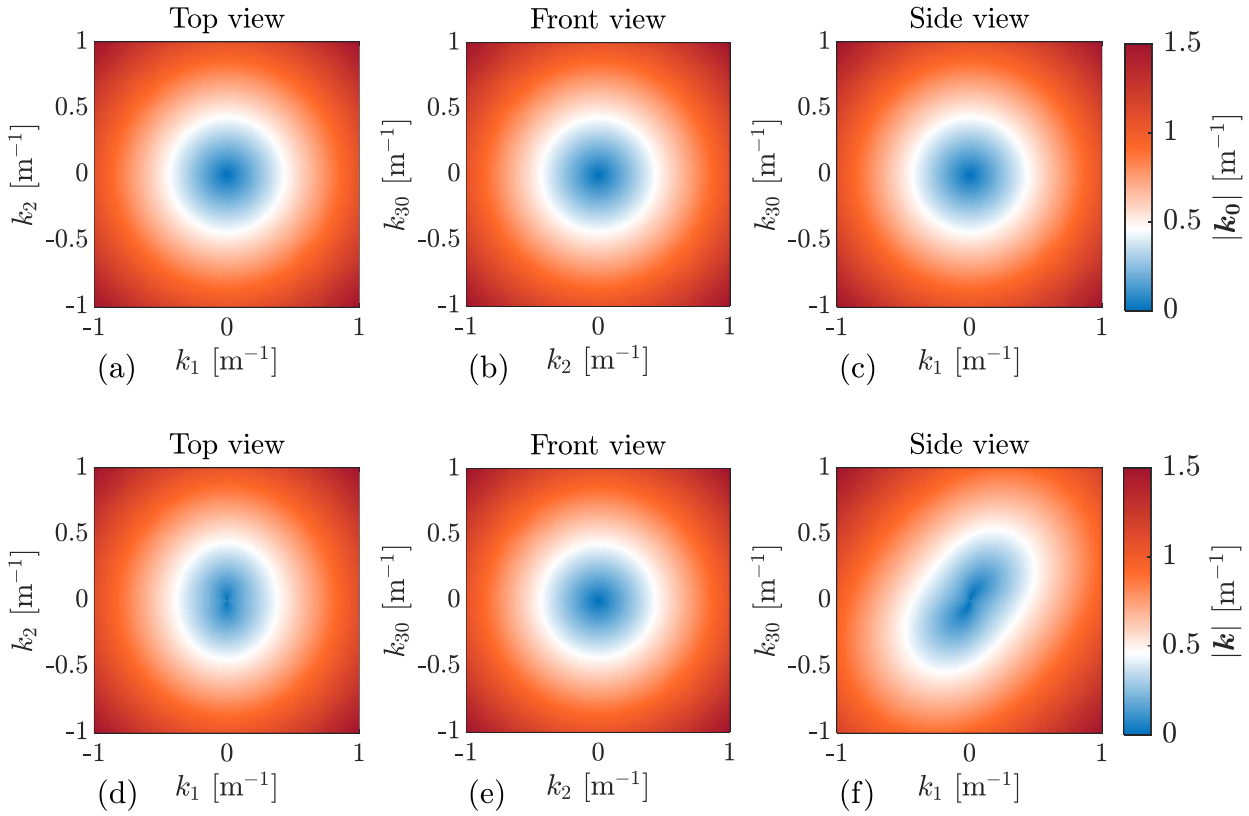

Figure 2.7: Illustrations of the shear distortion effect on the wave number magnitude. (a) to (c): The isotropic scenario with Γ=0. (d) to (f): The shear-included scenario with Γ=3.4. All the views are sliced at $k_1 = 0$, $k_2 = 0$ or $k_{30} = 0$.

Figure 2.8 shows the impact of shear distortion on the magnitude of the turbulent velocity field. The turbulence fields are generated using the Mann method, which is discussed in more detail in Section 3.1.2. In (a) to (c), the field does not appear very different from the three views because the turbulence is homogeneous and isotropic. In the sheared condition indicated by (f), the turbulence is no longer homogeneous, and the shear effect distorts the large coherent structure to arrive first at a higher height z and later at a lower height. In the top view (d), the coherent structure is compressed in the x direction. In the front view (e), the impact caused by the shear effect is not observable. Moreover, Γ impacts the spectra of different velocity components and the spatial coherence of the turbulence field [36].

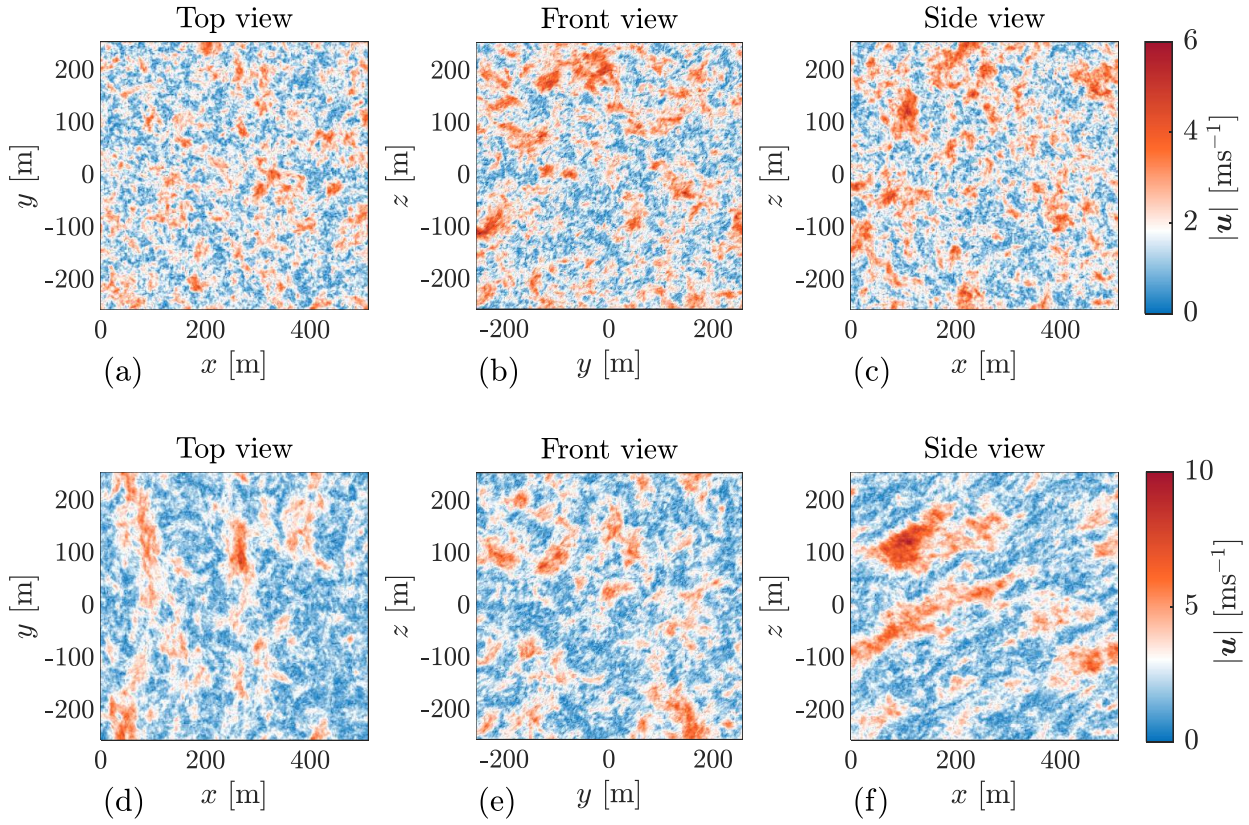

Figure 2.8: Comparisons of the turbulent flow fields in isotropic and shear distorted conditions. Simulated using $L = 49\,\mathrm{m}$ and $\alpha\varepsilon^{2/3} = 0.18\,\mathrm{m}^{4/3}\mathrm{s}^{-2}$. (a) to (c): The isotropic scenario with Γ=0. (d) to (f): The shear-included scenario with Γ=3.4.

With k, L, $\alpha\varepsilon^{2/3}$, and Γ, the components of the sheared spectral tensor (the Mann model) are then calculated using

$$\Phi_{11}(\boldsymbol{k}) = \frac{E(k_0)}{4\pi k_0^4}(k_0^2 - k_1^2 - 2k_1k_{30}\zeta_1 + (k_1^2 + k_2^2)\zeta_1^2), \tag{2.20}$$

$$\Phi_{22}(\boldsymbol{k}) = \frac{E(k_0)}{4\pi k_0^4}(k_0^2 - k_2^2 - 2k_2k_{30}\zeta_2 + (k_1^2 + k_2^2)\zeta_2^2), \tag{2.21}$$

$$\Phi_{33}(\boldsymbol{k}) = \frac{E(k_0)}{4\pi k^4}(k_1^2 + k_2^2), \tag{2.22}$$

$$\Phi_{12}(\boldsymbol{k}) = \frac{E(k_0)}{4\pi k_0^4}(-k_1 k_2 - k_1 k_{30}\zeta_2 - k_2 k_{30}\zeta_1 + (k_1^2 + k_2^2)\zeta_1\zeta_2), \tag{2.23}$$

$$\Phi_{13}(\boldsymbol{k}) = \frac{E(k_0)}{4\pi k_0^2 k^2}(-k_1 k_{30} + (k_1^2 + k_2^2)\zeta_1), \tag{2.24}$$

$$\Phi_{23}(\boldsymbol{k}) = \frac{E(k_0)}{4\pi k_0^2 k^2}(-k_2 k_{30} + (k_1^2 + k_2^2)\zeta_2), \tag{2.25}$$

where

$$\zeta_1 = Q_1 - \frac{k_2}{k_1}Q_2, \quad \zeta_2 = \frac{k_2}{k_1}Q_1 + Q_2, \tag{2.26}$$

with

$$Q_1 = \frac{\beta k_1^2(k_0^2 - 2k_{30}^2 + \beta k_1 k_{30})}{k^2(k_1^2 + k_2^2)} \tag{2.27}$$

and

$$Q_2 = \frac{k_2 k_0^2}{(k_1^2 + k_2^2)^{\frac{3}{2}}} \arctan\left(\frac{\beta k_1 (k_1^2 + k_2^2)^{\frac{1}{2}})}{k_0^2 - k_{30} k_1 \beta}\right). \tag{2.28}$$

The detailed derivation for the spectral tensor components is provided in Appendix A.2. After calculating the spectral tensor, the spectra and coherence can be further calculated using Equations 2.10 and 2.11. The Mann model normally provides a two-sided spectrum such that the variance

$$\sigma_i^2 = \int_{-\infty}^{\infty} F_{ii}(k_1)\mathrm{d}k_1. \tag{2.29}$$

In practice, the wavenumber spectra are converted to the frequency spectra assuming Taylor's frozen hypothesis, which enables us to replace the longitudinal wavenumber with the frequency using $k_1 = 2\pi f / U_{\mathrm{ref}}$.

2.2 Wind Lidar

A wind lidar is an optical remote sensing device for capturing wind information in the atmosphere. Typical commercial wind lidars can measure the wind from dozens of meters to several kilometers. Lidar systems sense the wind using emitted laser beams. They can perform measurements over a large space by adjusting the beam directions and the measurement position along the laser beam. Compared with conventional meteorology mast towers, ground-based wind lidar can be more flexibly deployed and does not require additional robust supporting structures. In offshore wind energy applications, for which erecting a meteorological mast is more expensive, the lidar is becoming a preferred wind measurement device.

2.2.1 Applications of Wind Lidar

A wind lidar has various applications outside the wind energy section, for example, (a) turbulence measurement around buildings or bridges[1] [37], (b) real-time monitoring of unusual atmospheric flow patterns over airports to improve air safety[1], and (c) wind measurement from space using satellite lidar for weather forecast and resource assessment[1].
For wind energy, wind lidar has various types and is applied from different perspectives. Ground-based lidars are frequently used for site resource assessment, and they are more attractive than conventional meteorology mast towers if the measurement site is less accessible or a wind profile at a very high height is required [38]. Nacelle-mounted lidars can be used for wind turbine control, inflow turbulence characterization, power performance characterization, and turbine wake tracking. Long-range scanning lidars can measure up to several kilometers and are therefore often used in wind farm wake observations or power production forecasts.

2.2.2 Measurement Principles of Wind Lidar

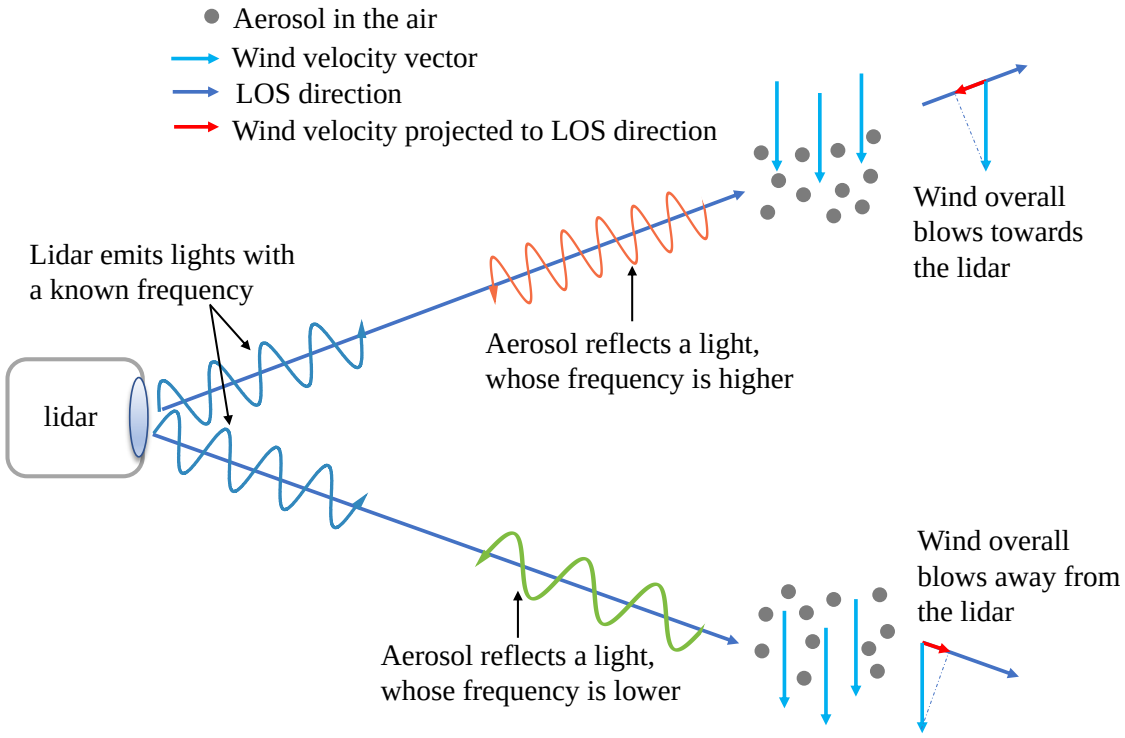

Figure 2.9: Illustration of the heterodyne detection-based lidar measurement principle [39].

Wind lidars rely on the Doppler effect (technically called "laser Doppler anemometry"). Figure 2.9 shows the basic principle of lidar measurement that uses heterodyne detection. The

[1]These research topics were investigated by other Early Stage Researchers within the Lidar Knowledge Europe (LIKE) project, see `https://www.msca-like.eu/esr-projects`.

principle of heterodyne detection is that a local oscillator (laser source) is shifted by a certain frequency, which facilitates the detection of whether the reflected frequency is higher or lower than the source frequency [39]. Wind flow causes the movement of aerosols suspended in our atmosphere. Lidar emits laser light into the atmosphere, which is then back-scattered by the aerosols. The detector then receives the back-scattered light. Based on the Doppler effect, a frequency shift (or Doppler shift) proportional to the aerosol speed will be imparted to the received light. By comparing the frequency of the emitted light (f_e) with that of the received light (f_r), the aerosol speed can be determined. The wind speed is then assumed to be equivalent to the aerosol speed. Because the lidar can only observe the Doppler effect in the line-of-sight (LOS) direction, lidar devices only measure the wind speed projected onto the LOS direction (Figure 2.9), which is often called LOS speed (v_los) or radial wind speed. The LOS speed can be determined by the frequency shift using

$$v_\mathrm{los} = \frac{\lambda_\mathrm{L}(f_\mathrm{r} - f_\mathrm{e})}{2}, \tag{2.30}$$

where λ_L is the laser wavelength.
Lidar does not measure a single point but a probe volume because the laser beam interacts with aerosols within a volume in the atmosphere. In other words, the lidar does not directly measure a unique Doppler frequency shift but a spectrum contributed by all LOS speed fluctuations of aerosols inside the probe volume. Therefore, depending on the emitted laser types, wind lidars can be classified as continuous wave (CW) or pulsed lidars. The volume measurement characteristics depending on the lidar types are explained further.

Continuous Wave Lidar

The CW lidar focuses on a continuously transmitted laser beam at a certain position and detects the back-scattered signals continuously to determine the Doppler shift [38]. By adjusting the telescope, the CW lidar can shift to the next measurement position. The volume of aerosols contributing to the Doppler shift depends on the focus distance from the lidar origin, laser wavelength, and aperture surface. The laser wavelength can be considered constant, but the volume increases quadratically with focus distance [39]. Thus, the volume averaging effect is more significant when the CW lidar focuses on far-away positions. Figure 2.10 shows the typical signal processing chain for CW lidar systems. First, the detector records a time series split into many blocks. The Fast Fourier Transform (FFT) is applied to each block to estimate the power spectrum. Thereafter, all spectra from all blocks are averaged, and then the LOS speed is obtained from the averaged spectrum using Equation 2.30. Several methods can be used to determine the LOS speed from the averaged spectrum, such as the centroid, median, or maximum value [40]. The centroid method is more widely used.

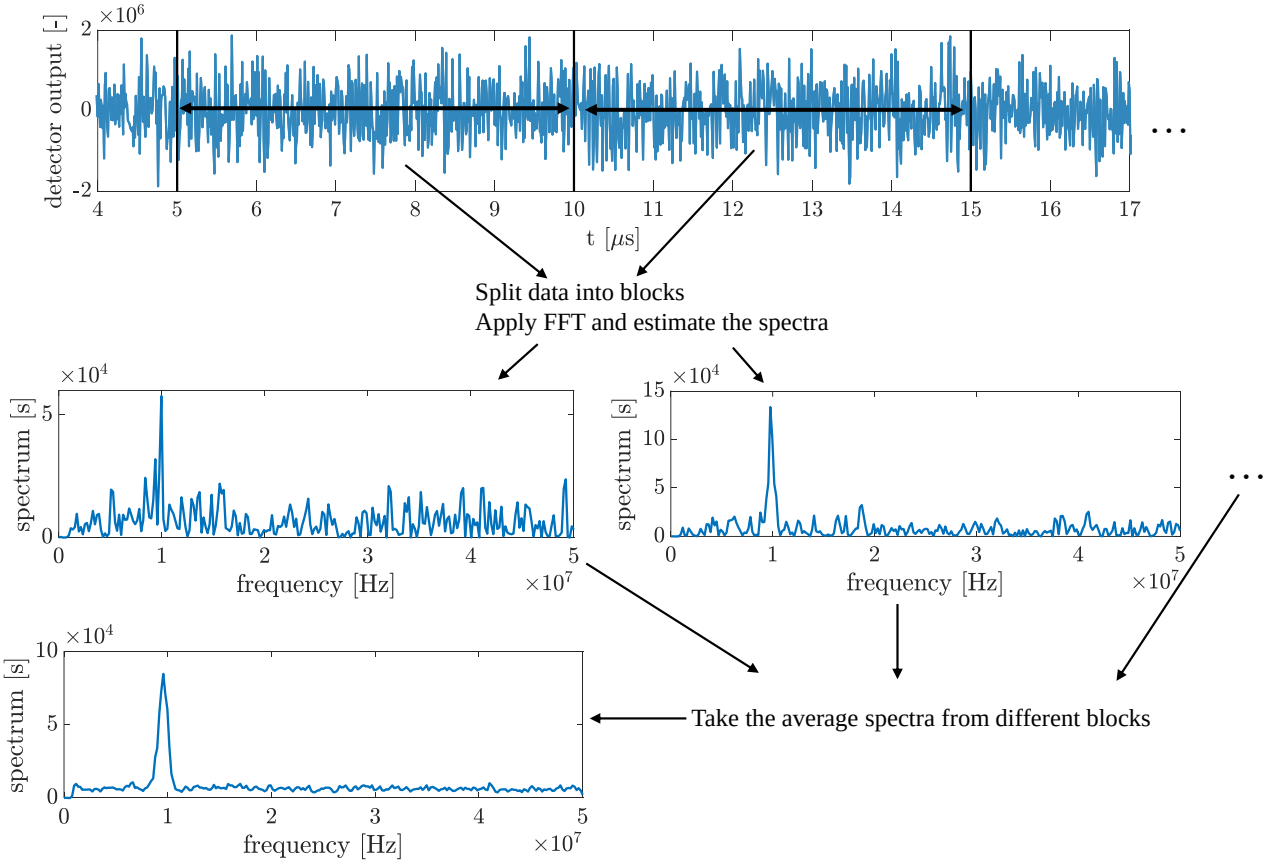

Figure 2.10: A typical signal processing flowchart for the CW lidar systems.

Pulsed Lidar

The pulsed lidar does not emit light continuously but intermittently as pulses. The volume averaging effect for pulsed lidar does not result from focusing the light. When a pulse light is emitted, it travels toward the atmosphere and is back-scattered continuously. The photons back-scattered at larger distances travel farther than those back-scattered at smaller distances. Assuming that the speed of light is constant, the time recorded by the detector is proportional to the distance that the photons have traveled, thus representing the back-scatters from different spatial positions along the laser beam. Figure 2.11 shows the typical signal processing flowchart for pulsed lidar systems. The detector time series is first split into different blocks that represent various measurement range gates (denoted as distance in the bracket). The size of each block determines the volume averaging effect. The FFT is applied to each range gate to estimate the power spectrum. The next pulse is then emitted, and a similar procedure is used to obtain the spectrum for each block. When the spectra from thousands of pulses are obtained, the spectra for each measurement gate are averaged to obtain the averaged Doppler spectrum. The LOS speed at each range gate is eventually determined from the averaged spectrum.

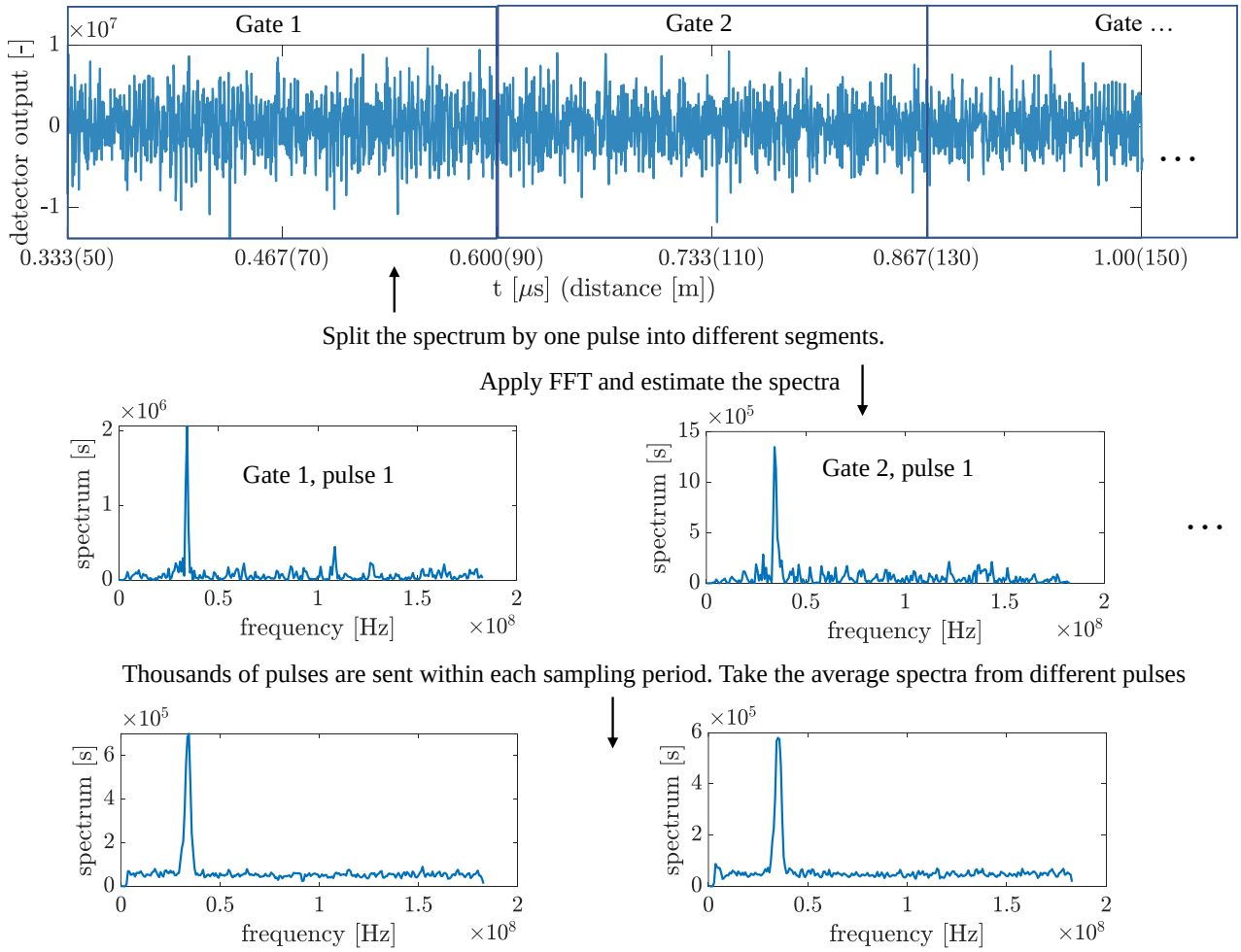

Figure 2.11: A typical signal processing flowchart for pulsed lidar systems. Note that the light travels twice the measurement distance because of the round trip.

2.3 Wind Turbines

This section provides general background on the development of modern wind turbines. The role of aeroelastic simulation in turbine design and load assessment is discussed. An open-source research-oriented reference turbine controller is introduced; it is selected as the baseline controller and modified to integrate LAC algorithms. Finally, the general properties of wind turbine wakes are presented.

2.3.1 Overview of Wind Turbine Development

Today, wind turbines already have an important role in the energy system and will continue to as we move toward net-zero greenhouse gas emissions [41]. By 2020, 15% (on average) of electricity consumption was generated from wind turbines in the European Union. The wind power penetration was 56% in Denmark, 36% in Lithuania, 35% in Ireland, 23% in Portugal, 24% in the UK, 23% in Germany, 20% in Spain, 18% in Greece, and 16% in Sweden. Outside Europe, Uruguay achieved a penetration rate of 40%, the United States 8%, and China 6%[2]. In 2021, 93.6 GW of new wind capacity was installed, for which China contributed 50.9%. The Global Wind Energy Council expects that the global wind power capacity will continue to grow at a rate of 6.6% over the next five years, meaning that 557 GW will be newly installed over the next five years [41].
Compared with the first generation of wind turbines, modern wind turbines now have significantly larger rotors and can produce much more electricity. The prototype of the modern three-bladed upwind wind turbine dates back to 1957, when Johannes Juul designed a wind turbine with a rotor diameter of 24 m and a power of 200 kW at Gedser, Denmark. This is why the three-bladed upwind wind turbine is often referred to as the "Danish design." In April 2022, Vestas released the V172-7.2MW turbine, which has the highest rated power of 7.2 MW and a rotor diameter of 172 m. In June 2022, Goldwind began the onsite testing of the GWH 191-4.0MW turbine, which has a rotor diameter of 191 m. Up to the time of writing this thesis, these are the largest onshore turbines in terms of rated power and rotor size. For offshore turbines, the currently largest commercially deployed turbine is the SG 11.0-200 DD by Siemens Gamesa, which has a diameter of 191 m and rated power of 11 MW. The largest offshore being tested onsite is the SG 14-222 DD again by Siemens Gamesa with a diameter of 222 m and rated power of 14 MW. Another 14 MW machine, Haliade-X by GE Wind Energy, is under testing and has a rotor diameter of 220 m. In addition, the V236 15 MW turbine by Vestas with a diameter of 236 m is being installed for testing. Among the turbines in the conceptual design stage, Mingyang Smart Energy announced that they are developing a 16 MW turbine prototype that has a diameter of 242 m. As the turbine rotor becomes larger, the blades interact with turbulence covering a larger spatial area. To investigate the wind flow in front of the large rotor turbine, in June 2022, Siemens Gamesa installed the ZX TM (by ZX Lidars) on the nacelle of the SG 14-222 DD turbine.

[2]The official documentation can be accessed via `https://en.wikipedia.org/wiki/Wind_power_by_country`, last access 30 September 2022

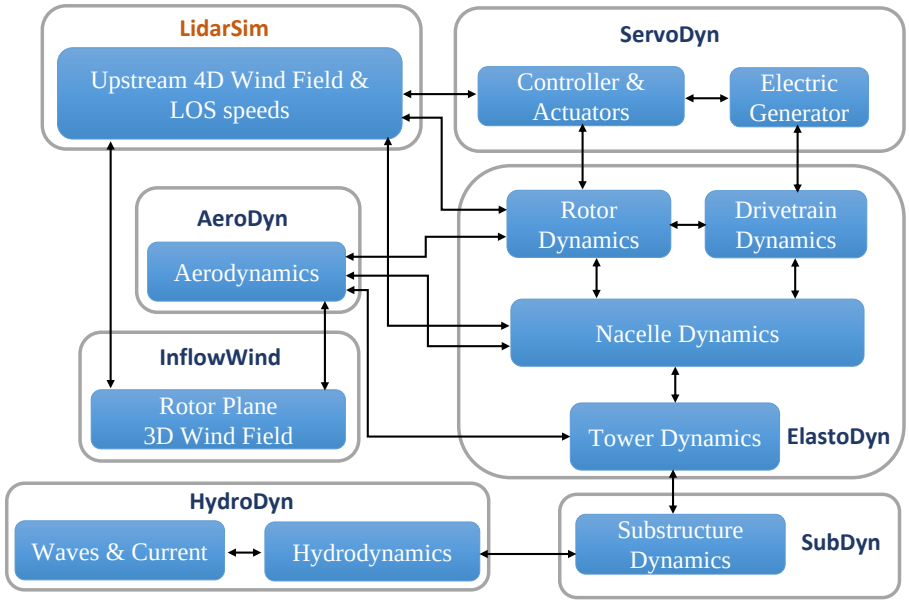

Figure 2.12: An overview of the OpenFAST (v3.0) modules used in this study. The "LidarSim" module was updated within this study. The arrows indicate the direct interaction between the two modules. Redrawn based on [46].

2.3.2 Aeroelastic Simulation: OpenFAST

The response of a wind turbine to an incoming wind flow is frequently assessed using aeroelastic simulation. It couples effects such as aerodynamic, structural dynamic, hydrodynamic, control, and electrical system (servo dynamic) [42]. In the wind turbine design stage, aeroelastic simulation is a reliable tool to validate the design solution. Because of its accuracy at the system level, aeroelastic tools are also used for turbine design certification [43, 44, 6].
In this study, the open-source aeroelastic code OpenFAST was used. OpenFAST is based on FAST version 8 [45] but is transited to a modular framework that better supports open source development[3]. Figure 2.12 shows an overview of the modules included in the OpenFAST tool used in this research. Each module will be described as follows.

InflowWind

The InflowWind module provides the external undisturbed wind flow for the simulation. The undisturbed wind flow is provided to the AeroDyn module as a 3-D (y,z,t) wind field. Because the rotor structural motion is in reality 3-D (x,y,z), Taylor's frozen hypothesis [2] is applied to obtain the wind flow in a 3-D space for each time step.

[3]The official documentation can be accessed via `https://openfast.readthedocs.io/en/main/index.html`, last access 30 September 2022

LidarSim

The LidarSim module is a novel module that has not been merged into the OpenFAST official release thus far. It was initially developed by Stuttgart Wind Energy (SWE) of the University of Stuttgart based on FAST (version 8.16 sFunction). After that, it was updated to the OpenFAST executable version 2.4[4] by SOWENTO GmbH. In this study, the LidarSim module was updated (in OpenFAST version 3.0) to include several new features to make the coupled simulation more realistic. The LidarSim module primarily aims to simulate realistic lidar LOS speed measurements that can be further processed for turbine control. To simulate the LOS speed measurement without Taylor's frozen theory, one must provide the upstream 4-D turbulence fields. Moreover, the upstream turbulence is correlated with but not equal to the rotor plane 3-D turbulent field. In addition, for a nacelle-mounted lidar, the nacelle motion, which drives the movement of the lidar, must be considered because the movement of the lidar itself influences the LOS speed measurement. In addition, interaction with rotor dynamics should be considered for nacelle-based lidar. The laser beam of the forward-looking lidar might be blocked by the turbine blade, at which point the LOS speed measurement cannot be retrieved. Further details of the new LidarSim module are provided in Chapter 6.

Aerodynamic

The aerodynamic module (AeroDyn version 15) calculates the aerodynamic loads on both the blades and tower [47]. At each time step, AeroDyn reads the undisturbed wind flow and structural motions and then uses blade elemental momentum (BEM) theory to calculate the aerodynamic loads. The structural motion of the turbine is provided by the ElastoDyn module.

ElastoDyn

For an onshore turbine, the structural dynamics are fully simulated by the ElastoDyn module. Currently, the dynamic of the foundation is not yet included [46]. The turbine structural dynamics are simulated by combining multibody simulation and modal analysis. The blades and tower dynamics are simulated using modal analysis (modal approach) covering the most important degrees of freedom (DOFs): (a) first and second-order blade flap-wise modes, (b) first edgewise blade mode, (c) first and second fore-aft tower bending modes and (d) first and second side-to-side tower bending modes. For the other components (nacelle, generator, shaft, and hub), the multibody simulation is applied to obtain the dynamics. Except for the above-mentioned DOFs, the drivetrain rotational, the generator azimuth, and the yaw DOFs are implemented in ElastoDyn.

[4] commit 829511a on 13 March 2020, `https://github.com/sowentoDavidSchlipf/openfast/tree/f/lidarsim`

SubDyn and HydroDyn

The SubDyn and HydroDyn modules are specific for offshore wind turbine simulations. SubDyn solves the structural dynamics for multimember fixed-bottom substructures. It supports substructure types such as monopiles, tripods, jackets, and other lattice types [48]. HydroDyn is the hydrodynamics module that is applicable to both fixed-bottom and floating offshore substructures. It can generate waves internally and calculate the hydrodynamic loads using a potential-flow theory solution, a strip-theory solution, or a hybrid combination of these two. In this thesis study, the SubDyn and HydroDyn modules were not activated because only the onshore scenario was considered in the aeroelastic simulations.

ServoDyn

The ServoDyn module primarily contains the turbine controller and electrical generator. Inputs to ServoDyn include the turbine structure motions such as rotor speed, tower top acceleration, and blade tip clearance (which can be measured by remote sensing), or reaction loads such as bending moments at the blade roots. The outputs include the turbine blade pitch angles, generator torques, and shaft breaking torque. ServoDyn supports the bladed style interface dynamic link library (DLL), which enables users to program the controllers and actuators dynamics [49].

2.3.3 Wind Turbine Control

The wind turbine control system includes the supervisory controller, real-time closed-loop controller, and safety control system [6]. For regular operation, the closed-loop controller has a prominent role. The control system receives input signals such as generator speed (Ω_{g}), tower top acceleration, and wind measurements from nacelle anemometers and generates output signals. The output signals can include blade pitch angles (θ), generator torque (M_{g}), yawing degrees, and brake activation commands [50]. The main focus of this thesis is lidar-assisted pitch feedforward control, which is activated for wind speeds above the rated value. For better code accessibility, the recently developed Reference Open-source Controller: (ROSCO, version 2.6.0) by NREL [51] was used as the reference feedback-only (FB-only) controller for the simulations in this thesis. In the following, the feedback controller of ROSCO and modified feedforward+feedback (FFFB) pitch controllers are introduced. Details about other control blocks are available in [51].

Feedback Only Controller

A typical variable-speed wind turbine is controlled by the blade pitch and generator torque controllers. ROSCO uses a proportional-integral (PI) controller for the pitch control in operations above rated wind speed, which can be expressed as

$$\theta_{\mathrm{FB}} = k_{\mathrm{p}}(\Omega_{\mathrm{gf}} - \Omega_{\mathrm{g,ref}}) + \frac{k_{\mathrm{p}}}{T_{\mathrm{I}}} \int_0^t (\Omega_{\mathrm{gf}} - \Omega_{\mathrm{g,ref}}) \mathrm{d}\tau \tag{2.31}$$

where θ_{FB} is the FB pitch command value, Ω_{gf} is the measured and low-pass filtered generator speed, $\Omega_{\mathrm{g,ref}}$ is the generator speed control command, k_{p} is the proportional gain, and T_{I} is the integrator time constant. The pitch controller is only active above the rated wind speed, and k_{p} and T_{I} are scheduled to have a constant closed-loop behavior through gain scheduling [51]. For the NREL 5.0 MW wind turbine used in the remainder of this thesis, the desired damping and angular frequency were tuned to be 0.7 and 0.5 rads^{-1}, respectively.
In terms of generator torque control in the above-rated operation, the option of constant power mode was selected in the simulations of later chapters. With the constant power mode, the generator torque command (M_{g}) is set according to the low-pass-filtered generator speed, the rated electrical power (P_{rated}), and the generator efficiency (η) by $M_{\mathrm{g}} = P_{\mathrm{rated}}/\eta\Omega_{\mathrm{gf}}$. This constant power mode ensures that the lower-frequency fluctuation of electrical power is attenuated. See [51] for a more detailed description of the reference controller.

Feedforward + feedback Controller

Based on the lidar wind preview, a REWS can be derived and used to provide a feedforward pitch signal. The forward pitch signal can be simply added to the conventional FB control [6], which is often referred to as lidar-assisted collective pitch feedforward control(CPFF). In addition to CPFF, other LAC concepts have been presented in the literature [52, 6, 53]. However, CPFF is currently the most promising technology, and it has been deployed in commercial projects [54]. Thus, CPFF is considered when evaluating the benefits of LAC in this study.
In CPFF, the feedforward pitch reference value is obtained by

$$\theta_{\mathrm{FF}} = \theta_{\mathrm{ss}}(u_{\mathrm{LLf}}), \tag{2.32}$$

where u_{LLf} is the filtered REWS estimated from lidar measurements and θ_{ss} is the steady-state pitch angle as a function of steady and uniform wind speed u_{ss} [6]. The steady-state pitch curve is often determined by running aeroelastic simulations using uniform and constant wind speeds with FB-only control. The lidar-estimated REWS is defined in detail in Section 5.2. Figure 2.13 shows the general control diagram with the lidar-assisted pitch feedforward control, where only the pitch feedforward signal θ_{FF} is added compared with the conventional control diagram. In

practice, the time derivative of the pitch feedforward signal $\dot{\theta}_{\mathrm{FF}}$ is fed into the integral block of the feedback PI controller. This yields the overall collective pitch control reference as

$$\theta_{\mathrm{ref}} = \theta_{\mathrm{FB}} + \int_0^t \dot{\theta}_{\mathrm{FF}} \mathrm{d}\tau. \tag{2.33}$$

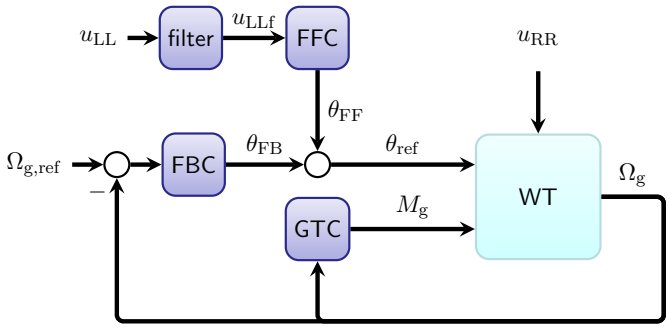

Figure 2.13: The overall control diagram of a Feedforward + feedback Controller. FFC: feedforward pitch controller, FBC: collective feedback pitch controller, GTC: generator torque controller.

To filter the lidar estimated REWS u_{LL}, a first-order low-pass filter with the following transfer function:

$$G_{\mathrm{LPF}}(s) = \frac{2\pi f_{\mathrm{cutoff}}}{s + 2\pi f_{\mathrm{cutoff}}}, \tag{2.34}$$

is applied to filter the u_{LL} signal. Here, $s = 2\pi f\mathrm{i}$ is the complex frequency. The cutoff frequency f_{cutoff} is selected based on the frequency-domain correlation between the lidar and turbine, which is presented in Section 5.2.

Because lidar provides the estimated REWS in the future, the buffer time of lidar-estimated REWS should be carefully designed to ensure the pitch feedforward signal is activated not too late or too early. To achieve this target, the pitch feedforward signal is recorded in a time data buffer, and the signal that has a time close to the buffer time is activated. The buffer time can be determined using

$$T_{\mathrm{buffer}} = T_{\mathrm{lead}} - T_{\mathrm{filter}} - T_{\mathrm{pitch}} - \frac{1}{2}T_{\mathrm{lidar}}, \tag{2.35}$$

where T_{lead} is the leading time of a specific lidar range gate measuring in front of the turbine, T_{filter} is the pitch actuator delay, T_{window} is the half of the lidar full scan time, and T_{filter} is the time delay introduced by filtering the lidar-estimated REWS.

The leading time can be calculated using the mean wind speed and the longitudinal separation of the lidar range gate, i.e., $T_{\mathrm{lead}} = \Delta x / U_{\mathrm{ref}}$, assuming the turbulence propagates by the mean wind speed.

Half of the lidar full scan time is used because a moving average time window is applied to the LOS speed measurements from one full scan. The phase delay property of the time averaging filter indicates that the time delay is simply the half of averaging time [55].

The time delays of the pitch actuator and filter can be both calculated using the frequency responses of their transfer functions as

$$T_{\text{filter}}(f) = \theta_{\text{filter}}(f)/(360f), \quad \text{and} \quad T_{\text{pitch}}(f) = \theta_{\text{pitch}}(f)/(360f). \tag{2.36}$$

where θ_{filter} and θ_{pitch} are the phase responses (lagging) of the filter and pitch actuator transfer functions in degrees, respectively. Both T_{filter} and T_{pitch} are functions of frequency. For the NREL 5.0 MW wind turbine, their values at 0.08 Hz are selected for the feedforward controller because the turbine rotor speed has more fluctuations at this frequency (see Chapter 7). The pitch actuator model is included in the ROSCO (version 2.6.0) controller, and it is modeled as a second-order system with a natural frequency of 1 Hz and a damping ratio of 0.7 [56].

In addition, a threshold is applied to the feedforward pitch command to ensure that it is only activated when the lidar-estimated REWS is above $14\,\text{ms}^{-1}$. The reason for this consideration is that the pitch curve has a much higher gradient with respect to wind speed in the wind speed range between $12\,\text{ms}^{-1}$ and $14\,\text{ms}^{-1}$ [6], where the turbine thrust force is the highest. If the feedforward pitch is activated only depending on the lidar-estimated REWS, a short interval of wind increase or decrease in this range can cause a large pitch rate, followed by a significant change in rotor thrust force. The change in thrust can impose additional loads; therefore, the benefits of LAC are offset by the additional load caused by these pitch actions.

Controller Implementation in Aeroelastic Simulations

The Bladed-style interface [49] is used to configure lidar-assisted control (LAC) in the OpenFAST aeroelastic simulation. The interface is responsible for exchanging variables between the OpenFAST executable and external controllers compiled as DLLs. A main open-source DLL (written in FORTRAN) called "wrapper DLL" has been programmed to make each controller module as modular as possible. The main function of the wrapper DLL is to call the sub-DLLs in a specified sequence. Note that all the sub-DLLs operate based on the same variable exchange pattern specified by the Bladed-style interface. This means that each sub-DLL can also be called independently and directly by OpenFAST. Alternatively, several sub-DLLs can be called by the wrapper DLL sequentially. An overview of the LAC and OpenFAST interfaces is shown in Figure 2.14. Three sub-DLLs are called by the wrapper DLL following the sequence from top to bottom as shown in the figure.

The first DLL is responsible for lidar data processing (LDP), which processes the lidar LOS speed measurement v_{los} and provides the lidar-estimated REWS. The second module feedforward pitch (FFP) filters and times the lidar-estimated REWS, and outputs the collective pitch rate. In the final step, the pitch rate is fed into the integrator of the PI controller in ROSCO. The ROSCO source code has been adjusted to enable it to accept the feedforward pitch rate

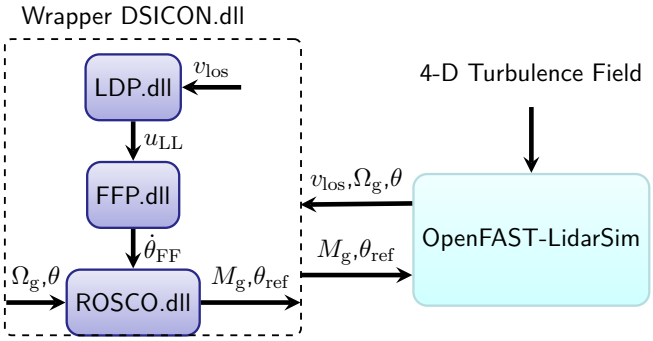

Figure 2.14: An overview of the interface between OpenFAST and the DLLs implemented for LAC. LDP: lidar data processing. FFP: feedforward pitch. ROSCO: the reference FB controller.

signal.

2.3.4 Wind Turbine Wakes

Wind turbine wakes are generally defined as the flow structure behind a wind turbine. Because of the energy extraction by the blade, the flow velocity is reduced after the turbine rotor. The decrease in velocity is frequently called the wake deficit.

In addition to the deficit, the turbulence intensity increases in the wake because a) smaller-scale eddies are generated by the interaction between the blade and wind flow; b) the velocity gradient promotes the kinetic exchange between the wake and ambient atmospheric turbulence. These additional turbulent fluctuations are often called wake-induced turbulence.

The wake deficit area is also perturbed by the ambient large-scale averaged lateral and vertical velocities. Consequently, it moves downstream with oscillations in the lateral and vertical directions. This phenomenon is often called wake meandering.

The properties of turbine wakes have been studied extensively, as reviewed by [57]. However, the three characteristics listed above are of special interest because they are related to turbine load and power performance.

3

Background on Conventional Three-dimensional Turbulence Generation

This chapter summarizes existing literature and aims to provide some theoretical knowledge for Chapters 4 and 5. Details of turbulence generation methods currently used for aeroelastic simulations are presented.

3.1 Stochastic Turbulent Wind Field Generation

As introduced in Section 2.3.2, a 3-D turbulence field is required to simulate the wind turbine rotor and tower aerodynamics. This section introduces the typical methods used to generate stochastic turbulence fields with spectral characteristics defined by the Kaimal or Mann model.

3.1.1 Veers Method

Frequently, the Veers method [58] is applied to generate the turbulent wind field described by the Kaimal model. It relies on the generation of correlated random processes [59]. Each random process is represented by Fourier coefficients in the frequency domain that has a specific spectrum.

For simplicity, the simulation of the fluctuation part of the u components is considered as an example to illustrate the algorithm. The turbulence fluctuations (hereinafter referred to as signals) are assumed to be located at n different positions in the same y-z plane, which can be

described by a set of frequency domain Fourier series (coefficients) as

$$\hat{\boldsymbol{u}}_{yz}(f) = [\hat{u}_{yz,1}(f)\ \hat{u}_{yz,2}(f)\ \ldots\ \hat{u}_{yz,n}(f)]^{\top}. \tag{3.1}$$

Here, $^{\top}$ denotes the matrix transpose. Each Fourier series may be expressed as

$$\hat{u}_{yz,i}(f) = A_{u,i}(f) H_{u,yz,ij}(f) X_{u,yz,j}(f) \quad \text{(ESC)}. \tag{3.2}$$

A detailed derivation of Equation 3.2 is provided in Appendix A.1. The three terms on the right-hand side of the equation are explained as follows.

(1) $A_{u,i}(f)$ is the amplitude of the Fourier series at a specific frequency, and can be calculated using

$$A_{u,i}(f) = \sqrt{\frac{\Delta f \cdot S_{u,i}(f)}{2}}, \tag{3.3}$$

where $S_{u,i}(f)$ is the one-sided power spectrum of the simulated signal at position i under a certain frequency, and Δf is the step length of the discrete frequency vector. If homogeneous turbulence in the y-z plane is assumed, $A_{u,i}(f)$ is identical for all n simulated signals. Moreover, different $A_{u,i}(f)$ can be defined for simulating inhomogeneous turbulence.

(2) $\boldsymbol{H}_{u,yz}$ is a matrix resulting from applying Cholesky factorization (denoted as "chol( )") [60] to the coherence matrix $\boldsymbol{C}_{u,yz}$ at each frequency step:

$$\boldsymbol{H}_{u,yz}(f) = \mathrm{chol}\left(\boldsymbol{C}_{u,yz}(f)\right), \tag{3.4}$$

with

$$\mathbf{C}_{u,yz}(f) = \begin{bmatrix} \gamma_{u,yz,11}(f) & \ldots & \gamma_{u,yz,1n}(f) \\ \vdots & \ddots & \vdots \\ \gamma_{u,yz,n1}(f) & \ldots & \gamma_{u,yz,nn}(f) \end{bmatrix}, \tag{3.5}$$

where $\gamma_{u,yz,ij}(f)$ is the co-coherence (real part of the coherence, no square) between any two signals. For the IEC Kaimal model, the coherence can be calculated using Equation 2.16. If the simulated signals do not have any repetitive coherence in the coherence matrix, the coherence matrix is Hermitian, and the classical Cholesky factorization can be applied. If the matrix is not Hermitian, LDL decomposition (square-root-free Cholesky decomposition) might be considered [61]. The matrix $\boldsymbol{H}_{u,yz}(f)$ is a lower triangular matrix:

$$\boldsymbol{H}_{u,yz}(f) = \begin{bmatrix} h_{u,yz,11}(f) & & 0 \\ \vdots & \ddots & \\ h_{u,yz,n1}(f) & \ldots & h_{u,yz,nn}(f) \end{bmatrix}, \tag{3.6}$$

which satisfies

$$\boldsymbol{C}_{u,yz}(f) = \boldsymbol{H}_{u,yz}\boldsymbol{H}_{u,yz}^{\top}. \tag{3.7}$$

(3) The last term $\boldsymbol{X}_{u,yz}$ is an n-by-1 vector of complex random numbers:

$$\boldsymbol{X}_{u,yz} = [e^{\mathrm{i}\phi_1}\ e^{\mathrm{i}\phi_2}\ \ldots\ e^{\mathrm{i}\phi_n}]^{\top}. \tag{3.8}$$

The complex numbers have a constant magnitude of one, but the phase angles $\boldsymbol{\phi} = [\phi_1\ \phi_2\ \ldots\ \phi_n]$ are uniformly distributed between 0 to 2π. The distribution of phase angles $\boldsymbol{\phi}$ ensures that the simulated time series approach a Gaussian process when the number of simulated stochastic wind components and frequency length increase [58].

When the Fourier coefficients are calculated, the time series can be simply obtained using the one-dimensional discrete inverse fast Fourier transform (IFFT):

$$u_{yz,i}(t) = \sum_{f} \exp(\mathrm{i}ft)\hat{u}_{yz,i}(f), \tag{3.9}$$

where $\sum_f$ denotes the summation over the discrete frequency vector.

The Veers method can theoretically generate turbulent wind fields that include all velocity components and cover multiple y-z planes. The critical point is to organize the signals into a vector as shown by Equation 3.1. However, note that the computation effort of Cholesky decomposition is theoretically proportional to the cube of the matrix size n, denoted as $O(n^3)$ [59, 62]. Therefore, directly applying the Veers method to generate 4-D wind fields can be time-consuming. Section 4.1.2 discusses a method that utilizes a two-step Cholesky decomposition, significantly reducing the computational effort for generating 4-D wind fields. Another feature of the Veers method is that the y-z plane for generating the turbulence field should not necessarily be a discrete rectangle and can be a discrete circle or another irregular shape.

3.1.2 Mann Method

The numerical simulation of a 3-D Mann model-based turbulence field [35] can be achieved using a discrete inverse Fourier transform [63] over three dimensions. At a certain time t_0, a random realization of the turbulence field with the size $L_x \times L_y \times L_z$ can be calculated using

$$u_i(\boldsymbol{x}) = \sum_{\boldsymbol{k}} \exp\left(\mathrm{i}\boldsymbol{k}\cdot\boldsymbol{x}\right) C_{ij}(\boldsymbol{k}) g_j(\boldsymbol{k}) \quad \text{(ESC)}, \tag{3.10}$$

where indexes $i, j = 1, 2$ and 3 and $\sum_{\boldsymbol{k}}$ denotes the triple sum [35]

$$\sum_{\boldsymbol{k}} = \sum_{k_1=-\pi N_x/L_x}^{\pi N_x/L_x} \sum_{k_2=-\pi N_y/L_y}^{\pi N_y/L_y} \sum_{k_3=-\pi N_z/L_z}^{\pi N_z/L_z} . \tag{3.11}$$

Here N_x, N_y, and N_z are the discrete steps such that the spatial domain $\boldsymbol{x}$ is discretized with step lengths $\Delta x = L_x/N_x$, $\Delta y = L_y/N_y$, and $\Delta z = L_z/N_z$ in the three spatial directions, respectively. For each wavenumber vector, $\boldsymbol{C}(\boldsymbol{k})$ is a 3 by 3 matrix of coefficients, and $\boldsymbol{g}(\boldsymbol{k})$ is a 3 by 1 vector of independent Gaussian stochastic complex variables with unit variance [35]. As derived by [35], for wavenumber vectors $|\boldsymbol{k}| \geq 3/L$ (outside a sphere volume with radius $3/L$), the matrix $\boldsymbol{C}$ can be approximated using

$$C_{ij}(\boldsymbol{k}) = \frac{(2\pi)^{3/2}}{(L_x L_y L_z)^{1/2}} A_{ij}(\boldsymbol{k}), \tag{3.12}$$

where the matrix $\boldsymbol{A}(\boldsymbol{k})$ is determined by

$$\boldsymbol{A} = \left(\frac{E(k_0)}{4\pi k_0^4}\right)^{\frac{1}{2}} \begin{bmatrix} 1 & 0 & \zeta_1 \\ 0 & 1 & \zeta_2 \\ 0 & 0 & k_0^2/k^2 \end{bmatrix} \begin{bmatrix} 0 & k_{30} & -k_2 \\ -k_{30} & 0 & k_1 \\ k_2 & -k_1 & 0 \end{bmatrix}. \tag{3.13}$$

The matrix $\boldsymbol{A}$ fulfills

$$\boldsymbol{A}\boldsymbol{A}^* = \frac{E(k_0)}{4\pi k_0^4} \begin{bmatrix} 1 & 0 & \zeta_1 \\ 0 & 1 & \zeta_2 \\ 0 & 0 & k_0^2/k^2 \end{bmatrix} \begin{bmatrix} k_0^2 - k_1^2 & -k_1 k_2 & -k_1 k_3 \\ -k_2 k_1 & k_0^2 - k_2^2 & -k_2 k_3 \\ -k_3 k_1 & -k_3 k_2 & k_0^2 - k_3^2 \end{bmatrix} \begin{bmatrix} 1 & 0 & \zeta_1 \\ 0 & 1 & \zeta_2 \\ 0 & 0 & k_0^2/k^2 \end{bmatrix}^* = \boldsymbol{\Phi}. \tag{3.14}$$

Here, the first term multiplied by the second matrix (in the middle) is the isotropic von Kámán tensor: [34, 11, 32]

$$\Phi_{ij,\mathrm{iso}}(\boldsymbol{k_0}) = \frac{E(k_0)}{4\pi k_0^4}(\delta_{ij} k_0^2 - k_i k_j). \tag{3.15}$$

The detailed calculation of Equation 3.14 is provided in Appendix A.2. Inside the sphere volume ($|\boldsymbol{k}| < 3/L$), matrix $\boldsymbol{C}$ needs to be calculated using numerical integration (Equation (47) in [35]) to avoid loss of variance owing to discretization [33].

Because of the 3-D IFFT, the Mann method for generating 3-D turbulence fields is generally faster than the Veers method [11]. The reliance on 3-D IFFT also indicates that the y-z plane must be rectangular, and both N_y and N_z must be integer powers of 2. Therefore, the computational effort is significantly lower, particularly for simulating a field with a larger number of discrete points in the y-z plane. Compared with the Kaimal model, the Mann model additionally includes the spatial coherence of v and w components (v or w at different

spatial positions) and the coherence between u and w components at the same position. The coherences of other components can also be derived from the spectral tensor, although they are frequently small and therefore not emphasized. Because of the incompressible wind flow, the spatial coherence of both the v and w components are physically realistic. The coherence between u and w may not be important for the turbine aerodynamics because mainly the u component is dominant. However, it is important for the lidar measurement properties, which are discussed in more detail in Chapter 5.
In addition, the Mann uniform shear model assumes homogeneous turbulence in the y-z plane. The inhomogeneous spectral tensor (uniform shear + blockage model) was introduced in [11, 32], but the corresponding turbulence generation method has not been revealed in the existing literature.

3.2 Simulation of Wake-included Turbulence

The turbulence generation methods described in the previous sections are applicable to the scenarios for which the statistical spectral properties of turbulence are known. However, because of the wake deficit, wake meandering, and wake-induced turbulence introduced in Chapter 2, the wake-included turbulence is not homogeneous in space, and the statistics depend on the operational status of the upstream turbines. Therefore, the statistical spectral properties of the wake-included turbulence can be highly site-specific; thus, obtaining a representative spectral model is difficult.
The LES method or other computational fluid dynamics (CFD) methods can be used to partly solve the N-S equations and provide higher fidelity results for the wake-included turbulence [64]. However, LES is still very computationally intensive and not suitable for the aeroelastic simulation in the wind turbine design stage. The IEC 61400-1 standard [12] recommends using the DWM method to model the wake-included turbulence for turbine design. This section explains the three sub-modules of the DWM model used in this study.

3.2.1 Wake Deficit

As recommended by IEC 61400-1 [12], the wake deficit is modeled using the thin layer approximation of the N-S equations in their rotational symmetric form, neglecting the pressure term [12, 11]. The eddy-viscosity formulation is used for turbulence closure [65]. The mean wake velocities in longitudinal direction U_x and radial direction V_r are governed by the momentum equation

$$U_x \frac{\partial U_x}{\partial x} + V_r \frac{\partial U_x}{\partial r} = \frac{1}{r} \frac{\partial}{\partial r} \left(r \nu_T \frac{\partial U_x}{\partial r} \right), \tag{3.16}$$

and the continuity equation

$$\frac{1}{r}\frac{\partial}{\partial r}(rV_r) + \frac{\partial U_x}{\partial x} = 0. \tag{3.17}$$

In the equations above, both U_x and V_r are functions of radial (r) and longitudinal (x) displacements from the wake center. The IEC 61400-1 standard [12] suggests an expression for the eddy viscosity ν_T that depends only on x. However, this thesis uses the eddy viscosity formulation implemented within FAST.Farm [65], which depends on both r and x. Several studies have been performed to validate the FAST.Farm either using LES or measurement data [66, 67]. In the actual implementation, the wake velocity is calculated as follows: a) obtain the steady-state axial induction factors and thrust coefficients of blade elements using the aeroelastic tool OpenFAST; (b) deliver free-stream turbulence parameters (the mean wind speed and turbulence intensity are required) and calculate the eddy viscosity; (c) solve Equations 3.16 and 3.17 using the finite-difference method discussed by [65].

3.2.2 Wake Meandering

The same method as suggested by the IEC 61400-1 standard is used to model the wake meandering, which is modeled by considering it as a passive tracer [12]. The deficits are assumed to transport downstream by the mean ambient longitudinal wind speed [68]. At a given moment, the wake center coordinate (y_c,z_c) is assumed to be driven by the large-scale lateral and vertical velocity fluctuations v_c and w_c [69, 70], which can be formulated as

$$\dot{y}_c(x,t) = v_c(x,t) = \frac{1}{\pi R_{\text{wake}}^2}\iint_{A_{\text{wake}}} v(x,y,z,t)\mathrm{d}y\mathrm{d}z, \tag{3.18}$$

$$\dot{z}_c(x,t) = w_c(x,t) = \frac{1}{\pi R_{\text{wake}}^2}\iint_{A_{\text{wake}}} w(x,y,z,t)\mathrm{d}y\mathrm{d}z, \tag{3.19}$$

where the integration area A_{wake} is the wake cross-section area, and R_{wake} is the radius of the wake. Because of this spatial average of the fluctuations, the wake center is driven by the large eddies in the free-stream turbulence field. Although the spatial averaging already acts as a low-pass filter [71], as suggested by [69, 12], a reference low-pass filter with a cutoff frequency of $V_{\text{hub}}/4R_{\text{w}}$ is further applied to filter v_c and w_c.

3.2.3 Wake-induced Turbulence

The wake-induced turbulence primarily originates from the mechanical interaction between the turbine blade and wind flow [12]. The recommended modeling procedure by the IEC 61400-1 standard [12] is followed, in which the wake-induced turbulence meanders with the deficit and is independent of the free-stream (ambient) turbulence. Additionally, the wake-induced turbulence is approximated by scaling an isotropic turbulence field whose length scale is smaller than or equal to the rotor diameter [12] and has a standard deviation of $1\,\mathrm{ms}^{-1}$. Following [70, 68], the isotropic turbulence field is assumed to have a length scale equal to 25% of the ambient turbulence length scale. The empirical scaling factor is calculated using [12]

$$k_{\mathrm{wt}}(x,r) = 0.6\Big|1 - \frac{U_x}{V_{\mathrm{hub}}}\Big| + \frac{0.35}{V_{\mathrm{hub}}}\Big|\frac{\partial U_x}{\partial r}\Big|. \tag{3.20}$$

The implementation of the DWM model is shown in Figure 3.1. Here, the free-stream (ambient) turbulence is generated based on the Mann model [35]. The steady-state wake velocity U_x and induced wake scaling factor k_{wt} can be pre-calculated. In contrast, the wake meandering must be calculated dynamically in the simulation. The wake center at a particular moment is shown in the second panel. In each time step, the wake velocity field and wake-induced turbulence field u_{ind} are calculated and added to the free-stream (ambient) turbulence field to obtain the wake-included turbulence u_{wake}.

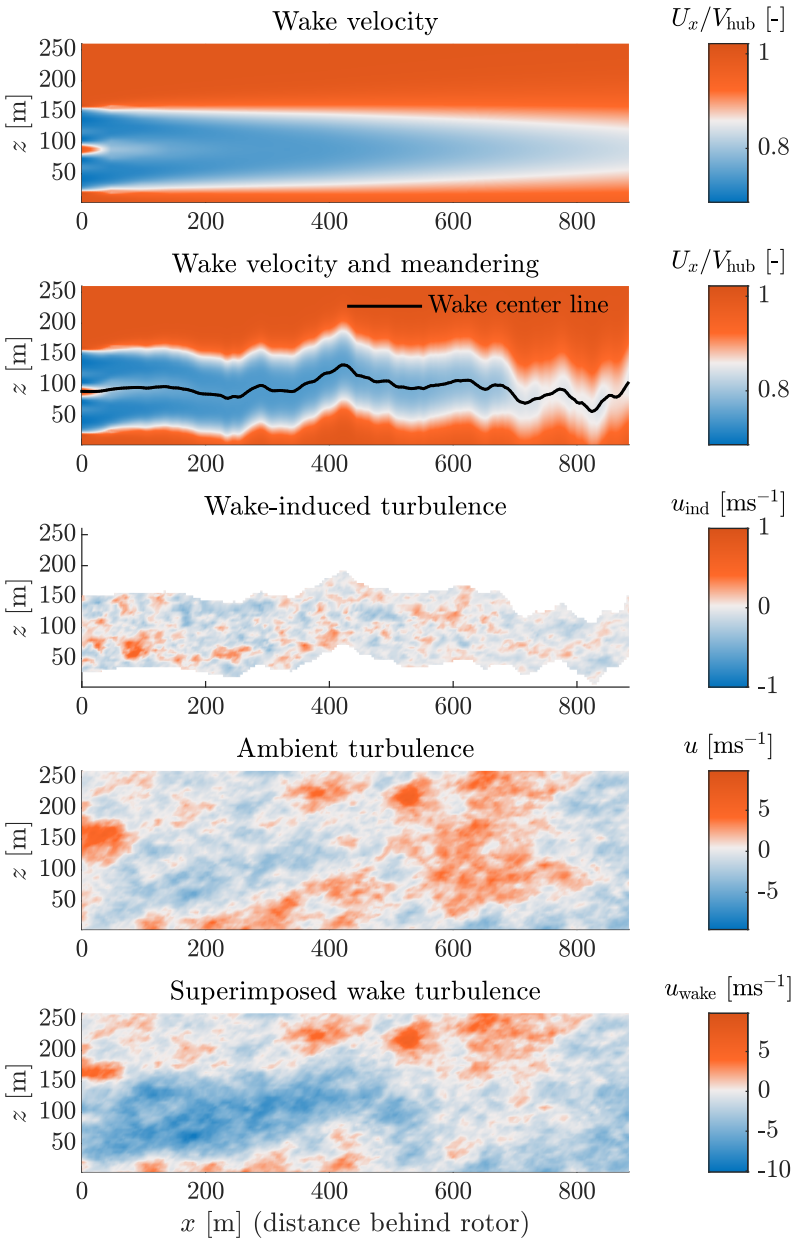

Figure 3.1: Side views of the wake characteristics and wake-included turbulent wind field with a hub height mean wind speed of 16 ms^{-1}. For wake-induced turbulence, the points outside the wake area are not plotted. Note that the ambient mean wind speed is not included in the plots.

4

Modeling of Turbulence Evolution

The temporal evolution of the turbulence field is the phenomenon in which eddies reshape when they propagate from upstream to downstream. Frequently, it is quantified by the longitudinal coherence, i.e., the coherence between two turbulent fluctuations located at two longitudinally separated locations. Because of the preview control, a nacelle lidar system measures the turbulence at upstream positions and a certain time is required for the turbulence field to travel from upstream to the downstream rotor position. Therefore, it is necessary to incorporate turbulence evolution into the turbulence models currently used for aeroelastic simulations to assess the impact of turbulence evolution on LAC. In this chapter, the methods that extend the IEC 61400-1 [12] Kaimal and Mann models to include longitudinal coherence are discussed, and the methods are validated using measurements from a five-beam pulsed lidar and a meteorological mast. This chapter is primarily based on [59] and [20].

4.1 Including Longitudinal Coherence in the Kaimal Model

This section first introduces a typical longitudinal coherence model similar to the lateral-vertical coherence model provided by the IEC 61400 standard [12]. Subsequently, it discusses the generation of a 4-D turbulent wind field containing longitudinal coherence using the Veers method. Finally, an algorithm that uses a two-step Cholesky decomposition to efficiently generate Kaimal model-based 4-D turbulence fields is discussed.

4.1.1 Exponential Longitudinal Coherence Model

In previous research, the turbulence evolution was modeled as a simple exponential function with a single decay parameter a_x [3]. More recently, the exponential coherence model listed in the IEC 61400-1 standard [12] was adjusted by [7] to represent the longitudinal coherence as follows

$$\gamma_x^2(\Delta x, f) = \exp\left(-a_x \Delta x \sqrt{\left(\frac{f}{U_{\text{ref}}}\right)^2 + b_x^2}\right), \tag{4.1}$$

where the transverse and vertical separation Δyz in Equation 2.16 is replaced by the longitudinal separation Δx. The parameter b_x determines the intercept (value at 0 frequency) [9] and a zero b_x value results in the model proposed by [3]. Equation 4.1 was validated by [7] using LES simulations of different atmospheric stability classes. Moreover, the exponential coherence model was verified by [8] and [9] using lidar measurements. Overall, the validation studies from the previous research demonstrated that the model agrees well with the high-fidelity LES simulations and measurements. As a result, the coherence decay parameter a_x was observed in the range $0 < a_x < 6$ and the intercept parameter b_x was observed in the order of magnitude $\leq 10^{-3}$ [20].

4.1.2 Four-dimensional Turbulence Generation by Veers Method

In principle, the Veers method (Equation 3.2) is not limited by the dimension of the generated random processes. One only needs to organize the stochastic processes into rows and provide a coherence matrix describing the correlation of any two stochastic processes, which is not limited by the dimensionality. For the assessment of LAC in aeroelastic simulations, several upstream y-z planes that are parallel to the rotor y-z plane may be required. Therefore, we can rewrite Equation 3.2 to represent spatial points distributed in 3-D space, resulting in a 4-D wind field $\boldsymbol{u}_{xyz}(t)$. Again, we consider the u components only and assume that they are distributed in m identical y-z discrete planes. Each y-z plane is assumed to have n positions in total. The Fourier coefficients of the field are then determined by

$$\hat{u}_{xyz,i}(f) = A_{u,i}(f) H_{u,xyz,ij}(f) X_{u,xyz,j}(f) \quad \text{(ESC)}. \tag{4.2}$$

Now, $\boldsymbol{A}_u$ and $\boldsymbol{X}_{u,xyz}$ become $m \times n$ by 1 vectors. $\boldsymbol{H}_{u,xyz}$ becomes an $m \times n$ by $m \times n$ matrix, which can be calculated using

$$\boldsymbol{H}_{u,xyz}(f) = \text{chol}\left(\boldsymbol{C}_{u,xyz}(f)\right). \tag{4.3}$$

For each frequency step, the Cholesky decomposition must be applied to a matrix with a size of $m \times n$. To simulate typical pulsed lidar systems, we require up to 10 upstream measurement planes (the number of m). As mentioned in Section 3.1.1, the computation effort can be large because it is proportional to $O((mn)^3)$ [59, 62]. To solve this problem, [59] proposed a two-step Cholesky decomposition method relying on the assumption that the combined longitudinal, lateral and vertical coherence can be obtained by simple multiplication:

$$\gamma_{u,xyz}(f) = \gamma_{u,yz}(f)\gamma_{u,x}(f). \tag{4.4}$$

This assumption has been widely used in the literature [72, 14, 21, 7] but slightly underestimates the combined coherence compared with the LES result [16]. However, because the exponential coherence model only has two parameters that can be easily adjusted, the underestimation can be alleviated by adjusting the model parameters empirically. A significant advantage introduced by this assumption is that the coherence matrix can now be expressed as

$$\boldsymbol{C}_{u,xyz} = \boldsymbol{C}_{u,x} \otimes \boldsymbol{C}_{u,yz} = \begin{bmatrix} \gamma_{u,x,11}\boldsymbol{C}_{u,yz} & \cdots & \gamma_{u,x,1m}\boldsymbol{C}_{u,yz} \\ \vdots & \ddots & \vdots \\ \gamma_{u,x,m1}\boldsymbol{C}_{u,yz} & \cdots & \gamma_{u,x,mm}\boldsymbol{C}_{u,yz} \end{bmatrix}, \tag{4.5}$$

where

$$\boldsymbol{C}_{u,x} = \begin{bmatrix} \gamma_{u,x,11} & \cdots & \gamma_{u,x,1m} \\ \vdots & \ddots & \vdots \\ \gamma_{u,x,m1} & \cdots & \gamma_{u,x,mm} \end{bmatrix} \tag{4.6}$$

is a matrix containing the longitudinal coherence (co-coherence) of any two points with only longitudinal separation. The operator "$\otimes$" denotes the Kronecker product [73]. Subsequently, the Cholesky decomposition can be expressed in two steps:

$$\boldsymbol{H}_{u,xyz} = \mathrm{chol}(\boldsymbol{C}_{u,xyz}) = \mathrm{chol}(\boldsymbol{C}_{u,x} \otimes \boldsymbol{C}_{u,yz}) = \mathrm{chol}(\boldsymbol{C}_{u,x}) \otimes \mathrm{chol}(\boldsymbol{C}_{u,yz}) = \boldsymbol{H}_{u,x} \otimes \boldsymbol{H}_{u,yz}. \tag{4.7}$$

Refer to [59, 74] for the step-by-step derivations. Equation 4.7 indicates that the Cholesky decomposition can be applied to two smaller matrices $\boldsymbol{C}_{u,x}$ and $\boldsymbol{C}_{u,yz}$ instead of the large matrix $\boldsymbol{C}_{u,xyz}$. Correspondingly, the computational effort is reduced to $O(m^3) + O(n^3)$ [59]. Note that the Kronecker product is based on simple product operations; thus, its computational effort is negligible.

Assuming that the turbulence is homogeneous in all directions (A_u is the same for all signals),

instead of Equation 4.2, we can rewrite the Fourier coefficient of a 4-D turbulence field as

$$\begin{aligned}\hat{\boldsymbol{u}}_{xyz}(f) &= A_u(\boldsymbol{H}_{u,x} \otimes \boldsymbol{H}_{u,yz})\boldsymbol{X}_{u,xyz} \\ &= A_u \begin{bmatrix} h_{u,x,11}\boldsymbol{H}_{u,yz} & & 0 \\ \vdots & \ddots & \\ h_{u,x,m1}\boldsymbol{H}_{u,yz} & \dots & h_{u,x,mm}\boldsymbol{H}_{u,yz} \end{bmatrix} \boldsymbol{X}_{u,xyz}.\end{aligned} \tag{4.8}$$

Moreover, the complex random number matrix $\boldsymbol{X}_{u,xyz}$ can be expressed in a vector-in-vector format:

$$\boldsymbol{X}_{u,xyz} = \begin{bmatrix} \boldsymbol{X}_{u,yz,1} \\ \vdots \\ \boldsymbol{X}_{u,yz,m} \end{bmatrix}, \tag{4.9}$$

where $\boldsymbol{X}_{u,yz,i}$ is a n by 1 vector of complex random numbers. Substituting Equation 4.9 into Equation 4.8 results in

$$\hat{\boldsymbol{u}}_{xyz}(f) = \begin{bmatrix} \sum_{i=1}^{1} h_{u,x,1i} A_u \boldsymbol{H}_{u,yz} \boldsymbol{X}_{u,yz,i} \\ \sum_{i=1}^{2} h_{u,x,1i} A_u \boldsymbol{H}_{u,yz} \boldsymbol{X}_{u,yz,i} \\ \vdots \\ \sum_{i=1}^{m} h_{u,x,mi} A_u \boldsymbol{H}_{u,yz} \boldsymbol{X}_{u,yz,i} \end{bmatrix}. \tag{4.10}$$

Because the term $A_u\boldsymbol{H}_{u,yz}\boldsymbol{X}_{n,i}$ is the Fourier coefficient of turbulence fluctuations at an arbitrary y-z plane and different $\boldsymbol{X}_{u,yz,i}$ values are statistically independent, Equation 4.10 can be interpreted as follows: the 4-D turbulence field with several correlated y-z planes can be obtained by summing several independent y-z plane turbulences after multiplying it by the factorization coefficients $h_{u,x,mi}$. This implies that we may generate the 4-D turbulence field with the aid of conventional 3-D turbulence generation codes and a longitudinal coherence model. The open-source tool *evoTurb*[1] (evolving turbulence) was developed by [59] to enable the generation of 4-D turbulence fields using conventional 3-D turbulence generation codes and a longitudinal coherence model. It can be coupled with TurbSim [75], which is a turbulence generation tool developed by NREL and supports the Veers method [58] to generate 3-D turbulence on a y-z plane. Depending on the number of y-z planes required, *evoTurb* calls TurbSim to generate several statistically independent 3-D turbulence fields. Statistical independence is achieved by specifying independent and random number seeds. Subsequently, the y-z plane Fourier coefficients are obtained by simply applying the one-dimensional discrete Fourier transform (denoted as $\mathcal{F}\{\}$):

$$A_u\boldsymbol{H}_{u,yz}\boldsymbol{X}_{n,i} = \mathcal{F}\{\boldsymbol{u}_{yz,i}(t,y,z)\}. \tag{4.11}$$

[1] Last accessed on 26 March 2022, `https://github.com/SWE-UniStuttgart/evoTurb`

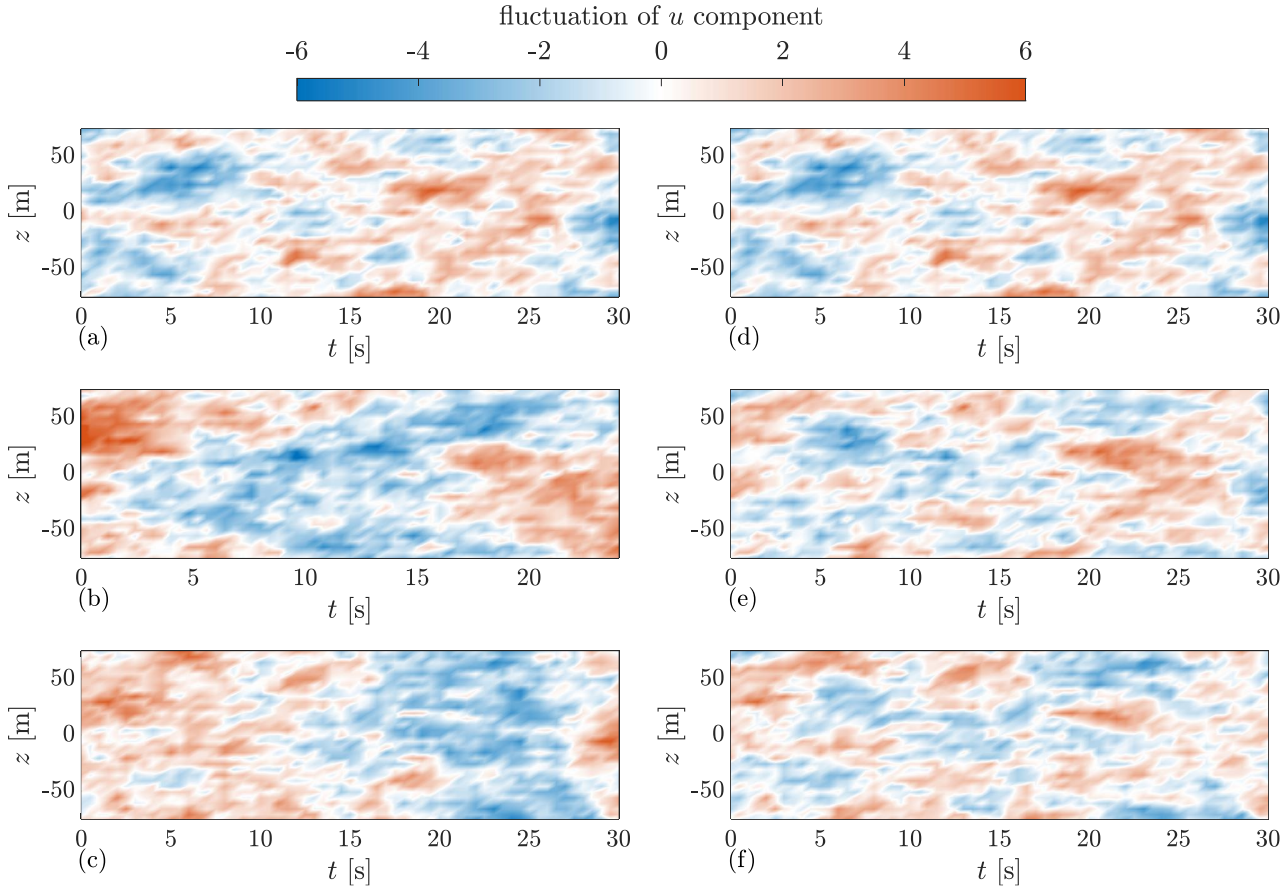

Figure 4.1: The demonstration of a 4-D turbulence field composited by three independent 3-D turbulence fields. (a–c): three independent realizations of 3-D turbulent wind fields generated using TurbSim. (d–f): 4-D turbulence field at three longitudinal positions $x = 0\,\mathrm{m}$, $x = 60\,\mathrm{m}$, and $x = 120\,\mathrm{m}$, that are composited using Equation 4.10. The 4-D turbulence is generated assuming the exponential longitudinal coherence (Equation 4.1) with $U_{\mathrm{ref}} = 16\,\mathrm{ms}^{-1}$, $a_x = 2$ and $b_x = 0$. Note that the temporal shifts owing to the turbulence transport by the mean wind speed is not shown.

Thereafter, Cholesky decomposition is applied to the longitudinal coherence model to obtain $\boldsymbol{H}_{u,x}$ and Equation 4.10 is applied to obtain the Fourier coefficients. In the final step, IFFT is applied to obtain the time series of the 4-D turbulence field. An example of the generated 4-D turbulence field is shown in Figure 4.1. Sub-figures (a), (b), and (c) are the time series of vertical turbulence profiles from three independent realizations of 3-D turbulent wind fields. They are generated using TurbSim using different random seeds corresponding to the IEC Kaimal turbulence class 1A. After applying Equation 4.10, the resulting 4-D turbulence field sliced at $x = 0\,\mathrm{m}$, $x = 60\,\mathrm{m}$, and $x = 120\,\mathrm{m}$ is shown in (d), (e), and (f), respectively. Because the element in the first row and first column in the matrix $\boldsymbol{H}_{u,x}$ is always 1, the fields shown by (d) and (a) are equal. Sub-figures (e) and (f) are correlated with (d) by the exponential longitudinal coherence (Equation 4.1). Compared with (f), (e) is more correlated with (d) because the longitudinal separation is smaller. Additionally, (e) and (f) are correlated.

Except for the reduction in computational effort when using the two-step Cholesky decompo-

sition, *evoTurb* has other advantages. First, the design load cases in the IEC 61400-1 standard [12] require performing aeroelastic simulation using wind fields generated with different random seeds [76], and these wind fields differ only in the random seeds. Therefore, the pre-generated 3-D wind fields can be used to generate 4-D wind fields. Additionally, manipulating the sequence of the 3-D wind fields (the sequence of $A_u \boldsymbol{H}_{u,yz} \boldsymbol{X}_{n,i}$ in Equation 4.10) can produce independent 4-D wind fields. This enables the use of a pre-generated 3-D turbulence field multiple times, thus further reducing the computational effort required to generate 4-D wind fields. Second, the different amplitudes of A_u can be assigned to different y-z planes or vertical positions to easily generate an inhomogeneous turbulence field.

4.2 Including Longitudinal Coherence to the Mann Model

This section introduces a method that extends the Mann model (spatial tensor) to a space-time tensor. The space-time tensor assumes a stationary process, which means that each 3-D turbulence field has the statistical properties described by the Mann spectral tensor. Owing to temporal evolution, these 3-D fields are not entirely correlated. Their correlations depend on a newly introduced eddy life expression in which the wavenumbers with smaller magnitudes (larger wavelengths in space) tend to survive longer and are therefore more correlated.

4.2.1 Derivation of the Space-time Tensor

At a certain time t_0, we can perform the 3-D Fourier transform of the stochastic turbulence fluctuation over a space, obtaining the Fourier coefficients

$$\hat{\boldsymbol{u}}(\boldsymbol{k}, t_0) = \frac{1}{(2\pi)^3} \int \boldsymbol{u}(\boldsymbol{x}, t_0) \exp(-\mathrm{i}\boldsymbol{k} \cdot \boldsymbol{x}) \mathrm{d}\boldsymbol{x}, \tag{4.12}$$

where the integration $\int \mathrm{d}\boldsymbol{x} \equiv \int_{-\infty}^{\infty} \int_{-\infty}^{\infty} \int_{-\infty}^{\infty} \mathrm{d}x\mathrm{d}y\mathrm{d}z$. The ensemble average of the stochastic Fourier coefficients is connected to the spectral tensor by [36]

$$\Phi_{ij}(\boldsymbol{k}) \delta(\boldsymbol{k} - \boldsymbol{k'}) = \langle \hat{u}_i^*(\boldsymbol{k}, t_0) \hat{u}_j(\boldsymbol{k'}, \boldsymbol{t_0}) \rangle, \tag{4.13}$$

where * denotes the complex conjugate, $\delta()$ is the Dirac delta function, and $\boldsymbol{k}$ (or $\boldsymbol{k'}$) $= (k_1, k_2, k_3)$ is the wavenumber vector. The Dirac delta function means that if $\boldsymbol{k'} \neq \boldsymbol{k}$, then the ensemble average is zero.

The turbulence evolution phenomenon was included in the Mann model using the eddy lifetime-based solution [20]. The eddy lifetime-based concept was proposed by Ropelewski, Tennekes and Panofsky [77, 33], and it assumes that the eddies decay exponentially according to the passed time Δt and lifetime of the eddy $\tau_\mathrm{e}(\boldsymbol{k})$ (the subscript e means "evolution"). Note that

τ_e should be distinguished from τ_s. τ_s was used by Mann [11] to model the effect of uniform shear. For an eddy with wavenumber $\boldsymbol{k}$, the probability that it maintains its original structure after a period of time Δt is [20, 5, 33]

$$P \sim \exp\left(-\frac{\Delta t}{\tau_e(\boldsymbol{k})}\right). \tag{4.14}$$

Subsequently, the space-time tensor $\boldsymbol{\Theta}$ is defined as

$$\Theta_{ij}(\boldsymbol{k}, \Delta t) = \exp\left(-\frac{\Delta t}{\tau_e(\boldsymbol{k})}\right) \Phi_{ij}(\boldsymbol{k}), \tag{4.15}$$

which is related to the Fourier coefficient of two turbulence fields as

$$\Theta_{ij}(\boldsymbol{k}, \Delta t)\delta(\boldsymbol{k} - \boldsymbol{k'}) = \langle \hat{u}_i^*(\boldsymbol{k}, t_0)\hat{u}_j(\boldsymbol{k'}, t_0 + \Delta t)\rangle. \tag{4.16}$$

Here, $\hat{u}_j(\boldsymbol{k'}, t_0)$ and $\hat{u}_j(\boldsymbol{k'}, t_0 + \Delta t)$ are the Fourier coefficients of the turbulence fields at times t_0 and $t_0 + \Delta t$, respectively. In addition to the temporal decorrelation, the turbulence field is assumed to be transported by the mean reference wind speed U_{ref}. After time Δt, the entire field moves downstream in the positive x direction by $U_{\text{ref}}\Delta t$ (Figure 4.2). The spatial structure of the downstream turbulence field is also assumed to be governed by the Mann spectral tensor $\boldsymbol{\Phi}$ [11], implying stationary turbulence.

Compared with the Mann spectral tensor $\boldsymbol{\Phi}$, the newly introduced component is the eddy lifetime τ_e, which models the temporal evolution of the turbulence field. Several eddy lifetime expressions were summarized by Mann [11], which have the following in common:

$$\tau(\boldsymbol{k}) \quad \begin{cases} \propto |\boldsymbol{k}|^{b_1}, & \text{for } |\boldsymbol{k}| \to \infty, \\ \propto |\boldsymbol{k}|^{b_2}, & \text{for } |\boldsymbol{k}| \to 0, \end{cases} \tag{4.17}$$

where b_1 and b_2 are two constants standing for the slopes of $\tau(\boldsymbol{k})$ in the logarithmic scale. Based on the dimensional analysis in the inertial subrange, Mann summarized that $b_1 = -2/3, -1, -2$, or $-7/2$, and $b_2 = -2/3$. The hypergeometric function (Equation 2.19) was used by Mann to model the shear effect on the turbulence, and the function forces the eddy lifetime to follow the slopes corresponding to $b_1 = -1$ and $b_2 = -2/3$ [11]. Because the hypergeometric function is not very straightforward to observe the slopes that they represent, within this thesis project, [20] proposed another expression for the eddy lifetime that is more flexible to adjust the slopes, i.e.,

$$\tau_e(\boldsymbol{k}) \quad \text{or} \quad \tau_s(\boldsymbol{k}) = \gamma\left[a\left(|\boldsymbol{k}|L\right)^{b_1}\left(\left(|\boldsymbol{k}|L\right)^{10} + 1\right)^{\frac{b_2 - b_1}{10}}\right], \tag{4.18}$$

where γ is a constant (with a unit of second) related to the eddy lifetime, and a is a constant

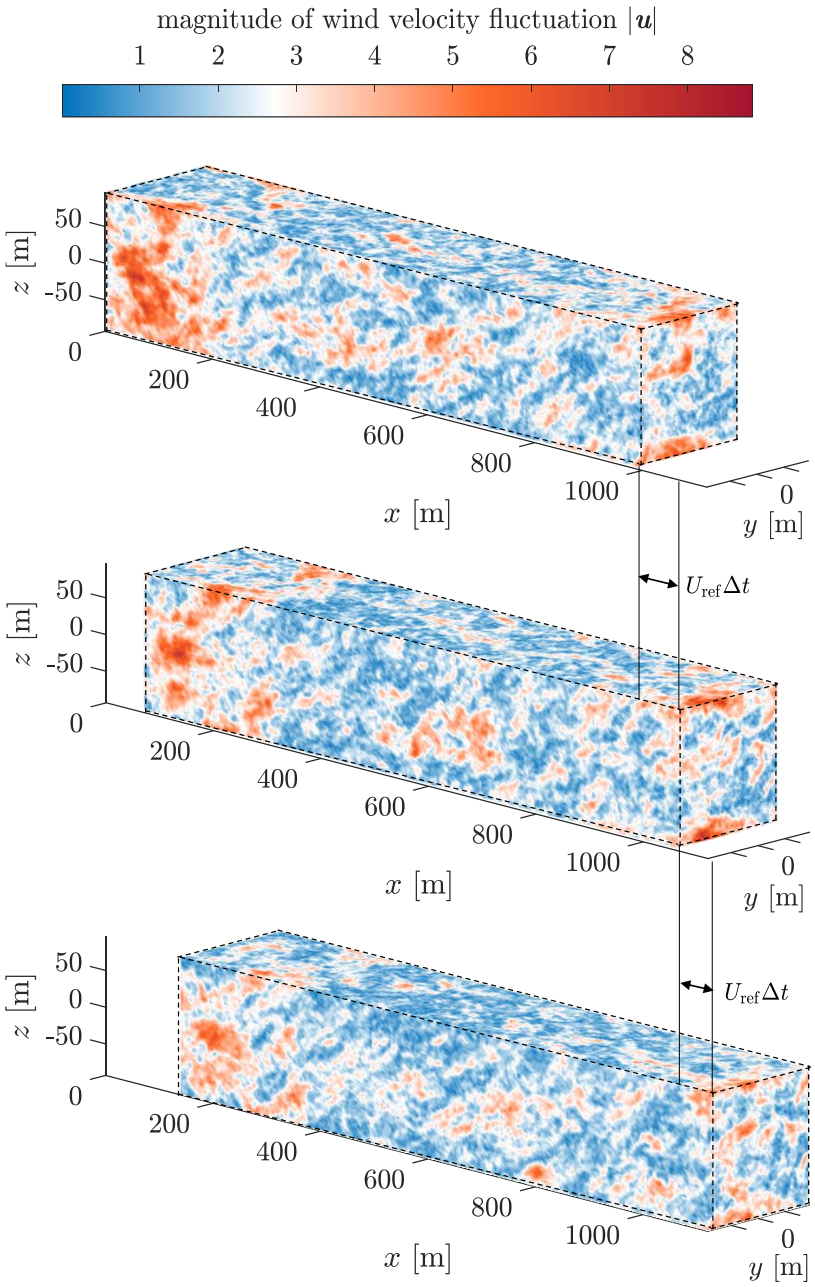

Figure 4.2: Illustration of turbulence evolution simulated using the space-time tensor $\boldsymbol{\Theta}$, with the following parameters: $\Delta t = 5\,\mathrm{s}$, $U_{\mathrm{ref}} = 12\,\mathrm{ms}^{-1}$, $\alpha\epsilon^{2/3} = 0.184\,\mathrm{m}^{4/3}\mathrm{s}^{-2}$, $L = 49.2\,\mathrm{m}$, $\Gamma = 3.38$, $b_2 = -2$, $\gamma = 270.4\,\mathrm{s}$. The 3-D turbulence field is assumed to propagate downstream with the reference mean wind speed U_{ref} and the eddies decaying exponentially.

that results in $\tau_e(\boldsymbol{k})$ or $\tau_s(\boldsymbol{k}) \approx a$ when $|\boldsymbol{k}|L = 1$ and $\gamma = 1\,\mathrm{s}$. It can be simply determined by $a = \left[{}_2F_1\left(\frac{1}{3}, \frac{17}{6}; \frac{4}{3}; -1\right)\right]^{-\frac{1}{2}}$. As shown in Figure 4.3, Equation 4.18 forces $\tau(\boldsymbol{k})$ to follow the slope governed by b_1 when $|\boldsymbol{k}|L < 1$ and the slope governed by b_2 when $|\boldsymbol{k}|L > 1$. The main benefits of Equation 4.18 are that it is more flexible to adjust the slopes b_1 and b_2, and it is computationally less demanding than the hypergeometric function. A good approximation to the original Mann model eddy lifetime (Equation 2.19) can be obtained using Equation 4.18 by setting $b_1 = -1$ and $b_2 = -2/3$.

It would be more natural to have only one eddy lifetime, representing both the shear effect and the temporal evolution. Through comparisons with lidar measurements, [20] observed that adjusting the eddy lifetime from the original expression for τ_e is necessary to achieve good agreements with the coherence from lidar measurements. More details are provided in Section 4.3. Because Equation 4.18 is flexible, both $\tau_s(\boldsymbol{k})$ and $\tau_e(\boldsymbol{k})$ can be calculated using its expression.

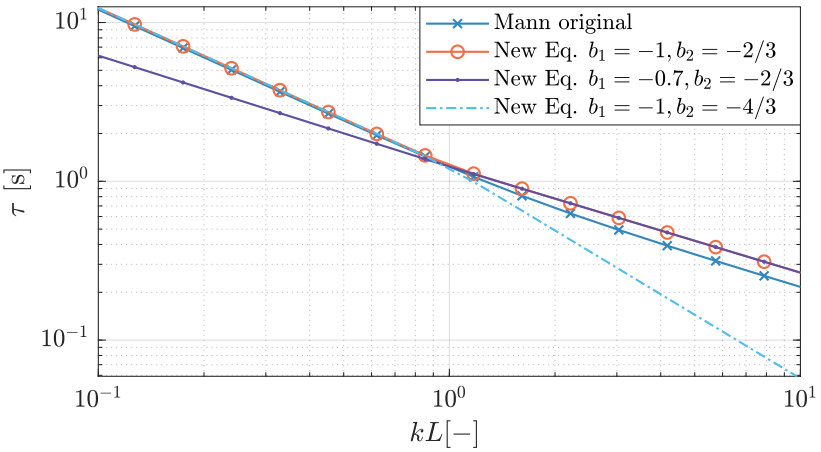

Figure 4.3: Eddy lifetimes using the original Mann model expression ($\Gamma\frac{\mathrm{d}U}{\mathrm{d}z} = 1\,\mathrm{s}$) and the new adjustable slope function Equation 4.18 ($\gamma = 1\,\mathrm{s}$, denoted as New Eq.).

When the space-time tensor is calculated, the cross-spectra containing the turbulence evolution can be obtained using

$$F_{ij}(k_1, \Delta t, \Delta y, \Delta z) = \int_{-\infty}^{\infty}\int_{-\infty}^{\infty} \Theta_{ij}(\boldsymbol{k}, \Delta t)\exp(\mathrm{i}(k_2\Delta y + k_3\Delta z))\mathrm{d}k_2\mathrm{d}k_3, \tag{4.19}$$

and the coherence can be calculated using

$$\mathrm{coh}^2_{ij}(k_1, \Delta t, \Delta y, \Delta z) = \frac{|F_{ij}(k_1, \Delta t, \Delta y, \Delta z)|^2}{F_{ii}(k_1)F_{jj}(k_1)}. \tag{4.20}$$

In actual applications, time series can often be measured with instruments on a mast or using a lidar. To derive a spatially distributed time series, we shall rely on Taylor's hypothesis [2] to

convert the wavenumber (k_1) spectra to frequency spectra, i.e., $k_1 = 2\pi f/U_{\text{ref}}$ [35]. Additionally, we can determine the longitudinal coherence between two positions with a separation of Δx using $\Delta t = \Delta x/U_{\text{ref}}$. Here, we assumed that the Mann spectral tensor [35] accurately represents the frequency spectra, which was proven by [36, 78].

4.2.2 Four-dimensional Turbulence Generation by Space-time Tensor

As discussed in Section 3.1.2, the Fourier coefficients of the turbulence field at time t_0 can be determined using

$$u_i(\boldsymbol{x}, t_0) = \sum_{\boldsymbol{k}} \exp\left(\mathrm{i}\boldsymbol{k}\cdot\boldsymbol{x}\right) C_{ij}(\boldsymbol{k}) g_j(\boldsymbol{k}, t_0) \quad \text{(ESC)}, \tag{4.21}$$

where, although mentioned earlier, for each wavenumber vector and time, $\boldsymbol{C}(\boldsymbol{k})$ is a 3×3 matrix of coefficients and $\boldsymbol{g}(\boldsymbol{k}, t_0)$ is a 3×1 vector of independent Gaussian stochastic complex variables with unit variance [35]. For a concise derivation later, we express the relation between the matrix $\boldsymbol{C}(\boldsymbol{k})$ and the spectral tensor as

$$C_{im}(\boldsymbol{k}) C^*_{jm}(\boldsymbol{k}) \propto \Phi_{ij}(\boldsymbol{k}), \tag{4.22}$$

where the index $m = 1, 2, 3$, and $\propto$ denotes "proportional to." The ensemble average of the Fourier coefficients at t_0 is

$$\begin{aligned} &\langle C_{im}(\boldsymbol{k}) g_m(\boldsymbol{k}, t_0) [C_{jn}(\boldsymbol{k}) g_n(\boldsymbol{k}, t_0)]^* \rangle \\ =&C_{im}(\boldsymbol{k}) \langle g_m(\boldsymbol{k}, t_0) g^*_n(\boldsymbol{k}, t_0) \rangle C^*_{jn}(\boldsymbol{k}), \end{aligned} \tag{4.23}$$

where the index $n = 1, 2, 3$. Because $\langle g_m(\boldsymbol{k}, t_0) g^*_n(\boldsymbol{k}, t_0) \rangle = 2\delta_{mn}$ is the 3×3 covariance matrix of the independent complex Gaussian variables that have unit variance in the real and imaginary parts. It is not zero only when $m = n$; therefore, we can write

$$\begin{aligned} &\langle C_{im}(\boldsymbol{k}) g_m(\boldsymbol{k}, t_0) [C_{jn}(\boldsymbol{k}) g_n(\boldsymbol{k}, t_0)]^* \rangle \\ =&2 C_{im}(\boldsymbol{k}) C^*_{jm}(\boldsymbol{k}) \propto \Phi_{ij}(\boldsymbol{k}). \end{aligned} \tag{4.24}$$

Because the turbulence field is assumed to be stationary, the turbulence field at time $t_0 + \Delta t$ has the same spectral properties as that at t_0, and the identical matrix $\boldsymbol{C}(\boldsymbol{k})$ can be applied to calculate the Fourier coefficients. However, because of temporal evolution, another group of independent complex Gaussian variables $\boldsymbol{g}(\boldsymbol{k}, t_0 + \Delta t)$ is used, and they should be able to result in the correlations defined by the space-time tensor. Thus, the field at $t_0 + \Delta t$ is

$$\boldsymbol{u}_i(\boldsymbol{x}, t_0 + \Delta t) = \sum_{\boldsymbol{k}} \exp\left(\mathrm{i}\boldsymbol{k}\cdot\boldsymbol{x}\right) C_{ij}(\boldsymbol{k}) g_j(\boldsymbol{k}, t_0 + \Delta t). \tag{4.25}$$

in which $\boldsymbol{g}(\boldsymbol{k}, t_0 + \Delta t)$ fulfills

$$\begin{cases} \langle C_{im}(\boldsymbol{k}) g_m(\boldsymbol{k}, t_0 + \Delta t)[C_{jn}(\boldsymbol{k}) g_n(\boldsymbol{k}, t_0 + \Delta t)]^* \rangle \propto \Phi_{ij}(\boldsymbol{k}), & \text{for stationarity,} \\ \langle C_{im}(\boldsymbol{k}) g_m(\boldsymbol{k}, t_0)[C_{jn}(\boldsymbol{k}) g_n(\boldsymbol{k}, t_0 + \Delta t)]^* \rangle \propto \exp\left(-\frac{\Delta t}{\tau_\mathrm{e}}\right) \Phi_{ij}(\boldsymbol{k}), & \text{for temporal evolution.} \end{cases} \tag{4.26}$$

The equation for stationarity can be extended as

$$\begin{aligned} &\langle C_{im}(\boldsymbol{k}) g_m(\boldsymbol{k}, t_0 + \Delta t)[C_{jn}(\boldsymbol{k}) g_n(\boldsymbol{k}, t_0 + \Delta t)]^* \rangle \\ &= C_{im}(\boldsymbol{k}) \langle g_m(\boldsymbol{k}, t_0 + \Delta t) g_n^*(\boldsymbol{k}, t_0 + \Delta t) \rangle C_{jn}^*(\boldsymbol{k}) \\ &\propto \Phi_{ij}(\boldsymbol{k}), \end{aligned} \tag{4.27}$$

and the equation to satisfy the temporal evolution correlation decay can be expanded as

$$\begin{aligned} &\langle C_{im}(\boldsymbol{k}) g_m(\boldsymbol{k}, t_0)[C_{jn}(\boldsymbol{k}) g_n(\boldsymbol{k}, t_0 + \Delta t)]^* \rangle \\ &= C_{im}(\boldsymbol{k}) \langle g_m(\boldsymbol{k}, t_0) g_n^*(\boldsymbol{k}, t_0 + \Delta t) \rangle C_{jn}^*(\boldsymbol{k}) \\ &\propto \exp\left(-\frac{\Delta t}{\tau_\mathrm{e}}\right) \Phi_{ij}(\boldsymbol{k}). \end{aligned} \tag{4.28}$$

Following Equations 4.23 and 4.24, the ensemble average of the Gaussian variables should satisfy

$$\begin{cases} \langle g_m(\boldsymbol{k}, t_0 + \Delta t) g_n^*(\boldsymbol{k}, t_0 + \Delta t) \rangle = 2\delta_{mn}, \\ \langle g_m(\boldsymbol{k}, t_0) g_n^*(\boldsymbol{k}, t_0 + \Delta t) \rangle = 2 \exp\left(-\frac{\Delta t}{\tau_\mathrm{e}}\right) \delta_{mn}. \end{cases} \tag{4.29}$$

Equation 4.29 can be achieved using the complex Ornstein-Uhlenbeck process [79, 20], in which the mth element in the vector $\boldsymbol{g}(\boldsymbol{k}, t)$ should obey

$$g_m(\boldsymbol{k}, t_0 + \Delta t) = g_m(\boldsymbol{k}, t_0) \exp\left(-\frac{\Delta t}{\tau_\mathrm{e}}\right) + g_m(\boldsymbol{k}) \sqrt{1 - \exp\left(-\frac{2\Delta t}{\tau_\mathrm{e}}\right)}, \tag{4.30}$$

where $g_m(\boldsymbol{k})$ are complex Gaussian variables independent of $g_m(\boldsymbol{k}, t_0)$. The independence between $g_m(\boldsymbol{k})$ and $g_m(\boldsymbol{k}, t_0)$ implies that the ensemble mean of their products will be zero. We

can easily prove that

$$\begin{aligned}
&\langle g_m(\boldsymbol{k}, t_0 + \Delta t) g_n^*(\boldsymbol{k}, t_0 + \Delta t)\rangle \\
=&\left\langle g_m(\boldsymbol{k}, t_0) g_n^*(\boldsymbol{k}, t_0) \exp\left(-\frac{2\Delta t}{\tau_\mathrm{e}}\right) + g_m(\boldsymbol{k}, t_0) g_n^*(\boldsymbol{k}) \exp\left(-\frac{\Delta t}{\tau_\mathrm{e}}\right) \sqrt{1 - \exp\left(-\frac{2\Delta t}{\tau_\mathrm{e}}\right)} \right\rangle \\
&+ \left\langle g_n^*(\boldsymbol{k}, t_0) g_m(\boldsymbol{k}) \exp\left(-\frac{\Delta t}{\tau_\mathrm{e}}\right) \sqrt{1 - \exp\left(-\frac{2\Delta t}{\tau_\mathrm{e}}\right)} + g_m(\boldsymbol{k}) g_n^*(\boldsymbol{k}) \left[1 - \exp\left(-\frac{2\Delta t}{\tau_\mathrm{e}}\right)\right] \right\rangle \\
=&\left\langle g_m(\boldsymbol{k}, t_0) g_n^*(\boldsymbol{k}, t_0) \exp\left(-\frac{2\Delta t}{\tau_\mathrm{e}}\right) \right\rangle + \left\langle g_m(\boldsymbol{k}) g_n^*(\boldsymbol{k}) \left[1 - \exp\left(-\frac{2\Delta t}{\tau_\mathrm{e}}\right)\right] \right\rangle \\
=&2\delta_{mn},
\end{aligned} \tag{4.31}$$

and

$$\begin{aligned}
&\langle g_m(\boldsymbol{k}, t_0) g_n^*(\boldsymbol{k}, t_0 + \Delta t)\rangle \\
=&\left\langle g_m(\boldsymbol{k}, t_0) g_n^*(\boldsymbol{k}, t_0) \exp\left(-\frac{\Delta t}{\tau_\mathrm{e}}\right) + g_m(\boldsymbol{k}, t_0) g_n^*(\boldsymbol{k}) \sqrt{1 - \exp\left(-\frac{2\Delta t}{\tau_\mathrm{e}}\right)} \right\rangle \\
=&2 \exp\left(-\frac{\Delta t}{\tau_\mathrm{e}}\right) \delta_{mn}.
\end{aligned} \tag{4.32}$$

The derivation above shows that the statistical representation of turbulence evolution from one moment to the next can be achieved using the Ornstein-Uhlenbeck process. Furthermore, turbulence evolution can be extended at different moments in time using the complex Gaussian variables, which are calculated as

$$g_m(\boldsymbol{k}, t_i) = g_m(\boldsymbol{k}, t_{i-1}) \exp\left(-\frac{t_i - t_{i-1}}{\tau_\mathrm{e}}\right) + g_m(\boldsymbol{k}) \sqrt{1 - \exp\left(-\frac{2(t_i - t_{i-1})}{\tau_\mathrm{e}}\right)}. \tag{4.33}$$

With a given eddy lifetime model τ_e, for any two fields with a time difference of $t_i - t_{i-1}$, their correlations purely depend on the time difference.

A *4-D Mann Turbulence Generator* was programmed in C++ language, and made available online, using this simulation method discussed above. Independent random seeds are used to generate 12 samples of 4-D turbulence fields to validate the simulation tool. The spectra and coherence are calculated from the generated 4-D turbulence fields (estimated using Welch's method [80]) and compared with the theoretical results using the space-time tensor (Figures 4.4 to 4.7). In each 4-D field, three moments in time ($t = 0, 5$, and $12\,\mathrm{s}$) are considered, and the same parameters as in Figure 4.2 are used. The good agreements between the theoretical and estimated curves verified the correctness of the simulation tool.

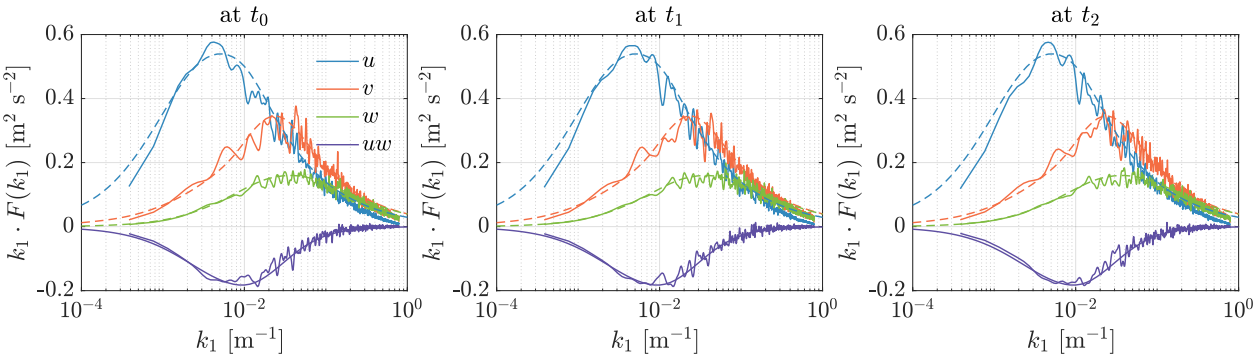

Figure 4.4: Comparisons spectra of three moments in time. Solid lines: estimated. Dashed lines: theoretical.

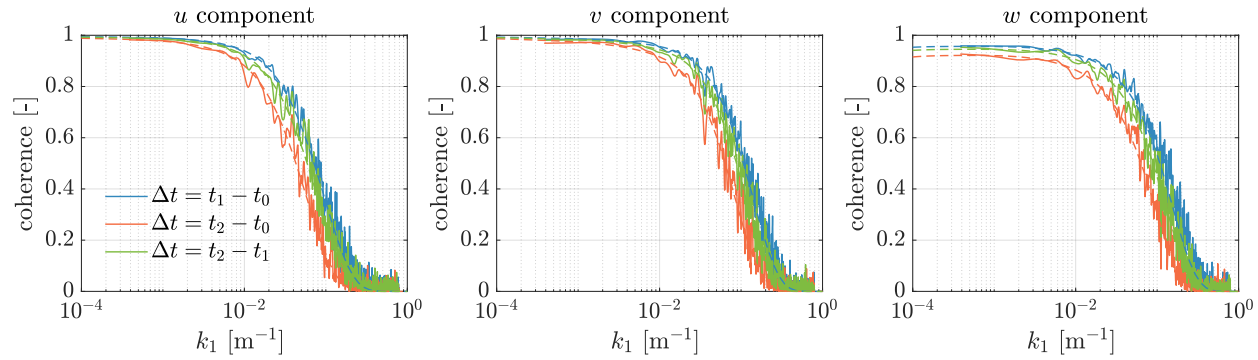

Figure 4.5: Comparisons of coherence with time differences. Solid lines: estimated. Dashed lines: theoretical.

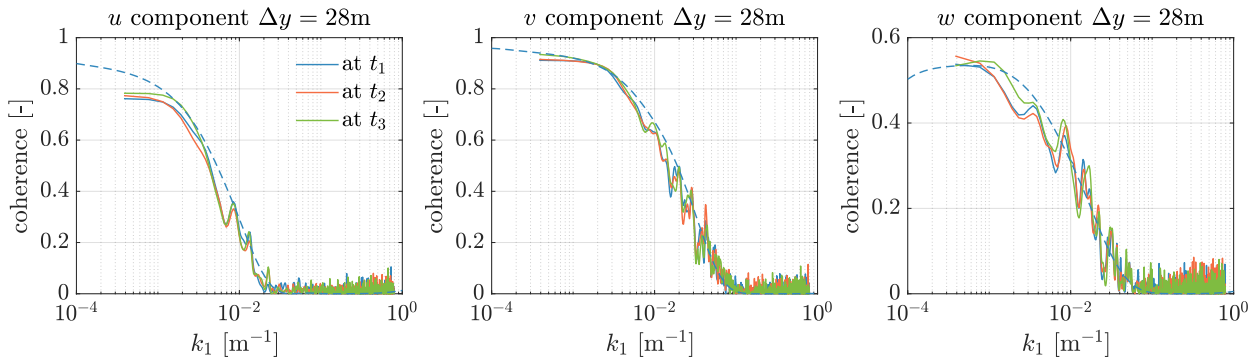

Figure 4.6: Comparisons of coherence with lateral separations. Solid lines: estimated. Dashed lines: theoretical.

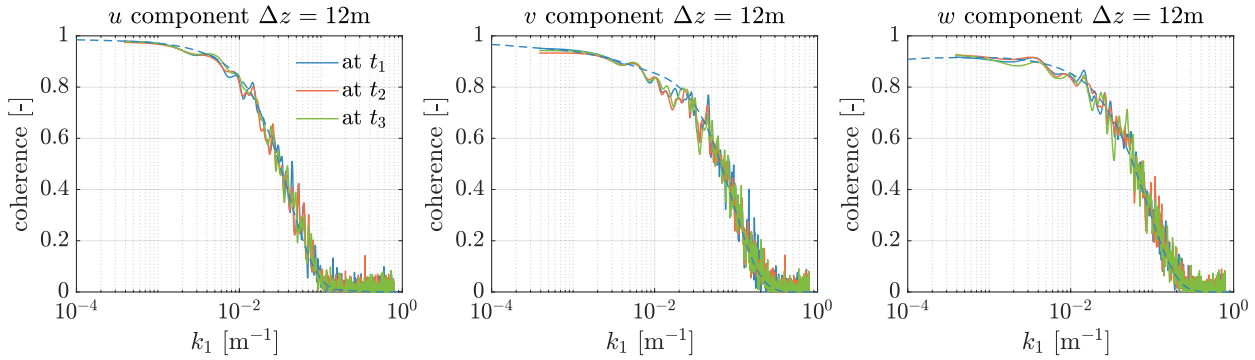

Figure 4.7: Comparisons of coherence with vertical separations. Solid lines: estimated. Dashed lines: theoretical.

4.3 Evaluation of Four-dimensional Turbulence Models

To validate the two 4-D turbulence modeling approaches introduced previously, we use the measurement data collected from a pulsed lidar and a meteorology mast. The model-based spectra and coherence are compared with those estimated from measurement data. Because lidar only provides LOS speed measurements, this section begins by deriving the spectral properties of lidar measurement from the 4-D turbulence models, introduces the measurement side and measurement devices, and finally compares the model-based spectra and coherence with those estimated from measurement data.

4.3.1 Spectral Properties of the Lidar Measurements

A pulsed lidar by Avent Lidar Technology was used to validate the 4-D turbulence models. The pulsed lidar can measure turbulence at different spatially distributed locations, thus providing turbulence coherence with different spatial separations. In particular, the lidar has a beam pointing in the longitudinal direction, which better quantifies the longitudinal coherence of the u component compared with other beams that have certain opening angles. Because lidar can only measure along the LOS direction, the lidar LOS auto-spectra and coherence are derived in this section for both models introduced earlier in this chapter. To be as consistent as possible with the equations in the literature, for Kaimal model-based spectra and coherence, the equations are primarily expressed in discrete format. For the Mann model-based space-time tensor, the equations are frequently expressed as being continuous.

For a lidar beam that measures at position $\boldsymbol{x} = (x, y, z)$, the fluctuation part of the lidar LOS speed measurement can be approximated using [81]

$$v_{\mathrm{los}}(\boldsymbol{x}, t) = \int_{-\infty}^{\infty} \varphi(s)\boldsymbol{n} \cdot \boldsymbol{u}(s\boldsymbol{n} + \boldsymbol{x}, t)\mathrm{d}s, \tag{4.34}$$

where $\boldsymbol{n} = (\cos\theta_{\mathrm{L}} \cos\phi_{\mathrm{L}}, \cos\theta_{\mathrm{L}} \sin\phi_{\mathrm{L}}, \sin\theta_{\mathrm{L}}) = (x_{\mathrm{n}}, y_{\mathrm{n}}, z_{\mathrm{n}})$ is a unit vector in the direction of a lidar beam that depends on the azimuth ϕ_{L} and elevation θ_{L} angles (Figure 4.8), s is the displacement along the lidar beam direction from the measured position $\boldsymbol{x} = (x, y, z)$, and $\varphi(s)$ is the weighting function owing to the lidar volume averaging. $\boldsymbol{u}(s\boldsymbol{n} + \boldsymbol{x}, t)$ is the vector of the turbulent wind components at position $(s\boldsymbol{n} + \boldsymbol{x})$ and time t. The discrete format of Equation 4.34 may be expressed as

$$v_{\mathrm{los}}(\boldsymbol{x}, t) = \sum_{i=1}^{N_{\mathrm{rw}}} f_{\mathrm{rw},i} \cdot v_{\mathrm{losP},i}(s_i\boldsymbol{n} + \boldsymbol{x}, t), \tag{4.35}$$

where N_{rw} is the number of discrete points, s_i is the ith discrete displacement point within the probe volume, $f_{\mathrm{rw},i}$ is the weighting factor, and $v_{\mathrm{losP},i}(s_i, t)$ is the single point LOS speed at position $(s_i\boldsymbol{n} + \boldsymbol{x})$ and time t. Because the weighting function is symmetric about the axis at $s = 0$, N_{rw} is frequently an odd number to ensure that the point at $s_i = 0$ is included. The weighting factors are normalized by the weighting function using

$$f_{\mathrm{rw},i} = \frac{\varphi(s_i)}{\sum_{i=1}^{N_{\mathrm{rw}}} \varphi(s_i)}, \tag{4.36}$$

to ensure that their summation equals one. The point-based LOS can be further expressed as

$$v_{\mathrm{losP},i}(s_i\boldsymbol{n} + \boldsymbol{x}, t) = u_i x_{\mathrm{n}} + v_i y_{\mathrm{n}} + w_i z_{\mathrm{n}}, \tag{4.37}$$

where u_i, v_i, and w_i are the wind velocity components. For the pulsed lidar used for model validation, the weighting function can be approximated as a triangular function [81]:

$$\varphi(s) = \begin{cases} \frac{h_\mathrm{p}-|s|}{h_\mathrm{p}^2}, & \text{if } |s| < h_\mathrm{p} \\ 0, & \text{otherwise} \end{cases}, \tag{4.38}$$

whose geometry is determined by half the length of a rectangular pulse h_p.

Kaimal Model-based Spectral Properties of Lidar Measurement

The spectral properties of lidar measurements based on the Kaimal model are first derived. Following the derivation by [6], the cross-spectrum of two LOS speed measurements is calculated using the Fourier transform of time:

$$S_{\mathrm{los,los'}}(f) = \mathcal{F}\{v_\mathrm{los}\}\mathcal{F}^*\{v'_\mathrm{los}\}, \tag{4.39}$$

where $\mathcal{F}^*\{\ \}$ denotes the conjugate of the Fourier transform and the symbol " $'$ " refers to another LOS speed measurement position. The discrete approximation of the two LOS speed measurements v_los and v'_los are obtained using Equation 4.35. Thus, Equation 4.39 can be extended as

$$\begin{aligned} S_{\mathrm{los,los'}} &= \mathcal{F}\{\sum_{i=1}^{N_\mathrm{rw}} f_{\mathrm{rw},i} \cdot v_{\mathrm{losP},i}\}\mathcal{F}^*\{\sum_{j=1}^{N_\mathrm{rw}} f_{\mathrm{rw},j} \cdot v'_{\mathrm{losP},j}\} \\ &= \sum_{i=1}^{N_\mathrm{rw}}\sum_{j=1}^{N_\mathrm{rw}} f_{\mathrm{rw},i} f_{\mathrm{rw},j} \mathcal{F}\{v_{\mathrm{losP},i}\}\mathcal{F}^*\{v'_{\mathrm{losP},j}\} \\ &= \sum_{i=1}^{N_\mathrm{rw}}\sum_{j=1}^{N_\mathrm{rw}} f_{\mathrm{rw},i} f_{\mathrm{rw},j} S_{\mathrm{losP,losP'},ij}, \end{aligned} \tag{4.40}$$

where $S_{\mathrm{losP,losP'},ij}$ is simply the cross-spectrum of two LOS wind speeds at the points i and j that belong to two beams. Here, the identical weighting factors are used for two LOS speed measurements because they are equivalent for the analyzed pulsed lidar. Using Equation 4.37, the cross-spectrum $S_{\mathrm{losP,losP'},ij}$ can be further extended as

$$\begin{aligned} S_{\mathrm{losP,losP'},ij} &= \mathcal{F}\{x_\mathrm{n}u_i + y_\mathrm{n}v_i + z_\mathrm{n}w_i\}\mathcal{F}^*\{x'_\mathrm{n}u_j + y'_\mathrm{n}v_j + z'_\mathrm{n}w_j\} \\ &= x_\mathrm{n}x'_\mathrm{n}S_{u,ij} + x_\mathrm{n}y'_\mathrm{n}S_{uv,ij} + x_\mathrm{n}z'_\mathrm{n}S_{uw,i,j} \\ &+ x'_\mathrm{n}y_\mathrm{n}S_{vu,ij} + y_\mathrm{n}y'_\mathrm{n}S_{v,ij} + y_\mathrm{n}z'_\mathrm{n}S_{vw,ij} \\ &+ x'_\mathrm{n}z_\mathrm{n}S_{wu,ij} + y'_\mathrm{n}z_\mathrm{n}S_{wv,ij} + z_\mathrm{n}z'_\mathrm{n}S_{w,ij}, \end{aligned} \tag{4.41}$$

by which the LOS cross-spectrum is decoupled as a series summation of the cross-spectrum between different velocity components.
In the Kaimal model, only the auto-spectra of the velocity components and the cross-spectra between the spatially separated u components are modeled, whereas other cross-spectra are assumed to be zero (because the coherence is not defined). Therefore, Equation (4.41) can be simplified as

$$S_{\mathrm{losP,losP}',ij} = x_{\mathrm{n}} x'_{\mathrm{n}} S_{u,ij}. \tag{4.42}$$

where $S_{u,ij}$ is the cross-spectrum of u components at points i and j. In a special scenario, the two LOS speed measurements are assumed to be identical, which means that the LOS cross-spectrum now becomes the LOS auto-spectrum. Subsequently, Equation 4.41 should be simplified differently as

$$S_{\mathrm{losP},ij} = \begin{cases} x_{\mathrm{n}}^2 S_{uu} + y_{\mathrm{n}}^2 S_{vv} + z_{\mathrm{n}}^2 S_{ww} & \text{if} \quad i = j, \\ x_{\mathrm{n}}^2 S_{u,ij} & \text{if} \quad i \neq j, \end{cases} \tag{4.43}$$

where S_{uu}, S_{vv}, and S_{uu} are the auto-spectra of the velocity components (Equation 2.12).
In practice, v or w components at different locations should be correlated because an incompressible wind flow is assumed and the continuity equation must be fulfilled [82]. If the v and w components are uncorrelated in space, the weighted average of LOS wind speeds within the lidar probe volume can result in unrealistically low contributions from v and w components because they are averaged out. This means that the contamination of non-longitudinal components is underestimated, which is discussed later in Section 4.3.4.
In a 4-D wind field, the exponential longitudinal coherence using Equation 4.1 accounts only for the coherence without a temporal shift. The turbulent wind field is assumed to be transported by the reference mean wind speed U_{ref}. If a longitudinal separation Δx_{ij} exists between point i and j, then the cross-spectrum $S_{u,ij}$ can be calculated using

$$\begin{aligned} S_{u,i,j} &= \mathcal{F}\{u_i(t - \Delta t_{ij})\}\mathcal{F}^*\{u_j(t)\} \\ &= e^{-j2\pi f \Delta t_{ij}} \mathcal{F}\{u_i(t)\}\mathcal{F}^*\{u_j(t)\}. \end{aligned} \tag{4.44}$$

where the time-shifting property of the Fourier transform is applied. The time shift is determined by $\Delta t_{ij} = U_{\mathrm{ref}}/\Delta x_{ij}$. This temporal shift introduces an additional sinusoidal-shape "coherence" into the cross-spectrum, and it should be differentiated from the longitudinal coherence γ_u caused by wind evolution. By definition, the 3-D coherence $\gamma_{xyz,i,j}$ is related to the

cross-spectrum $\mathcal{F}\{u_i(t)\}\mathcal{F}^*\{u_j(t)\}$ term by

$$\begin{aligned}\gamma_{xyz,ij} &= \sqrt{\frac{|\mathcal{F}\{u_i(t)\}\mathcal{F}^*\{u_j(t)\}|^2}{\mathcal{F}\{u_i(t)\}\mathcal{F}^*\{u_i(t)\}\mathcal{F}\{u_j(t)\}\mathcal{F}^*\{u_j(t)\}}} \\ &= \frac{|\mathcal{F}\{u_i(t)\}\mathcal{F}^*\{u_j(t)\}|}{S_u} \\ &\approx \frac{\mathcal{F}\{u_i(t)\}\mathcal{F}^*\{u_j(t)\}}{S_u}.\end{aligned} \tag{4.45}$$

Here, the absolute operator is removed because the imaginary part (quad-spectrum) in $\mathcal{F}\{u_i(t)\}\mathcal{F}^*\{u_j(t)\}$ is frequently negligible. Using the equation above, the two-point cross-spectrum is eventually obtained by

$$S_{u,ij} = e^{-j2\pi f \Delta t_{ij}} \gamma_{xyz,ij} S_{uu}. \tag{4.46}$$

Overall, the Kaimal model-based LOS speed measurement cross-spectrum can be determined using the linear property of the Fourier transform. The main point is to loop over all the cross-spectra between any two involved velocity components. Using the solution for the LOS cross-spectrum, we can easily consider two identical LOS speed measurements to obtain the LOS auto-spectrum and further calculate the LOS speed coherence using

$$\gamma^2_{\mathrm{los,los'}}(f) = \frac{|S_{\mathrm{los,los'}}(f)|^2}{S_{\mathrm{los}}(f) S_{\mathrm{los'}}(f)}. \tag{4.47}$$

Mann Model-based Spectral Properties of Lidar Measurement

The derivation of Mann model-based spectral properties of lidar measurement is primarily inspired by [83, 18]. The Fourier pair of Equation 4.12 can be expressed as

$$\boldsymbol{u}(\boldsymbol{x}, t) = \int \hat{\boldsymbol{u}}(\boldsymbol{k}, t) \exp(\mathrm{i}\boldsymbol{k} \cdot \boldsymbol{x}) \mathrm{d}\boldsymbol{k}, \tag{4.48}$$

where the integration $\int \mathrm{d}\boldsymbol{k} \equiv \int_{-\infty}^{\infty}\int_{-\infty}^{\infty}\int_{-\infty}^{\infty} \mathrm{d}k_1 \mathrm{d}k_2 \mathrm{d}k_3$. The Fourier representation of the velocity field is further used to substitute $\boldsymbol{u}(\boldsymbol{x}, t)$ in Equation 4.34, yielding

$$v_{\mathrm{los}}(\boldsymbol{x}, t) = \int_{-\infty}^{\infty} \varphi(s) \boldsymbol{n} \cdot \int \hat{\boldsymbol{u}}(\boldsymbol{k}, t) \exp(\mathrm{i}\boldsymbol{k} \cdot (s\boldsymbol{n} + \boldsymbol{x})) \mathrm{d}\boldsymbol{k} \mathrm{d}s. \tag{4.49}$$

Expanding the exponential term and adjusting the integration order results in

$$\begin{aligned}v_{\mathrm{los}}(\boldsymbol{x}, t) &= \int \boldsymbol{n} \cdot \hat{\boldsymbol{u}}(\boldsymbol{k}, t) \exp(\mathrm{i}\boldsymbol{k} \cdot \boldsymbol{x}) \int_{-\infty}^{\infty} \varphi(s) \exp(\mathrm{i}\boldsymbol{k} \cdot \boldsymbol{n} s) \mathrm{d}s \mathrm{d}\boldsymbol{k} \\ &= \int \boldsymbol{n} \cdot \hat{\boldsymbol{u}}(\boldsymbol{k}, t) \exp(\mathrm{i}\boldsymbol{k} \cdot \boldsymbol{x}) \hat{\varphi}(\boldsymbol{k} \cdot \boldsymbol{n}) \mathrm{d}\boldsymbol{k},\end{aligned} \tag{4.50}$$

where $\hat{\varphi}()$ is the Fourier transform of the range weighting function

$$\hat{\varphi}(\nu) = \int_{-\infty}^{\infty} \varphi(s) \exp(-\mathrm{i}\nu s)\mathrm{d}s. \tag{4.51}$$

For the Avent lidar whose range weighting function is represented by the triangular function (Equation 4.38), the Fourier transform is simply

$$\hat{\varphi}(\nu) = \mathrm{sinc}^2\left(\nu\frac{h_\mathrm{p}}{2}\right). \tag{4.52}$$

Further, the Fourier transform (non-unitary convention) of the LOS speed measurement in the x direction is

$$\begin{aligned}
\hat{v}_\mathrm{los}(k_1, t) &= \int_{-\infty}^{\infty} v_\mathrm{los}(\boldsymbol{x}, t) \exp(-\mathrm{i}k_1 x)\mathrm{d}x \\
&= \int_{-\infty}^{\infty} \int \boldsymbol{n}\cdot\hat{\boldsymbol{u}}(\boldsymbol{k}, t) \exp(\mathrm{i}\boldsymbol{k}\cdot\boldsymbol{x})\hat{\varphi}(\boldsymbol{k}\cdot\boldsymbol{n})\mathrm{d}\boldsymbol{k} \exp(-\mathrm{i}k_1 x)\mathrm{d}x \\
&= \int_{-\infty}^{\infty}\int_{-\infty}^{\infty} \boldsymbol{n}\cdot\hat{\boldsymbol{u}}(\boldsymbol{k}, t) \exp(\mathrm{i}(k_2 y + k_3 z))\hat{\varphi}(\boldsymbol{k}\cdot\boldsymbol{n})\mathrm{d}k_2\mathrm{d}k_3.
\end{aligned} \tag{4.53}$$

Similar to the derivation for the Kaimal model before, we consider another measurement position at $\boldsymbol{x'} = (x', y', z')$ with a unit vector $\boldsymbol{n'}$. The cross-spectrum of the two LOS speed measurements is then obtained using the following products:

$$\begin{aligned}
F_{\mathrm{los,los'}}(k_1) &= \hat{v}_\mathrm{los}(k_1, t)[\hat{v}'_\mathrm{los}(k_1, t)]^* \\
&= \int_{-\infty}^{\infty}\int_{-\infty}^{\infty} \boldsymbol{n}\cdot\hat{\boldsymbol{u}}(\boldsymbol{k}, t) \exp(\mathrm{i}(k_2 y + k_3 z))\hat{\varphi}(\boldsymbol{k}\cdot\boldsymbol{n})\mathrm{d}k_2\mathrm{d}k_3 \\
&\int_{-\infty}^{\infty}\int_{-\infty}^{\infty} \hat{\boldsymbol{u}}^*(\boldsymbol{k'}, t)\cdot\boldsymbol{n'} \exp(\mathrm{i}(-k'_2 y' - k'_3 z'))\hat{\varphi}(\boldsymbol{k'}\cdot\boldsymbol{n'})\mathrm{d}k_2\mathrm{d}k_3,
\end{aligned} \tag{4.54}$$

Again, the weighting function of a pulsed lidar does not change with the focused position; thus, the two identical $\hat{\varphi}()$ functions appear in the equation. Note that the product of Fourier coefficients with $\boldsymbol{k} \neq \boldsymbol{k'}$ is zero. Moreover, because the dot product $\boldsymbol{n}\cdot\hat{\boldsymbol{u}}(\boldsymbol{k})$ or $\hat{\boldsymbol{u}}^*(\boldsymbol{k'}, t)\cdot\boldsymbol{n'}$ applies to three elements in the unit vector and three velocity components, there are nine elements to be summed. It is more convenient to express the equation using ESC [25], i.e.,

$$F_{\mathrm{los,los'}}(k_1) = n_i n'_j \int_{-\infty}^{\infty}\int_{-\infty}^{\infty} \Phi_{ij}(\boldsymbol{k}) \exp(\mathrm{i}k_2\cdot(y-y') + \mathrm{i}k_3\cdot(z-z'))\hat{\varphi}(\boldsymbol{k}\cdot\boldsymbol{n})\hat{\varphi}(\boldsymbol{k}\cdot\boldsymbol{n'})\mathrm{d}k_2\mathrm{d}k_3 \quad \text{(ESC)}. \tag{4.55}$$

Additionally, the two LOS speed measurements might have a longitudinal separation; therefore, a shift by $\exp(\mathrm{i}k_1(x - x'))$ must be considered, and it is more general to express the cross-

spectrum as

$$F_{\mathrm{los,los'}}(k_1) = n_i n'_j \int_{-\infty}^{\infty}\int_{-\infty}^{\infty} \Phi_{ij}(\boldsymbol{k}) \exp(\mathrm{i}\boldsymbol{k}\cdot(\boldsymbol{x'}-\boldsymbol{x}))\hat{\varphi}(\boldsymbol{k}\cdot\boldsymbol{n})\hat{\varphi}(\boldsymbol{k}\cdot\boldsymbol{n'})\mathrm{d}k_2\mathrm{d}k_3 \quad \text{(ESC)}. \quad (4.56)$$

In the above derivation, a snapshot of the turbulence field is considered, and the lidar is assumed to measure along the x direction. In practice, lidar measures time series; thus, Taylor's frozen theory [2] should be assumed to convert the wavenumber spectrum to a frequency spectrum. However, the temporal evolution of the field can be considered by introducing the time delay of the lidar measurements, with which the space-time tensor replaces the spectral tensor and yields

$$\begin{aligned} F_{\mathrm{los,los'}}(k_1) &= \hat{v}_{\mathrm{los}}(k_1,t)[\hat{v}'_{\mathrm{los}}(k_1,t+\Delta t)]^* \\ &= n_i n'_j \int_{-\infty}^{\infty}\int_{-\infty}^{\infty} \Theta_{ij}(\boldsymbol{k},\Delta t) \exp(\mathrm{i}\boldsymbol{k}\cdot(\boldsymbol{x'}-\boldsymbol{x}))\hat{\varphi}(\boldsymbol{k}\cdot\boldsymbol{n})\hat{\varphi}(\boldsymbol{k}\cdot\boldsymbol{n'})\mathrm{d}k_2\mathrm{d}k_3 \quad \text{(ESC)}, \end{aligned} \quad (4.57)$$

where the time difference is approximated as $\Delta t = |x - x'|/U_{\mathrm{ref}}$, with $|x - x'|$ being the longitudinal separation of two measurement positions (see Section 4.2.1).
For the LOS auto-spectrum, it can be simply obtained by considering identical measurement positions in Equation 4.57, as follows:

$$F_{\mathrm{los}}(k_1) = n_i n_j \int_{-\infty}^{\infty}\int_{-\infty}^{\infty} \Phi_{ij}(\boldsymbol{k})\hat{\varphi}^2(\boldsymbol{k}\cdot\boldsymbol{n})\mathrm{d}k_2\mathrm{d}k_3 \quad \text{(ESC)}, \quad (4.58)$$

which is identical to the result derived by [81]. The auto-spectrum was investigated by [36] to characterize the turbulence measured using nacelle lidars. Here, the cross-spectrum is also important as it determines the spatial coherence. After obtaining the cross-spectrum and auto-spectrum, the wavenumber-based magnitude squared coherence between LOS speed measurements is calculated using

$$\mathrm{coh}^2_{\mathrm{los,los'}}(k_1) = \frac{|F_{\mathrm{los,los'}}(k_1)|^2}{F_{\mathrm{los}}(k_1)F_{\mathrm{los'}}(k_1)}. \quad (4.59)$$

4.3.2 Model Validation Against Simulation

In this section, numerical simulations are performed to cross-validate the derivations of lidar spectral properties presented in Section 4.3.1.

Simulation Setup

For the validation using real lidar measurements described later in this chapter, a pulsed lidar manufactured by Avent is considered for the numerical simulation. It has five beams pointing in different directions (Figure 4.8). The elevation and azimuth angles of the beams are summarized in Table 4.1. Specifically, beam 0 is pointing in the negative longitudinal direction (x axis). For each beam, the lidar can provide measurements from 10 range gates that are defined by the longitudinal separations (Δx) relative to the lidar position. In the analysis later, only three measurement gates (72 , 121 and 235 m) are used as examples. Using these three gates, longitudinal separations of 49 , 114 , and 163 m are obtained, which are representative of quantifying the longitudinal coherence. Additionally, the lateral and vertical separations from these gates are within the blade span of the medium-sized NREL 5.0 MW wind turbine (used in the remainder of this thesis). Therefore, it is also interesting to analyze the lateral-vertical coherence represented by these gates.

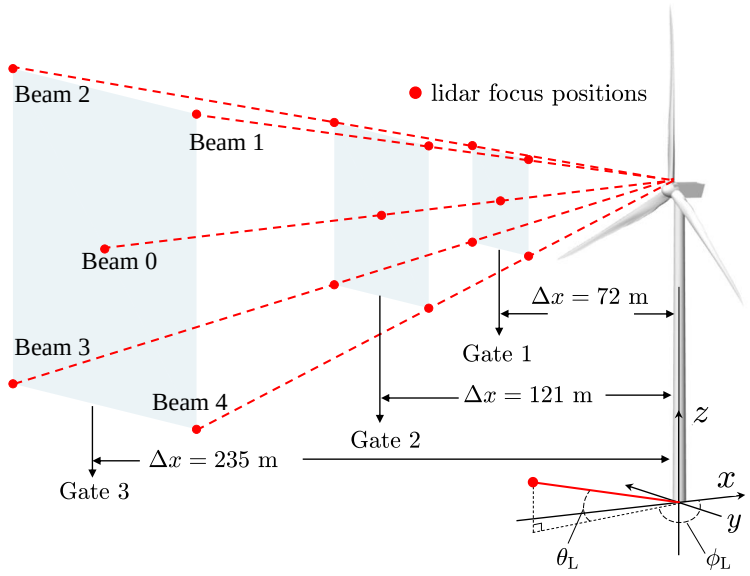

Figure 4.8: A sketch of the five-beam Avent lidar measurement characteristics. Only three measurement gates are shown as examples.

To simulate the lidar LOS speed measurements, the 4-D turbulence fields are generated using the *4-D Mann Turbulence Generator* and the *evoTurb* introduced previously. For the Mann model-based turbulence field, each field has a size of $3\times4096\times64\times64$ grid points, corresponding to the time, and the x, y, and z directions, respectively. The lengths in the x, y, and z directions

Table 4.1: Scan configuration of the Avent lidar system.

Number of beams	5
Beam azimuth-angles [°]	0, -169.2, 169.2, 169.2,-169.2
Beam elevation-angles [°]	0, 10.6, 10.6, -10.6,-10.6
Measurement distance	49 to 281 m (10 gates in total)
Full scan time	5.0s
Pulse half length	24.75 m

are 24576 , 320 , and 320 m, respectively. The defined domain size in y and z directions are significantly larger than the required size for the LOS simulation for the Avent lidar because the periodicity of the Mann model-based turbulence should be avoided [35]. The three moments in time of the fields are 6.00, 10.08, and 19.58 s. A reference mean wind speed $U_{\mathrm{ref}} = 12\,\mathrm{ms}^{-1}$ is assumed, which resulted in the longitudinal separations of 49 , 114 , and 163 m between the three 3-D spatial turbulence fields. In the actual application, Taylor's frozen hypothesis is applied to convert the x axis to time and conversely convert the moments in time to the longitudinal positions. For the Kaimal-model-based turbulence field, each field has a size of $3 \times 4096 \times 31 \times 31$ grid points, corresponding to the x positions, time t, y, and z directions, respectively. The lengths in the y and z directions are 150 and 150 m, respectively. For both turbulence models, each 3-D turbulence field (y, z, t) at one longitudinal position is used to simulate the LOS speed measurement at one range gate. When calculating the LOS time series, Equation 4.34 is discretized in the LOS direction with s varying from -15 to $+15$ m with steps of 15 m. Taylor's frozen hypothesis is also applied within the probe volume, which is demonstrated by [59] not to affect the spectral properties of the simulated LOS speed. The turbulence parameters are listed in the next section corresponding to those derived from stability class 1 (See Table 4.3 and 4.4).

To obtain the ensemble-averaged spectra, we generate 12 independent 4-D turbulence fields with the same properties as discussed above but with different random number seeds. The LOS speed measurements are simulated using the same sampling frequency (2 Hz) as the turbulence fields.

Comparisons between Models and Simulations

Figure 4.9 (a) shows the auto-spectra of LOS speed measurements using the Mann model and lidar measurement simulations. Owing to symmetry, the results of beam 2 are identical to those of beam 1, and the results of beam 3 are identical to those of beam 4. Thus, only the results from beams 1 and 3 are shown. Additionally, because the auto-spectrum is independent of the measurement gate (because of the assumed homogeneity and stationarity), only the results from gate 2 are shown. It is clear that the downwards-looking beam 3 has a much lower variance

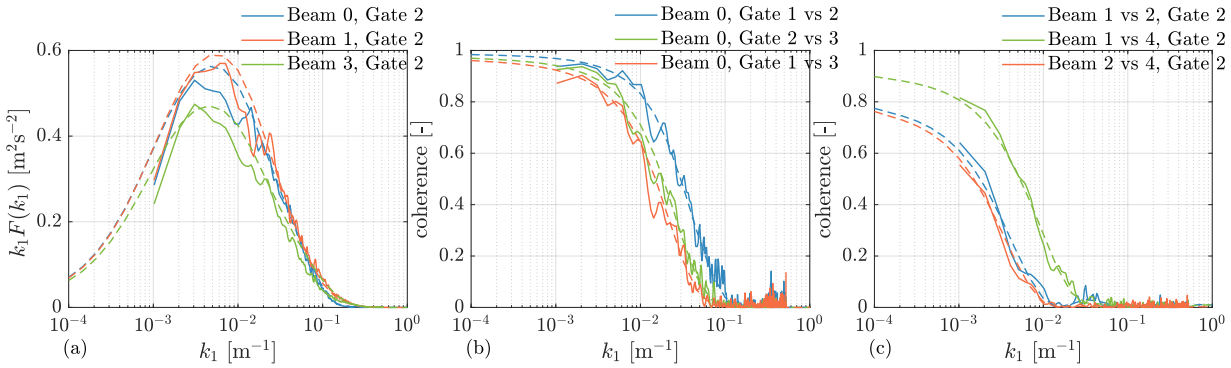

Figure 4.9: Lidar LOS speed measurement spectra (a), longitudinal coherence (b), and vertical-lateral coherence (c) from the numerical simulation (solid lines) and theory using the Mann model (dashed lines). The Mann model parameters used are listed in Table 4.3 (stability 1).

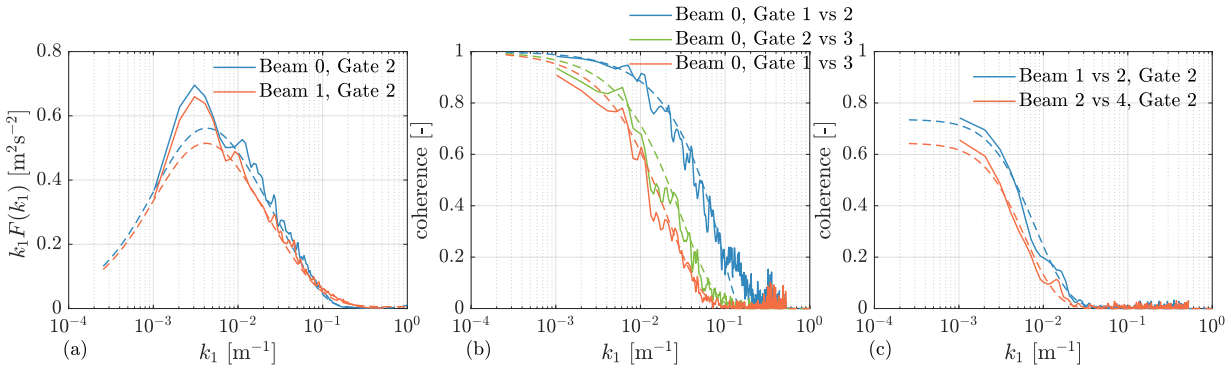

Figure 4.10: Lidar LOS speed measurement spectra (a), longitudinal coherence (b), and vertical-lateral coherence (c) from the numerical simulation (solid lines) and theory using the Kaimal model (dashed lines). The Kaimal model parameters used are listed in Table 4.3 (stability 1)

(area below the spectra) compared with that of the other beams. Figure 4.9 (b) compares the model and simulated coherence decay between different gates of beam 0. Beam 0 points in the longitudinal direction (x axis); thus, it reflected the coherence decay owing to the longitudinal separation or temporal delay. The separation between gates 1 and 3 is the largest, and over this distance, the eddies evolved for a longer time, which results in the lowest coherence. The largest coherence is between gates 1 and 2 because of the smallest separation. In Figure 4.9 (c), beams 1, 2, and 4 are shown as examples of the decorrelation caused by lateral or vertical separations in both the model and simulations. Although the separation distances for the beam pairs 1-2 and 1-4 are the same, the coherence for the first pair is much smaller than that of the latter pair. This is because beams 1 and 2 are separated vertically, and the spatially correlated v component acts oppositely on beams 1 and 2. Similarly, the spatially correlated w component acts oppositely on beams 1 and 4. However, the larger energy of the v component compared with that of the w component causes a larger decorrelation for beams 1 and 2 than that for beams 1 and 4.

Figure 4.10 (a) shows the auto-spectra of LOS speed measurements from the Kaimal model and lidar measurement simulations. Owing to symmetry, the results of beams 1 to 4 are identical;

thus, only the results from beam 1 are shown. Again, the auto-spectrum is independent of the measurement gate (because of the assumed homogeneity and stationarity). Therefore, only the results from gate 2 are shown. For the Kaimal model, no difference is observed between the downward-looking and upward-looking beams because the uw co-spectrum is not modeled (a more detailed analysis is presented in Section 4.3.4). Figure 4.10 (b) compares the model and simulated coherence decay between different gates of beam 0, from which a larger separation results in a faster coherence decay, as expected. Figure 4.10 (c) shows the LOS speed coherence decay owing to lateral-vertical separations in both the model and simulations. In the Kaimal model, the coherence only depended on the absolute separation distance in the y-z plane. Only beam pairs 1-2 and 2-4 are shown because other pairs are the same as these pairs.
Overall, the numerical simulations (solid lines) match the theoretical values (dashed lines) for both the Mann and Kaimal models. Some small discrepancies can be attributed to the nature of the simulations, as we use discrete turbulence fields, discrete lidar LOS simulations, and limited random seed numbers.

4.3.3 Measurement Site

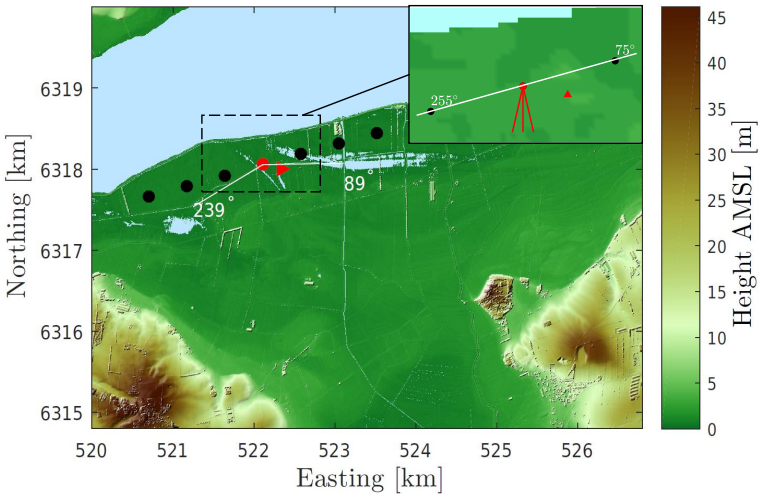

Figure 4.11: The top view of the measurement site. The color map shows the digital elevation of the terrain above mean sea level (AMSL). Wind turbines are marked by circles. Turbine 4 with the lidar is shown by a red circle. The red triangle is the meteorological mast. Red lines in the zoomed-in view of the dashed rectangle indicate the lidar beams. Figure source [20].

To further evaluate the 4-D turbulence models, the data from the measurement campaign at the Nørrekær Enge wind farm was collected. The Nørrekær Enge wind farm (Figure 4.11) locates in northern Jutland, Denmark. It has 13 Siemens 2.3 MW-93 wind turbines installed in a row. The wind turbine row aligns approximately 73.9° from the north. The turbines have a hub height of 81.8 m and a rotor diameter of 92.6 m and are numbered sequentially from west to east. An Avent pulsed lidar was installed on the nacelle of turbine 4 (red dot).

A meteorological mast (red triangle) was located 232 m away from turbine 4, at 101.2° from the north. The nearby wind turbines of turbine 4 are located 75° and 255° from the north, respectively. More details of the site are available in [36].

Instruments

Pulsed lidar: The five-beam Avent pulsed lidar (hereafter known as Avent) was mounted on the nacelle of turbine 4, staring upstream [36]. The beam trajectory is provided in Table 4.1 and is depicted in Figure 4.8. In total, the lidar has 10 different range gates (49, 72, 95, 109, 121, 142, 165, 188, 235, and 281 m) and the measurements from these range gates could be considered as simultaneous (see Section 2.2.2 for the measurement principle). For each beam direction, 1 s was required to record the LOS speeds of the 10 range gates. Thus, each beam was sampling at 0.2 Hz.
Meteorological mast: The height of the meteorological mast was 80 m. Cup anemometers (P2546A) were mounted at heights of 80, 78, 57, and 33 m. A 3-D sonic anemometer (CSAT3) was deployed at a height of 76 m. Moreover, two temperature sensors (Pt500 Sensor) were installed at heights of 78 and 2 m. Wind vanes (Vector W200P) were installed at heights of 78, 57, and 33 m.
Turbine data: Because the lidar was mounted on the nacelle roof, the yawing direction signal from the supervisory control and data acquisition system of turbine 4 was collected as the lidar yaw direction. The yaw misalignment of the lidar relative to the mean wind direction was further used to select the wake-free sectors, as discussed in the following section.

Data Selection

Overall, the measurement data were recorded from October 27, 2015 to January 7, 2016. Similar to [36], the data are analyzed using the typical 10 min intervals. For each 10 min interval, the following criteria are applied to select the data for model evaluation:

(a) Because the turbine wake can deteriorate the assumption of homogeneous turbulence in the turbulence models [36, 70], to avoid the wake effects from other turbines, we select the data only when the turbine yawing direction was within the wake-free directions [36] (89° to 239° in Figure 4.11).

(b) Data in which the yaw error was larger than 10° are not selected based on the direction of the vane at a height of 78 m and the turbine yaw direction.

(c) We select hub-height mean wind speeds within the range of 11–13 ms^{-1} because wind speeds above the rated wind speed of turbines are the focus of lidar-assisted pitch feed-forward control. The upper wind speed limit is also selected to ensure a larger number of

10 min samples because the number of samples with higher mean wind speeds decreases in the collected data.

(d) Because of lidar beam blockage from the turbine blades, the data availability of beam 3 was significantly lower than that of other beams. Therefore, this beam is not considered in the analysis.

Data Processing

Similar to [36], for each 10 min time series, the lidar LOS speed time series of each measured position is de-trended linearly. Subsequently, the spikes of the time series are removed when the values exceeds ±3 times the standard deviation of the LOS speed within the 10 min. Finally, the linear interpolation is applied to fill the missing data. Additionally, the same de-trending and de-spiking methods described in [36] are used to process the 1 Hz sonic and cup anemometer data. Thereafter, the sonic measurements are projected to ensure the u component is aligned with the mean wind direction.
With the sonic anemometer measurements, the friction velocity u_f is firstly computed as

$$u_\mathrm{f} = \left(\overline{uw}^2 + \overline{vw}^2\right)^{1/4}, \tag{4.60}$$

where the velocity components are the fluctuation part. Subsequently, the Obukhov length [84] is calculated as

$$L_\mathrm{O} = -\frac{{u_\mathrm{f}}^3 \overline{T}}{\kappa g \overline{w\theta_\mathrm{v}}}, \tag{4.61}$$

where κ is the von Kármán constant (≈0.40), g is the gravitational acceleration, $\overline{T}$ is the mean reference temperature, and θ_v is the fluctuation part of the virtual potential temperature. The Obukhov length is used later to classify our measurements into different atmospheric stability classes. Atmospheric stability indicates the buoyancy effects on turbulence generation, and it is frequently related to the temperature gradient by height. Studies of [36, 33, 78] have shown that the turbulence spectral parameters are related to atmospheric stability.
It would be interesting to evaluate how effectively the original Mann model eddy lifetime expression (Equation 2.19) presents the longitudinal coherence. For the evaluation, the mean shear wind profile is required. The second-order polynomial fit by [85] was used to approximate the vertical mean wind profile as

$$U(z) = U_0 + A_b \ln(z) + B_a \ln^2(z), \tag{4.62}$$

where U_0, A_b, and B_a are three constants to be solved via least-square fitting using $U(z)$ from the cup anemometers at the heights of 33, 57, and 80 m. The mean vertical shear is then

estimated using [86]

$$\frac{\mathrm{d}U(z)}{\mathrm{d}z} = \frac{A_b + 2B_a \ln(z)}{z}. \tag{4.63}$$

Based on the collected data, the shear profile dU/dz is estimated at $z = 80$ m.
The 10 min periods are classified into five atmospheric stability classes based on the dimensionless atmospheric stability parameter z/L_{O}, as shown in Table 4.2, and the classification criteria are similarly considered by [36]. $z = 67$ m is the height considered for the atmospheric stability estimates. The stability is close to neutral under stability class 1, and it became more stable in classes with larger numbers. However, the samples under unstable stability conditions were insufficient; therefore, this condition is not analyzed. For each stability class, the spectra of the Avent LOS speed and sonic anemometer velocity components are calculated. Subsequently, an anti-aliasing method developed by Kirchner [87] is applied to filter the LOS spectra from the Avent lidar owing to noise above the sampling frequency of 0.2 Hz [36]. After the noise caused by aliasing is filtered, the ensemble-averaged LOS spectra and coherence are computed by averaging the samples within each stability class. Table 4.2 summarizes the processed variables under each stability class.

Table 4.2: Atmospheric flow parameters calculated using the measurement data. "No." indicates the number of 10 min samples

Class	z/L_{O}	No.	$\langle z/L_{\mathrm{O}} \rangle$	$\langle U_{80\,\mathrm{m}} \rangle [\mathrm{ms}^{-1}]$	$\langle \mathrm{d}U/\mathrm{d}z \rangle$ $[\mathrm{s}^{-1}]$	Description
Stability 1	$[-0.1, 0.1)$	93	0.0244	12.01	0.0195	Neutral
Stability 2	$[0.1, 0.2)$	220	0.1514	12.26	0.0333	Near stable
Stability 3	$[0.2, 0.3)$	133	0.2434	12.08	0.0359	Near stable
Stability 4	$[0.3, 0.4)$	79	0.3460	12.08	0.0370	Stable
Stability 5	$[0.4, 0.5)$	43	0.4471	11.97	0.0383	Stable

4.3.4 Model Evaluation

This section compares the model-based lidar spectra and coherence against the lidar measurements from the Nørrekær Enge wind farm to evaluate the models. Both the Kaimal and Mann models are evaluated.

Model Parameters

First, the ensemble-averaged auto-spectra of the u, v, and w velocity components and the cross-spectrum between u and w components from the sonic measurements are used to determine the model parameters.
For the Mann model, only three parameters $\alpha\varepsilon^{2/3}$, L, and Γ should be determined. This is achieved through least-square fitting the Mann model spectra and co-spectra to the measured sonic spectra. Note that the original formulation of the eddy lifetime (Equation 2.19) is used for the fitting process. The fitting can be expressed as the optimization problem below

$$\begin{aligned} \min_{\alpha\varepsilon^{2/3},L,\Gamma} \quad & \sum_{n=1}^{N} \left[\left(\sum_{i=1}^{3} \left(S_{\mathrm{so},ii}(f_n) \cdot f_n - 2F_{ii}(k_{1,n}) \cdot k_{1,n} \right) + S_{\mathrm{so},13}(f_n) \cdot f_n - 2F_{13}(k_{1,n}) \cdot k_{1,n} \right)^2 \right] , \\ \text{s.t.} \quad & k_{1,n} = \tfrac{2\pi f_n}{U_{\mathrm{ref}}}, f_n > 0. \end{aligned} \tag{4.64}$$

Here, n is the index of the discrete frequency vector f_n and wavenumber vector $k_{1,n}$ and N is the total number of discrete vectors. $S_{\mathrm{so},ii}$ is the spectra estimated from the sonic data. Note that the Mann model spectra $F_{ii}(k_{1,n})$ are multiplied by 2 because they are two-sided spectra, whereas the sonic spectra estimated from data are single-sided. In addition to the three parameters, other parameters b_1, b_2, and γ determined the coherence. These parameters were determined by [20] and are listed in Table 4.3.

Table 4.3: Observed turbulence parameters for the space-time tensor. The fourth column onward corresponds to the adjusted parameters of the temporal-evolving τ_{e}. Here, "*" means that the parameters approximate the original Mann eddy lifetime expression.

Class	$\alpha\varepsilon^{2/3}$ [$\mathrm{m}^{4/3}\mathrm{s}^{-2}$]	L [m]	Γ [-]	b_1 of τ_{s} [-]	b_2 of τ_{s} [-]	b_1 of τ_{e} [-]	b_2 of τ_{e} [-]	γ of τ_{s} [s]	γ of τ_{e} [s]
stability 1	0.184	49	3.4	-1*	-2/3*	-1	-7/3	Γ	432
stability 2	0.205	38	2.9	-0.8	-2/3	-1	-7/3	Γ	349
stability 3	0.158	34	2.7	-0.75	-2/3	-1	-7/3	Γ	340
stability 4	0.161	31	2.7	-0.75	-2/3	-1	-7/3	Γ	239
stability 5	0.142	30	2.4	-0.70	-2/3	-1	-7/3	Γ	207

Similarly, the Kaimal spectra are fitted using

$$\begin{aligned} &\min_{L_i,\sigma_i} \quad \sum_{n=1}^{N} \left[\left(S_{\mathrm{so},ii}(f_n) \cdot f_n - S_{ii}(f_n) \cdot f_n \right)^2 \right] , \\ &\text{with} \quad i = 1, 2, \text{ or } 3. \end{aligned} \tag{4.65}$$

The main difference to the Mann model is that each velocity component in the Kaimal model requires two parameters L_i and σ_i. Because the Kaimal model is used with the exponential coherence model, for each stability class, the coherence parameters are obtained by least-squares-fitting the model-based LOS speed coherence with that estimated from the Avent lidar. The longitudinal coherence parameters are fitted using the measurement positions at range gates 2 and 3 of beam 0 as

$$\begin{aligned} &\min_{a_x,b_x} \quad \sum_{n=1}^{N} \left[\tfrac{1}{f_n} \left(\mathrm{coh}^2_{\mathrm{los,los'}}(f_n) - \mathrm{coh}^2_{\mathrm{avent,los,los'}}(f_n) \right)^2 \right] , \\ &\text{s.t.} \quad \Delta y = \Delta z = 0\mathrm{m}, \quad \Delta x = 114\,\mathrm{m}, \quad \text{and} \quad a_x, b_x \geq = 0, \end{aligned} \tag{4.66}$$

which only has a longitudinal separation of 114 m. Moreover, the lateral-vertical coherence parameters are fitted using the measurements of beams 0 and 1 at range gate 1:

$$\begin{aligned} &\min_{a_{yz}} \quad \sum_{n=1}^{N} \left[\tfrac{1}{f_n} \left(\mathrm{coh}^2_{\mathrm{los,los'}}(f_n) - \mathrm{coh}^2_{\mathrm{avent,los,los'}}(f_n) \right)^2 \right] , \\ &\text{s.t.} \quad \Delta y = \Delta z = 13.7\mathrm{m}, \quad \Delta x = 0\,\mathrm{m}, \quad \text{and} \quad a_{yz} \geq = 0. \end{aligned} \tag{4.67}$$

Note that the interception parameter b_{yz} is not fitted, and the default value is used because fitting this parameter introduces an additional gradient and deteriorates the optimization algorithm. The squared errors are divided by f_n to ensure equal weightings in the frequency bins [88]. The fitted parameters for the Kaimal spectra and exponential coherence model are listed in Table 4.4.

Table 4.4: Fitted turbulence parameters for the Kaimal spectra and exponential coherence model under the observed stability classes. Here, "*" means that the optimization algorithm reached the constraint value.

Class	σ_1 [ms^{-1}]	σ_2 [ms^{-1}]	σ_3 [ms^{-1}]	L_1 [m]	L_2 [m]	L_3 [m]	a_x [-]	b_x [m^{-1}]	a_{yz} [-]
stability 1	2.286	1.705	1.339	355.8	149.8	88.2	2.05	0*	9.94
stability 2	1.967	1.665	1.243	176.5	108.9	70.0	1.92	3.05×10^{-4}	11.4
stability 3	1.717	1.486	1.107	139.2	98.5	61.7	1.88	3.93×10^{-4}	13.53
stability 4	1.546	1.363	1.018	125.7	86.6	52.3	1.74	7.11×10^{-4}	16.84
stability 5	1.349	1.273	0.919	102.1	77.0	46.7	1.70	9.60×10^{-4}	20.23

Spectra of Velocity Components

Figure 4.12 shows the results using the original and adjusted formulations of τ_s (Equation 4.18) in the Mann model. These adjusted τ_s parameters are presented in Table 4.3. In stability class 1 (neutral), the expression of τ_s is not adjusted so that the lines overlap in the figure. Because the coherence between the LOS speeds of different beams at the same range gate are overestimated with the original formulation of τ_s in a more stable atmosphere, [20] suggested adjusting the expressions for τ_s in a more stable atmosphere. For neutral conditions, the Mann model fits the measurements well, because it was originally formulated for the neutral atmospheric condition. Overall, good agreements between the sonic-based and Mann model-based spectra and co-spectra for all stability conditions are observed. The largest differences are observed in the stable side (classes 3 to 5) for the v spectrum and the uw cross-spectrum. For stability classes 2 to 5, adjusting the τ_s's slope b_1 mainly reduced the energy of the u spectrum at low frequencies/wavenumbers, which is in agreement with the sonic measurements. The turbulence length scale L decreased as the atmosphere became more stable, similar to the results of [36, 78].

Figure 4.13 compares the sonic spectra with the fitted Kaimal spectra. Better agreements are observed for the u component. The model-based spectra tended to overestimate the energy of other components (particularly the v components) in the lower frequencies/wavenumbers range. Additionally, the uv co-spectra is not included in the IEC Kaimal model; thus, no model-based curves are shown. The fitted Kaimal spectra parameters are provided in Table 4.4.

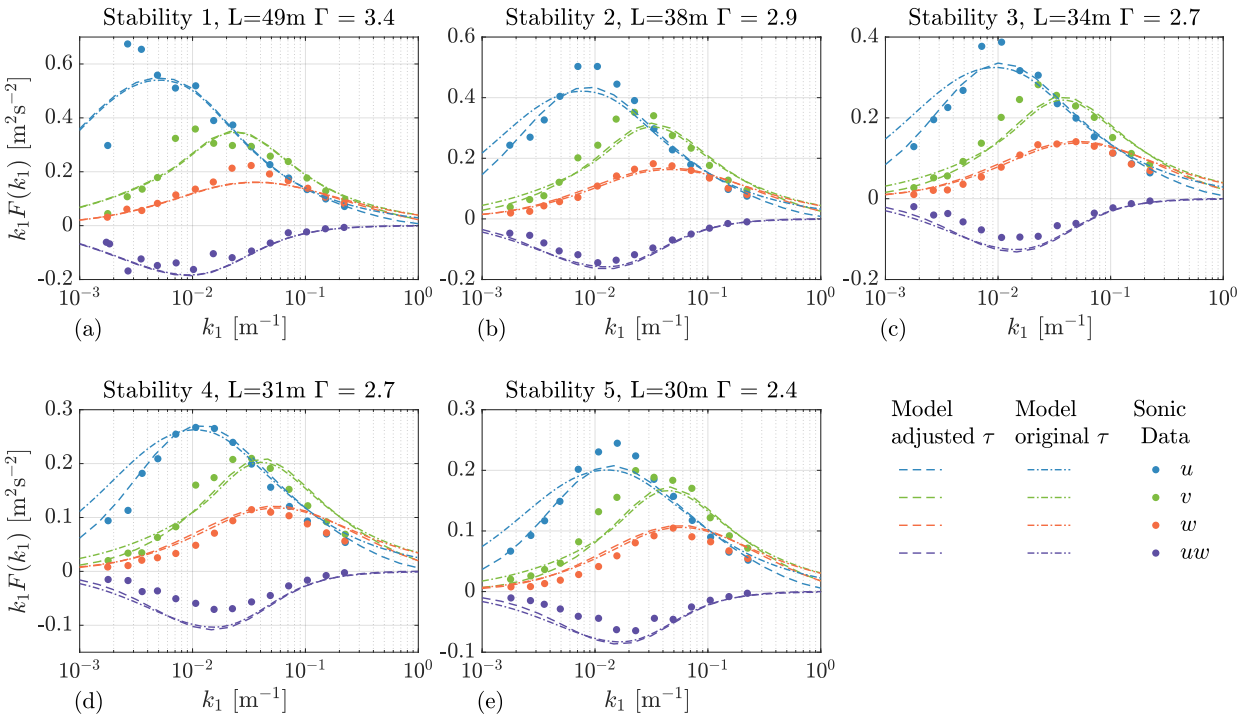

Figure 4.12: Comparisons of turbulence spectra between the Mann model and sonic measurements. "Model adjusted τ" refers to adjusted slopes of τ_s. "Model original τ" refers to the original τ_s expression (Equation 2.19).

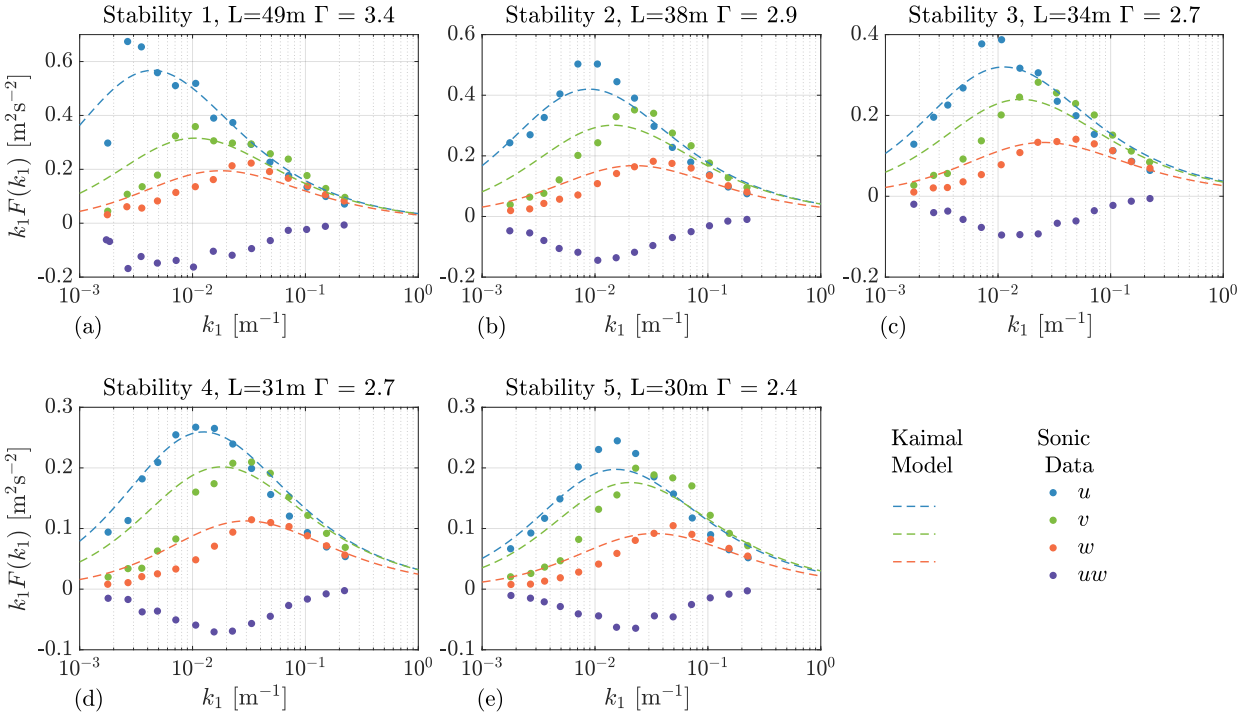

Figure 4.13: Comparisons of turbulence spectra between the Kaimal model and sonic measurements.

LOS Speed Spectra

To compare the auto-spectra of LOS speed, Equations 4.39 and 4.58 are used to calculate the model-based LOS auto-spectra. Here, measurement gate 2 is considered for comparison.
The comparison between the Mann model-based and Avent data-derived spectra is shown in Figure 4.14. The best agreements are observed in stability classes 2 and 3, which have more 10 min samples (220 and 130, respectively) than the other stability classes. The data-based spectra exhibited more scatters in stability 5, which could have been caused by the smallest number of samples (43 samples). For stability class 1, the model-based spectra are overall higher than those of the Avent measurements, but the spectral shapes are similar [20]. Because the u component spectra determined by the model and sonic data also have disagreements in lower frequency ranges, the overestimation of the LOS spectra might have been caused by the uncertainties resulting from the fitting using sonic data. Additionally, better agreements are observed using the adjusted τ_e expressions. Within the low wavenumber range, the LOS speed spectrum has large contributions from the u component. Reducing the τ's slope b_1 primarily reduced the model-based u spectrum within the same low wavenumber range, which resulted in a better agreement with the measurements [20].
For all the Mann model-based spectra, the spectra of beams 2 and 3 are equal because of the symmetry. However, beam 4 looking downward differs from beam 1 looking upward because of the negative covariance between the u and w components. This covariance induces additional variance in the beams looking upward but reduces the variances looking downward. This phenomenon is also exhibited by the Avent data, where the green and orange scatters are generally higher than the blue scatters, and the purple scatters are the lowest.
Figure 4.15 compares the Kaimal model-based spectra and Avent data-derived spectra. Because the covariance between u and w components is not considered, the Kaimal model-based LOS spectra are symmetrical on the top and bottom and on both sides. Therefore, only the orange line is shown, representing the model-based spectra for beams 1, 2, and 4. We observe that the overall agreements exhibit more discrepancies compared with those of the Mann model. For stability classes 2 to 5, the beam 0 spectra exhibit better agreements, but the spectra of beams 1 and 2 are underestimated. Thus, when estimating turbulence intensity using nacelle lidar and the Kaimal model, the impacts of underestimation on the upward-looking beams and overestimation on the downward-looking beams should be assessed.

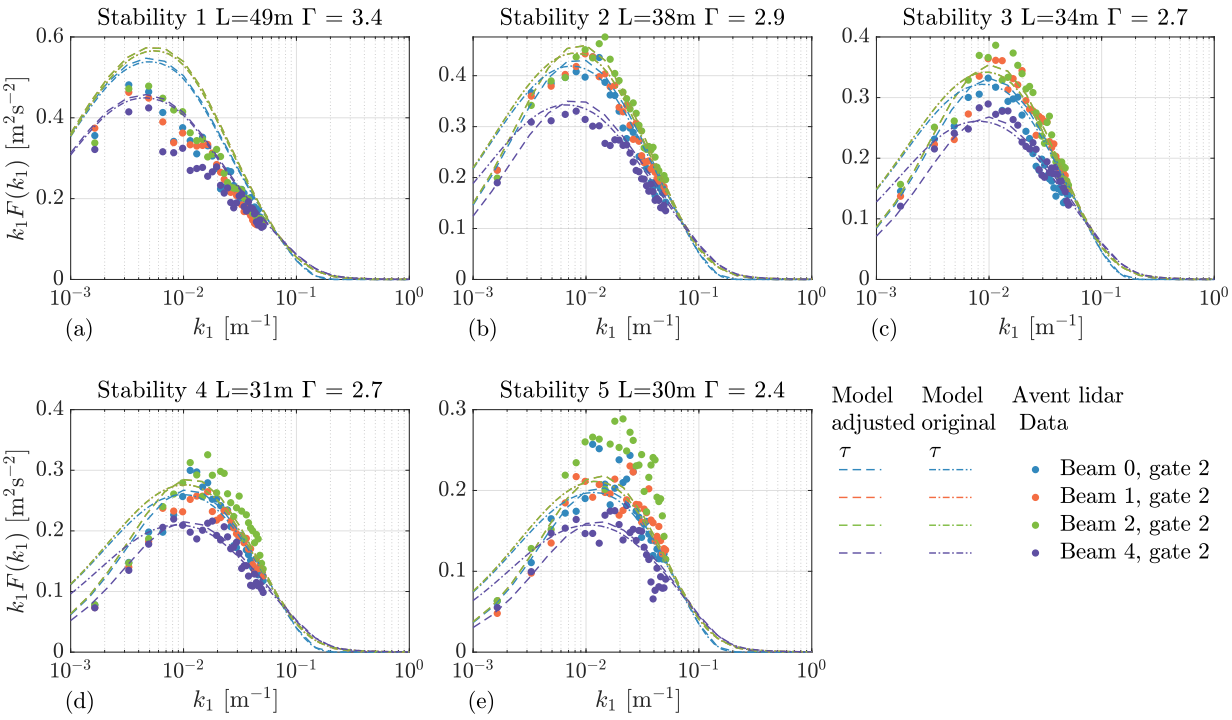

Figure 4.14: Comparisons of lidar LOS speed spectra derived by the Mann model and those calculated from Avent measurements. "Model adjusted τ" refers to adjusted slopes of τ_s and τ_e. "Model original τ" refers to the original τ_s expression (Equation 2.19) and $\tau_s = \tau_e$.

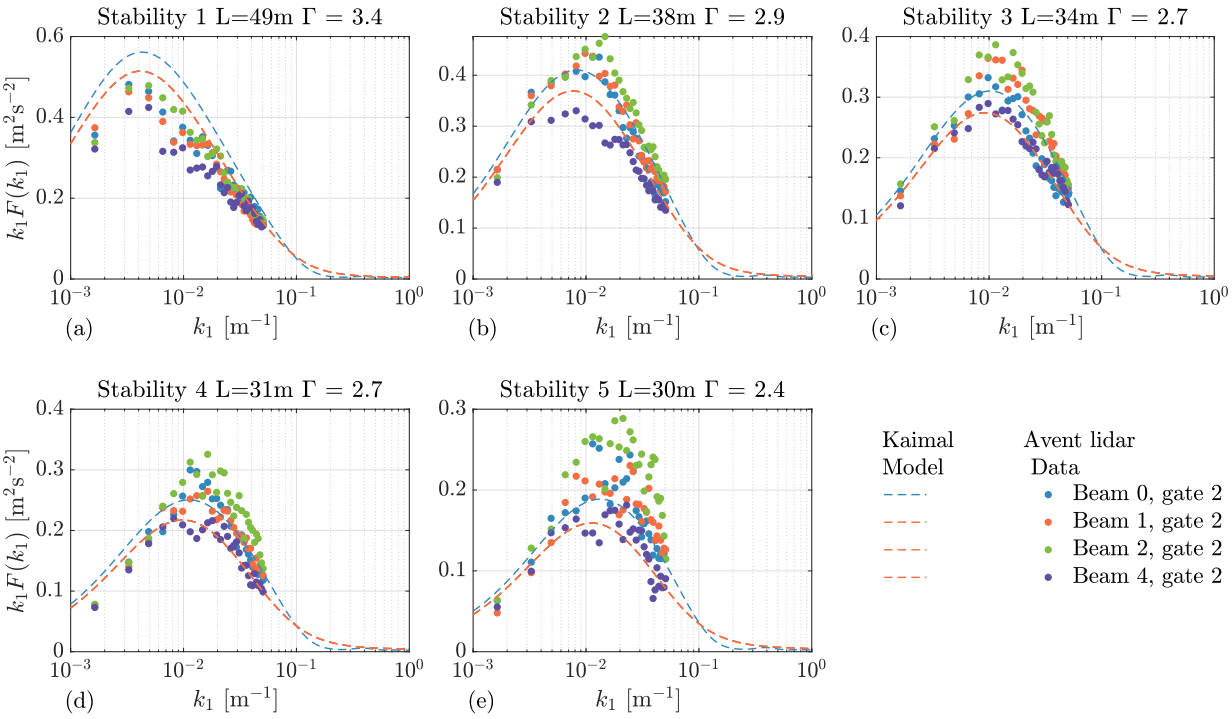

Figure 4.15: Comparisons of lidar LOS speed spectra derived by the Kaimal model and those calculated from Avent measurements.

LOS Speed Coherence with Only Longitudinal Separation

The Avent lidar data from beam 0 has only longitudinal separations between different range gates, neglecting the small yaw misalignment. It is selected to assess the longitudinal coherence represented by the space-time tensor $\mathbf{\Theta}$ and the exponential coherence model. As shown by Figure 4.8, three range gates (1 to 3), are considered for the comparison.

Figure 4.16 compares the Mann model-based coherence with that estimated from the Avent data. The dotted lines show the coherence derived using the original eddy lifetime expression (Equation 2.19) for τ_e, which decays significantly slower than that calculated from the measurements. Therefore, [20] suggested adjusting the slopes of the eddy lifetime expression and using Equation 4.18 for τ_e. The slope of τ_e determines the rate of coherence decay with increasing wavenumber. For example, by adjusting the slope parameter b_2 to $b_2 = -7/3$, good agreements between the coherence calculated from the space-time tensor and that calculated from the lidar measurements are obtained, as shown by the dashed lines in Figure 4.16. For the three possible longitudinal separations, the space-time tensor could reflect the coherence from data correctly. In addition to b_2, the parameter γ also needs to be adjusted. In the original eddy lifetime of the Mann model [11], γ is equivalent to the product $\Gamma \left(\frac{\mathrm{d}U}{\mathrm{d}z}\right)^{-1}$. The adjusted parameters for different stability classes are listed in Table 4.3.

Figure 4.17 compares the Kaimal model-based coherence with that estimated from the Avent data. The coherence decay parameters a_x and b_x are fitted using the data between range gates 2 and 3 (as listed in Table 4.4); therefore, good agreements are observed for this separation. The coherence between range gates 1 and 3 is also reasonably predicted. However, the exponential coherence model overestimates the coherence between range gates 1 and 2, which have the smallest distance. A possible solution to this problem might be to fit the other coherence decay parameters a_x and b_x and make them dependent on the separation distances or to fit all the coherence collected from data simultaneously, using a method similar to that used by [17] to fit the correlation coefficient.

By comparing panels (a) to (e), no considerable differences in longitudinal coherence are observed between the investigated stability classes. The coherence decays only slightly faster in stable conditions compared with the neutral condition. Within the low wavenumber range, the coherence is lower and more sensitive to longitudinal separations for stable conditions compared with near-neutral conditions, which may have been caused by the smaller turbulence length scales inherent in stable atmosphere conditions [20].

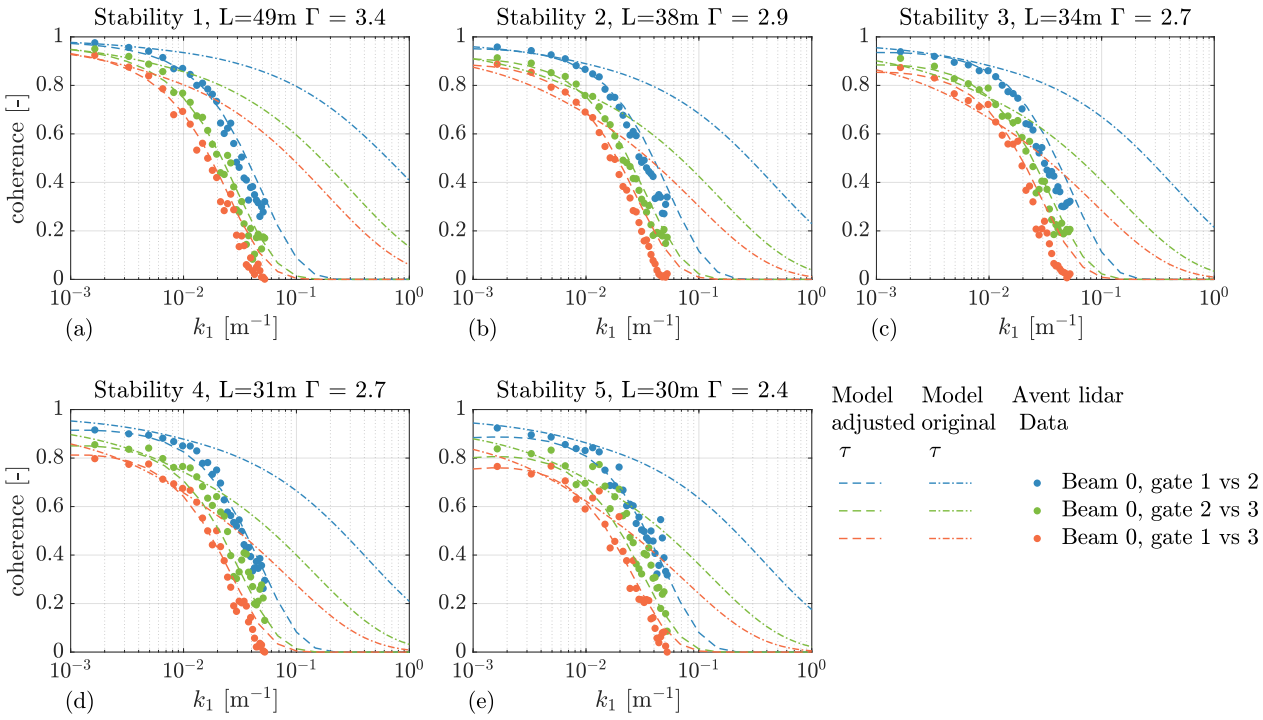

Figure 4.16: Comparisons of the LOS speed coherence (with longitudinal separation only) derived using the space-time tensor model and Avent measurements of beam 0. "Model adjusted τ" refers to adjusted slopes of τ_s and τ_e. "Model original τ" refers to the original τ_s expression (Equation 2.19) and $\tau_s = \tau_e$.

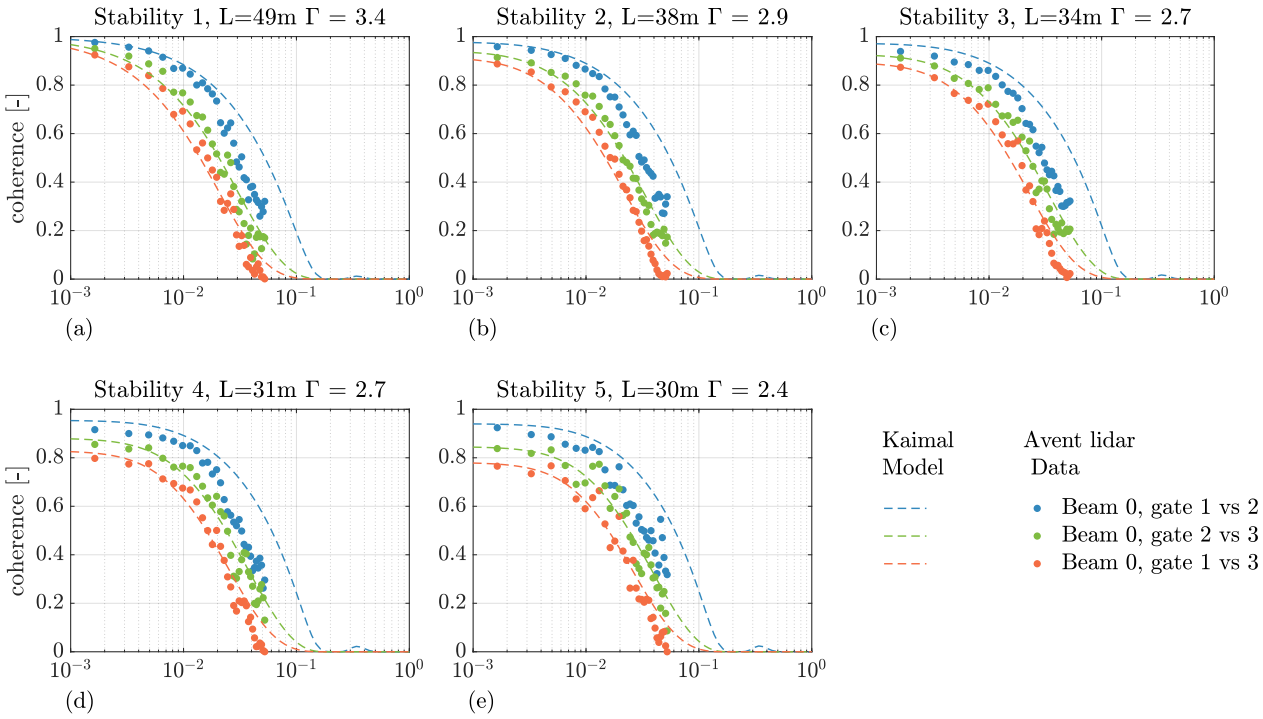

Figure 4.17: Comparisons of the LOS speed coherence (with longitudinal separation only) derived using the Kaimal model and Avent measurements of beam 0.

Coherence with Lateral and Vertical Separations

Next, the coherence with lateral and vertical separations are analyzed using measurements of the LOS speeds from different lidar beam directions at the same range gate. Note that the temporal delays also occurred between these LOS speeds because the lidar did not measure at different beam directions simultaneously. However, for the used lidar system, the delays are only within 1 s to a few seconds, and the coherence decay caused by the temporal delays is expected to be weaker compared with that caused by the spatial separations. By using the four beams (beam 3 is not used owing to low data availability), there are six possible combinations of beams to evaluate. Figures 4.18 and 4.19 show the coherence between beam 0 and the other beams. In each panel, the coherence from both range gates 1 and 2 are shown.

Based on the Avent data, the coherence of the three pairs are more similar at range gate 1 and in the more neutral stability conditions. At range gate 2 and in the more stable stability classes 4 and 5, the coherence between beams 0 and 1 is higher than that between beams 0 and 2 and is followed by that between beams 0 and 4.

For the Mann model-based space-time tensor, the coherence between beams 0 and 1 and between beams 0 and 2 are equal because of the symmetry and homogeneity. Their coherence differs slightly from the one between beams 0 and 4, which is caused by the opposite contributions from the uw coherence to the upward and downward-looking beams. However, the difference is slight because the contribution from the w component to the LOS speed is small. Generally, the LOS speed coherence are accurately predicted at gate 1 for all stability conditions, and the model prediction is better the closer to the neutral stability class. For gate 2, for which the spatial separations are larger, the model matched the measurement for stability classes 1 to 3, whereas some disagreements are observed under the two most stable stability classes. For the original τ_s expression and in the stable condition, the model overestimated the coherence at low wavenumber range. By adjusting the parameters in τ_s using the same method as for τ_e (i.e., Equation 4.18), the overestimation is alleviated. However, for the most stable stability class 5, a certain overestimation of the coherence is still observed between beams 0 and 4.

The model prediction using the Kaimal model is similar to that using the Mann model-based space-time tensor. Because of complete symmetry and neglected uw coherence, the coherences of any one of the three pairs are equal. For range gate 1, the coherence is well predicted, particularly in a more neutral condition. However, at range gate 2 and in the stable classes 4 and 5, an overestimation is also observed, and it is more overestimated than that by the space-time tensor.

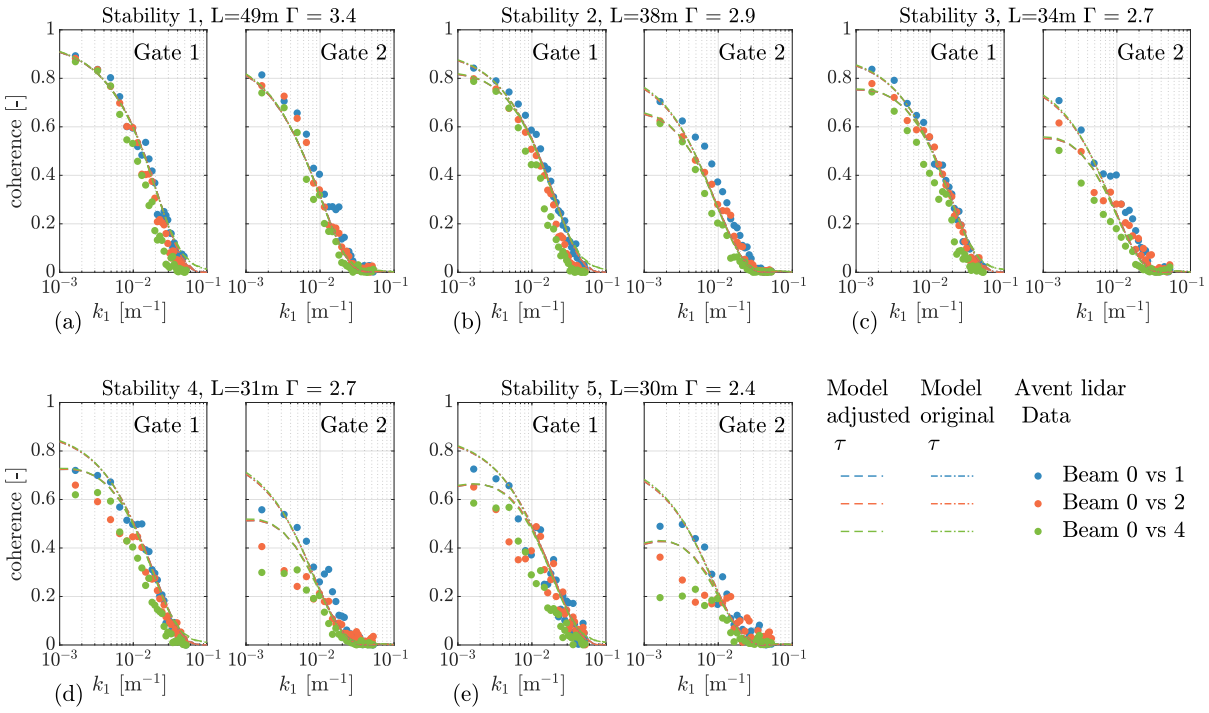

Figure 4.18: Comparisons of the LOS speed coherence (with lateral and vertical separations) derived using the space-time tensor model and Avent measurements. The coherences between beam 0 and the other beams are shown. "Model adjusted τ" refers to adjusted slopes of τ_s and τ_e. "Model original τ" refers to the original τ_s expression (Equation 2.19) and $\tau_s = \tau_e$.

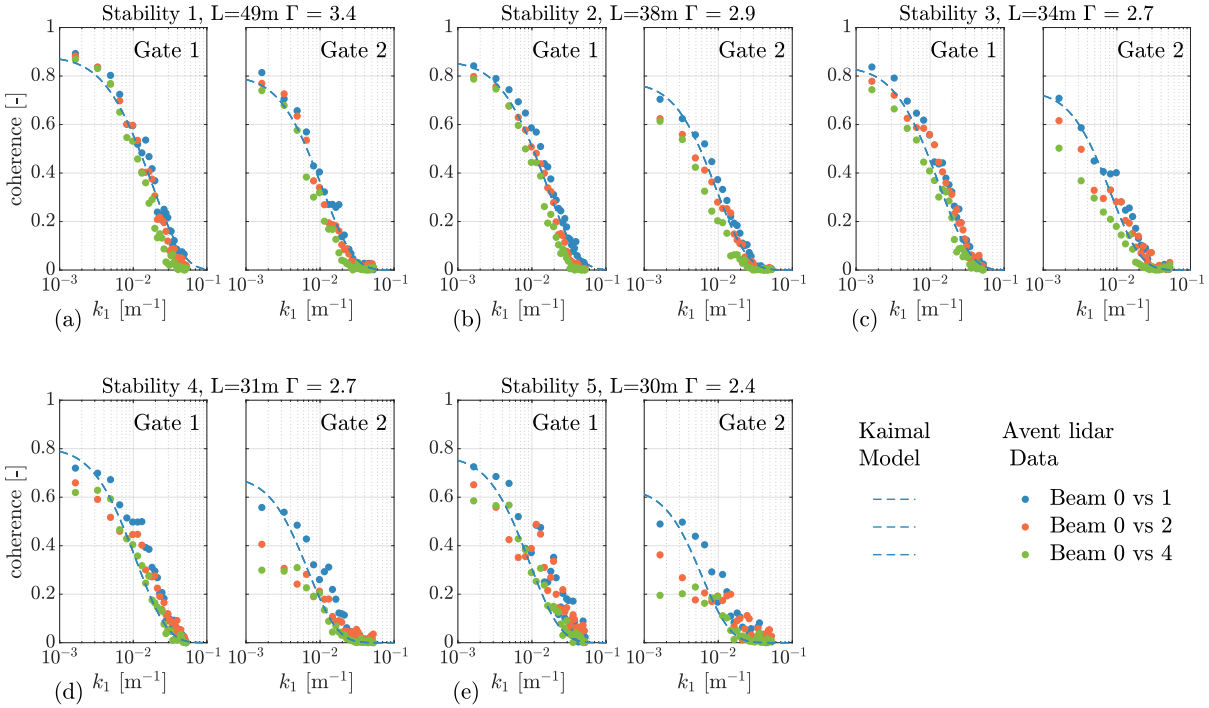

Figure 4.19: Comparisons of the LOS speed coherence (with lateral and vertical separations) derived using the Kaimal model and Avent measurements. The coherences between beam 0 and the other beams are shown.

In the comparisons above, the coherence is primarily contributed by the u component because beam 0 is frequently aligned (or with a small misalignment) in the longitudinal direction. An interesting aspect to investigate is the coherence between beams that are both contaminated by the non-longitudinal components.

Figures 4.20 and 4.21 show the coherence between all beams except beam 0. Similarly, for each frame, both the coherence from gates 1 and 2 are shown. Because of the symmetry of the beams, the separation distance between beams 1 and 2 and that between beams 1 and 4 are equal. The largest spatial distance is between beams 2 and 4.

Figure 4.20 shows the comparisons of the coherences using the Mann model-based space-time tensor. Overall, the agreement between the space-time tensor model and measurements is much better for neutral stability class 1 than for the other stability classes, although the measured coherence between beams 1 and 2 is underestimated by the model. The model predicts the coherence between beams 1 and 2 to be slightly lower than that between beams 2 and 4. However, the lidar measurements indicated that the coherence between beams 1 and 2 is significantly higher than that between beams 2 and 4. As discussed in Section 4.3.2, this is due to the opposite signs of the beams' unit vector. The correlated v components on beams 1 and 2 resulted in decorrelation on LOS speed measurements between beams 1 and 2. Because the v component auto-spectrum is accurately predicted by the model (when we examined the sonic spectra), the spatial coherence of the v component is more likely overestimated by the model. For stability classes 2 to 5, larger discrepancies between the model and measured data are observed as the atmosphere becomes more stable. The original eddy lifetime of the Mann model is modified to reduce these discrepancies. After applying the adjusted τ_{s} values, the overestimation of the coherence in the stability classes 2 to 4 decreases slightly. However, relatively large biases are still present in the last two stability classes (4 and 5) for gate 2. We can conclude that the LOS speed coherence decays much faster than predicted by the model when the separation becomes more prominent than the turbulence length scale L.

For the Kaimal model, as shown in Figure 4.21, only two curves of the coherence are predicted by the model because the ones between beams 1 and 2 and that between beams 1 and 4 are equivalent. Generally, the coherence exhibited more discrepancies than the space-time tensor model estimates. Primarily, the coherence between beams 1 and 2 in stability classes 1 to 3 are predicted more correctly. In the other comparisons, the Kaimal model tended to overestimate the LOS speed coherence, particularly in a more stable condition.

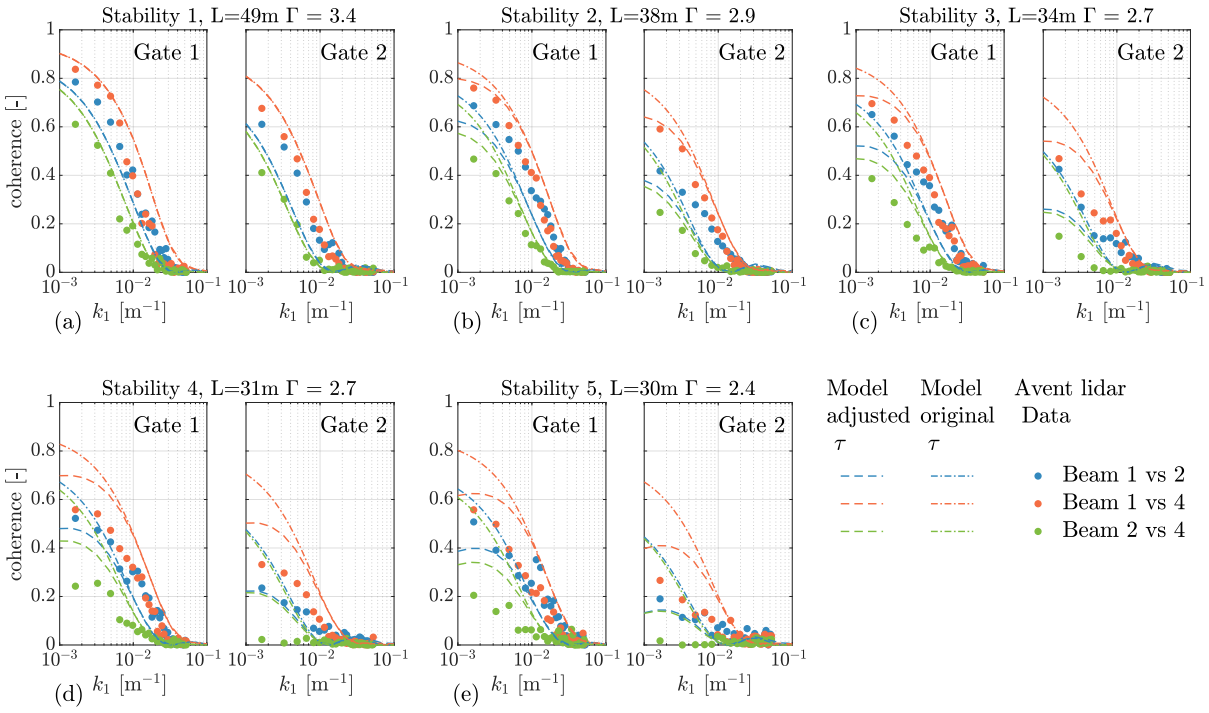

Figure 4.20: Comparisons of the LOS speed coherence (with lateral and vertical separations) derived using the space-time tensor model and Avent measurements. The coherence between the beams except for beam 0 are shown. "Model adjusted τ" refers to adjusted slopes of τ_s and τ_e. "Model original τ" refers to the original τ_s expression (Equation 2.19) and $\tau_s = \tau_e$.

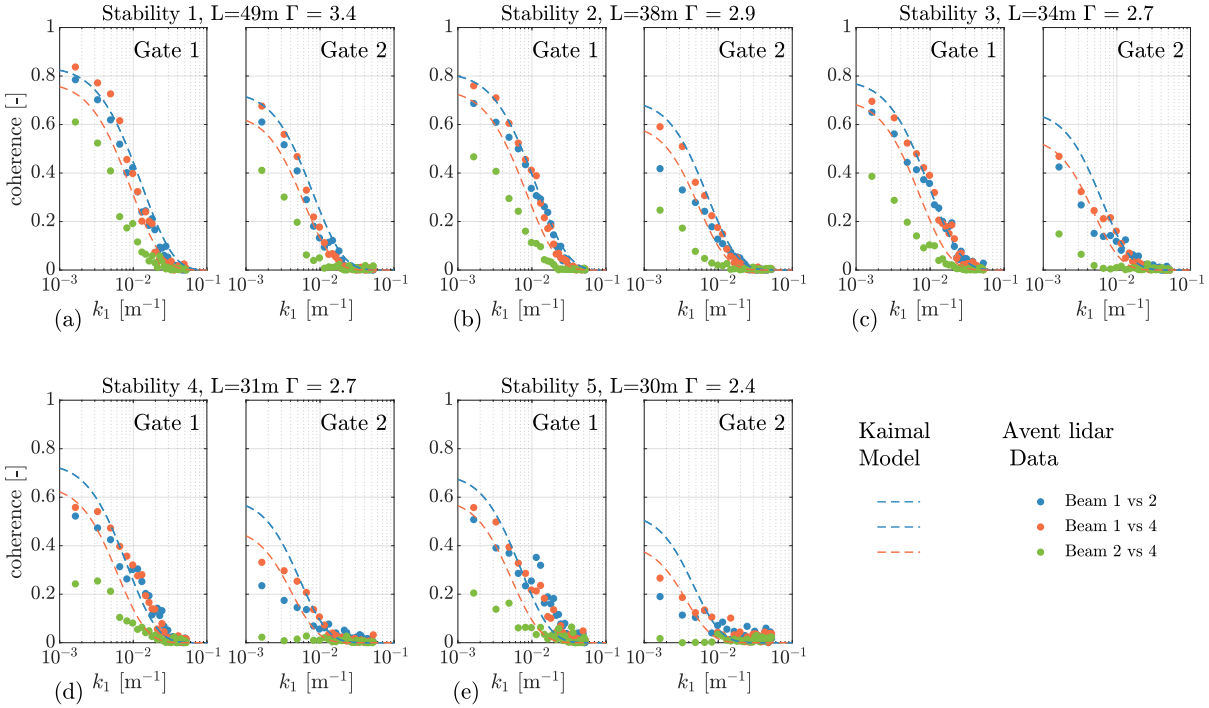

Figure 4.21: Comparisons of the LOS speed coherence (with lateral and vertical separations) derived using the Kaimal model and Avent measurements. The coherence between the beams except for beam 0 are shown.

Coherence with Separation in all Directions

Additionally, we evaluated the models' abilities to predict the coherence between LOS speeds with all longitudinal, lateral, and vertical separations. Except for beam 0, the measurements along different gates and from different beams could be used for such a purpose, and the results are shown in Figures 4.22 and 4.23. Generally, both the Mann and Kaimal models match the lidar data. However, similar to the previous coherence comparisons, the agreements between the model and measurements deteriorate the more stable the atmosphere is.
For the Mann model, the model-based coherence between range gates 1 and 2 at beam 1 is the same as that between gates 1 and 2 at beam 2, owing to symmetry. In all stability classes, the results using the adjusted τ_{s} do not significantly differ from those using the original τ, because the vertical and lateral separations do not exceed the range in which the results are sensitive to the temporal evolution-related eddy lifetime τ_{e}. By comparing Figures 4.22 and 4.16, we observe that the overall coherence is not very sensitive to the eddy lifetime τ_{e} because the coherence decay due to lateral and vertical separations is more dominant than that due to longitudinal separations for these compared lidar beam pairs. However, the longitudinal coherence is overestimated when using the original τ_{s} expression as τ_{e}.
For the Kaimal model, the model-based coherence is equal for all compared LOS pairs because of symmetry. The model predicts the first two stability classes accurately, but the coherence is slightly underestimated in a more stable class. The reason could be that the direct product (Equation 4.4) is used when combining longitudinal coherence with lateral-vertical coherence. A similar overestimation was also observed by [16] using LES simulations.

4.4 Chapter Summary and Outlook

Under the demand for modeling turbulence evolution for the assessment of lidar-assisted turbine control, this chapter presents the methods that can add turbulence evolution to existing turbulence models for turbine load simulations.
For the Kaimal model, previous studies revealed that longitudinal coherence can be accurately expressed by an exponential coherence model. The 4-D (space-time) stochastic turbulence field can be generated using the traditional Veers method [58], which is currently widely used to generate 3-D turbulent wind fields. However, the main limitation of directly applying the Veers method is the massively increased computational effort required to perform Cholesky decomposition on a very large matrix. With the assumption that the aggregated coherence can be obtained by combining the coherence using a "direct product" approach, a two-step Cholesky decomposition approach is proposed. This method can avoid performing the Cholesky decomposition on a single large matrix. Instead, the Cholesky decomposition is applied to two smaller matrices, and the total coherence matrix is obtained using the Kronecker product.

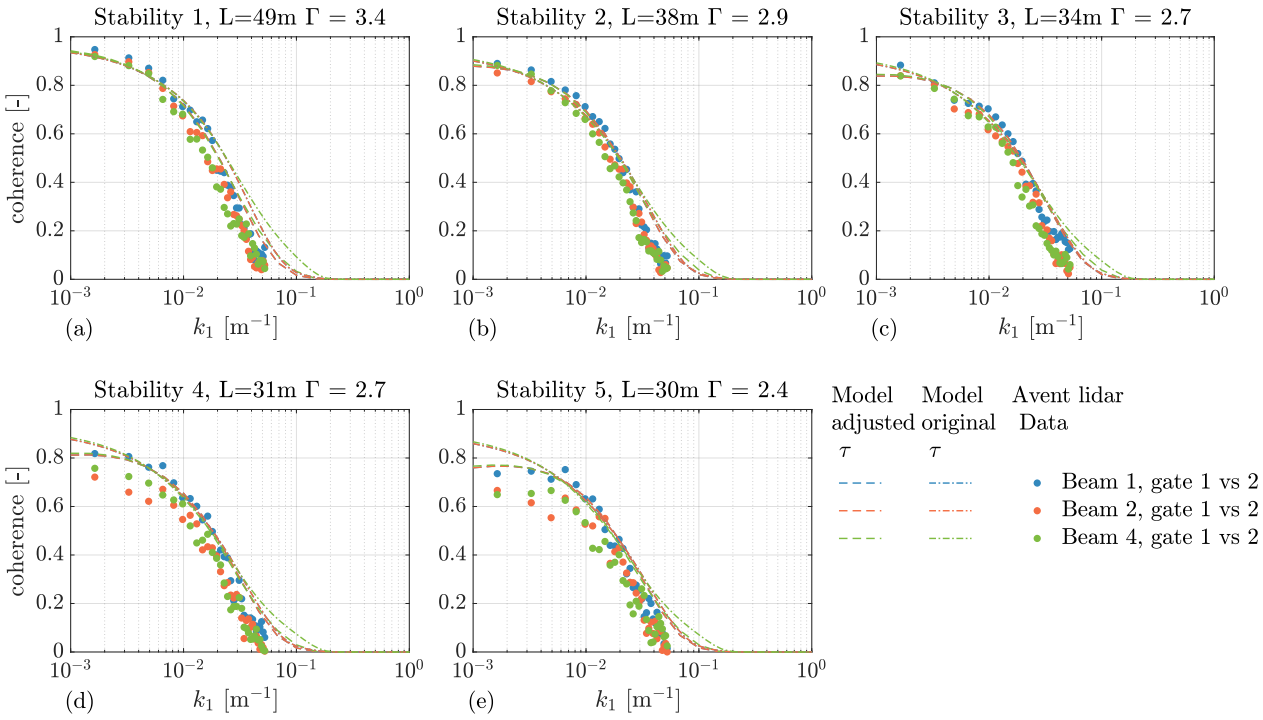

Figure 4.22: Comparisons of the LOS speed coherence derived from the space-time tensor model and Avent measurements. The coherence between the LOS speed measurements at gates 1 and 2 on different beams is shown. "Model adjusted τ" refers to adjusted slopes of τ_s and τ_e. "Model original τ" refers to the original τ_s expression (Equation 2.19) and $\tau_s = \tau_e$.

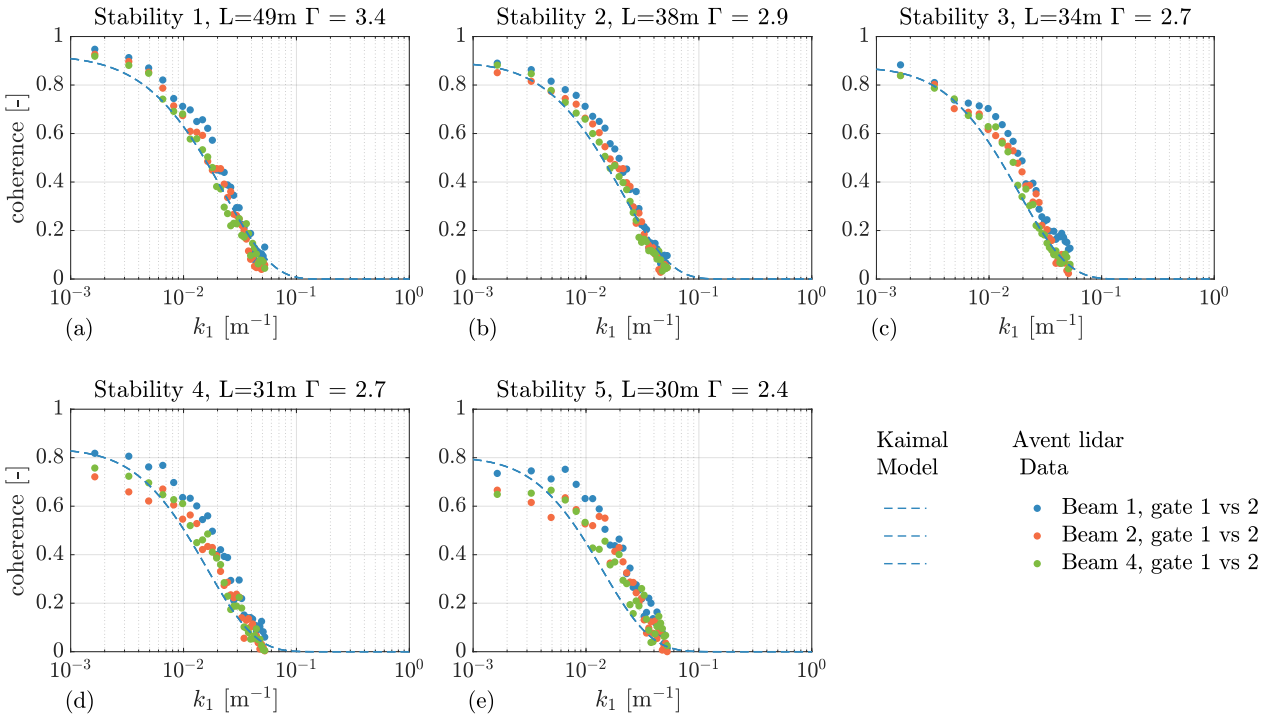

Figure 4.23: Comparisons of the LOS speed coherence derived from the Kaimal model and Avent lidar measurements. The coherence between the LOS speed measurements at gates 1 and 2 on different beams are shown.

Therefore, the two-step Cholesky decomposition approach significantly increases the computational efficiency of the Kaimal model-based 4-D turbulence generation. In addition, the two-step Cholesky decomposition approach results in the concept that a 4-D wind field can be obtained by combining multiple statistically independent 3-D turbulent wind fields. Based on this concept, an open-access 4-D wind field generator called *evoTurb* is developed [59], which is coupled with *TurbSim*.

In terms of the Mann model extension, a space-time tensor based on the Mann model and an eddy lifetime model are proposed. The space-time tensor assumes stationary turbulence fields, describes the correlation decay of turbulence due to temporal evolution, and can represent both the temporal and spatial structure of turbulence [20]. A practical eddy lifetime expression is proposed to make the eddy lifetime model more flexible to use. The proposed expression has several parameters that can be adjusted to change the slopes of the eddy lifetime. It can be adjusted to match the turbulence spectral characteristics under neutral stability (the original Mann model) or modified to represent a more stable atmosphere. A numerical turbulence simulation method using the Ornstein-Uhlenbeck process is presented that can produce the 4-D turbulence field with statistical characteristics governed by the space-time tensor. An open-source software called *4-D Mann Turbulence Generator* was programmed based on this numerical simulation method. In the aeroelastic simulation, the x axis of the generated turbulence field can be converted to time using Taylor's frozen theory (assuming the wavenumber and frequency spectra have the same variance). The time slots of the turbulence fields can be converted to several distances along the main wind direction as the turbulence propagates by a mean reference wind speed. The correlation between all 3D fields is governed by the eddy lifetime model in the space-time tensor. In the generated 4-D turbulence field, the one at the rotor location can then be used for standard aeroelastic simulations, and the upstream ones can be used for lidar measurement simulations.

The lidar LOS speed spectral properties are first derived analytically to evaluate the extended Kaimal and Mann models. Subsequently, the derivations are validated by simulating the lidar measurement numerically. Thereafter, the models are evaluated using measurements from a pulsed lidar and a sonic anemometer. The measurement data are first split into 10 min intervals and then classified into different atmospheric stability conditions. The select periods for the model evaluation are those with a hub-height mean wind speed close to $12\,\mathrm{ms}^{-1}$, i.e., periods above the rated wind speed of typical turbines, because lidar-assisted pitch feedforward control becomes beneficial under such conditions. We observed that the model agreed quite well with the measured spectra and coherence from the lidar measurements when the atmospheric stability was close to the neutral condition, and the spatial separation was small. However, the coherence are overestimated by both models for the most stable class, and the Kaimal model generally exhibited more discrepancies with the data than the Mann model. The discrepancy occurs primarily in scenarios in which the spatial separations of LOS speed measurements are

larger than the turbulence length scale. The eddy lifetime expression in the Mann model is adjusted, which improves the agreements with the measurements.
The model evaluation indicates that both the Mann and Kaimal models tend to overestimate the coherence when the separation distance surpasses the turbulence length scale. With the current trend that the turbine rotor is designed to be larger and larger, the turbulence models may be unable to provide a good representation of the coherence between blade sections with a large spatial separation. In the future, the impact of this incorrect coherence on the turbine loads should be further studied, preferably through field testing. Additionally, the nacelle lidar measurement may also be used to provide a good reference for spatial coherence and therefore be used to improve turbulence models.

5

Lidar Wind Preview Quality under Various Turbulence Conditions

Based on the previous chapter, the conventional 3-D turbulence models are improved to include the turbulence evolution phenomenon. Additionally, it demonstrates that the spectral characteristics of the freestream turbulence (without turbine wakes) can be represented by the turbulence spectral model. The parameters of both the Mann and Kaimal turbulence models under neutral and stable atmospheric stability conditions are studied using meteorological mast and lidar measurements.

For lidar-assisted feedforward control, the quality of lidar wind preview is defined by how accurately the lidar predicts the rotor-effective disturbance, or in other words, the REWS. The control-oriented nacelle- or spinner- lidar system is typically designed to measure several upstream positions. A wind turbine interacts with turbulence through its three blades. Therefore, a single-point longitudinal coherence is not sufficient to reflect the preview quality of a lidar system. Instead, the turbine- and lidar-based REWSs must be defined and derived from the turbulence models, and the correlation between these two REWSs must be investigated.

The lidar wind preview quality is related to the filter design of the feedforward pitch controller. It defines the amount of frequency-domain content of the lidar estimated REWS that can be used for control. If a filter is designed to filter out usable frequency content, the feedforward control performance can be diminished. Oppositely, the uncorrelated pitch action can be activated, causing additional loads if the uncorrelated REWS estimation is not filtered out.

This chapter discusses the lidar wind preview quality under different turbulence spectral characteristics that are representative of different atmospheric stability classes. The preview quality

with turbine wake-included conditions is also studied using the DWM model. The measurement trajectory of a four-beam pulsed lidar is optimized with the aim of providing a better quality of wind preview for the NREL 5.0 MW reference wind turbine.
This chapter is extended from the following publications: [20, 71].

5.1 Turbulence Parameters of Different Atmospheric Stability Classes

As introduced in Section 4.3.3, atmospheric stability indicates the buoyancy effects on turbulence generation and is related to the turbulence spectral characteristics. Its impact on lidar wind preview quality for LAC is an interesting area to investigate as the turbine experiences different atmospheric stability conditions during operation. In this section, the typical turbulence parameters for unstable, neutral, and stable atmosphere conditions are summarized, and these parameters are used in the remainder of this thesis to assess the lidar wind preview quality and the benefits of LAC.
Based on the studies by [89] and [78], the turbulence spectral parameters at a given site can vary significantly with atmospheric stability. Using the measurement data from the Østerild wind turbine test station in northern Denmark, [78] found that the length scale L varies significantly by different atmospheric stability classes. The length scale L is found to be the largest in unstable stability, medium in neutral stability, and smallest in stable stability. To visualize the impact of turbulence length scale on the eddy structure, Figure 5.1 shows three turbulence fields generated using the *4-D Mann Turbulence Generator* [20]. The corresponding turbulence length scales are described in the caption. It is clear that larger coherent eddy structures are more frequently observed in the unstable stability. In contrast, the eddy structure is much smaller under the stable stability. In the neutral scenario, the eddy structure is between the two scenarios. In the rest of this thesis, we use Mann turbulence parameter sets representative of neutral and stable conditions based on Section 4.3.4. For the unstable atmosphere, the turbulence parameters are selected based on [78]. These parameters are listed in Table 5.1. Note that the $\alpha\varepsilon^{2/3}$ parameter is scaled such that the turbulence intensity corresponds to the IEC 61400-1 [12] class 1A definition. In practice, the TI value is also related to the atmospheric conditions. Frequently, TI is generally high in an unstable atmosphere, moderate in a neutral atmosphere, and low in a stable atmosphere [36]. In this study, our focus is on the effect of turbulence length scales on turbine loads and LAC benefits; therefore, the same TI level was assumed for the three stability classes. Although this assumption often contradicts the actual measurements, it ensures a certain engineering design envelope for wind turbines. Also, it helps to identify the impact of the turbulence length scale on turbine load, as later presented in Chapter 7.
For the Kaimal model parameters, the parameters listed by the IEC 61400-1 standard [12] are selected for the neutral stability because these parameters have already been observed to provide

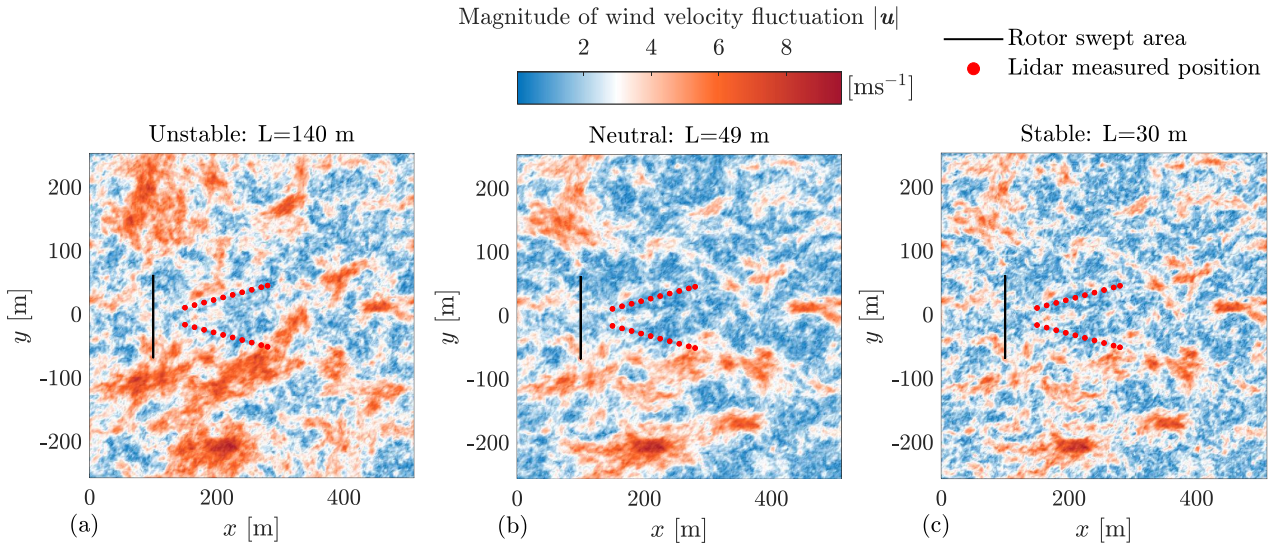

Figure 5.1: Top views of three turbulence fields with different turbulence length scales, which show the eddy structures under different atmospheric stabilities. The turbulence fields are simulated using the *4-D Mann Turbulence Generator* with parameters listed in Table 5.1 and using the identical random seed number. The lidar-measured positions are plotted based on a typical four-beam pulsed lidar. Moreover, the rotor swept-area is drawn based on the NREL 5.0 MW reference wind turbine with a rotor diameter of 126 m.

similar spectra and coherence compared with the Mann model in neutral stability parameters. Additionally, maintaining these parameters enables us to compare the results with that from existing literature, e.g., [6, 90, 19]. For unstable and stable stability classes, the Kaimal spectra are fitted using Mann model-based spectra using the following optimization process:

$$\begin{aligned} \min_{L_i,\sigma_i} \quad & \textstyle\sum_{n=1}^{N} \left[S_{ii}(f_n)\cdot f_n - 2F_{ii}(k_{1,n})\cdot k_{1,n}\right]^2 \ , \\ \text{s.t.} \quad & k_{1,n} = \tfrac{2\pi f_n}{U_{\text{ref}}} \quad \text{and} \quad i = 1, 2, \text{ or } 3. \end{aligned} \tag{5.1}$$

Here, n is the index of the discrete frequency vector f_n and wavenumber vector $k_{1,n}$ and N is the total number of discrete vectors. Note that the Mann model spectra $F_{ii}(k_{1,n})$ are multiplied by 2 as they are two-sided spectra, whereas the Kaimal spectra are single-sided. Similarly, we fit the y-z plane exponential coherence for the Kaimal model by the Mann model using

$$\begin{aligned} \min_{a_{yz},L_c} \quad & \textstyle\sum_{n=1}^{N} \left[\tfrac{1}{k_{1,n}}\left(\gamma_{yz}(f_n) - \Re(\text{coh}_{11}(k_{1,n}))\right)^2\right] \ , \\ \text{s.t.} \quad & k_{1,n} = \tfrac{2\pi f_n}{U_{\text{ref}}} \quad \text{and} \quad \Delta y = \Delta z = 20\text{m}, \end{aligned} \tag{5.2}$$

where $\Re$ denotes the real number operator. The real number operator means that we only fit the co-coherence and ignore the imaginary part introduced by the cross-spectrum in Equation 2.11. The medium separation Δy=Δz=20m has been selected for the optimization problem. For the coherence optimization equations, the squared error in each discrete vector is divided by $k_{1,n}$ to ensure equivalent weighting of the optimization function at different frequency or wavenumber

ranges. The fitted spectra and y-z plane coherence are shown in Figures 5.2(a) and (b), and the turbulence parameters are summarized in Table 5.1. We can observe that the turbulence length scale L in the Mann model [11] generally increases from very stable to unstable conditions, whereas the variation in the anisotropy parameter Γ does not exhibit a clear trend toward the atmosphere stability. Accordingly, the larger length scale L also results in a smaller coherence decay constant a_{yz}.

Except for the spectra and y-z plane coherence, [20] demonstrated that the turbulence evolution (or longitudinal coherence) is related to the atmospheric stability conditions. In [20], a smaller intercept was observed for a more stable class. Additionally, [7] studied the turbulence evolution under different stability classes using LES, and the smaller intercept was also observed in a stable atmosphere. To compare the longitudinal coherence under different atmospheric stability conditions, we use three sets of $\gamma = 200, 400$, and 600 s to calculate the longitudinal coherence based on the space-time tensor $\mathbf{\Theta}$ introduced earlier. Thereafter, the exponential coherence (Equation 4.1) is fitted using the following optimization process:

$$\begin{aligned} \min_{a_x, b_x} \quad & \sum_{n=1}^{N} \left[\frac{1}{f_n} \left(\gamma_x(f_n) - \Re(\mathrm{coh}_{11}(k_{1,n})) \right)^2 \right] , \\ \text{s.t.} \quad & k_{1,n} = \frac{2\pi f_n}{U_{\mathrm{ref}}} \quad \text{and} \quad \Delta x = 100\mathrm{m}. \end{aligned} \tag{5.3}$$

Here, the separation at $\Delta x = 100$m is selected for the fitting, which is the medium separation for a typical nacelle lidar measuring in front of the turbine [90, 91]. The fitted coherence is shown in Figure 5.2(c). The fitted exponential coherence parameters a_x and b_x are summarized in Table 5.2, and they exhibit a similar trend as the observation by [7] using LES. For an unstable atmosphere, a_x is generally larger, and b_x is in a very small order close to 0. In the neutral condition, a_x lies at a medium value, and b_x is also a small order close to 0. For the stable scenario, the a_x is the smallest, indicating a weaker coherence decay, whereas the b_x is larger and results in a smaller intercept in the coherence at low frequency ranges.

Based on Section 4.3.4, γ is observed to be 430 and 207 s for neutral and stable stability classes, respectively, whereas the eddy lifetime parameter τ_{e} in the unstable scenario is not derived owing to a lack of samples from the measurement. As studied by [9] using lidar measurement, the peak probability of a_x was observed to appear at values between 1 and 2. In addition, according to the analysis by [7], a_x tended to be the largest in an unstable condition compared with that in a neutral or stable condition. Because $\gamma = 200$ or 400 s gives large values of a_x in the unstable atmosphere that are less possible to happen [9], we decided to choose $\gamma = 600$ s for the unstable condition, which results in $a_x = 4.1$. Moreover, $\gamma = 400$ and $\gamma = 200$ s are used for neutral and stable stability classes.

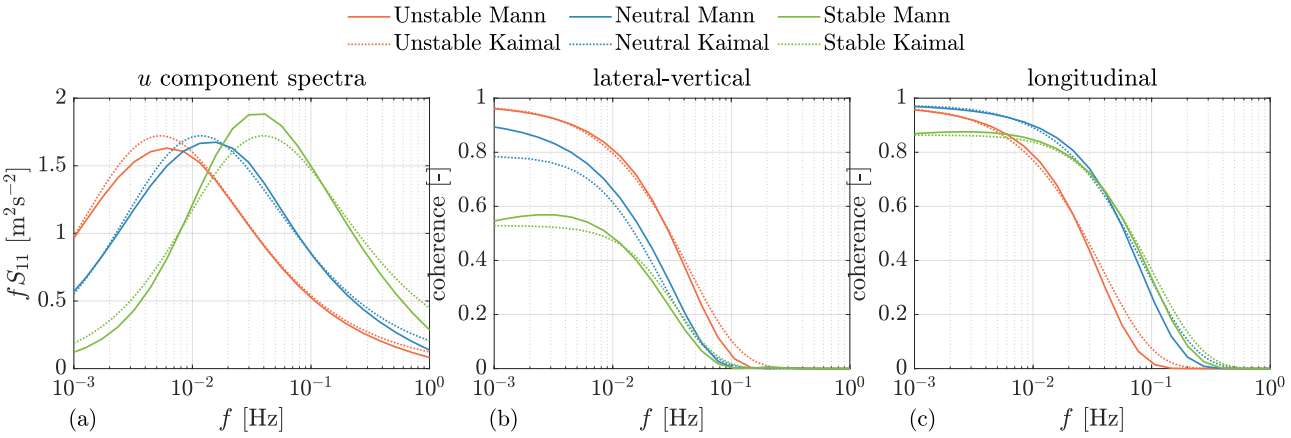

Figure 5.2: (a) Auto-spectra of the u component under different stability classes. (b) Lateral-vertical coherence of the u component calculated using the Mann spectral tensor and fitted using the exponential coherence model. Note that the co-coherence is shown for the Mann spectral tensor. (c) Longitudinal coherence of the u component calculated using the space-time tensor and fitted using the exponential coherence model.

Table 5.1: Mann model parameters under different atmospheric stabilities (based on [78]) and the fitted Kaimal model parameters. U: unstable, N: neutral, S: stable.

	Mann			Kaimal							
	$\alpha\varepsilon^{2/3}$ [m$^{4/3}$s^{-2}]	L [m]	Γ [-]	L_1 [m]	L_2 [m]	L_3 [m]	σ_1 [ms^{-1}]	σ_2 [ms^{-1}]	σ_3 [ms^{-1}]	a_{yz} [-]	L_c [m]
U	0.184	140	2.6	744.8	181.9	126.4	2.82	2.34	1.98	6.5	1502.0
N	0.311	49	3.1	340.2	113.4	27.72	2.82	2.25	1.41	12.0	340.2
S	0.652	30	2.4	101.1	33.3	27.0	2.82	2.26	1.83	13.1	101.1

Table 5.2: Fitted parameters for the exponential longitudinal coherence model. a_x is unitless and b_x has a unit of m^{-1}.

Stability		$\gamma = 200$ s	$\gamma = 400$ s	$\gamma = 600$ s
Unstable	a_x	8.2	5.1	4.1
	b_x	8.52×10^{-5}	8.02×10^{-5}	7.67×10^{-5}
Neutral	a_x	2.9	1.8	1.4
	b_x	1.59×10^{-4}	1.49×10^{-4}	1.42×10^{-4}
Stable	a_x	1.6	1.0	0.8
	b_x	9.18×10^{-4}	8.59×10^{-4}	8.27×10^{-4}

5.2 Correlations between Lidar and Turbine

In this section, the typical definition of REWS is first discussed. Subsequently, the auto-spectra of the turbine- and lidar-based REWSs and the cross-spectrum between them are discussed.

5.2.1 Rotor Effective Wind Speed

For lidar-assisted collective pitch feedforward control, as discussed by [6, 90], a typical definition of turbine REWS is the rotor disc averaged longitudinal component:

$$u_{\mathrm{RR}}(x) = \frac{1}{\pi R^2} \iint_{D_{xy}} u(\boldsymbol{x}) \mathrm{d}y \mathrm{d}z, \tag{5.4}$$

where the integration area D_{xy} is the rotor-swept area with a radius of R. When the Mann model is considered, as derived by [18], the auto-spectrum of u_{RR} can be calculated using the spectral tensor as

$$F_{\mathrm{RR}}(k_1) = \int_{-\infty}^{\infty} \int_{-\infty}^{\infty} \Phi_{11}(\boldsymbol{k}) \frac{4J_1^2(\kappa R)}{\kappa^2 R^2} \mathrm{d}k_2 \mathrm{d}k_3, \tag{5.5}$$

where $\kappa = \sqrt{k_2^2 + k_3^2}$, and J_1 is the Bessel function of the first kind. Refer to [18, 83] for the detailed derivations.

For the Kaimal model, the spectrum was derived by [72, 6] and can be calculated using the following discrete summation:

$$S_{\mathrm{RR}}(f) = \frac{S_{11}(f)}{n_{\mathrm{R}}^2} \sum_{i=1}^{n_{\mathrm{R}}} \sum_{j=1}^{n_{\mathrm{R}}} \gamma_{yz}(\Delta yz_{ij}, f), \tag{5.6}$$

where Δyz_{ij} is the separation distance between points i and j in the same y-z plane, and n_{R} is the total number of discrete points within the rotor area. The detailed derivation of the auto-spectrum is available in [6].

5.2.2 Lidar-estimated Rotor Effective Wind Speed

Because lidar only provides the wind speed measurement in the LOS direction, the u component must be reconstructed from the LOS speed. A simple algorithm assumes zero v and w components because they frequently contribute much less than the u component on the LOS speed. However, this is true if the misalignment of the lidar beam to the longitudinal direction is small. Based on this assumption, the lidar-estimated REWS is often obtained using [6]

$$u_{\mathrm{LL}}(t) = \sum_{i=1}^{n_{\mathrm{L}}} \frac{1}{n_{\mathrm{L}} \cos\theta_{\mathrm{L},i} \cos\phi_{\mathrm{L},i}} v_{\mathrm{los},i}(t), \tag{5.7}$$

where n_{L} is total number of lidar measurement positions, $\phi_{\mathrm{L},i}$ is the azimuth angle of the ith measured position, $\theta_{\mathrm{L},i}$ is the elevation angle of the ith measured position, and $v_{\mathrm{los},i}(x)$ denotes the lidar measurement at ith position. The auto-spectrum of the REWS estimated by the lidar can be computed from the Mann spectral tensor [11] using

$$\begin{aligned} F_{\mathrm{LL}}(k_1) = \sum_{i,j=1}^{n_{\mathrm{L}}} \sum_{l,m=1}^{3} \frac{1}{n_{\mathrm{L}}^2 \cos\theta_{\mathrm{L},i} \cos\phi_{\mathrm{L},i} \cos\theta_{\mathrm{L},j} \cos\phi_{\mathrm{L},j}} \int_{-\infty}^{\infty}\int_{-\infty}^{\infty} n_{il} n_{jm} \Phi_{lm}(\boldsymbol{k}) \\ \exp(\mathrm{i}\boldsymbol{k}\cdot(\boldsymbol{x}_i - \boldsymbol{x}_j))\hat{\varphi}(\boldsymbol{k}\cdot\boldsymbol{n}_i)\hat{\varphi}(\boldsymbol{k}\cdot\boldsymbol{n}_j)\mathrm{d}k_2\mathrm{d}k_3, \end{aligned} \tag{5.8}$$

where $\boldsymbol{x}_i$ and $\boldsymbol{n}_i$ denote the focus position and unit vectors of the ith lidar measurement, respectively, and n_{il} is the lth element in the unit vector $\boldsymbol{n}_i$. Details of the derivation of Equation 5.8 are available in [18, 83], where all lidar LOS cross-spectra are looped over (see Equation 4.57) and summed. When the temporal evolution of the turbulence field is considered, we simply need to replace Φ_{lm} by the space-time tensor $\Theta_{lm}(\boldsymbol{k}, \Delta t)$ in Equation 5.8. This is necessary when the lidar has a relatively large time delay or longitudinal separation between measurement positions [105].

In terms of the Kaimal model, the auto-spectrum can be calculated using the Fourier transform:

$$\begin{aligned} S_{\mathrm{LL}}(f) &= \mathcal{F}\{u_{\mathrm{LL}}\}\mathcal{F}^*\{u_{\mathrm{LL}}\} \\ &= \sum_{i,j=1}^{n_{\mathrm{L}}} \frac{1}{n_{\mathrm{L}}^2 \cos\theta_{\mathrm{L},i} \cos\phi_{\mathrm{L},i} \cos\theta_{\mathrm{L},j} \cos\phi_{\mathrm{L},j}} \mathcal{F}\{v_{\mathrm{los},i}\}\mathcal{F}^*\{v_{\mathrm{los},j}\}, \end{aligned} \tag{5.9}$$

where the cross-spectrum between the ith and jth LOS speeds can be calculated using Equation 4.40.

To evaluate how effectively the turbulence models predict the lidar estimated REWS (u_{LL}), the model parameters (Tables 4.3 and 4.4) are used to calculate the theoretical auto-spectrum of the lidar-estimated REWS. The theoretical results are then compared with the ones derived from the Avent measurements (Figure 5.3). The data selection criteria and stability classification have been discussed in Chapter 4. The lidar-estimated REWS is computed using the measurements from beams 0, 1, 2, and 4 at range gates 1 and 2. Before calculating the auto-spectrum from the lidar data, the time delays according to the longitudinal separations and the mean wind speed are applied to shift the measurements from gate 2 to have the same timing as gate 1. For the beam trajectories considered here, we observe that the lidar-based REWS is accurately predicted by both the Kaimal and Mann models.

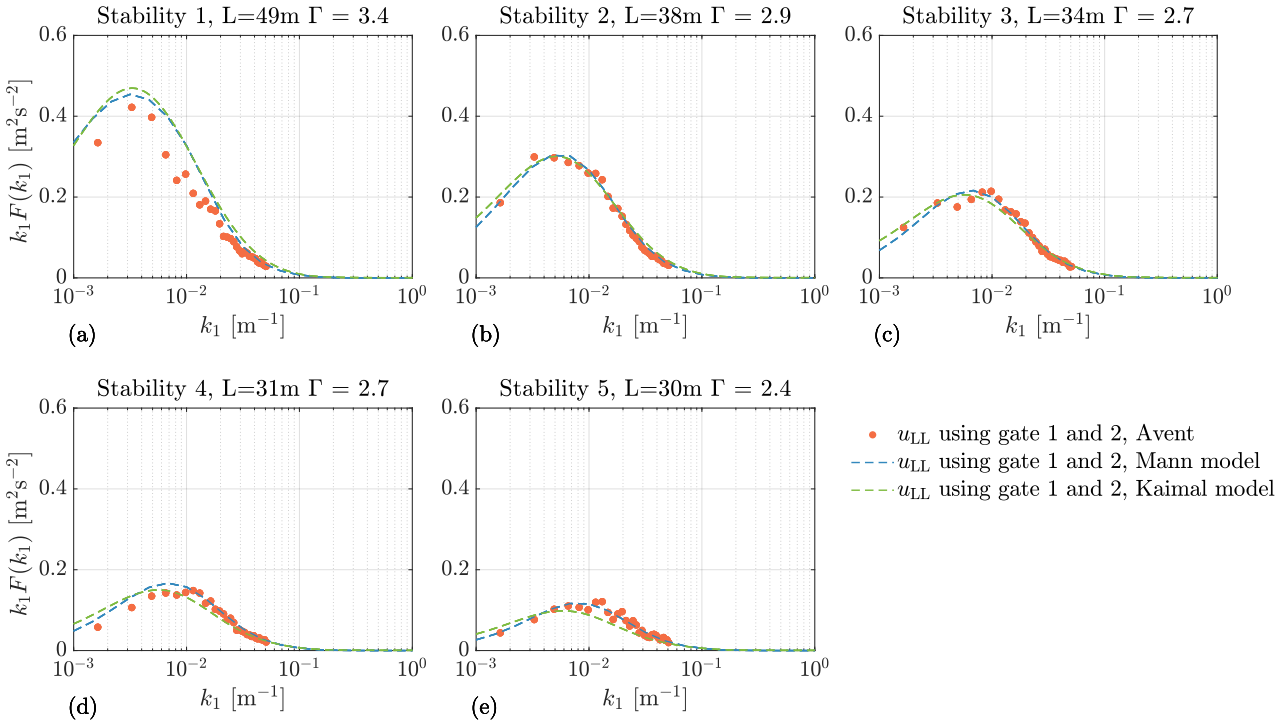

Figure 5.3: Comparisons of the lidar-estimated REWSs using the Avent lidar data and the turbulence models.

5.2.3 Cross-spectrum between Turbine and Lidar

When turbulence evolution is considered with the Mann model, the cross-spectrum between REWS u_{RR} and the lidar-estimated one u_{LL} can be calculated using the space-time tensor as follows [20, 105]:

$$F_{\mathrm{RL}}(k_1) = \sum_{i=1}^{n_{\mathrm{L}}} \sum_{j=1}^{3} \frac{1}{n_{\mathrm{L}} \cos\theta_{\mathrm{L},i} \cos\phi_{\mathrm{L},i}} \int_{-\infty}^{\infty} \int_{-\infty}^{\infty} n_{ij} \Theta_{j1}(\boldsymbol{k}, \Delta t_i) \hat{\varphi}(\boldsymbol{k} \cdot \boldsymbol{n}_i) \exp(\mathrm{i}\boldsymbol{k} \cdot \boldsymbol{x}_i - \mathrm{i}k_1 \Delta x_i) \frac{2J_1(\kappa R)}{\kappa R} \mathrm{d}k_2 \mathrm{d}k_3, \tag{5.10}$$

where, Δx_i is the longitudinal separation between the rotor plane and ith lidar measurement position. The rotor plane is often defined at $x_{\mathrm{R}} = 0$ m; therefore, $\Delta x_i = x_i - x_{\mathrm{R}} = x_i$. Δt_i is the time required for the turbulence field to move from the ith lidar measurement position to the rotor plane, which can be approximated using $\Delta t_i = |\Delta x_i| / U_{\mathrm{ref}}$.

In terms of the Kaimal model, following [6], the cross-spectrum is determined using the discrete

summation:

$$\begin{aligned} S_{\mathrm{RL}}(f) &= \mathcal{F}\{u_{\mathrm{RR}}\}\mathcal{F}^*\{u_{\mathrm{LL}}\} \\ &= \sum_{i=1}^{n_{\mathrm{R}}}\sum_{j=1}^{n_{\mathrm{L}}} \frac{1}{n_{\mathrm{R}} n_{\mathrm{L}} \cos\theta_{\mathrm{L},i} \cos\phi_{\mathrm{L},i}} \mathcal{F}\{u_i\}\mathcal{F}^*\{v_{\mathrm{los},j}\}, \end{aligned} \tag{5.11}$$

where u_i is the ith longitudinal wind component in the rotor-swept area. Refer to [6] for detailed calculation of the cross-spectrum between u_i and $v_{\mathrm{los},j}$, where the main algorithm loops over all the cross-spectrum between spatially distributed u components. The cross-spectra between the non-longitudinal components in the IEC Kaimal model are not modeled.

5.2.4 Lidar Wind Preview Quality

To evaluate the wind preview quality of lidar measurement, the coherence between lidar estimated REWS and the turbine-based REWS, i.e.,

$$\gamma^2_{\mathrm{RL}}(f) = \frac{|S_{\mathrm{RL}}(f)|^2}{S_{\mathrm{RR}}(f)S_{\mathrm{LL}}(f)} \quad \text{and} \quad \mathrm{coh}^2_{\mathrm{RL}}(k_1) = \frac{|F_{\mathrm{RL}}(k_1)|^2}{F_{\mathrm{RR}}(k_1)F_{\mathrm{LL}}(k_1)}, \tag{5.12}$$

are often reported [6, 90, 18]. Note that the frequency and wavenumber coherence (γ^2_{RL} and $\mathrm{coh}^2_{\mathrm{RL}}$) can be interchanged using the relationship $k_1 = 2\pi f/U_{\mathrm{ref}}$. The measurement coherence bandwidth (MCB), denoted as $k_{0.5}$, is defined to be the wavenumber at which the magnitude squared coherence $\mathrm{coh}^2_{\mathrm{RL}}(k_1)$ decreases to 50% [6, 92]. The MCB is related to the "smallest detectable eddy size d_{eddy}" by $d_{\mathrm{eddy}} = 2\pi/k_{0.5}$. A potentially good reduction in the turbine fatigue load can be expected if d_{eddy} is close to $1D$ (diameter) of a specific turbine [92].
Furthermore, in LAC applications, another useful indication of how effectively the lidar predicts the REWS is the following transfer function [6, 93]

$$|G_{\mathrm{RL}}(f)| = \frac{|S_{\mathrm{RL}}(f)|}{S_{\mathrm{LL}}(f)}. \tag{5.13}$$

As derived by Simley and Pao [93], by definition, a filter that has the gain $G_{\mathrm{RL}}(f)$ is an optimal Wiener filter [94]. The Wiener filter aids in filtering out the uncorrelated information from a stochastic process (in our application, the u_{LL}) and minimizes the mean square deviation between the filtered u_{LL} and desired signal (u_{RR}). A large gain at a certain frequency indicates that less information needs to be damped out before the signal is used. Thus, the gain indicates how much information measured by the lidar is usable for the feedforward control of wind turbines; therefore, a larger area below the transfer function gain results in a better preview quality. In practice, the Wiener filter design is more complicated and requires a higher-order filter. In contrast, a first-order linear filter that has similar damping as the Wiener filter can also

provide a similar filtering effect [95]. In this thesis, the first-order linear filter is considered to evaluate the benefits of LAC. The linear filter is frequently designed to have a cutoff frequency (f_{cutoff}) at which the gain of the Wiener filter drops to -3 dB [6, 93].

5.3 Lidar Wind Preview Quality under Freestream Turbulence

In this section, the lidar wind preview quality under freestream turbulence is analyzed using both the Mann and Kaimal turbulence models. Trajectory optimization is performed for a typical multi-range gate pulsed lidar and the NREL 5.0 MW reference turbine.

5.3.1 Lidar Trajectory Optimization

Based on previous derivations, the lidar wind preview quality has been shown to be dependent on turbulence parameters, turbine rotor size, and lidar measurement trajectory. For lidar manufacturing, the lidar trajectory affects the performance of LAC and is also linked to the cost of the lidar. Currently, the commercially available pulsed lidars used for turbine control are frequently designed to have four beams and up to ten measurement gates. The beam directions of these types of lidar are fixed and not adjustable. Some research-oriented pulsed lidars have the capability to adjust the beam directions following a certain pattern, such as the SWE scanning lidar [6]. For continuous wave lidars, the beam directions are usually adjustable to ensure a wide range of measurements, e.g., the and the DTU SpinnerLidar [96].
In the rest of this section, the optimization is based on a typical pulsed lidar configuration that has a full width at half maximum (FWHM) of 30 m. The considered optimization variables are

(a) x_{end}: the distance from the lidar position to the furthest focused position in the x axis;

(b) α_{L}: the opening angle of the lidar beam, which is the angle between the lidar beam and the x axis.

The number of beams is assumed to be 4. Each lidar beam has 10 range gates. These 10 range gates are eventually distributed from the nearest measurement position to the last position at x_{end}. The sampling frequency for each beam is assumed to be 1 Hz, and the measurements are performed sequentially from one beam to another.
Following [6], the brute force optimization is used to calculate $k_{0.5}$ and f_{cutoff}. The neutral turbulence parameters in Table 5.1 are considered for optimization because neutral stability is more often reported at above-rated wind speed conditions [78, 33]. However, the sensitivity of the preview quality to the turbulence parameters will be analyzed later. A mean wind speed of 16 ms^{-1} is considered for all the preview quality assessments in this section. Note that the optimization results are not dependent on the mean wind speed, which is discussed in Section 5.3.2.

The first measurement position is assumed to be at $x = 50\,\mathrm{m}$ for the four-beam lidar. The optimization result for the NREL 5.0 MW reference turbine and four-beam lidar using the Mann model is shown in Figure 5.4. We can observe that the peak MCB does not provide the peak cutoff frequency. Increasing the distance of the last measurement gates provides a higher cutoff frequency but also results in a lower MCB. In panel (c), the maximum value in the transfer function gain $|G_{\mathrm{RL}}|$ is plotted. The maximum value is also important. When this value is larger than 1, the lidar-estimated REWS must be augmented at some frequency ranges, which is not easy to achieve with a simple linear filter design. A typical first or second-order filter cannot enhance the signal only in a small frequency range but in a large frequency range below the cutoff frequency. A max $|G_{\mathrm{RL}}|$ greater than one frequently appears in the case if the lidar beams are outside the rotor-swept area when projected to the rotor plane. Therefore, the

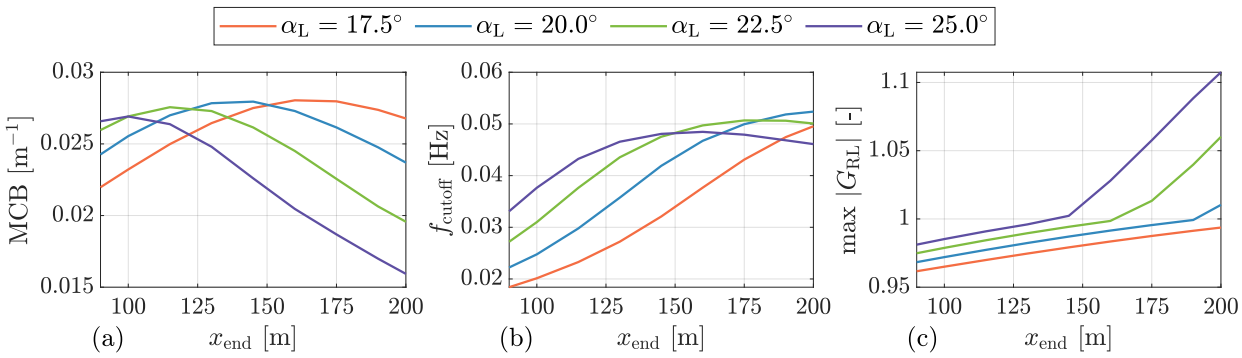

Figure 5.4: Preview quality indicators under several lidar trajectories, calculated using the extended Mann model-based space-time tensor.

optimal trajectory is selected based on the following criteria:

(a) The MCB and cutoff frequency are as large as possible,

(b) The maximum $|G_{\mathrm{RL}}|$ is less than 1.

Based on these criteria, for the Mann model-based optimal four-beam trajectory, the opening angle is selected to be 20°, and the last measurement distance of $x_{\mathrm{end}} = 170\,\mathrm{m}$ is selected.
The optimization result for the NREL 5.0 MW reference turbine and four-beam lidar using the Kaimal model is shown in Figure 5.5. The MCB and cutoff frequency are generally smaller than the results from the Mann model, which can be caused by the underestimated combined coherence using the direct product method (see Section 4.3.4). The results indicate that a better MCB is obtained when the opening angle is large and the last focused distance is small. This trend is opposite to the results using the Mann model. This can be due to the contamination of v and w components not being considered because their spatial coherence and the coherence between u and w components are ignored. A larger opening angle results in more contributions

to LOS speed by the v and w components. Because the contamination is not modeled, the optimization results prompt the use of larger opening angles. To observe the impact of the longitudinal coherence decay a_x on the trajectory optimization, we perform another optimization using the Kaimal model, and it is shown in Figure 5.6. Here, the only difference from Figure 5.5 is that a smaller $a_x = 0.6$ is used. In this scenario, the optimization results are more similar to those of the Mann model, where the larger MCB is obtained using a smaller opening angle. In this scenario, the longitudinal coherence with a smaller a_x is less dominant in the lidar-rotor coherence; thus, the results suggest focusing at a longer distance with a smaller opening angle. Because of the overall better agreements of spectra and coherence with the measurement data in Chapter 4, the optimal trajectory derived from the Mann model is used in the remainder of this thesis. This optimal measurement trajectory is summarized in Table 5.3 and plotted in Figure 5.7.

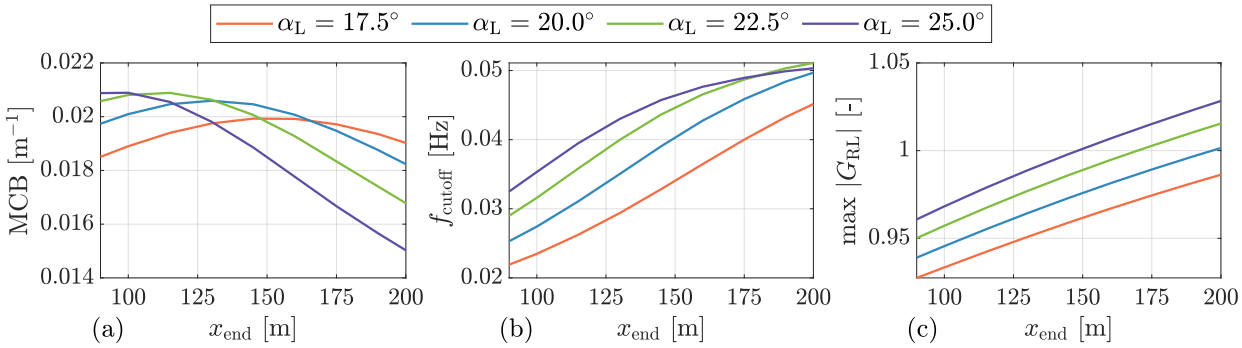

Figure 5.5: Preview quality indicators under several lidar trajectories, calculated using the Kaimal model. The longitudinal coherence decay a_x=1.9 is considered.

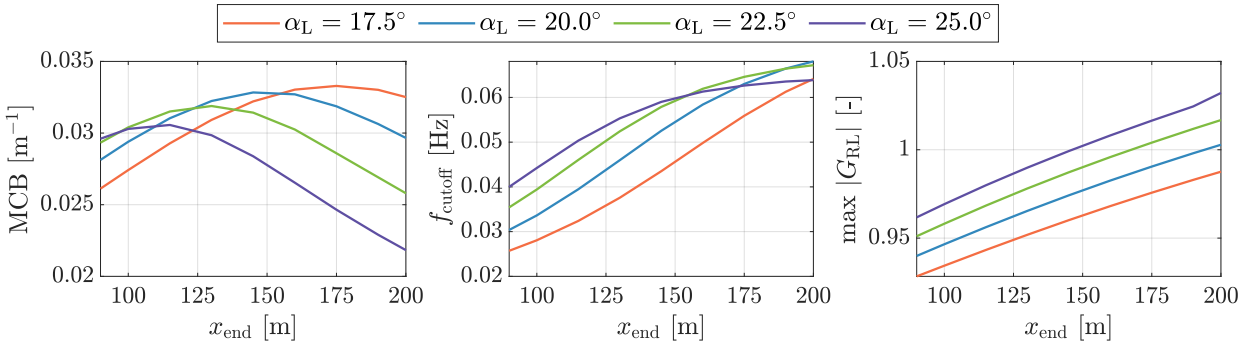

Figure 5.6: Preview quality indicators under several lidar trajectories, calculated using the Kaimal model. The longitudinal coherence decay a_x=0.6 is considered.

Table 5.3: Parameters of the optimal four-beam pulsed lidar system, which are optimized using the Mann model-based space-time tensor. Note that the azimuth and elevation angles are based on the local coordinate system of the lidar, where the positive x direction is the forward-looking direction of the lidar and the right-hand rule applies to other directions.

Parameters	Values	Units
Number of beams	4	[-]
Beam azimuth angles	14.4, 14.4, -14.4, -14.4	[°]
Beam elevation angles	14.0, -14.0, -14.0, 14.0	[°]
Range gates in x	50 to 170	[m]
Range gates step in x	13.3	[m]
Sampling frequency	1.0 (each beam)	[Hz]
FWHM	30	[m]

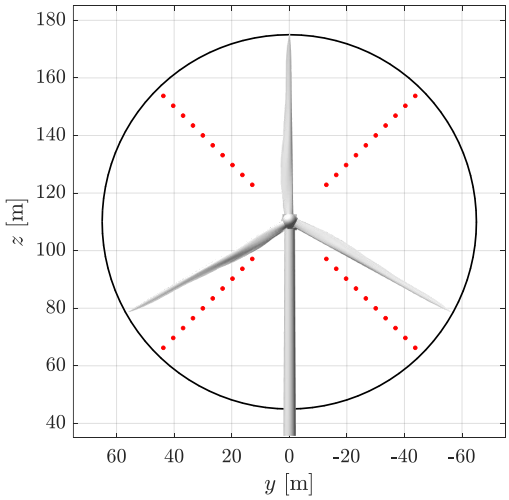

Figure 5.7: A front view of the NREL 5.0 MW turbine and the optimized four-beam lidar measurement trajectory.

5.3.2 Sensitivity of Lidar Wind Preview to Turbulence Parameters

Sensitivity to Atmospheric Stability

With the four-beam lidar trajectory optimized based on neutral stability, it is necessary to study the sensitivity of the lidar wind preview quality with respect to other stability classes represented by different turbulence parameters. Using the parameters listed in Table 5.1, the coherence γ^2_{RL} under different stability classes are shown in Figure 5.8 (a). We can observe that the coherence using the Mann model-based space-time tensor is generally better than that using the Kaimal model. For both models, the coherence in the neutral and stable stability classes is higher than that in unstable stability, which can be caused by the stronger turbulence evolution in the unstable scenario. The coherence in the unstable scenario is particularly low when using the Kaimal model, which can again be caused by the direct product method for

coherence combination.

The transfer functions under the three investigated stability classes are shown in Figure 5.8 (b). The transfer function gains are similar in the three stability classes for the space-time tensor-derived results. For the results using the Kaimal model, the transfer function gain is lower in the unstable stability class but similar in the neutral and stable stability classes.

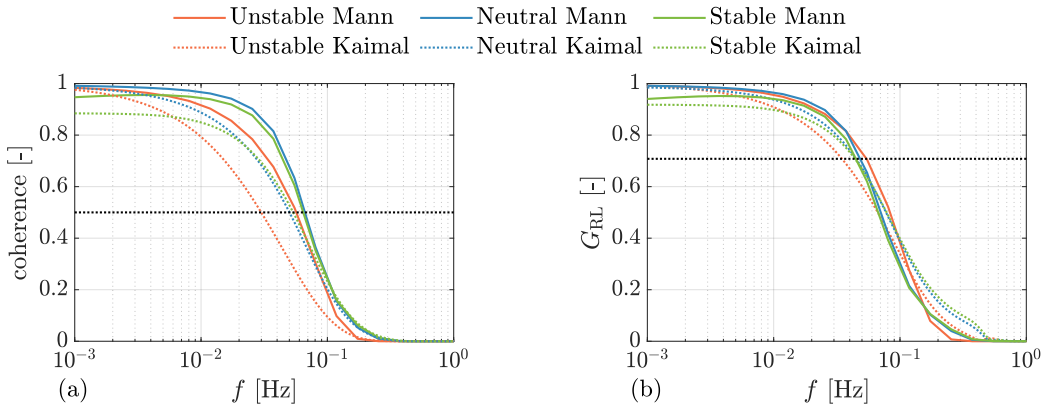

Figure 5.8: (a) Coherence γ^2_{RL} between lidar-estimated and the turbine REWSs. (b) Optimal transfer function gain. The black dot line corresponds to the MCB at 0.5 and the magnitude at -3dB.

Using the spectral turbulence model, which represents the mean spectral properties, we can obtain the expected Wiener transfer function gain, which is then used to fit a first-order linear filter with a cutoff frequency at -3 dB of the Wiener filter gain [6, 93]. A list of the cutoff frequencies obtained by fitting the G_{RL} in Figure 5.8 (b) is provided in Table 5.4. The cutoff frequencies obtained by the Mann model-based space-time tensor are generally larger than those using the Kaimal model. For the same turbulence model, the resulting cutoff frequency does not change significantly according to the analyzed turbulence stability conditions. We can observe that the turbulence parameters of different atmospheric stability classes do not significantly influence the cutoff frequency, and the difference is generally smaller than 0.01 Hz. This also indicates that the filter design is not sensitive to the change in turbulence parameters related to atmospheric stability, and a constant filter design is robust. In the remainder of this thesis, we use the constant cutoff frequency based on neutral stability for the assessment of LAC.

Table 5.4: Cutoff frequencies in Hz corresponding tp −3 dB at the G_{RL} magnitude, calculated using the NREL 5.0 MW turbine and the four beam optimized lidar trajectory with a mean wind speed of 16 ms^{-1}.

	Mann	Kaimal
Unstable	0.0544	0.0347
Neutral	0.0490	0.0449
Stable	0.0455	0.0439

Sensitivity to Mean Wind Speed

Because the turbine will operate at different above-rated wind speeds, it would be interesting to determine the lidar wind preview quality indicators for different mean wind speeds.
Figure 5.9 shows the lidar-rotor coherence and optimal transfer function for four different mean wind speeds. With a higher mean wind speed, the upstream wind field propagates faster to the rotor plane, and the turbulence field will have less time to evolve. Based on the theory discussed in Chapter 4, a smaller time difference results in a higher longitudinal coherence; therefore, the lidar wind preview quality is also better.

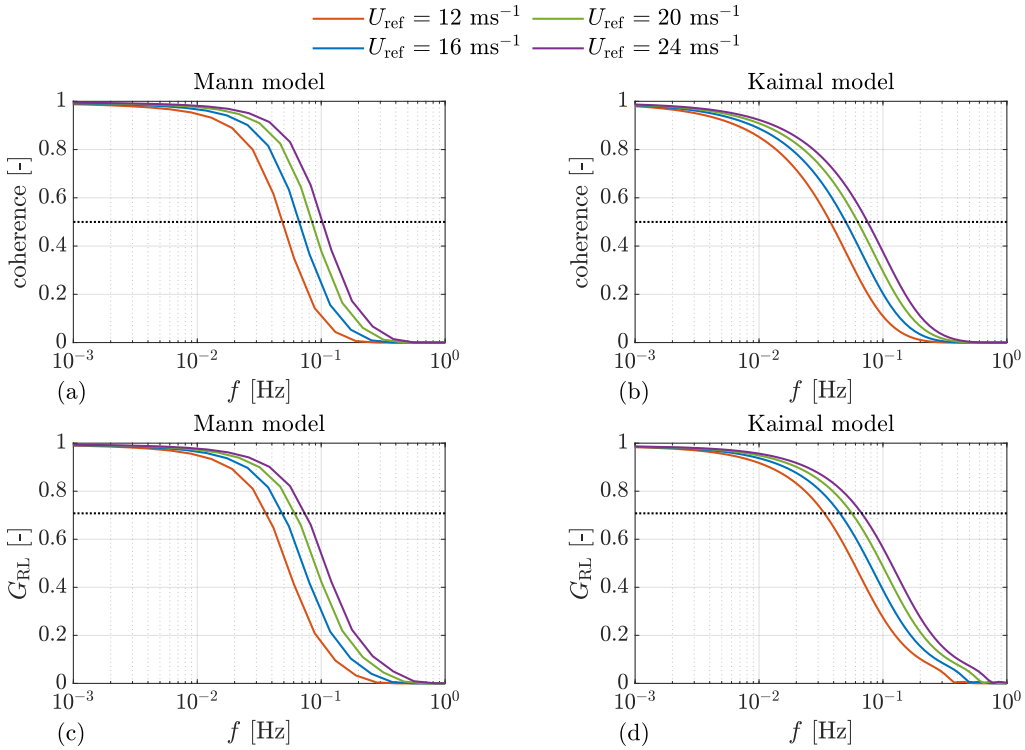

Figure 5.9: (a) and (b): Coherence γ^2_{RL} between lidar estimated RWES and the turbine-based REWS under different mean wind speeds. (c) and (d): The optimal transfer function gain under different mean wind speeds. The black dot line corresponds to the MCB at 0.5 and the gain at −3 dB.

Figure 5.10 shows the MCB and cutoff frequency at different mean wind speeds. We can observe that the MCB is not dependent on the mean wind speed, and the relationship between the cutoff frequency and mean wind speed is approximately linear. Based on this linear relationship, the cutoff frequency for the linear filter of LAC can be scheduled.

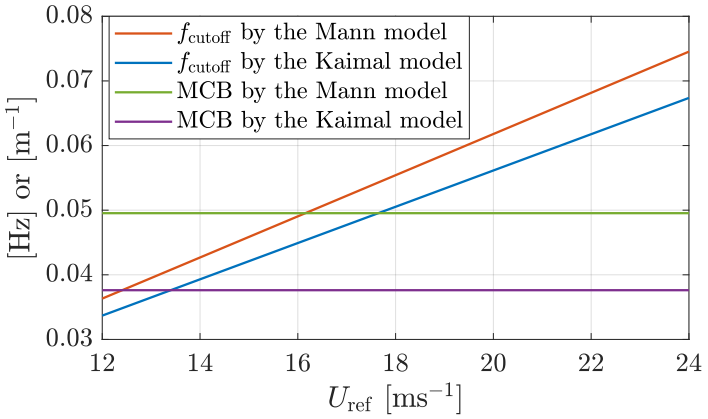

Figure 5.10: MCBs and cutoff frequencies under different mean wind speeds.

In addition to the cutoff frequency, the buffer time introduced in Chapter 2 is also important for the feedforward control. Figure 5.11 shows the leading time T_{lead} as a function of mean wind speed by the first two measurement gates (nearest to the turbine rotor) of the optimized lidar from Section 5.3.1. The required leading time ($T_{\text{filter}} + T_{\text{pitch}} + \frac{1}{2}T_{\text{window}}$) is also plotted. The leading time must be larger than the required leading time to avoid the feedforward pitch signal being activated too late. For LAC implementation in Chapter 7, we use the lidar measurement range gates from 2 to 10 for estimating the REWS when the mean wind speed is above 20 ms^{-1}. The leading time of gate 2 is sufficient to provide enough leading time for wind speeds above 20 ms^{-1}. For mean wind speed below 20 ms^{-1}, all 10 range gates are used to estimate the REWS.

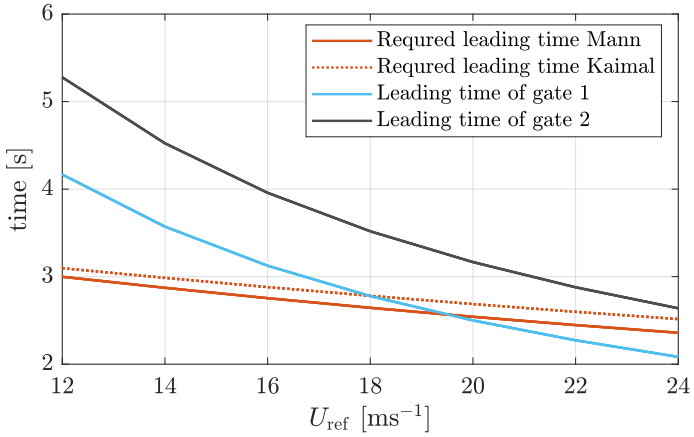

Figure 5.11: The leading time and required leading time for pitch feedforward command.

5.4 Lidar Wind Preview Quality under Wake Conditions

This section assesses the impact of turbine wakes on the lidar wind preview quality of a downstream turbine.

5.4.1 Potential Impact of Turbine Wake

The existing literature primarily concentrates on the lidar wind preview for control in the freestream turbulence scenario [6, 90, 18]. In this context, the turbulence is assumed to be homogeneous and Gaussian, which can be modeled using spectral models.
As introduced earlier, three main characteristics are presented in the turbine wakes [12, 70], i.e.,

(a) the reduced wind speed region (wake deficit);

(b) the meandering (wake deficit moves in the lateral and vertical directions);

(c) the smaller-scale added turbulence caused by the interaction between the rotor and the flow.

Based on these phenomena, we can conceive the possible impacts of turbine wakes on lidar wind preview quality. For example, the wake is measured by lidar in an upstream y-z plane (Figure 5.12). Subsequently, it propagates (in the x-direction) to the turbine with meandering such that the sectional overlap of the wake at the rotor disk changes in time. When the wake reaches the rotor plane, it might be partially overlapped with the rotor, miss the rotor entirely, or become less important owing to the wake recovery. These might cause other errors between the lidar-estimated REWS and that experienced by the rotor.
Because the lidar wind preview quality under wake conditions has not been fully explored in the literature, this section contributes by studying the impact of wake on lidar wind preview quality in the frequency domain. The Mann model [11] is combined with the DWM model, both suggested by the IEC 61400-1 standard [12], to model wake-included turbulence. The analysis is performed using different turbulence parameters representing three atmospheric stability classes (see Table 4.2) and considering several wind direction scenarios. The Kaimal model is not considered because the spatial correlation of the v and w components is not defined. The spatially uncorrelated v and w components will lead to unrealistically low fluctuations of large-scale lateral and vertical motions, which results in unreasonable wake meandering.

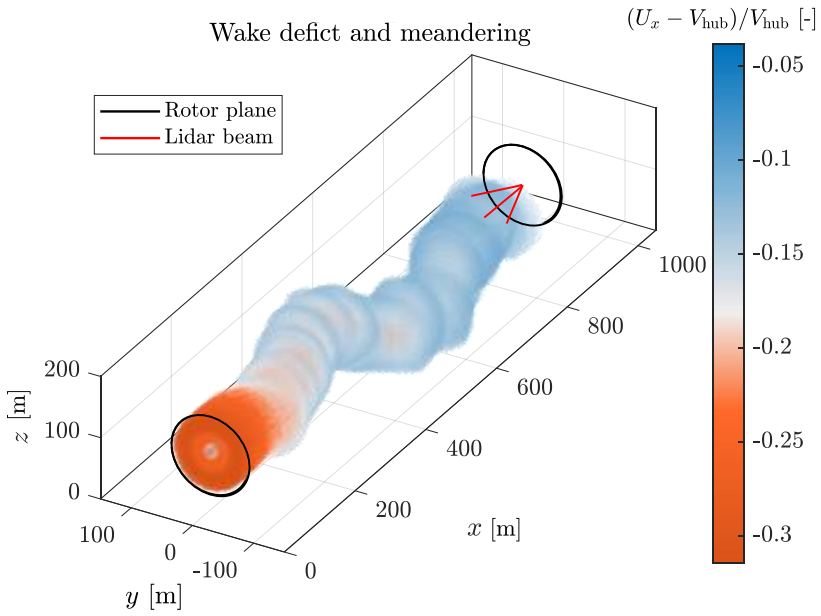

Figure 5.12: A sketch of the meandering wake deficit for a downstream turbine and a lidar system. V_x denotes the mean longitudinal wind speed deficit in the wake, and V_{hub} is the freestream hub height mean wind speed.

5.4.2 Simulation Configurations

Before the development of the Mann model-based space-time tensor and the corresponding 4-D turbulence generation tool, the DWM model and Taylor's frozen theory were used by [71] to study the lidar wind preview quality under wake conditions. This section adopts the space-time tensor-based turbulence when applying the DWM model. The 4-D turbulence field is generated at the y-z planes, including the upstream turbine rotor plane, the range gates of the lidar mounted on the downstream turbine, and the rotor plane of the downstream turbine. The wake center is calculated using Equation 3.19 and using the y-z plane turbulence at the upstream turbine plane. Taylor's frozen theory is used when calculating the wake center because the large-scale lateral and vertical velocity components represented by the eddies with larger sizes are supposed to evolve weakly. After the wake center at each downstream plane that the lidar measures are obtained, the wake deficit and wake-induced turbulence are added to the ambient turbulence generated using the *4-D Mann Turbulence Generator*. Additionally, the smaller scale wake-induced turbulence is also generated using the *4-D Mann Turbulence Generator* with the same eddy lifetime parameters defined for the ambient free stream turbulence.

For the turbine layouts, the layouts in which two turbines align in a row with the typical $5D$ and $7D$ (diameter) spacing are considered. Three wind directions are considered to simulate partial and full wake scenarios for the downstream turbine. As shown in Figure 5.13, three wind directions based on the $7D$ separation are defined. The full wake scenario corresponds to the $7D$ downstream turbine being aligned with the upstream turbine and the wind direction. The

half-aligned scenario means that half of the turbine rotor at $7D$ is in the mean wake boundary. The critical-unaligned condition means that the turbine is critically outside the wake boundary. For the $5D$ scenario, the downstream turbine is moved toward the upstream turbine by twice the rotor diameter along the line between the $7D$ position and the upstream turbine. The Mann parameters listed in Table 5.1 are used to simulate various atmospheric stability classes. For each simulation configuration, 12 different random seeds are used to generate the turbulence fields. For each seed, a wake-included turbulence field with the dimensions of $4096\times11\times64\times64$ and resolutions of 0.5 s, and 8 m × 6.25 m × 6.25 m in the t, x, y, and z directions, respectively, is simulated. Each field has a total simulation time of 2048 s. For comparison, the same turbulence field but without wake is used to simulate the lidar- and turbine-based REWS for the wake-free scenario. The mean hub height reference wind speed is assumed to be 16 ms^{-1} and the parameter $\alpha\varepsilon^{2/3}$ is adjusted to satisfy the turbulence intensity corresponding to class 1A, as specified by the IEC 61400-1 standard [12]. The simulated time series are collected and detrended by the mean value. Subsequently, the spectra are calculated using Welch's method [80] with hamming windows.

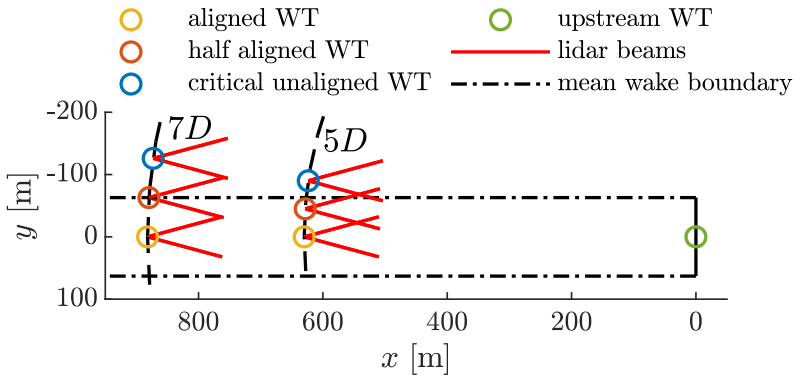

Figure 5.13: A top view of the considered turbine layout. For both $7D$ and $5D$ separations, three different aligning conditions corresponding to different wind directions are considered.

5.4.3 Simulation Results

The simulation results of the REWS time series from one of the turbulence fields with the "5D aligned" configuration in an unstable atmosphere are shown in Figure 5.14. The time series are shifted according to the lidar measured upstream positions and assuming the turbulence propagates through the mean wind speed. By comparing panels (a) with (b), we observe that the wake deficit causes lower mean values in (b) than in (a). The mean u_{LL} is slightly lower than the mean u_{RR} in (b) because of the wake recovering. However, the difference is relatively small, which may be due to the upstream wind turbine operating with smaller thrust coefficients under the mean wind speed of $16\,\mathrm{ms}^{-1}$. Panel (c) compares the difference of RWESs in the wake-included and in the freestream scenarios. The fluctuation in the difference is much smaller than the ambient turbulence fluctuation. Overall, the lidar wind preview exhibits good agreement with the turbine-based REWS in both wake-included and freestream scenarios. We can also observe that the additional fluctuations caused by wakes in (c) are coherent. The lidar measures the additional fluctuations, and they reach the rotor with a slight change. Therefore, the correlation between u_{LL} and u_{RR} in the wake condition is overall not affected significantly, although the mean values are different owing to the wake recovery.

The REWS time series from one of the turbulence fields with the "5D aligned" configuration in a stable atmosphere is shown in Figure 5.15. Note that the same random number seed used for Figure 5.14 is used for the stable scenario here. Thus, the time series exhibits a similar overall trend as that in Figure 5.14. However, owing to the significantly smaller turbulence length scale, the fluctuation in the stable atmosphere exhibits more high-frequency components. Again, because of the small length scale, the spatial filtering effect of the turbulence is more obvious, and the wake center that meanders following the large-scale lateral and vertical components tends to have smaller magnitudes. This can be observed in panel (c) in Figure 5.15. Compared with that in Figure 5.14 (c), the additional fluctuations caused by turbine wake in the stable condition have noticeably smaller magnitudes.

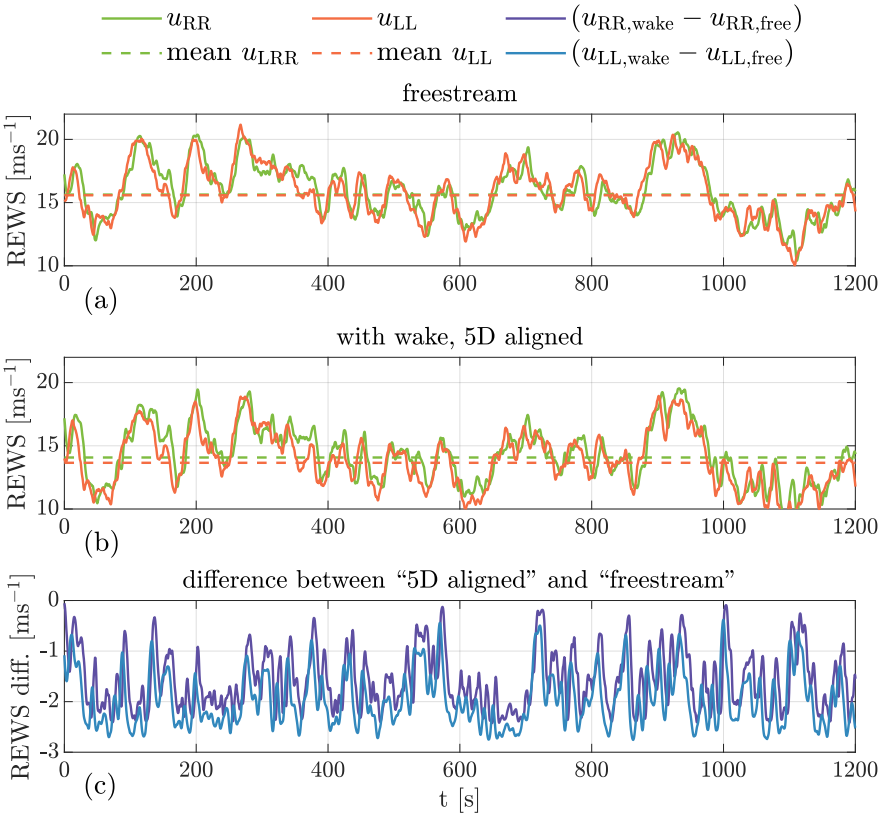

Figure 5.14: The time series of the simulated REWSs, simulated using the DWM model and Mann model-based space-time tensor under an unstable atmosphere.

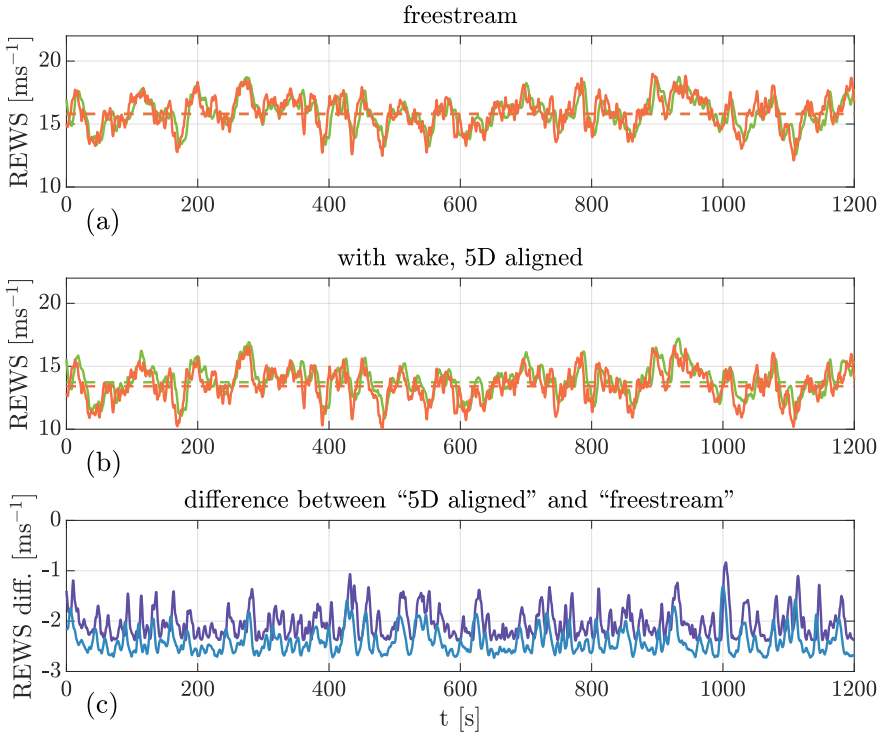

Figure 5.15: The time series of the simulated REWSs, simulated using the DWM model and Mann model-based space-time tensor under a stable atmosphere.

The comparisons of coherence γ^2_{RL} are shown in Figure 5.16. In all the stability classes, the simulated freestream coherence (green solid lines) has good agreement with the theoretical coherence (black dashed lines), which validates the simulation results. In the neutral and stable stability conditions and in all the spatial alignments, the difference between the freestream coherence and wake-included coherence is considerably small. Comparing the green lines with the orange, blue, and purple lines, we observe that the lidar-rotor coherence increases slightly because of the additional coherent fluctuations caused by the wake. However, because the additional fluctuations caused by a wake in the neutral and stable scenarios have a much smaller magnitude and are much weaker than the ambient turbulent fluctuations, the differences are overall smaller. Because of the smaller length scale, the differences are even smaller in the stable scenarios. In the unstable atmosphere and in all the spatial alignments, the coherence even increases owing to the additional coherent wake meandering that is measured by the lidar and experienced by the downstream turbine rotor. In the $5D$ scenario, the wake-included coherence is similar for all the alignments. In the $7D$ separation, the critical-unaligned scenario has a slightly smaller coherence compared with the other two alignments because the wake has a lower possibility of hitting both the lidar and turbine with this alignment.

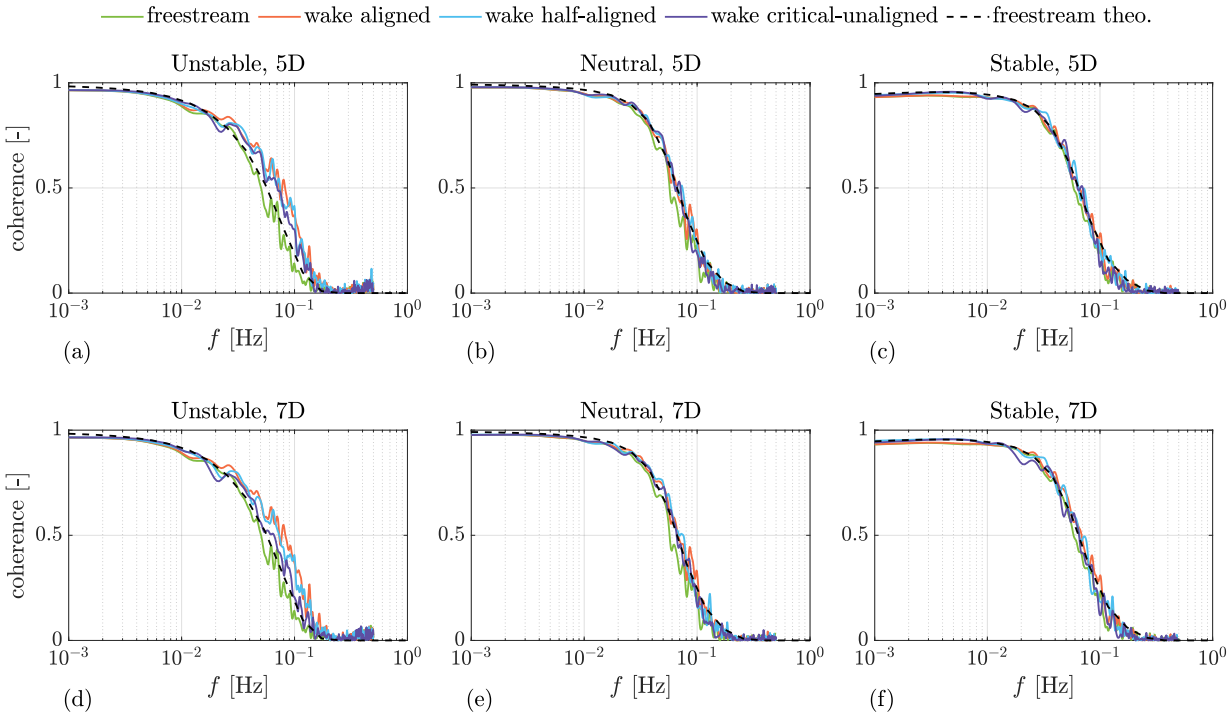

Figure 5.16: Comparisons of lidar-rotor coherence γ^2_{RL} under the wake-included and the freestream turbulences.

The comparisons of the optimal filter gain are shown in Figure 5.17. Similar to the coherence comparisons performed earlier, the transfer functions are not considerably influenced by the wakes in the neutral and stable scenarios. In the unstable scenario, we observe that the transfer

function gain is slightly better than that of the freestream scenario, which is caused by the additional coherent turbulence structure added by the wake effect. With the current wake modeling approach, this also indicates that the filter design is not sensitive to the turbine wakes. The filter gain at $-3\,\mathrm{dB}$ increases slightly by $0.02\,\mathrm{Hz}$ in the unstable situation. Designing a filter using the freestream turbulence models will ensure a conservative design for the filter.

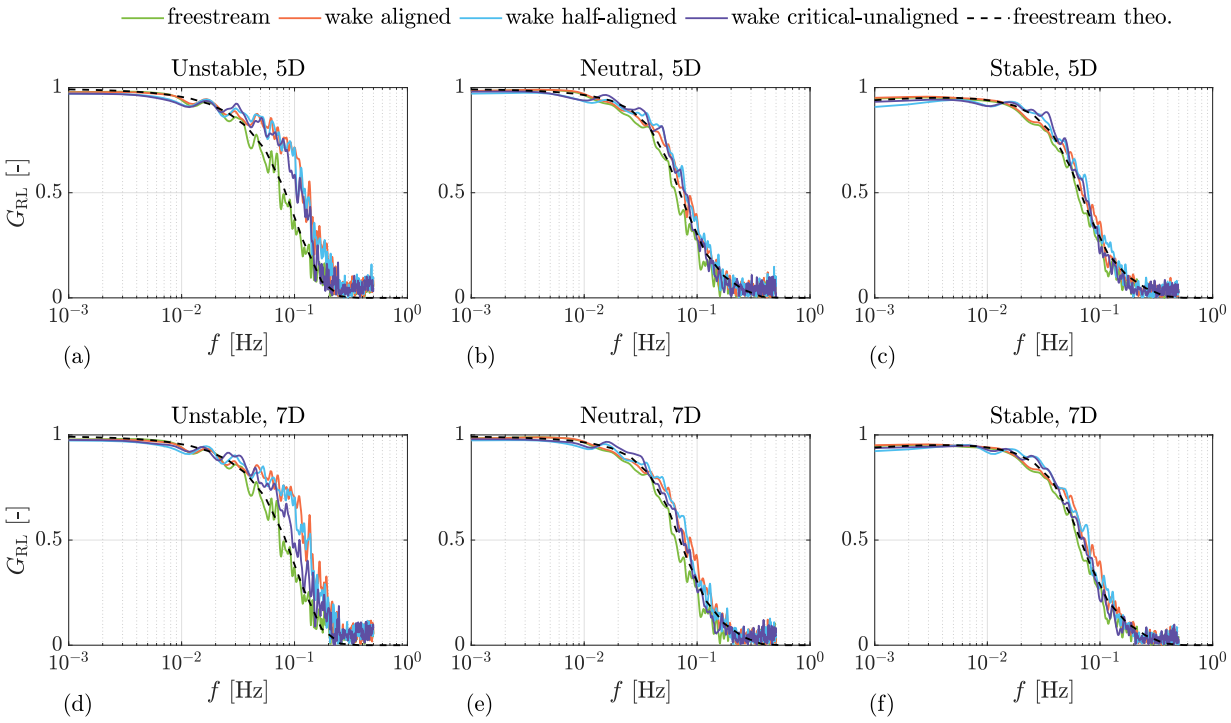

Figure 5.17: Comparisons of the optimal transfer function gains under the wake-included and freestream turbulences.

5.5 Chapter Summary and Outlook

In this section, the variation in the turbulence spectrum and spatial coherence via atmospheric stability are summarized based on the literature. Three atmospheric stability classes are considered: unstable, neutral, and stable. For each atmospheric stability class, the Mann model parameters are collected, and then the Kaimal model parameters are fitted to have similar spectra and coherence as compared with the Mann model. We observe that a more unstable atmosphere results in a larger turbulence length scale. A larger length scale results in greater lateral-vertical coherence. Moreover, we observe that longitudinal coherence, or in other words, turbulence evolution, is linked to atmospheric stability. By comparing with observations from the previous chapter and those from LES-based literature, the longitudinal coherence decay is observed to be faster in a more unstable atmosphere.

Based on evolution-integrated turbulence models discussed in Chapter 4, the lidar wind preview

quality is derived using the turbulence spectral models. The derivations are performed for both the Mann model-based space-time tensor [11, 20] and the Kaimal model [13] in incorporating the longitudinal coherence.

A four-beam lidar measurement trajectory is optimized considering the optimal preview for the NREL 5.0 MW reference turbine under neutral turbulence parameters. The trajectory optimization is performed using both the Mann and Kaimal models. The results optimized using the Kaimal model exhibit high sensitivity to the longitudinal coherence parameters owing to the direct product approach of combining spatial coherence. The Mann model-based optimization results are selected for the remainder of the analysis, where the best option is to have opening angles of 20°, the first measurement gate at $x = 50\,\mathrm{m}$, and the last measurement distance at $x_{\mathrm{end}} = 170\,\mathrm{m}$.

With the optimized four-beam trajectory, the preview quality under the freestream scenario is analyzed using different turbulence parameters representing the three investigated atmosphere stability classes. The conclusion is that the preview quality of the four-beam lidar and NREL 5.0 MW turbine is not very sensitive to atmospheric stability. A simple filter design based on the neutral turbulence condition is robust to other stability classes.

In addition to the freestream turbulence analysis, the preview quality under wake conditions is investigated. The DWM model is combined with the space-time tensor to simulate wake-included turbulent wind fields. The wake-included wind field is generated by combining the freestream 4-D Mann turbulence [20] and the wake characteristics described by the DWM model. The DWM model is combined by the wake deficit, wake meandering, and wake-induced turbulence. The lidar wind preview quality under various wake conditions is assessed using simulated lidar measurements and turbine-based REWSs calculated from the simulated turbulence fields. Turbulence parameters representing different atmospheric stability classes, different spacing between downstream and upstream turbines, and different wind directions corresponding to different wake exposure scenarios are considered.

Overall, the simulation result shows that the wake described by the DWM model has a negligible impact on the lidar wind preview quality. For neutral and stable stability classes, the preview quality under different turbine separations and directions in wake conditions is similar to that in the freestream. In the unstable scenario, the preview quality is slightly increased by the wake because of the coherent turbulence structure introduced primarily by the wake meandering.

However, the DWM model does not solve the turbulent flow using the N-S equation physically. In future research, higher fidelity wake solutions, such as the LES-based approach, can be applied to verify the DWM model on lidar wind preview quality estimation. In addition, the temporal delay effect caused by the wake, which is not addressed in this thesis, can be further studied. Finally, field investigations are necessary to further validate the results.

6

Improving Lidar Module in Aeroelastic Simulations

In the previous chapters, lidar measurement simulation was performed by projecting the velocity components onto the LOS direction and then applying the probe volume weighting function. This approach assumes that the lidar is static. In practice, the nacelle lidar interacts with the turbine tower and rotor dynamics. The nacelle motion causes undesired contributions to the LOS speed measurement, and the passing blade can block the lidar beams and make the measurements invalid. To further assess the benefits of LAC in aeroelastic simulations, a lidar simulation module should be integrated into the aeroelastic codes.

Before this thesis research, a lidar simulation module was integrated into OpenFAST, covering some lidar measurement characteristics such as the different scan patterns, the volume averaging along the beam, and the coupling with the nacelle motion owing to turbine tower dynamics[1]. This chapter focuses on the integration of three new features into the OpenFAST lidar simulation module to make the coupled simulation more realistic. This chapter is primarily based on the research outcomes published in [91].

[1] commit 829511a on 13 March 2020, `https://github.com/sowentoDavidSchlipf/openfast/tree/f/lidarsim`

6.1 Overview of the Updated Features

An overview of the three new features is shown in Figure 6.1.
The first feature is the ability to read a 4-D turbulent wind field with the turbulence evolution phenomenon. In the previous version, the lidar system scanned the exact same wind field, which was also used for the aeroelastic simulation of the wind turbine, assuming Taylor's frozen turbulence theory [2]. As a result, only a shift in time occurs between the lidar-measured and turbine-experienced winds. Specifically, when assessing the benefits of lidar-assisted turbine control, this assumption may overestimate the benefit brought by lidar. In practice, the turbulence is evolving as it propagates towards the turbine, as modeled in Chapter 4; thus, the turbine will not be exposed to the identical disturbances as that measured by the lidar in advance [9]. Therefore, wind evolution should be included in the aeroelastic simulation to provide a more accurate and realistic simulation of a lidar system.

The second new feature is the blade blockage effect. A forward-looking nacelle lidar is frequently installed behind the rotor. The lidar beam can be blocked by the turbine blades during operation, and the blades induce additional peaks in the Doppler spectrum for the lidar, resulting in wrong LOS speed measurements [97]. For high wind speeds, the spectral peaks caused by the blades can be distinguished from that caused by the wind because they appear in different frequency ranges. Additionally, the CNR values at the measurement positions are usually low when the lidar beam is blocked by the blade. For turbines with thick root blades or a low value of rated rotational speed, the blade blockage can affect the quality of the derived signals because some of the desired measurements cannot be obtained. For assessing LAC performance, in particular, this blockage effect should be included to verify the lidar data processing algorithms.

The third updated feature is adjustable data availability. Wind lidars are based on the Doppler effect, and they are designed to provide LOS speed measurements for all the specified measuring range gates [98]. The availability defines the percentage of usable data retrieved by lidar over all the measurement attempts [99]. In the previous version of the lidar simulator, full availability was assumed. However, the availability can decrease when the back-scattered power cannot form a distinguishable Doppler spectrum [99]. The availability of LOS speed measurements is often quantified by the CNR of the laser signal, which depends on aerosol back-scatter, humidity, and precipitation in the atmosphere [100]. Measurements with CNR values below a certain threshold will be considered invalid. When the data availability decreases, special treatment must be conducted to interpolate the missing lidar data to avoid interference with important turbine structural modes [101]. The changeable data availability should be taken into consideration for simulating lidar because the lidar is subjected to various atmospheric conditions in an actual application.

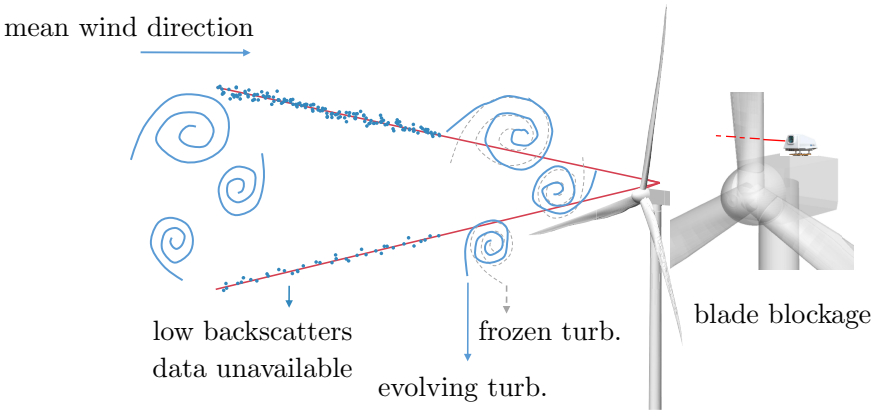

Figure 6.1: A sketch of the new features that are updated in the OpenFAST lidar simulation module. Note that the frozen turbulence remains unchanged from upstream to downstream. The right-hand side shows the scenario in which one lidar beam (dashed lines) is blocked by a blade [91].

6.2 Integrating the Evolving Turbulence

To calculate the LOS speed at upstream positions, the 4-D wind field, including several upstream 3-D wind fields, is imported into the *LidarSim* module of OpenFAST. In the previous version, the same wind field at the rotor plane, which was used to simulate the wind turbine aerodynamics, was also used for simulating the lidar measurements assuming Taylor's frozen theory.

The updated lidar simulator supports only the Bladed-style wind field (with an extension of ".wnd"). One must write a 3-D turbulent wind field in the ".wnd" format to be used for the simulation of the aeroelastic response of the turbine at the position of the rotor, and other 3-D upstream wind fields (at several upstream y-z planes) in the ".evo" format to be used for the simulation of lidar measurements. The ".evo" file must provide the x positions of the upstream planes, which are frequently the x positions of the lidar measurement. The main benefit of writing the wind fields in separate files is that the simulation results at the rotor position without LAC can be performed independently. If another lidar upstream measurement distance is specified or another longitudinal coherence model or parameter is used, only the ".evo" format file needs to be updated. In addition to the wind field data, a ".sum" file must also be written, which includes some additional information about the wind field, e.g., the hub-height mean wind speed and the turbulence intensity.

After importing the turbulent wind field, the identical algorithm developed by the previous simulator version is used to simulate the lidar measurement. First, the wind velocity components u, v, and w are projected onto the beam direction to determine the single-point LOS wind speed. Subsequently, within the probe volume, Taylor's frozen theory [2] is applied to obtain the velocity distribution along the probe volume. Thereafter, a weighted sum of several single-point LOS speeds along a beam is calculated to approximate the weighting effect caused

by the lidar probe volume. This method of assuming Taylor's frozen theory within the probe volume was called the "semi-frozen" method by [59] and has been shown to not affect the wind preview quality of a pulsed lidar with a typical probe volume size (FWHM=30 m).

6.3 Simulating the Blade Blockage Effect

This section presents the algorithm used for detecting the blade blockage status during the OpenFAST simulation. The code implementation in the OpenFAST framework is also presented.

6.3.1 Blade Blockage Detection

Generally, forward-looking nacelle lidar systems are installed behind the turbine rotor. In practice, because nacelle lidar systems frequently have small opening angles, the measurements are affected by the blade sections close to the root, where the blade geometry is mostly transitioning from a circle to the thickest airfoils. The detailed geometry of these sections can be derived if the airfoil coordinates, twist angles, and chord lengths are provided. In OpenFAST, the above information is usually defined for several representative blade element nodes [102]. To detect the blockage caused by the blades, instead of using the detailed blade geometry, the problem is approximated by simplifying the blade geometry as two triangles, whose 3-D Cartesian coordinates can be derived from the information carried by the blade element nodes. After the coordinates of the two triangles are obtained, the ray-triangle intersection algorithm by Möller and Trumbore [103] is used to further detect the blockage status.

As shown in Figure 6.2, c_1 and c_2 denote the aerodynamic centers of the two airfoil cross-sections, l_1 and l_2 correspond to the leading edges of the airfoils, and m_1 and m_2 are the trailing edges. The lidar beam originates from d_0 and measures at d_2. The coordinates of the two triangles ($\triangle m_1 l_1 m_2$ and $\triangle l_1 l_2 m_2$) are the targets for blockage detection. To determine the blade elements that may block the lidar beam, we first calculate the position of point d_1, which lies on both the lidar beam and rotational plane. Note that the rotational plane is the one perpendicular to the rotational axis in Figure 6.2. The position coordinate of d_1 can be computed using

$$\boldsymbol{d}_1 = \boldsymbol{d}_0 + \overrightarrow{d_0 d_2} \frac{\overrightarrow{d_0 o} \cdot \boldsymbol{n}_\mathrm{r}}{\overrightarrow{d_0 b_2} \cdot \boldsymbol{n}_\mathrm{r}}, \tag{6.1}$$

where $\boldsymbol{d}_0$ is the position vector of point d_0, $\boldsymbol{n}_\mathrm{r}$ is the normal vector of the rotational plane, and $\overrightarrow{d_0 d_2}$ and $\overrightarrow{d_0 o}$ are vectors defined by the specific start and end points. Thereafter, the radial distance $|\overrightarrow{o d_1}|$ is compared with the radial distances ($|\overrightarrow{o c_1}|$ and $|\overrightarrow{o c_2}|$) from the blade element nodes to the rotor rotational center o. If $|\overrightarrow{o c_1}| < |\overrightarrow{o b_1}| < |\overrightarrow{o c_2}|$, then the two blade nodes are

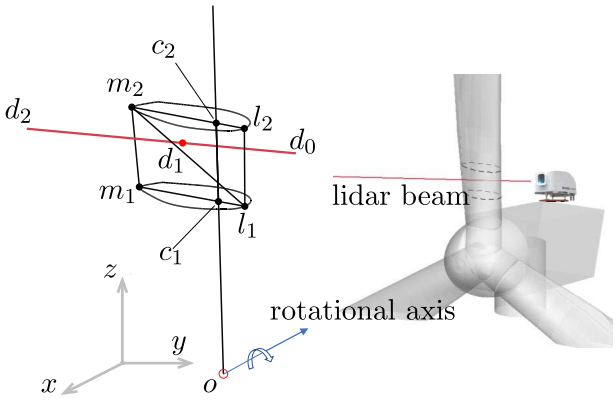

Figure 6.2: A geometrical sketch of the blade blockage detection algorithm. The lidar figure is provided through the courtesy of Movelaser. The figure is redrawn based on [91].

selected to detect the blockage in the next step. Using this simple algorithm, the computational effort is reduced because the calculation of blockage for all the blade element nodes is avoided. In the next step, the leading edge coordinates for l_1 and l_2, and the trailing edge coordinates for m_1 and m_2 are obtained using

$$\boldsymbol{l}_i = \boldsymbol{c}_i - 0.25 L_{\text{chord},i} \boldsymbol{n}_{\text{c}} \quad \text{and} \quad \boldsymbol{m}_i = \boldsymbol{c}_i + 0.75 L_{\text{chord},i} \boldsymbol{n}_{\text{c}}, \tag{6.2}$$

where $L_{\text{chord},i}$ is the chord length of the ith blade element node, $\boldsymbol{c}_i$ is the coordinate of the ith aerodynamic center, and $\boldsymbol{n}_{\text{c}}$ is the orientation vector that aligns with the chord length direction. Here, we assume that the aerodynamic center is located at 25% of the chord line. After $\boldsymbol{l}_i$ and $\boldsymbol{m}_i$ are calculated, the blockage status is finally determined by calculating the geometric relationship of whether the lidar beam ray $\overrightarrow{d_0 d_2}$ intersects with triangles $\triangle m_1 l_1 m_2$ and $\triangle l_1 l_2 m_2$. If the ray has an intersection that lies in one of the two triangles, the blade blockage status is satisfied; otherwise, the lidar beam is not blocked. The details of the ray-triangle intersection algorithm are available in [103].

6.3.2 Verification of Implementation

To verify the code implementation, we simulated the lidar system, whose trajectory is provided in Table 5.3, together with the NREL 5.0 MW reference wind turbine [75]. The lidar system was assumed to be installed on the top of the nacelle (3.5 m above the nacelle floor) and 3 m behind the blade root. Figure 6.3 shows a polar scatter plot between the azimuth angle of the first blade and the blockage status of lidar beam 1. We observed that the blade blockage occurred at three ranges of azimuth angles, which is reasonable as these three ranges correspond to the blocking by the three blades of the rotor.

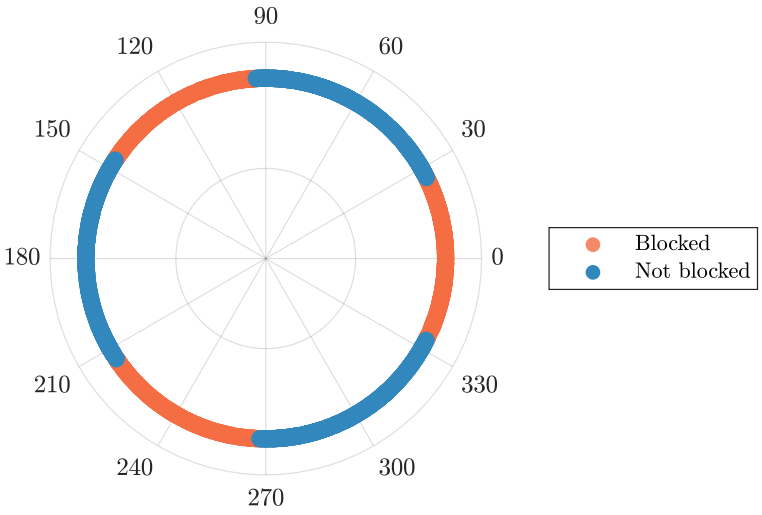

Figure 6.3: A polar scatter plot of the blade blockage status of the lidar beam based on OpenFAST simulation. The polar coordinates indicate the azimuth angle of the first blade in the rotational frame. Only the blockage status of beam 1 is plotted. The lidar measurement trajectory is provided in Table 5.3.

6.4 Simulating the Lidar Measurement Availability

In this section, a statistical spectral analysis of the CNR measurement from a pulsed lidar system is performed. Subsequently, the implementation of the adjustable data availability function in OpenFAST is introduced.

6.4.1 Measurement Campaign for Lidar Data Availability Model

A measurement availability model was proposed by [99] to simulate the availability over the measurement distance recorded for a certain period. The model provides a good reference for selecting the measurement distance to provide higher availability. However, in the aeroelastic simulation, the time series of availability status is required. Thus, we decided to derive a novel spectral model for the CNR signal based on lidar measurements. The model aims to produce a CNR time series that has similar auto-correlation and availability statistics as the measurement data.

The measurement was performed at the campus of Flensburg University of Applied Sciences in northern Germany, using the four-beam pulsed lidar (Molas NL200) produced by Movelaser (Figure 6.4). The detailed beam trajectory is provided in Table 6.1. The data obtained from May 10, 2021 to July 9, 2021 was used for our analysis, during which the lidar was positioned towards the atmosphere and there were no obstacles in the LOS direction.

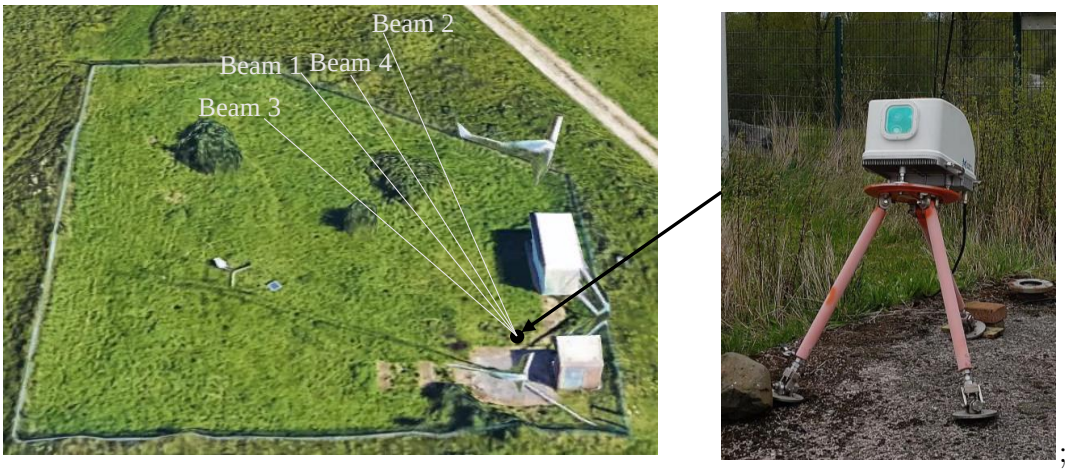

;

Figure 6.4: An overview of the lidar measurement site for CNR data analysis.

Table 6.1: Scan configurations for the Molas lidar system. Note that the azimuth and elevation angles are based on the local coordinate system of the lidar, where the positive x direction is the forward-looking direction of the lidar and the right-hand rule applies to other directions.

Parameters	Values	Units
Number of beams	4	[-]
Beam azimuth angles	15.0, -15.0, 15.0, -15.0	[°]
Beam elevation angles	12.1, 12.1, -12.1, -12.1	[°]
Range gates in x	50 to 190	[m]
Sampling frequency	1.0 (each beam)	[Hz]
FWHM	30	[m]

6.4.2 Spectral Analysis of CNR

The stationarity of the CNR time series is first investigated to observe the power spectral density of the CNR signals. The measurement data were divided into continuous 10 min samples, because 10 min is a typical time interval used for atmospheric turbulence in wind energy applications [12]. As shown by Figure 6.5, the 10 min mean CNR had spikes on some days when the mean CNR values were considerably high; thus, it could not be considered stationary in general [104]. However, Figure 6.5 shows that the samples with a mean CNR below the threshold are closer to being statistically stationary. Thus, only the CNR 10 min samples whose 10 min mean value was below 0.79 dB are selected for the spectral estimation, and the spectrum is obtained by calculating the sample mean spectrum from all the low CNR intervals. The rectangular windows (size of 512 data points) are applied to each 10 min CNR sample. Before applying the Fourier transform, the mean values are first removed from the signals, and outliers (five times larger than the mean CNR) are removed and replaced using zero padding. As mentioned

earlier, the lidar measurement is considered unavailable when the CNR value is below a certain threshold (0.79 dB for the used lidar). The reason for analyzing the spectra using low CNR samples is to emphasize scenarios with low CNRs because those with high mean CNRs are unlikely to result in unavailable data.

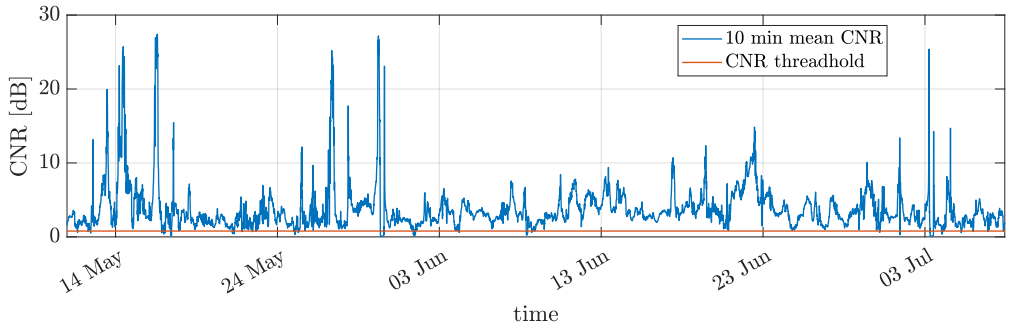

Figure 6.5: 10min mean CNRs of beam 1 from the Molas NL200 lidar.

The spectra estimation results are shown by Figure 6.6, where the dashed lines show the spectra estimated from the data from the four lidar beams (range gate at $x = 190\,\mathrm{m}$). Additionally, an empirical model is proposed to fit the spectrum based on the measurement. The empirical model is expressed as

$$S_{\mathrm{CNR}}(f) = a_{\mathrm{c}}(1 - 10^{-d_{\mathrm{c}}f})^{-1} + e_{\mathrm{c}} \tag{6.3}$$

with three empirical parameters: a_{c}, d_{c} and e_{c}. The model is fitted to the estimated spectrum using the least-squares fit. A detailed description of the CNR sources is provided by [38], which implies that the higher frequency components of the CNR are related to the instrument, whereas the lower frequency parts are related to the atmospheric conditions. As shown in Figure 6.6, the spectra transited to the white noise spectrum (constant over frequencies) after 0.1 Hz. After 0.1 Hz, the spectra were more contributed by the noise caused by the physical characteristics of optical and electrical instruments. The proposed spectral model shows good agreement with the spectra estimated using the lidar CNR data.

The coherences of CNRs from the four beams are also compared, as plotted in Figure 6.7. The other pairs exhibited weak correlations in the analyzed frequency range, except for beams 1 and 2 measured at the same higher height above the ground, which have some correlations in the lower frequency range.

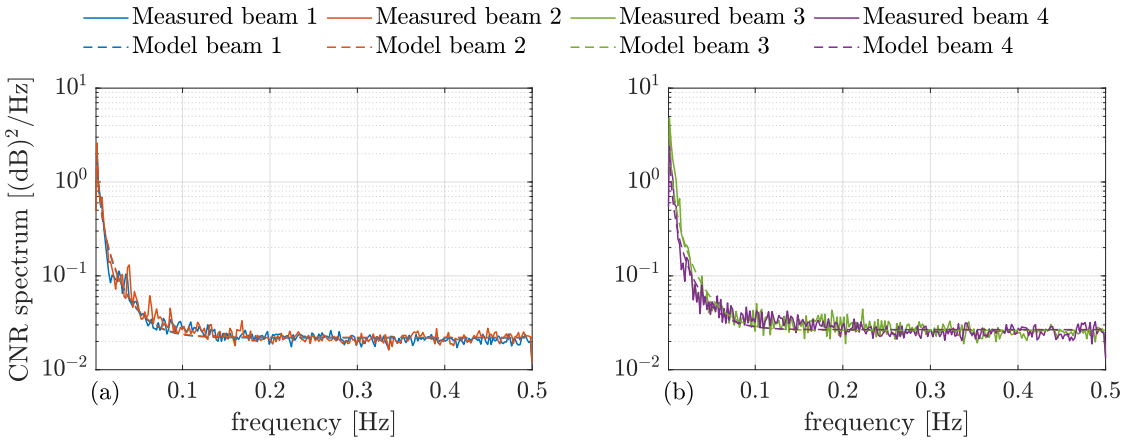

Figure 6.6: CNR spectra estimated using measurements (range gate at x =190 m) and fitted using the spectral models.

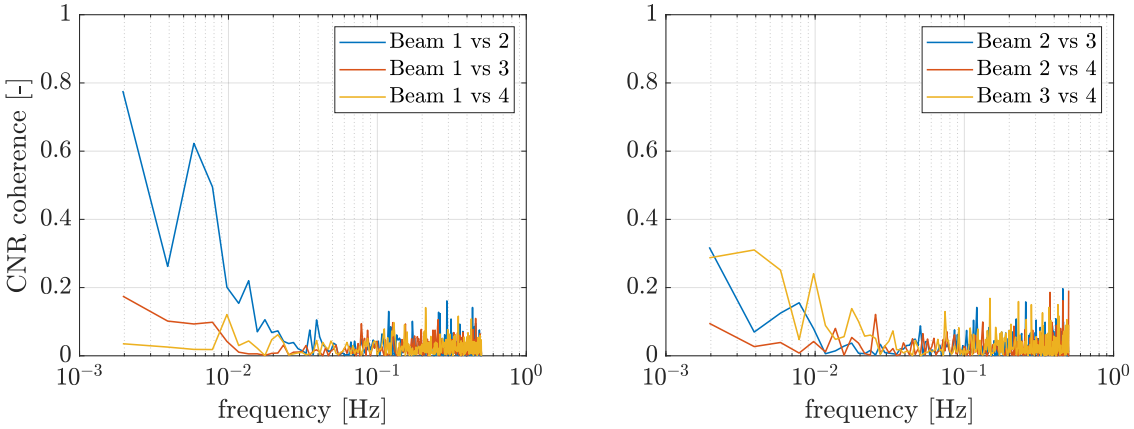

Figure 6.7: The CNR coherence of different beams (gate 190m) using low mean CNR samples.

To verify the proposed spectral model, the CNR time series are generated by applying the IFFT to the spectrum. After the fluctuation part of the time series is generated, the mean value is added, and the same CNR threshold as the lidar manufacturer is used to distinguish availability. Because the spectral model has a high degree of similarity with that of white noise, a white noise spectrum with a constant value of $0.023\,\mathrm{dB^2Hz^{-1}}$ is also used to simulate the CNR time series for comparison. The scatter plots of the 10 min availability and the 10 min mean CNR from beams 1 and 2 are shown in Figure 6.8. We can observe that the proposed spectral model results in very good agreement compared with the measurement data. Additionally, the CNR simulated using a white noise spectrum also has a good agreement with the data. Only a small difference is observed between the results of the spectral model and the white noise spectrum.

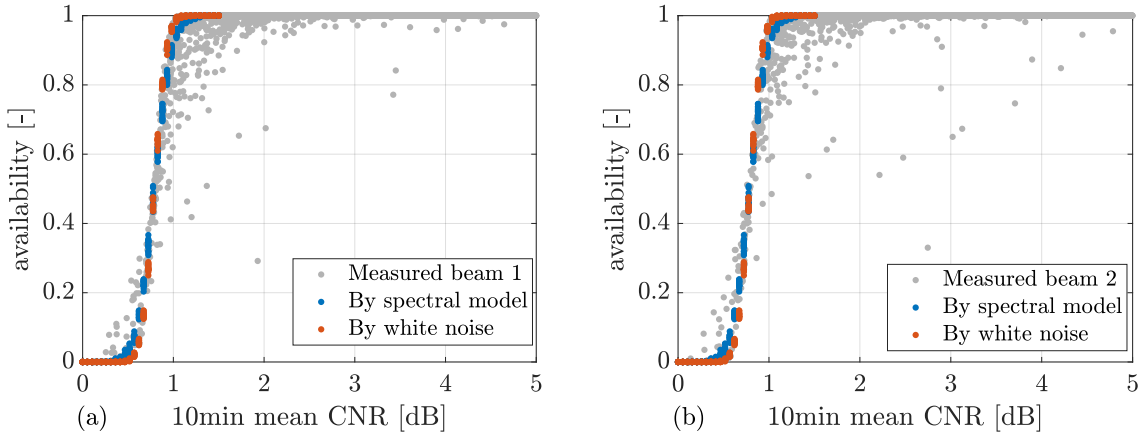

Figure 6.8: Comparisons of measurement availability simulated using spectral models and calculated from measurement. The measurement data from the range gate at x =190 m are plotted.

6.4.3 Data Availability Implementation in OpenFAST

Because lidar data availability can be site- or lidar- specific, simulating the data availability externally (not within OpenFAST) would be more flexible. Therefore, the data availability module is implemented to read external files that contain the data availability time series. In addition to the time series, the sampling time, total time, and number of lidar measurement positions are required in the file. The information listed above is read into OpenFAST, and a check for suitability with the lidar simulation configuration is performed, e.g., the *LidarSim* module will check if the number of measurement positions is correct or if the time series have the correct time length.

At each simulated lidar measurement, the availability of the specific measured position is checked. If the availability is true, the normal LOS speed will be simulated. Otherwise, the

LOS speed will be returned as an error value of -99, which is a distinguishable number for the lidar data processing, and it does not require additional allocation of variables in OpenFAST.

6.5 Assessment of Lidar Preview Quality with the Updated Lidar Simulator

This section introduces a lidar data processing algorithm responsible for processing LOS speed simulation from the updated lidar simulator. Subsequently, different simulations, aiming to assess the impact of the new features on the lidar wind preview quality, are presented.

6.5.1 Lidar Data Processing Algorithm

In Equation 5.7, the lidar-estimated REWS is calculated by averaging the LOS speed from different positions that are measured simultaneously. In practice, both CW and pulsed lidar systems are designed to perform measurements sequentially, so that the measurements are not synchronized. In other words, they are not sampled at the same time. In addition, owing to the blade blockage and availability related to low CNR values, the measurement at one position is not always available. Thus, a lidar data processing algorithm is necessary to estimate the lidar-based REWS in real time from the available measurements.

Owing to the multi-distance measurements of a pulsed lidar system, the measurements from different range gates arrive at the rotor plane at different times. Similar to the study in [6], data buffers are necessary for the lidar data processing algorithm to record the measurements. First, a LOS speed data buffer is designed to be a two-dimensional data array. The first size is equal to the number of measurement positions. The second size is related to time, and it should be sufficiently large to store the maximum possible amount of data. The second size can be determined based on the lidar beam sampling time, the furthest measurement position, and the mean wind speed; for instance, a lidar that has the furthest measurement position at 200 m and the mean wind speed is 20 ms^{-1}. The leading time of the furthest measurement can be estimated as 10 s, assuming the turbulence field propagates by the mean wind speed. Considering the sampling frequency to be 4 Hz, the second size must be at least 400 to store the LOS speed data. In addition to the LOS speed data buffer for storing LOS speed, another time data buffer with an identical size to the LOS speed data buffer is required to store the time of the LOS speed measurements.

At a certain time, if successful new measurement data is available for one position, the LOS speed measurement is recorded in the LOS speed data buffer. The leading time of the LOS speed measurement is added to the current time and then recorded to the time data buffer. Otherwise, when the data is not available owing to blade blockage or low CNR, the LOS speed

and time data buffers are updated as an error value, such as the -99 mentioned earlier. For each time, the processed u_{LL} will be calculated only with suitable LOS speed data from the LOS speed buffer. The LOS speed data is suitable only if

(a) the LOS speed is not recorded as an error value;

(b) the current leading time of the LOS speed measurement reaches the leading time of the first measurement plane (the nearest range gate).

The second criterion ensures that the multi-distance LOS speed measurements are shifted to the nearest measurement distance. Note that the sufficiency of leading time should be checked for a certain mean wind speed, as illustrated in Figure 5.11.

6.5.2 Simulation Setup

The extended Mann turbulence model [91] is considered as the turbulent wind input. The turbulence is assumed to have a reference wind speed of $16\,\mathrm{ms}^{-1}$ and a reference turbulence intensity corresponding to the IEC class 1A [12]. The neutral turbulence parameters listed in Table 5.1 are considered. The impact of turbulence evolution on the lidar preview quality of the four-beam lidar is analyzed as follows. First, the turbulence evolution is considered, and the 4-D turbulence field is generated using the *4-D Mann Turbulence Generator* [20]. Subsequently, Taylor's frozen theory [2] is considered, with which the rotor plane turbulence field is also used to simulate the lidar LOS speed measurements, but with temporal shifts.

In all the simulations, the lidar is assumed to have the trajectory shown in Table 5.3 and be installed on the nacelle of the NREL 5.0 MW reference turbine [75]. The 10 measurement range gates are considered to estimate the lidar-based REWS. Because the mean wind speed of $16\,\mathrm{ms}^{-1}$ is considered in the simulations, the leading time of the nearest range gate 1 is larger than the required leading time, so all the range gates can be utilized.

To study the impact of availability on lidar wind preview quality, we select a low CNR duration based on the measurement campaign introduced in Section 6.4.1. The 10 min mean CNRs of all the lidar measurement positions are shown in Figure 6.9. In the selected duration (the second trough in Figure 6.5), the overall mean CNR values were much lower than most of the rest periods. However, Figure 6.9 shows that the focus distances between 80 and 100 m had the highest mean CNR, and the mean CNR decreases as the measurement distance increases.

To generate the data availability time series, we select the mean CNR values based on Figure 6.9. For each lidar measured position, the CNR time series is generated using both the spectral model and white noise spectrum (see Section 6.4.2 for the method); subsequently, the threshold of 0.79 dB is applied to obtain the availability time series. As discussed in Section 6.4.2, the CNR values of different lidar measurement positions exhibit weak coherence. Thus, the simulated

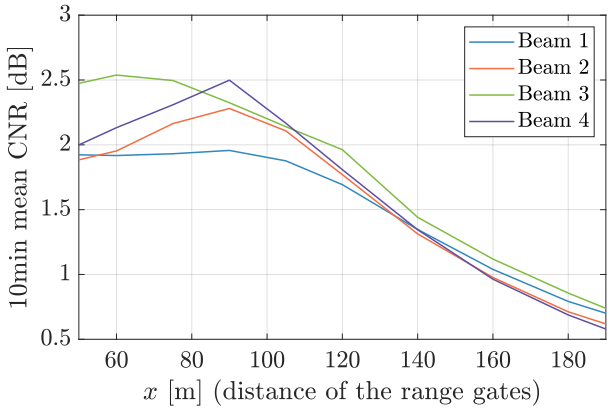

Figure 6.9: The 10min mean CNRs of all the lidar measurement positions from a low CNR duration.

CNR time series for different positions are assumed to be statically independent. In addition, the CNR time series is assumed to be independent of the turbulence time series.
For each setup, 12 simulations with different random seed numbers for the turbulence and CNR time series are performed.

6.5.3 Results and Discussions

Comparisons of coherence γ^2_{RL} and optimal transfer function G_{RL} under different simulation scenarios are shown in Figure 6.10. In (a) and (c), the coherence and G_{RL} values for the frozen turbulence fields and evolving turbulence fields are compared. For the considered lidar, turbine, and Mann turbulence model, the frozen turbulence only slightly overestimates the coherence and G_{RL} values with neutral turbulence parameters. Similar observations were found by [20]. The reason can be that the limited measuring positions are dominant in determining the wind preview quality for the four-beam lidar configuration. In [20], a lidar that can scan the LOS wind speed over a rotor plane in front of the turbine was analyzed. If the lidar can perform such dense measurements, the overestimation of the lidar wind preview quality with frozen turbulence becomes severe. As for the Kaimal model-based analysis performed by [91], the coherence was observed to be overestimated using the Kaimal model and assuming the frozen theory. Once the turbulence evolution is included using the direct product method, the lidar wind preview quality clearly decreases according to the longitudinal coherence decay constant. Figure 6.10 (b) and (e) show the impact of blade blockage on the lidar wind preview quality. By comparing the coherence and G_{RL} with and without the blade blockage effect, we observe that the preview quality decreases only slightly. The decrement in the MCB and cutoff frequency caused by the blade blockage effect were within 0.005 Hz .
Figure 6.10 (c) and (f) show the impact of low CNR events. Here, the measurement unavailability owing to low CNR is simulated using both the spectral model and white noise spectrum. The resulting coherence and G_{RL} are similar using the two spectra. Moreover, including the low

CNR events provides similar results compared with considering only the evolution and blade blockage. This indicates that the considered low CNR event does not have a significant impact on the wind preview quality of the selected lidar and turbine. From Figures 6.8 and 6.9, we can conclude that only the range gates with x distance larger than 150 m are likely to have unavailable data. The nearer range gates have overall higher mean CNR values, therefore ensuring that most of the LOS speed measurements are available. For the four-beam lidar and NREL 5.0 MW turbine, losing the LOS speed measurements at these far-range gates has a negligible impact on the lidar wind preview quality.

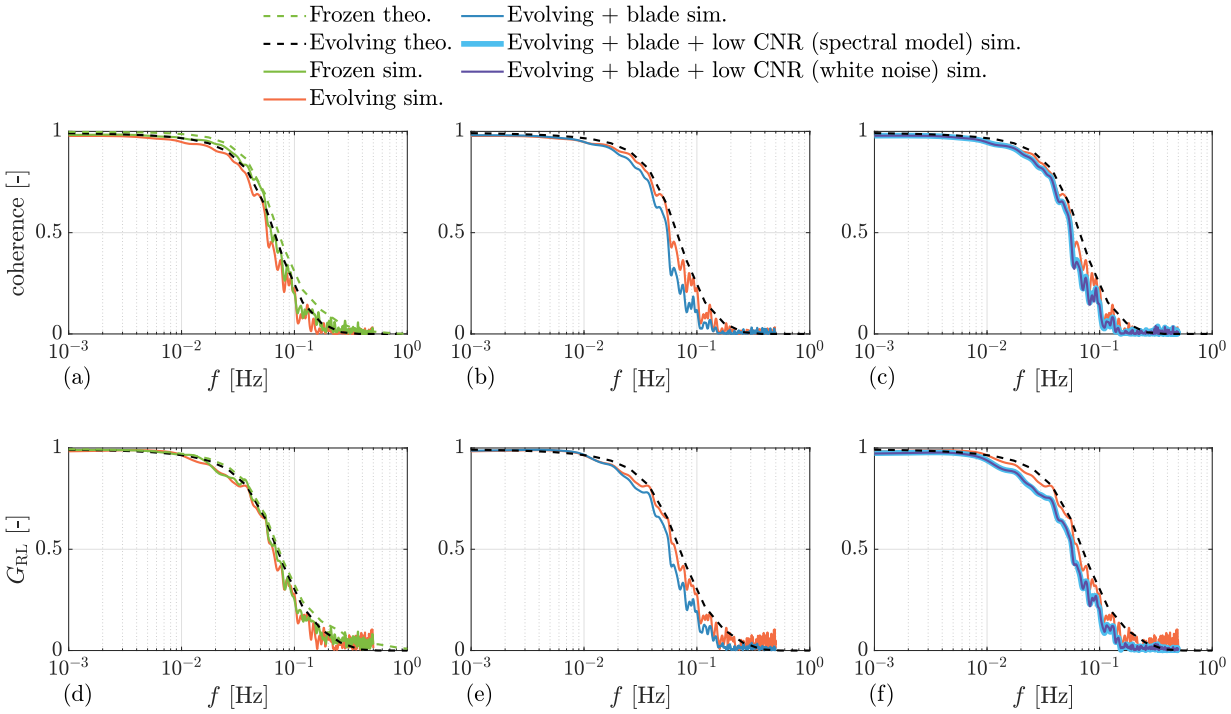

Figure 6.10: Comparisons of lidar-rotor coherence γ^2_{RL} and optimal transfer functions under different simulation setups. "theo." denotes the theoretical values and "sim." denotes the estimated values from simulations. "blade" means that the blade blockage phenomenon is considered.

6.6 Chapter Summary and Outlook

This chapter describes the incorporation of three new features, namely the evolving turbulence, blade blockage effect, and adjustable data availability, into the existing OpenFAST lidar simulator to make it more realistic. These new features support the performance of simulations when these phenomena are of special interest, for example, for the certification of lidar-assisted wind turbine control.

The wind evolution module is updated in OpenFAST, which can be easily interacted with an existing open-source 4-D turbulence generation tool, the *evoTurb* or *4-D Mann Turbulence*

Generator. An additional file with an extension of ".evo" is required to include the turbulence evolution when simulating lidar measurements. The ".evo" file records the upstream turbulence time series at different y-z planes.

For the blade blockage effect, an easy and robust algorithm relying on ray-triangle intersection detection is deployed. The geometry of each blade section is approximated using two triangles, and the blockage is determined by checking whether the lidar beam intersects with any of the two triangles. The two triangles are composed of by two leading edge points and two trail edge points of the blade section. The algorithm was tested and verified to be reasonable through OpenFAST simulations.

A data availability module has been developed in OpenFAST to read in availability time series. A statistical spectral analysis for lidar CNR values is conducted using actual lidar measurements. Based on the investigation, we can conclude that the low data availability event can be simulated using a white noise spectrum. The lidar-rotor coherence and optimal transfer function are analyzed using the updated lidar simulator. For the four-beam lidar and the NREL 5.0 MW wind turbine, we observe that the frozen turbulence only slightly overestimates the lidar wind preview quality. The impact of the blade blockage is also considerably small because the reductions in the MCB and the cutoff frequency are within 0.005 Hz. Using the observed low CNR duration from the measurement campaign, we observe that only the measurements at range gates further than $x = 150$ m tend to have unavailable data. Moreover, the low CNR event does not additionally influence the lidar wind preview quality.

In this study, the lidar measurement campaign was conducted on the ground. In the future, the statistical analysis of the CNR signals can be performed for a nacelle-mounted lidar. It would also be interesting to investigate the preview quality for other lidar and turbine configurations using a realistic lidar simulation environment. During the measurement campaign that lasted for two months, no extreme abnormal weather, such as snowing, frog, and heavy rain occurred. The CNR or lidar measurement availability during such extreme weather conditions can also be further investigated.

7

Evaluation of Lidar-assisted Control

As described in the previous chapters, the lidar wind preview for turbine control is investigated. A more realistic lidar simulation module is implemented in the aeroelastic simulation code OpenFAST (version 3.0). In this chapter, the benefits of LAC are evaluated using the updated lidar-integrated aeroelastic code.

When evaluating the benefits of LAC, reference [6] used the Kaimal model with the turbulence spectral parameters provided by the IEC 61400-1 standard [6] through aeroelastic simulations using FAST (the previous version of OpenFAST). With a circular scanning lidar and NREL 5.0 MW turbine, LAC was observed to cause an apparent reduction in the lifetime damage equivalent load (DEL) in the tower base fore-aft bending moment, low-speed shaft torque, and blade root out-of-plane bending moment. However, the variations in turbulence parameters were not considered.

The variation in turbulence parameters from the standard value given in [12] can be interesting for wind energy. Turbulence parameters under different atmospheric stability conditions are investigated and summarized in Chapter 5. Larger coherent eddy structures are more likely to be observed in an unstable atmosphere, whereas the eddy structure is much smaller under a stable condition. In the neutral scenario, the eddy structure is between the two scenarios. The length scale can have an impact on the power spectrum and turbulence spatial coherence. Because the turbulence spectral peaks can be distributed at different frequency ranges, the different frequencies can produce different excitations for the turbine's structural motions. In this chapter, three classes of atmospheric stability are considered to evaluate LAC benefits: unstable, neutral, and stable. For each atmospheric stability class, both the Mann and Kaimal models are used, and the corresponding 4-D stochastic turbulence fields are generated. The

benefits of LAC are then assessed using a typical four-beam commercial lidar configuration and the NREL 5.0 MW turbine. The simulation results using LAC are compared with those using the traditional FB-only controller. ROSCO is considered the reference FB-only controller. This chapter is based mainly on the publication [105].

7.1 Simulation Setups

This section describes the simulation configurations for evaluating LAC in the aeroelastic tool.

7.1.1 Lidar Simulation

Based on Chapter 6, OpenFAST (version 3.0) was modified to update the lidar simulation module [91], and this new version of the lidar simulation module is used for the simulations described in this chapter. The lidar probe volume, the turbulence evolution (lidar measures at the upstream wind field), the LOS speed contributed by the nacelle motion, and the lidar beam blockage by the turbine blade are all considered when simulating lidar LOS speed measurements. A sample OpenFAST input file for the lidar module can be accessed using the repositories provided in Appendix A.3. Additionally, if the lidar beams are not blocked, full lidar measurement availability is assumed, meaning that the low CNR event is not considered in the simulation. Based on the discussions in Chapter 6, a typical low CNR duration does not have a significant impact on the wind preview quality for the NREL 5.0 MW turbine using a four-beam pulsed lidar.

7.1.2 Turbulence Simulation

A 4-D stochastic turbulence field is required to include the turbulence evolution for the aeroelastic simulation. The newly developed *4-D Mann Turbulence Generator* [20] and *evoTurb* [59] are used to generate the Mann model- and Kaimal model-based 4-D turbulence fields, respectively. The turbulence parameters representative of the three atmospheric stability classes are used (see Table 5.1 in Section 5.1).

For the *4-D Mann Turbulence Generator*, because the generated turbulence contains only the fluctuation part of the velocity components, the mean field is added (only for the u component) considering a power law shear profile with a shear exponent of 0.2. Each 4-D turbulence field has a size of $4096 \times 11 \times 64 \times 64$ grid points, corresponding to the time and the x, y, and z directions. The lengths in the y and z directions are selected to be both 310 m, which are much larger than the rotor size. The reason for choosing these sizes is to avoid the periodicity of the turbulence field in the y and z directions [35], which causes incorrect spatial coherence.

For the Kaimal model-based 4-D wind field, *evoTurb* is used, which calls *TurbSim* [75] to generate statistically independent 3-D turbulence fields and then composites 4-D turbulence with the exponential longitudinal coherence model discussed in Section 4.1.2. Only the coherence of the u component is considered. The other velocity components are assumed to be not correlated (not realistic but widely used in engineering design). Each turbulence field has a size of $4096 \times 11 \times 31 \times 31$ grid points, corresponding to the time and the x, y, and z directions. The lengths in the y and z directions are both 150 m.
For both types of 4-D turbulence field, hub-height mean wind speeds ranging from 12 to 24 ms^{-1} are considered. The positions in the x direction contain both the rotor plane position and the lidar range gate positions (see Table 5.3). Taylor's [2] frozen theory is applied within the probe volume, which has been shown to not influence the lidar measurement spectral properties [59]. For example, the lidar measurement gate at $x = 50$ m is calculated using the y-z plane wind field at $x = 50$ m, which is further shifted using Taylor's frozen theory to calculate the LOS speed distribution within the probe volume. The time length of each field is 2048 s which is close to a 30 min simulation. For each stability class and mean wind speed, 12 turbulence fields were generated with 12 different random seed numbers. Each simulation is executed for 30 min.

7.1.3 Turbine Configurations

For each turbulent wind field, the OpenFAST simulation is executed with the following configurations: (a) FB-only control using ROSCO, (b) FFFB control by activating LAC. Both controllers are discussed in Section 2.3.3. All the DOFs for a fixed-bottom turbine except for the yawing are activated. For each simulation result, the initial 50 s of the simulated time series containing the initialization are ignored.

7.2 Results and Discussions

This section presents and discusses the simulation results.

7.2.1 Time Series

Figure 7.1 takes one simulation using 4-D Mann turbulence with the neutral stability condition as an example to show the time series.
Panel (a) compares the REWS estimated using the lidar data processing algorithm with that estimated using the extended Kalman filter (EKF) [106] implemented in ROSCO. The lidar-estimated REWS was shifted according to the time buffer by the FFP module to ensure that it does not exhibit any time lag in the plot. The lidar-estimated REWS exhibits good agreement with that estimated using the EKF. Some additional fluctuations with higher frequencies appeared in the time series of the EKF-based REWS. This can be attributed to the EKF in ROSCO using only one DOF model containing the rotor rotational motion to predict the effective wind. Therefore, all the other structural motions affecting the rotor speed, such as the tower fore-aft motion, can be "mistakenly" estimated as wind speed.
Panel (b) shows that the rotor speed fluctuates significantly less using FFFB control compared with using FB-only control. Additionally, the peak values with FFFB control were less severe. The tower fore-aft bending moments are compared in panel (c), which shows that the tower bending moment (M_{yT}) generally fluctuates less through FFFB control. Furthermore, the blade root out-of-plane bending moment ($M_{\mathrm{y,root}}$) is shown in panel (d). We observe that the FFFB slightly reduces the fluctuation compared with the FB-only control. The low-speed shaft torques (M_{LSS}) are compared in panel (e), which clearly shows that the fluctuation with FFFB control is slightly lower than that with FB-only control.
Panel (f) depicts the pitch action between the two control strategies. The pitch angle in the FFFB control generally leads the one by the FB-only control in time, as expected. The pitch angle trajectory was overall similar between the FFFB and FB-only controls.
Finally, the generator power is shown in panel (g), where a much lower power fluctuation is observed in FFFB control. Because the power fluctuation is highly coupled with the rotor speed fluctuation, less fluctuating power can be expected from the lower rotor speed fluctuation in FFFB control.

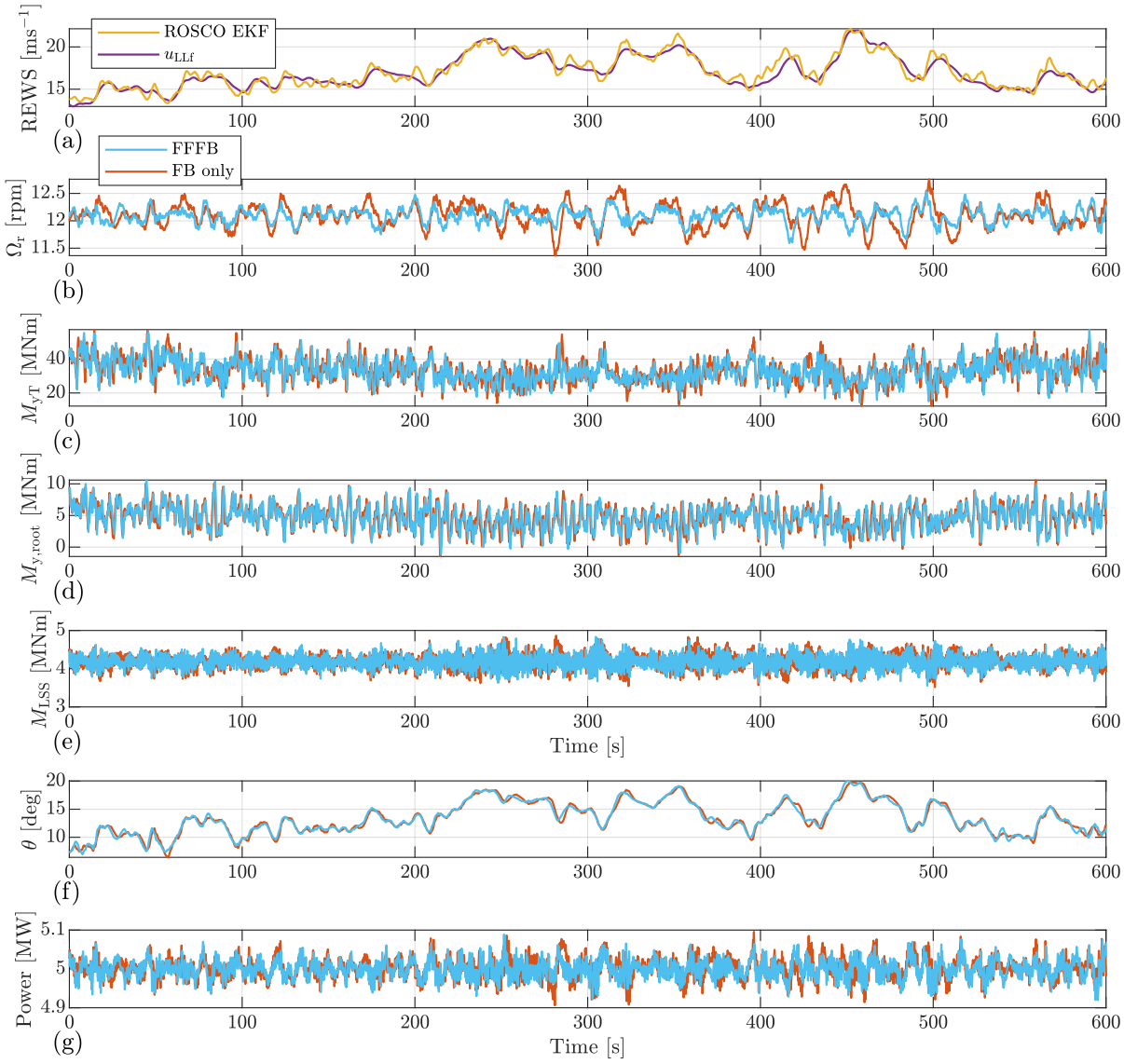

Figure 7.1: Time series collected from the OpenFAST simulation. A scenario with Mann model and neutral stability parameters is shown. Note that the same 3-D wind field (y, z, t) was applied to the rotor when performing simulations with the FFFB and FB-only controls, simulated with a mean wind speed of 16 ms^{-1}. EKF: extended Kalman filter. Source: [105].

7.2.2 Spectral Analysis

The spectra are estimated from the collected time series using Welch's method [80]. The spectra are averaged using different samples corresponding to the simulated results using different random seed numbers.

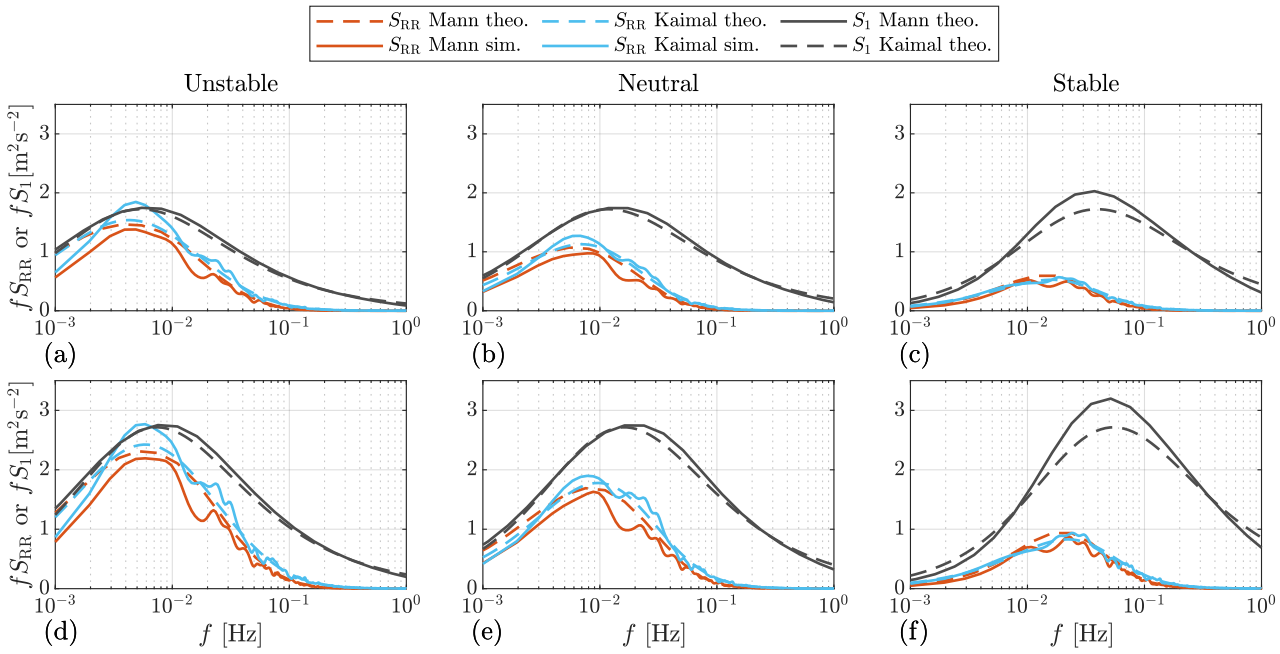

Figure 7.2: Auto-spectra of REWS. "theo.": theoretical spectra using the models discussed in Section 5.2.1, i.e., Equations (5.5) and (5.6). "sim.": spectra estimated from the time series of the turbulent wind fields in OpenFAST simulations using Welch's method [80]. (a) to (c): the results with a mean wind speed of 16 ms^{-1}. (d) to (f): the results with a mean wind speed of 22 ms^{-1}. Source: [105].

Before comparing the spectra of output variables from OpenFAST, the spectra of the REWS from the input turbulent wind fields are first compared in Figure 7.2. Here, the simulated REWS is calculated by averaging the u components within the rotor-swept area from the discrete turbulent wind field. Figure 7.2 shows that the simulated spectra follow the theoretical ones, which validate the turbulence simulation. Section 5.1 describes the fitting of the single-point u component spectrum using the two models. Additionally, the y-z plane coherence is fitted using a single separation. Here, the REWS spectra from two models exhibit a similar trend in different atmospheric stability classes. In the unstable scenario, the RWES spectrum does not decrease significantly compared with the single point u spectrum, and the spectrum peak appears at a lower frequency because the turbulence field has more large-scale coherent eddy structures (Figure 5.1). In the stable scenario, everything is opposite to the unstable scenario, where the REWS spectrum is much lower than the single-point u spectrum because of the low-level coherence and spatial filtering effect of the rotor. In addition, the neutral stability exhibits a medium spatial filtering effect, and the spectrum peak is between that of

unstable and stable conditions. By comparing the panels in Figure 7.2 vertically, where the only difference is the mean wind speed, we observe that a higher mean wind speed results in higher spectra, and the spectra are shifted to the right-hand high-frequency side. The shifting of the spectral peaks is caused by the fact that turbulence fields transport faster by a higher mean wind speed. For each stability class, the Kaimal model-derived REWS generally has a higher spectrum compared to that derived by the Mann model. This can be caused by the fact that the y-z plane coherence of the Mann model is more complicated than the exponential coherence model used in the Kaimal model. Fitting the coherence using one separation is insufficient to represent all possible separations.

Figures 7.3 and 7.4 compare the auto-spectra of some of the most interesting output variables using FB-only and FFFB controls. Figures 7.3 and 7.4 show the results using the Mann and Kaimal models, respectively.

Panels (a), (b), and (c) compare the rotor speed spectra of FFFB control and FB-only control under three stability classes. The FFFB control generally reduces the rotor speed spectrum in the frequency range of 0.01 to 0.1 Hz. Additionally, the spectra using the Mann and Kaimal models exhibit some differences, which can be summarized as higher spectra in the rotor motion with the Kaimal model than the Mann model. The observation here agrees with the trends in the REWS spectra (Figure 7.2). Generally, the spectra of the Mann and Kaimal models have similar shapes.

Comparisons of tower fore-aft bending moments are shown in panels (d), (e), and (f). In neutral and stable stability scenarios, the main benefit introduced by FFFB control is the decrement in the frequency range from 0.01 to 0.2 Hz, which is expected because the lidar-rotor transfer function reaches zero at 0.2 Hz. Below 0.01 Hz, the differences between FB-only and FFFB controls are small because the tower fore-aft mode is naturally and effectively damped in this frequency range.

Panels (g), (h), and (i) show the blade root out-of-plane moment of blade 1. The decrease in the blade root out-of-plane moment is not very clear in the plots because the spectrum is primarily composited by the excitation at 1p frequency.

The low-speed shaft torques are compared in panels (j), (k), and (l). The use of FFFB control offers some benefits in the frequency range of 0.01 to 0.1 Hz, which is similar to the reduction range of the rotor speed.

Overall, the relative reductions in the spectra from the use of LAC primarily lie in the frequency range in which the lidar-rotor transfer function is above zero. For very low-frequency ranges, the turbine motions are naturally damped; thus, no benefits are gained by adding the blade pitch feedforward signal. Based on the spectral analysis, we observe reductions primarily in rotor speed, part in the tower base fore-aft bending moment, and slightly in low-speed shaft torque. Additionally, the reductions are observed for both turbulence models in three different atmospheric stability classes.

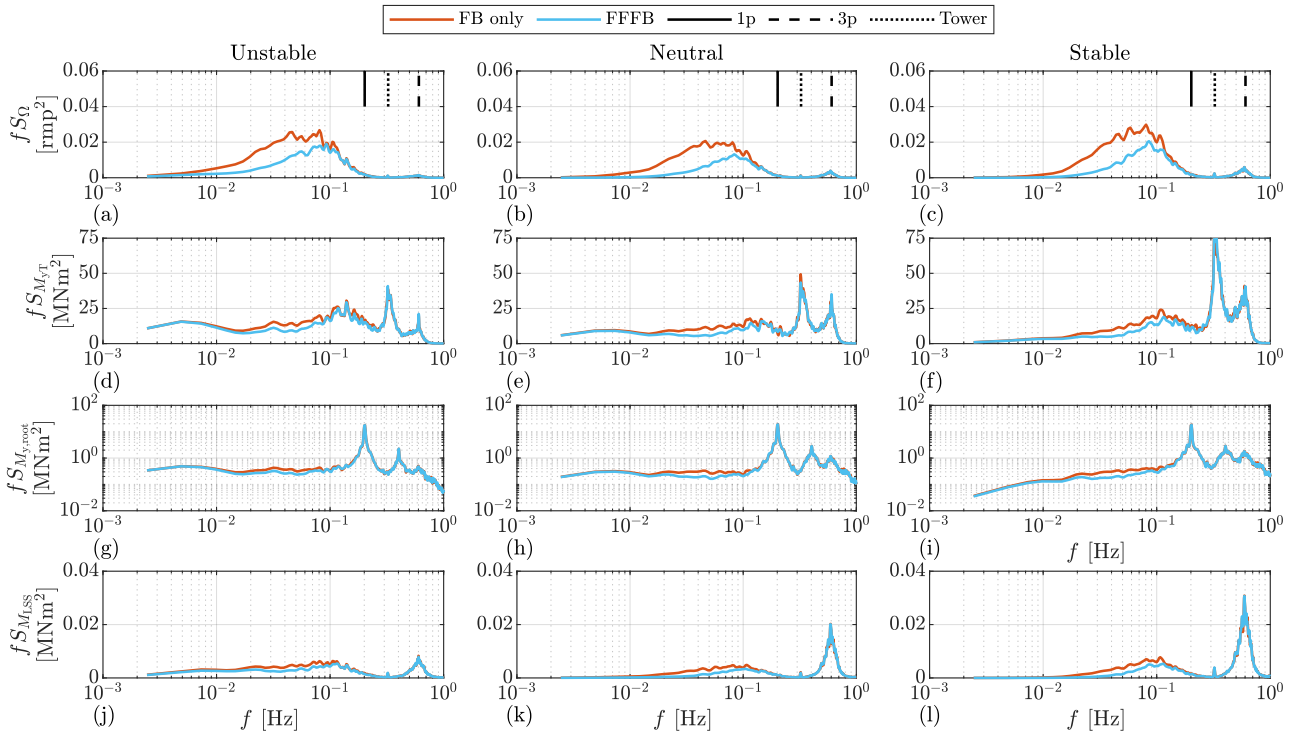

Figure 7.3: Spectra estimated from OpenFAST output time series, using the Mann model. The results with a mean wind speed of 16 ms^{-1} are shown. Note that the y axis of the blade root bending moment is set to a logarithmic scale for better readability. Source: [105].

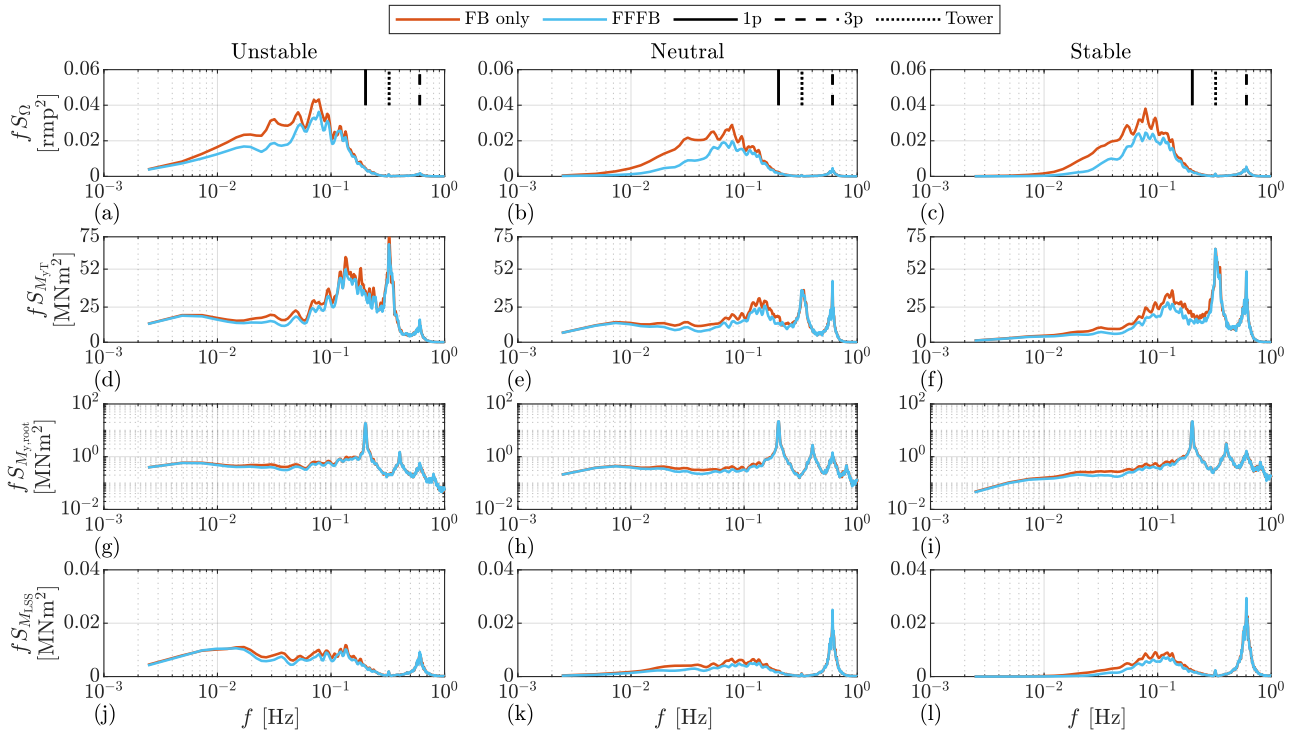

Figure 7.4: Spectra estimated from OpenFAST output time series, using the Kaimal model. The results with a mean wind speed of 16 ms^{-1} are shown. Note that the y axis of the blade root bending moment is set to a logarithmic scale for better readability. Source: [105].

7.2.3 Simulation Statistic

To further assess the benefits of LAC, we calculate the DEL using the rain flow counting method [107] with 2 $\times 10^6$ as a reference number of cycles and a lifetime of 20 years. A Wöhler exponent of 4 is used for the tower base fore-aft bending moment and the low-speed shaft torque. A Wöhler exponent of 10 is used for the blade root out-of-plane bending moment. The averaged DEL is calculated from the results with different random seed numbers for the turbulence fields. The overall statistics are shown in Figures 7.5 and 7.6. For rotor speed, pitch rate, and electrical power (P_{el}) signals, the standard deviation (STD) obtained by each simulation sample is calculated, and then the mean value is calculated from all samples. We use the standard deviation of pitch rate (rotational speed) to evaluate the impact of FFFB control on the pitch actuator because pitch rate causes damping torque in the pitch gear and is related to the friction torque of the pitch bearing [108, 109]. The STD of pitch rate was also used by other studies, e.g., references [110] and [111], to evaluate the damage to the pitch actuator, .

Mann Model-based Results

Figure 7.5 compares the DEL, STD, and energy production (EP) results using the Mann model. The difference between FB-only and FFFB controls is plotted by the gray lines. Here the difference is indicated using the relative reduction defined in the figure caption. Overall, the difference between FB-only and FFFB controls becomes apparent when the mean wind speed is higher than 16 ms^{-1}.

Significant overall reductions in the tower base fore-aft bending moment DEL are observed in all the investigated atmospheric stability classes. The largest reduction is 16.7% at a mean wind speed of 22 ms^{-1} and under an unstable atmosphere. In the unstable scenario, before a mean wind speed of 22 ms^{-1}, it can be seen that the reduction is clearer at higher wind speeds. In contrast, the reduction is larger at 16 ms^{-1} and 18 ms^{-1} under the stable scenario (about 7.5 to 8.8%). For the neutral scenario, the benefit is the greatest at 18 ms^{-1} (13.4%). However, with mean wind speeds below 14 ms^{-1} and in the unstable and neutral scenarios, the FFFB benefits become marginal. This can be caused by the fact that there are higher possibilities for the REWS to pass the wind speed range (below 14 ms^{-1}) where the pitch feedforward control is inactivated. The intention to deactivate feedforward pitch control is to avoid the thrust force being changed significantly close to the rated wind speed, as discussed in Section 2.3.3.

For the low-speed shaft torque, the DEL decreases by approximately 4.0% under the unstable scenario and at a higher wind speed (above 18 ms^{-1}). In comparison, the reductions under neutral and stable scenarios are approximately 1.5 to 3.3% and 1.4 to 2.3%, respectively.

The DEL of the blade root out-of-plane bending moment is reduced by introducing LAC. More benefits (approximately 2.7 to 6.0%) are observed under the unstable stability class. In the

neutral stability, the reduction is better at 20 ms^{-1}, reaching 4.3%, and it drops to 2.5% at higher wind speeds. As for the stable atmosphere, the reduction is more observable (around 3.0%) at wind speeds ranging from 16 ms^{-1} to 20 ms^{-1}.

The STD of the rotor speed is observed to decrease significantly under FFFB control. The reductions are more than 20% and up to 40%. Additionally, it can be seen that the reductions are more significant under higher mean wind speeds, which is similar in all three atmosphere stability classes.

The introduction of the FF pitch also generally reduces the pitch rate $\dot{\theta}$. The STD of pitch rate decreases approximately by 2.0 to 6.1% from 14 to 20 ms^{-1} under the three stability scenarios. The reduction stops at the mean wind speed of 24 ms^{-1} for unstable and neutral scenarios. In a stable atmosphere, with a mean wind speed higher or equal to 22 ms^{-1}, the FFFB control has a higher STD of pitch rate than the FB-only control.

Through the use of FFFB control, the electrical power STD is obviously reduced by about 16.0% in unstable case for wind speeds above 18 ms^{-1}, by about 17.0% in neutral scenario for wind speeds above 16 ms^{-1}, and by 13.0% in stable scenario for wind speeds above 14 ms^{-1}.

In all stability scenarios and mean wind speeds, the electricity production is similar whether LAC is used or not, as indicated by the small numbers of relative reduction.

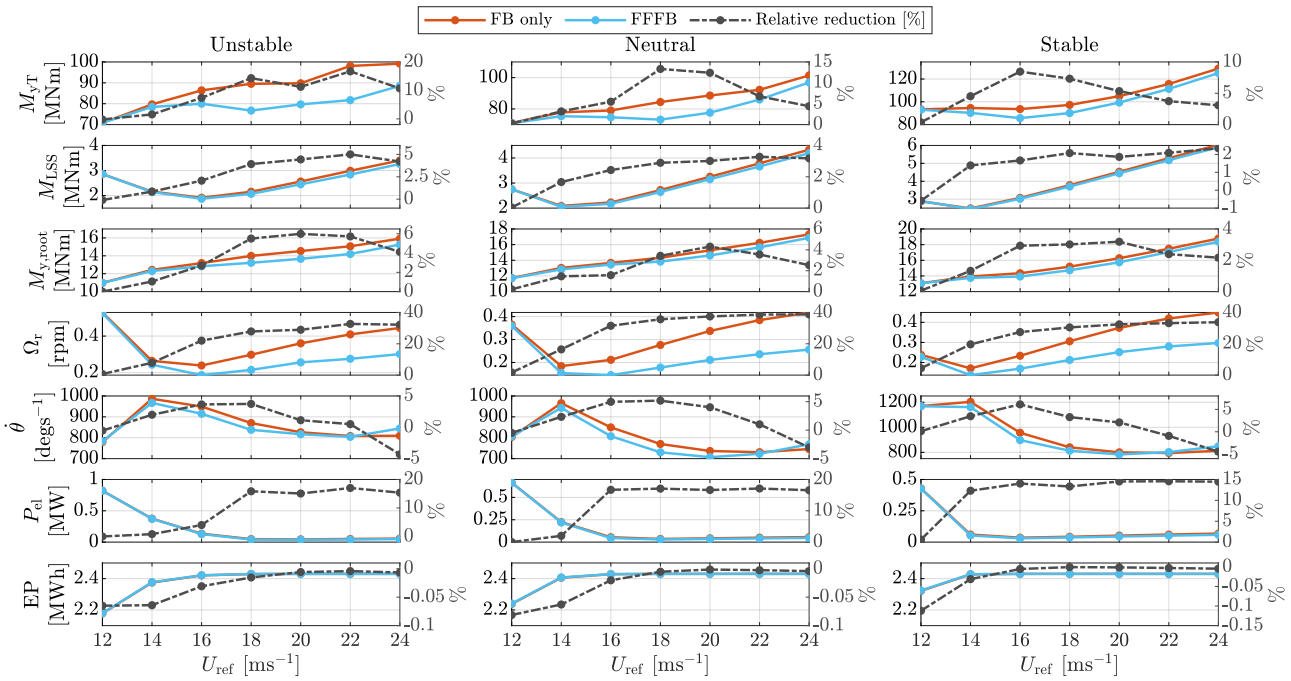

Figure 7.5: Comparisons of DEL (M_{yT}, M_{LSS}, $M_{y,root}$), STD (Ω_r, $\dot{\theta}$, P_{el}), and EP, simulated using the Mann model. Note that the value of the relative reduction are reflected on the right right-hand side of the y axis. Relative reduction: the results using FB-only are extracted by the results using FFFB and then divided by the results of FB-only. Source: [105].

Kaimal Model-based Results

The results using the Kaimal model are shown in Figure 7.6. Generally, under different stability classes and mean wind speeds, the statistics exhibit a similar trend as the results obtained using the Mann model. However, the values have some differences.

In terms of tower base fore-aft bending moment, the DEL decreases by approximately 10.4% to 13.4% with a mean wind speed of 18 to 22 ms^{-1} under the unstable and neutral scenarios. In the stable scenario, the reduction is close to 11.5% with a mean wind speed of 16 ms^{-1} and it decreases with higher mean wind speeds.

The results of low-speed shaft DEL show similar trends to those of the Mann model. On average, for wind speeds above 16 ms^{-1}, the shaft load is reduced by around 2.3%, 1.9%, and 1.7%, under unstable, neutral, and stable stability classes, respectively.

Generally, the reduction in the blade root DEL simulated using the Kaimal model is similar to that based on the Mann model. On average, the blade root DEL decreases by approximately 4.1%, 3.0%, and 3.0%, under the three investigated stability classes, respectively.

The STD of rotor speed is observed to decrease significantly under FFFB control. The reductions are more than 15% and are up to 30%. The trend is similar to the Mann model-based result, but the decrement is lower.

The pitch actions are also observed to decrease when using FFFB control. At mean wind speeds from 16 ms^{-1} to 20 ms^{-1}, the reductions in pitch rate STD are about 3.0% to 3.5% under unstable and neutral stability classes, respectively, and they become less at other mean wind speeds. For the stable case, the reduction is higher at 16 ms^{-1}, reaching 6.2%, but decreases rapidly as the mean wind speed increases. For very high mean wind speeds above 22 ms^{-1}, the pitch rate STD is increased using LAC.

Because the variation in electrical power is highly linked to the rotor speed, the reductions in the STD of power are approximately 10.0%, 13.0%, and 11.0%, under the three investigated stability classes, respectively. These values are smaller than those observed using the Mann model.

Again, the electricity productions are similar, whether LAC was used or not, in all stability scenarios and mean wind speeds.

Generally, for the NREL 5.0 MW turbine, the benefits of LAC in load reduction by a four-beam lidar are clear. However, we also demonstrate that some uncertainties and differences occur when assessing LAC using different IEC turbulence models. Among the compared turbine loads, LAC has the most significant load reduction effect in the tower base fore-aft bending moment. Considerable reductions in speed and power variations also occur. Slight reductions are observed for the blade and shaft loads. In addition, the reductions in blade pitch rate are observed in most of the mean wind speed ranges, which have the potential to alleviate damage to the pitch bearings and gears. The generation of electrical power is not affected by

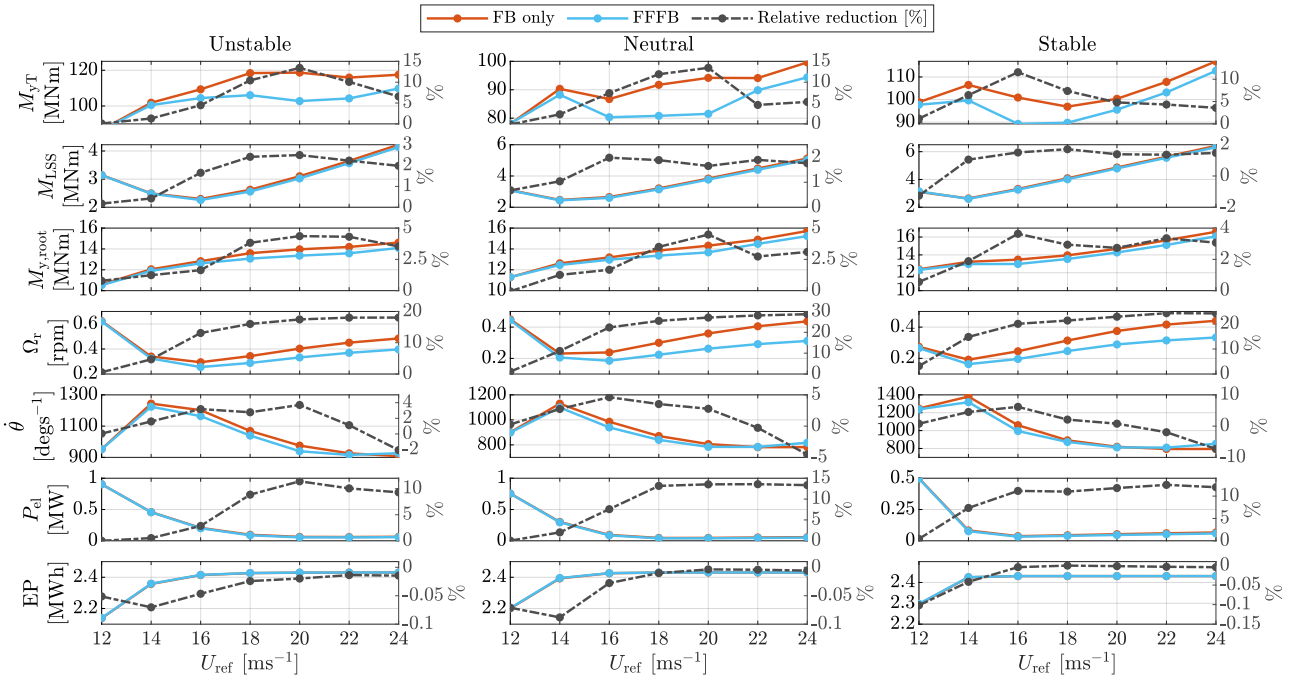

Figure 7.6: Comparisons of DEL (M_{yT}, M_{LSS}, $M_{y,root}$), STD (Ω_r, $\dot{\theta}$, P_{el}), and EP, simulated using the Kaimal model. Note that the value of the relative reduction are reflected by the right-hand side of the y axis. Relative reduction: the results using FB-only are extracted by the results using FFFB and then divided by the results of FB-only. Source: [105].

introducing LAC.

The load reductions also exhibit differences under different turbulence parameters, represented by different atmosphere stability classes. For different stability conditions but the same mean wind speed, we observe that the LAC benefits for the load reductions are overall highest in unstable stability, medium in neutral stability, and lowest in stable stability. The reason could be the differences in turbulence length scales. The turbulence length scale is lower under the stable scenario, which means that the peak of the turbulence spectrum appears at a higher wavenumber/frequency (based on the conversion $f = k_1 U_{ref}/2\pi$, as shown by Figure 7.2). The turbine's structural loads are mainly excited by frequencies above 0.1 Hz, e.g., the tower natural frequency, the shaft natural frequency (above 1.0 Hz), the 1p frequency, and the 3p frequency. If the turbulence spectrum has a higher peak frequency, the loads will be more dominated by the higher frequency parts due to the higher excitation of the turbine's natural vibration modes. Then, the LAC benefits become less significant because LAC mainly reduces the loads below 0.1 Hz (for the lidar and turbine we used). When different mean wind speeds are considered, a higher mean wind speed shifts the spectral peak-frequency to a higher value (see Figure 7.2)); thus, the LAC benefits become less. For the stable condition, the spectral peak frequency is naturally high due to the smaller turbulence length scale, so that the LAC benefits are more sensitive to changes in the mean wind speed. For unstable and neutral cases, the spectral peak frequency is naturally lower than that in the stable condition, thus the LAC benefits do not

decrease as fast as those in the stable scenario.

7.3 Chapter Summary and Outlook

This chapter evaluates lidar-assisted wind turbine control under various turbulence characteristics using a four-beam lidar and the NREL 5.0 MW reference turbine.
The benefits of LAC are evaluated using both the Mann model and Kaimal model-based 4D turbulence. Simulations are performed for the mean wind speed level from 12 to 24 ms^{-1}. The results simulated using the Mann model-based turbulence indicate that using LAC significantly reduces the variations in rotor speed and electrical power. Among the three investigated stability classes and above the mean wind speed of 16 ms^{-1}, the load reductions for the tower base fore-aft bending moment, blade root out-of-plane bending moment, and low-speed shaft torque are observed to be approximately 3.0% to 16.7%, 1.5% to 6.0%, and 1.7% to 5.0%, respectively. The greatest potential of LAC in load reduction is observed in the tower base fore-aft bending load, and the benefits were observed to vary by turbulence spectral properties and mean wind speeds. The results simulated using the Kaimal model-based turbulence also indicate that LAC clearly reduces the variation in rotor speed and electrical power. The load reduction of the tower base fore-aft bending moment is observed in all stability classes for wind speeds above 16 ms^{-1}, and it varies from 3.6% to 13.4%. The load reduction for the blade root out-of-plane bending moment is between 1.6% and 4.5%, and for the low-speed shaft torque, it is between 1.6% and 2.5%. In addition, with the use of LAC, for both turbulence models, the standard deviation of pitch rate is observed to be reduced (up to 6%,) for most of the mean wind speed ranges (below 20 ms^{-1}) and for all stability classes. The pitch rate STD reduction can bring potential load alleviation for the pitch bearing and gear. Overall, we observe that the LAC benefits with the Kaimal model are slightly different from the results using the Mann model. The LAC benefits simulated using the Kaimal model are generally less than those simulated using the Mann model.
Overall, this chapter shows that the mean wind speed, turbulence spectrum, coherence, and the used turbulence models all have certain impacts on the results of evaluating LAC. In the future, it is recommended to assess the benefits of lidar-assisted control depending on site-specific turbulence characteristics and statistics. Additionally, the uncertainties of using different turbulence models should be considered when performing fatigue load analysis using aeroelastic simulations. Furthermore, some improvements can be made to the lidar-assisted pitch feedforward control. The activation algorithm of the feedforward pitch in the transition range between the below-rated and above-rated operations should be further improved. The weighting of feedforward and feedback is considered to be both 50%. The different weightings can be considered, which might improve the overall LAC benefits [23].

8

Conclusions and Recommendations

This final chapter first concludes the research outcomes of this Ph.D. project in Section 8.1 and discusses recommendations for further research in Section 8.2. Finally, the main contributions of this project are listed in Section 8.3.

8.1 Conclusions

In this thesis, the main focus has been on (a) studying the turbulence evolution phenomenon, (b) investigating lidar wind preview for turbine control under various external conditions, and (c) evaluating lidar-assisted pitch feedforward control under various turbulence characteristics. The following are the conclusions for these three objectives.

8.1.1 Turbulence Evolution Phenomenon

First, the turbulence evolution phenomenon is studied using an empirical exponential longitudinal coherence model. Through a validation using a pulsed lidar measurement, we observed that the exponential longitudinal coherence model can accurately predict the actual longitudinal coherence for a single separation distance. Some discrepancies appear when one coherence decay parameter is used for multiple separations in the longitudinal direction.
Second, the eddy lifetime approach is applied to the Mann spectral tensor to develop a space-time tensor, which can reflect the spatial and temporal coherence for all the velocity components. The performance of the space-time tensor is evaluated using lidar measurements. We observed that the space-time tensor predicts the longitudinal coherence of multiple separations

better than the exponential longitudinal coherence model.
The exponential longitudinal coherence is included in the Kaimal model to describe the four-dimensional turbulence field. An assumption that coherence with longitudinal, lateral, and vertical separations is obtained from the product of longitudinal, lateral, and vertical coherences is made. This assumption is called the "direct product," which has both advantages and disadvantages. The positive aspect is that it allows using a two-step Cholesky method to efficiently generate the Kaimal model-based four-dimensional turbulence field. In contrast, the negative aspect is that it tends to underestimate the overall coherence and lidar wind preview quality. In particular, when optimizing the lidar measurement trajectory for better lidar wind preview quality, the optimization results are sensitive to the used coherence decay parameter.
Based on the space-time tensor, a method of generating a four-dimensional Mann turbulence field is proposed. This method assumes a stationary process, meaning that three-dimensional turbulence fields at different times have the same statistical prosperity governed by the three-dimensional Mann spectral tensor.
The performance of both the extended Mann and Kaimal models in predicting the spectral properties of the measurements are evaluated through site measurement. The two models can reflect the actual auto-spectra of lidar measurements and the coherence between spatially distributed lidar measurements. Overall, the extended Mann model (space-time tensor) exhibits better agreement with the data.
The turbulence evolution parameters under different atmospheric stability conditions are also summarized in this thesis. The longitudinal coherence decreases most significantly in the unstable atmosphere and least in the stable atmosphere. The longitudinal coherence in the stable atmosphere also appears with an apparent intercept, meaning that the coherence does not tend to 1 when the frequency is very small.

8.1.2 Lidar Wind Preview for Turbine Control

Using the extended Mann and Kaimal models, the lidar wind preview study is mathematically derived and presented. Analysis shows that the control-oriented lidar wind preview quality primarily depends on the lidar trajectory, turbulence spectra and coherence, and turbine rotor size. These analytical models provide solutions to the coherence between the lidar- and turbine-based rotor effective wind speed and optimal filter transfer function.
Based on a typical four-beam pulsed lidar and medium-sized NREL 5.0 MW wind turbine, the lidar beam trajectory is optimized to obtain a better lidar-rotor correlation for control. The optimizations are performed using both the extended Mann and Kaimal models. The results using the Kaimal model are observed to be sensitive to the turbulence evolution parameters because of the "direct product" assumption for combined coherence.
The sensitivity of lidar wind preview with respect to the atmosphere stability condition is

investigated. The turbulence parameters representative of unstable, neutral, and stable atmospheres are selected for the analysis. The resulting lidar-rotor coherence and optimal transfer functions are observed to be nonsensitive to the three atmospheric stability conditions. This indicates that the filter design of the lidar-assisted controller is not necessary to be adaptive to the atmospheric conditions. The models indicate that lidar preview is more coherent with the rotor-experienced effective wind speed when the mean wind speed increases. A higher cutoff frequency of the filter can be used in scenarios with higher mean wind speeds.
The impact of upstream turbine wakes on the lidar preview quality of a downstream turbine is investigated using the engineering model: dynamic wake meandering. The wake adds additional coherent fluctuations in both the lidar- and turbine-based rotor effective wind speeds. The upstream wake is observed to have a negligible impact on the lidar wind preview quality of a downstream turbine under neutral and stable atmospheric conditions. In contrast, downstream lidar preview quality increases in an unstable atmosphere because of the additional coherent fluctuations caused by wake meandering.
A realistic lidar simulation module is updated in the aeroelastic code OpenFAST. The updated lidar module can simulate the turbulence evolution, the blade blockage, and the adjustable lidar measurement availability. Statistical spectral analysis for lidar carrier-to-noise ratio values is conducted using actual lidar measurements. Based on the statistical spectral analysis using lidar data, we can conclude that the low lidar data availability event with a low mean carrier-to-noise ratio can be simulated using a white noise spectrum. The lidar-rotor coherence and optimal transfer function are analyzed using the updated lidar simulator. For the four-beam pulsed lidar and NREL 5.0 MW wind turbine, it is observed that the frozen turbulence only slightly overestimates the lidar wind preview quality. The effect of blade blockage and low data availability on the quality of the lidar wind preview is also quite small.

8.1.3 Evaluating of Lidar-assisted Pitch Feedforward Control

The benefits of lidar-assisted control are evaluated using both the Mann model and Kaimal model-based 4D turbulence fields. The open-source aeroelastic tool OpenFAST integrated with the updated lidar simulation module is used for the evaluations. The simulations are performed for the mean wind speed level from 12 to 24 ms^{-1}, using the NREL 5.0 MW reference wind turbine and a four-beam lidar system. For both turbulence models, the use of lidar-assisted control clearly reduces the variations in rotor speed and electrical power, and obviously alleviates the damage equivalent load of the tower fore-aft bending moment. By introducing pitch feedforward control, the reductions in pitch rate standard deviation are observed in most of the mean wind speed ranges, which can potentially reduce the damage to the pitch bearing and gear of the pitch actuator. Furthermore, lidar-assisted control results in slight reductions in the blade root out-of-plane bending and low-speed shaft torsional loads.

Overall, the unstable atmosphere has a much wider range of mean wind speeds, where the fore-aft bending load reduction is significant for the tower base. This range is smaller in the neutral condition and smallest in the stable condition. In terms of the results of different turbulence models, we observe that the lidar-assisted control benefits with the Kaimal model are slightly less than the results using the Mann model.

8.2 Recommendations

This section provides recommendations for future research based on the outcomes of this Ph.D. project.

8.2.1 Observing Turbulence Spectral Characteristics using Lidar

In Chapter 4, the spectral properties of lidar measurements are derived and used to validate the extended Mann and Kaimal models. Similar validation studies can be performed on other sites, particularly for sites with frequently unstable atmosphere. The model evaluation shows that both the Mann and Kaimal models tend to overestimate the coherence when the separation distance surpasses the turbulence length scale. With the current trend in which the turbine rotor is designed to be larger, the turbulence models may not provide a good representation of the coherence between blade sections with a large spatial separation. In the future, lidar measurements can be used to further analyze the turbulence coherence across a large turbine rotor. Additionally, if the coherence is over-predicted by the models, the impact of this incorrect coherence on the turbine loads should be further studied, preferably through field testing. If the incorrect coherence has a significant impact on the turbine loads, the nacelle lidar measurement can be further used to improve the turbulence coherence model.
The study on the coherence of lidar measurements can be further extended to obtain the coherence between the lidar measurement and velocity components. This can be further used for constraint turbulence simulation for fatigue or extreme load validation [70, 33]. For example, one can observe the coherence between lidar line-of-sight speed measurements and sonic velocity measurements.

8.2.2 Lidar Wind Preview Quality Investigations

The wind preview quality under freestream turbulence is analyzed using turbulence spectral models representing the three investigated atmosphere stability classes. We observe that the lidar wind preview is not very sensitive to atmospheric conditions. In the future, this conclusion can be further verified, preferably through field testing.
The analysis of wind preview quality under wake conditions can be improved by running higher-fidelity turbulence modeling approaches such as large eddy simulation or through field testing. In addition, the wake velocity has an overall lower mean wind speed than the ambient mean wind speed, and the wake velocity recovers from upstream to downstream. The recovering process means that the flow accelerates, which can potentially impact the temporal difference between the lidar-estimated and the rotor-experienced effective wind speeds. The impact of the induction zone, which causes a lower wind speed region in front of the turbine, is not addressed in this thesis. Therefore, further research can emphasize studying the impact of wake recovery and the induction zone.
The statistical analysis of the lidar carrier-to-noise ratio signals is performed using the lidar measurements conducted on the ground. In the future, the analysis can be further performed for a nacelle-mounted lidar. During the measurement campaign that lasted for two months, no extreme abnormal weather, such as snowing, frog, and heavy rain, occurred. The carrier-to-noise ratio or lidar measurement availability during such extreme weather conditions can also be further investigated.
Furthermore, an interesting aspect to investigate would be the preview quality for other lidar and turbine configurations using a realistic lidar simulation environment. For example, the lidar preview quality can be assessed for turbines with larger rotors and smaller rated rotational speeds and for lidars with more dense trajectories, e.g., scanning lidars.

8.2.3 Design and Evaluation of Lidar-assisted Control

This thesis shows that the mean wind speed, the turbulence spectrum, coherence, and the used turbulence models all have certain impacts on the results of evaluating lidar-assisted control. In the future, we recommend assessing the benefits of lidar-assisted control depending on site-specific turbulence characteristics and statistics. In addition, the uncertainty of the turbulence model should be considered when using aeroelastic simulations for load analysis, as we observed some differences in the results using the Mann and Kaimal models. In the current evaluations, the turbine yaw misalignment that appears during operation is not considered; this could be considered in future research.
Moreover, lidar-assisted pitch feedforward control can be improved further. The activation algorithm of the feedforward pitch in the transition range between the below-rated and above-

rated operations could be further improved. The weighting of feedforward and feedback is considered to be both 50%. The different weightings can be considered, which might improve the overall lidar-assisted benefits [23].

8.3 Main Contributions

This thesis contributes by improving wind preview modeling of lidar systems and evaluating lidar-assisted wind turbine control using the improved lidar preview modeling. The detailed contributions are listed below:

(a) The incorporation of the turbulence evolution phenomenon into the two turbulence models provided by the IEC 61400-1 standard [12]. For the Kaimal model, the longitudinal coherence is incorporated to have a four-dimensional description of the turbulence field. An efficient algorithm is proposed to generate four-dimensional turbulence based on the Kaimal model. For the Mann model, a space-time tensor is developed, which describes the turbulence evolution through an eddy lifetime concept. For both four-dimensional turbulence models, open-source turbulence generation methods are developed, which enable the simulation of turbulence evolution in aeroelastic simulations. In addition, the spectral properties of lidar measurements are derived, based on which both models are evaluated using actual lidar measurements.

(b) The development of a lidar preview quality model using four-dimensional turbulence models. The preview quality model provides an analytical solution for the control-oriented filter design for collective pitch feedforward control. This thesis also investigates the lidar preview quality under various turbulence characteristics and wake conditions.

(c) Updates on a realistic lidar simulation module in the open-source aeroelastic simulation tool OpenFAST, which considers the turbulence evolution, blade blockage, and adjustable lidar measurement availability. This thesis presents the statistical properties of the lidar carrier-to-noise ratio signal and presents methods to generate lidar carrier-to-noise ratio time series.

(d) Assessing the benefits of lidar-assisted collective pitch feedforward control through aeroelastic simulations considering different turbulence characteristics. These turbulence characteristics are representative of different atmospheric stability classes.

A

Appendix

A.1 Derivation of Veers Method for Turbulence Generation

Consider simulating n stochastic time-domain u component fluctuations in the y-z plane, the Fourier coefficients at one specific frequency are calculated using the matrix multiplications as

$$\hat{\boldsymbol{u}}_{yz} = \boldsymbol{A}_u \boldsymbol{H}_{u,yz} \boldsymbol{X}_{u,yz}, \tag{A.1}$$

where

$$\boldsymbol{A}_u = \begin{bmatrix} A_{u,1} & & & 0 \\ & A_{u,2} & & \\ & & \ddots & \\ 0 & & & A_{u,n} \end{bmatrix} \tag{A.2}$$

is a diagonal matrix with diagonal elements $A_{u,i}$. For simplicity, the independent variable frequency f is ignored in the following derivations. To have a better understanding of Equation A.1, the products of the Fourier coefficients are calculated by

$$\hat{\boldsymbol{u}}_{yz}\hat{\boldsymbol{u}}_{yz}^{*} = \begin{bmatrix} \hat{u}_{yz,1} \\ \hat{u}_{yz,2} \\ \vdots \\ \hat{u}_{yz,n} \end{bmatrix} \begin{bmatrix} \hat{u}_{yz,1} \\ \hat{u}_{yz,2} \\ \vdots \\ \hat{u}_{yz,n} \end{bmatrix}^{*} = \begin{bmatrix} u_{yz,1}u_{yz,1}^{*} & u_{yz,1}u_{yz,2}^{*} & \dots & u_{yz,1}u_{yz,n}^{*} \\ u_{yz,2}u_{yz,1}^{*} & u_{yz,2}u_{yz,2}^{*} & & \vdots \\ \vdots & & \ddots & \\ u_{yz,n}u_{yz,1}^{*} & \dots & & u_{yz,n}u_{yz,n}^{*} \end{bmatrix}, \tag{A.3}$$

where * denotes the complex conjugate or conjugate transpose (if applied to a matrix). On the right side of Equation A.1, we have

$$\hat{\boldsymbol{u}}_{yz}\hat{\boldsymbol{u}}_{yz}^{*} = \boldsymbol{A}_u\boldsymbol{H}_{u,yz}\boldsymbol{X}_{u,yz}\left(\boldsymbol{A}_u\boldsymbol{H}_{u,yz}\boldsymbol{X}_{u,yz}\right)^{*}. \tag{A.4}$$

Applying the ensemble average to both sides of Equation A.4 results in

$$\langle\hat{\boldsymbol{u}}_{yz}\hat{\boldsymbol{u}}_{yz}^{*}\rangle = \boldsymbol{A}_u\boldsymbol{H}_{u,yz}\langle\boldsymbol{X}_{u,yz}\boldsymbol{X}_{u,yz}^{*}\rangle\boldsymbol{H}_{u,yz}^{*}\boldsymbol{A}_u^{*} = \boldsymbol{A}_u\boldsymbol{C}_{u,yz}\boldsymbol{A}_u, \tag{A.5}$$

because the ensemble average $\langle\boldsymbol{X}_{u,yz}\boldsymbol{X}_{u,yz}^{*}\rangle$ is an identity matrix and $\boldsymbol{C}_{u,yz} = \boldsymbol{H}_{u,yz}\boldsymbol{H}_{u,yz}^{*}$ by definition (the conjugate transpose is equivalent to transpose if the matrix elements are real numbers). The right hand side of Equation A.5 is further expanded as

$$\langle\hat{\boldsymbol{u}}_{yz}\hat{\boldsymbol{u}}_{yz}^{*}\rangle = \begin{bmatrix} A_{u,1}A_{u,1}\gamma_{u,yz,11} & A_{u,1}A_{u,2}\gamma_{u,yz,12} & \dots & A_{u,1}A_{u,n}\gamma_{u,yz,1n} \\ A_{u,2}A_{u,1}\gamma_{u,yz,21} & A_{u,2}A_{u,2}\gamma_{u,yz,22} & & \vdots \\ \vdots & & \ddots & \\ A_{u,n}A_{u,1}\gamma_{u,yz,n1} & \dots & & A_{u,n}A_{u,n}\gamma_{u,yz,nn} \end{bmatrix}, \tag{A.6}$$

which can be simplified using the index notation as

$$\langle u_{yz,i}u_{yz,j}^{*}\rangle = A_{u,i}A_{u,j}\gamma_{u,yz,ij} = \frac{\Delta f}{2}\sqrt{S_{u,i}S_{u,j}\gamma_{u,yz,ij}^{2}}. \tag{A.7}$$

Because of the definition of co-coherence, we can further write

$$\langle u_{yz,i}u_{yz,j}^{*}\rangle = \frac{\Delta f}{2}S_{u,ij}, \tag{A.8}$$

where $S_{u,ij}$ is the co-spectrum between fluctuations i and j. The derivations above show that Equation A.1 can be applied to simulate stochastic processes that have certain ensemble averaged auto-spectra and co-spectra.

A.2 Derivation of the Mann Uniform Shear Model

The derivation of Mann uniform shear model was conducted by [32]. I would like to provide a derivation that covers some steps that have been skipped in existing literature. The derivation is primarily based on [32] and [82].

The turbulent velocity field may be expressed as

$$\tilde{\boldsymbol{u}} = \boldsymbol{U} + \boldsymbol{u}, \tag{A.9}$$

where $\boldsymbol{U}$ is the mean flow, and $\boldsymbol{u}$ is the fluctuation part. The mean flow $\boldsymbol{U} = (U, 0, 0)$ is non-zero only in the longitudinal direction. Moreover, only the uniform vertical shear profile $\partial U/\partial z$ is non-zero. Ignoring external force, e.g., gravity and Coriolis force, and assuming the atmosphere in turbine related height is incompressible, the N-S equation can then be expressed as

$$\frac{\partial \tilde{u}_i}{\partial t} + \tilde{u}_j \frac{\partial \tilde{u}_i}{\partial x_j} = -\frac{1}{\rho}\frac{\partial p}{\partial x_i} + \nu \frac{\partial^2 \tilde{u}_i}{\partial x_j \partial x_j} \quad \text{(ESC)}. \tag{A.10}$$

Inserting Equation A.9 this into Equation A.10 yields

$$\frac{\partial u_i}{\partial t} + U_j \frac{\partial U_i}{\partial x_j} + U_j \frac{\partial u_i}{\partial x_j} + u_j \frac{\partial U_i}{\partial x_j} + u_j \frac{\partial u_i}{\partial x_j} = -\frac{1}{\rho}\frac{\partial p}{\partial x_i} + \nu \frac{\partial^2 \tilde{u}_i}{\partial x_j \partial x_j} \quad \text{(ESC)}. \tag{A.11}$$

Because only $\mathrm{d}U/\mathrm{d}z$ and only U are non-zero, the terms $U_j \frac{\partial U_i}{\partial x_j}$ are always zero. Neglecting the non-linear term $u_j \frac{\partial u_i}{\partial x_j}$ on the left-hand side and the viscosity related term on the right-hand side (second term) [32], the equations are simplified to be

$$\frac{\partial u_i}{\partial t} + U_j \frac{\partial u_i}{\partial x_j} + u_j \frac{\partial U_i}{\partial x_j} = -\frac{1}{\rho}\frac{\partial p}{\partial x_i} \quad \text{(ESC)}. \tag{A.12}$$

As explained by Mann [32], we are more interested in a larger scale of the turbulence for turbine structure load analysis, whereas the viscosity is primarily responsible for smaller scale turbulent dissipation. To represent the pressure terms by velocities, taking the divergence on both side of Equation A.12 and ignoring non-linear terms, we obtain

$$\frac{\partial U_j}{\partial x_i}\frac{\partial u_i}{\partial x_j} + \frac{\partial u_j}{\partial x_i}\frac{\partial U_i}{\partial x_j} = -\frac{1}{\rho}\frac{\partial^2 p}{\partial x_i \partial x_i} \quad \text{(ESC)}, \tag{A.13}$$

which is rearranged as

$$2\frac{\partial u_j}{\partial x_i}\frac{\partial U_i}{\partial x_j} = 2\frac{\partial u_i}{\partial x_j}\frac{\partial U_j}{\partial x_i} = -\frac{1}{\rho}\frac{\partial^2 p}{\partial x_i \partial x_i} \quad \text{(ESC)}. \tag{A.14}$$

The pressure field velocity fields may be expressed as the Fourier-Stieltjes integrals [32, 30]:

$$p(\boldsymbol{x}) = \int \mathrm{e}^{\mathrm{i}\boldsymbol{k}\cdot\boldsymbol{x}} \mathrm{d}\Pi(\boldsymbol{k}) \tag{A.15}$$

$$\boldsymbol{u}(\boldsymbol{x}, t) = \int \mathrm{e}^{\mathrm{i}\boldsymbol{k}\cdot\boldsymbol{x}} \mathrm{d}\boldsymbol{Z}(\boldsymbol{k}, t) \tag{A.16}$$

Applying the Laplacian operator on both side of Equation A.15, we obtain

$$\nabla^2 p = -k^2 \int \mathrm{e}^{\mathrm{i}\boldsymbol{k}\cdot\boldsymbol{x}} \mathrm{d}\Pi(\boldsymbol{k}) = -k^2 p. \tag{A.17}$$

Replacing the pressure related term on the right-hand side of Equation A.14 by Equation A.17 and replacing the velocity field by the Fourier-Stieltjes integrals, we now obtain

$$2\int \mathrm{i}k_j \mathrm{e}^{\mathrm{i}\boldsymbol{k}\cdot\boldsymbol{x}}\mathrm{d}Z_i(\boldsymbol{k},t)\frac{\partial U_j}{\partial x_i} = \frac{1}{\rho}k^2 p \quad \text{(ESC)}, \tag{A.18}$$

whose gradient is

$$2\int \frac{k_l k_j}{k^2}\mathrm{e}^{\mathrm{i}\boldsymbol{k}\cdot\boldsymbol{x}}\mathrm{d}Z_i(\boldsymbol{k},t)\frac{\partial U_j}{\partial x_i} = -\frac{1}{\rho}\frac{\partial p}{\partial x_l} \quad \text{(ESC)}. \tag{A.19}$$

Again, the non-zero $\partial U_j/\partial x_i$ is obtained only when $j = 1$ and $i = 3$. By setting $j = 1$ and $i = 3$ in Equation A.19 and then replacing l by i, we can rewrite the pressure gradient as

$$2\int \frac{k_i k_1}{k^2}\mathrm{e}^{\mathrm{i}\boldsymbol{k}\cdot\boldsymbol{x}}\mathrm{d}Z_3(\boldsymbol{k},t)\frac{\partial U}{\partial z} = -\frac{1}{\rho}\frac{\partial p}{\partial x_i} \quad \text{(ESC)}. \tag{A.20}$$

Note that l is replaced by i after setting $j = 1$ and $i = 3$ in Equation A.19.

The second term in Equation A.12 may be expressed as

$$U_j\frac{\partial u_i}{\partial x_j} = \frac{\partial U_j}{\partial x_l}x_l\frac{\partial u_i}{\partial x_j} = \frac{\partial U_j}{\partial x_l}(\delta_{lj}u_i + x_l\frac{\partial u_i}{\partial x_j}) = \frac{\partial U_j}{\partial x_l}\frac{\partial(x_l u_i)}{\partial x_j} \quad \text{(ESC)}. \tag{A.21}$$

Subsequently, the term on the right-hand side $\frac{\partial(x_l u_i)}{\partial x_j}$ is transformed following

$$\begin{aligned}
\frac{\partial(x_l u_i)}{\partial x_j} &= \frac{\partial}{\partial x_j}\left(x_l\int \mathrm{e}^{\mathrm{i}\boldsymbol{k}\cdot\boldsymbol{x}}\mathrm{d}Z_i(\boldsymbol{k},t)\right) && \text{(A.22)}\\
&= \frac{\partial}{\partial x_j}\left(\int \frac{1}{\mathrm{i}}\frac{\partial}{\partial k_l}\mathrm{e}^{\mathrm{i}\boldsymbol{k}\cdot\boldsymbol{x}}\mathrm{d}Z_i(\boldsymbol{k},t)\right) && \text{(A.23)}\\
&= -\frac{\partial}{\partial x_j}\left(\int \frac{1}{\mathrm{i}}\mathrm{e}^{\mathrm{i}\boldsymbol{k}\cdot\boldsymbol{x}}\frac{\partial \mathrm{d}Z_i(\boldsymbol{k},t)}{\partial k_l}\right) && \text{(A.24)}\\
&= -\int k_j \mathrm{e}^{\mathrm{i}\boldsymbol{k}\cdot\boldsymbol{x}}\frac{\partial \mathrm{d}Z_i(\boldsymbol{k},t)}{\partial k_l} \quad \text{(ESC)}. && \text{(A.25)}
\end{aligned}$$

Note that the rule of integration by part is applied to obtain the third line from the second line.

The "average total derivative" of the velocity is defined as

$$\frac{\mathrm{D}u_i}{\mathrm{D}t} = \frac{\partial u_i}{\partial t} + U_j\frac{\partial u_i}{\partial x_j} \quad \text{(ESC)}, \tag{A.26}$$

which can be further rewritten as

$$\frac{\mathrm{D}u_i(\boldsymbol{x},t)}{\mathrm{D}t} = \int \mathrm{e}^{\mathrm{i}\boldsymbol{k}\cdot\boldsymbol{x}}\frac{\partial \mathrm{d}Z_i(\boldsymbol{k},t)}{\partial t} - \frac{\partial U_j}{\partial x_l}\int k_j \mathrm{e}^{\mathrm{i}\boldsymbol{k}\cdot\boldsymbol{x}}\frac{\partial \mathrm{d}Z_i(\boldsymbol{k},t)}{\partial k_l} \quad \text{(ESC)}. \tag{A.27}$$

The term $-k_j \frac{\partial U_j}{\partial x_l}$ is interpreted as the rate of change of wavenumber owing to the shear effect [11, 32], i.e.,

$$\frac{\mathrm{d}k_l}{\mathrm{d}t} = -k_j \frac{\partial U_j}{\partial x_l} \quad \text{(ESC)}. \tag{A.28}$$

This enables us to write

$$\frac{\mathrm{D}u_i(\boldsymbol{x},t)}{\mathrm{D}t} = \int \mathrm{e}^{\mathrm{i}\boldsymbol{k}\cdot\boldsymbol{x}} \left[\left(\frac{\partial}{\partial t} + \frac{\mathrm{d}k_l}{\mathrm{d}t} \frac{\partial}{\partial k_l} \right) \mathrm{d}Z_i(\boldsymbol{k},t) \right] = \int \mathrm{e}^{\mathrm{i}\boldsymbol{k}\cdot\boldsymbol{x}} \left(\frac{\mathrm{Dd}Z_i(\boldsymbol{k},t)}{\mathrm{D}t} \right) \quad \text{(ESC)}. \tag{A.29}$$

Inserting Equations A.20 and A.29 into the linearized N-S Equation A.12, we obtain

$$\int \mathrm{e}^{\mathrm{i}\boldsymbol{k}\cdot\boldsymbol{x}} \left(\frac{\mathrm{Dd}Z_i(\boldsymbol{k},t)}{\mathrm{D}t} \right) = -\frac{\partial U_i}{\partial x_j} \int \mathrm{e}^{\mathrm{i}\boldsymbol{k}\cdot\boldsymbol{x}} \mathrm{d}Z_j(\boldsymbol{k},t) + 2 \int \frac{k_i k_1}{k^2} \mathrm{e}^{\mathrm{i}\boldsymbol{k}\cdot\boldsymbol{x}} \mathrm{d}Z_3(\boldsymbol{k},t) \quad \text{(ESC)}, \tag{A.30}$$

which can be simplified as

$$\frac{\mathrm{Dd}Z_i(\boldsymbol{k},t)}{\mathrm{D}t} = \frac{\partial U}{\partial z} \left(\delta_{i1} + 2\frac{k_i k_1}{k^2} \right) \mathrm{d}Z_3(\boldsymbol{k},t) \quad \text{(ESC)}. \tag{A.31}$$

Equation A.31 is the rapid distortion equation for sheared flow [32]. The wavenumber vector $\boldsymbol{k_0} = (k_1, k_2, k_{30})$ is the initial and non-sheared vector and $\boldsymbol{k} = (k_1, k_2, k_3)$ is the wavenumber vector after shear effect, in which $k_3 = k_{30} - \beta k_1$, where $\beta = \frac{\partial U}{\partial z} t$. The time derivatives of the wavenumbers are

$$\frac{\mathrm{d}k_1}{\mathrm{d}t} = \frac{\mathrm{d}k_2}{\mathrm{d}t} = 0, \quad \text{and} \quad \frac{\mathrm{d}k_3}{\mathrm{d}t} = -\frac{\partial U}{\partial z} k_1. \tag{A.32}$$

Equation A.31 can be solved by integrating from zero time [82]. For example, the third term

$$\frac{\mathrm{Dd}Z_3(\boldsymbol{k},t)}{\mathrm{D}t} = 2\frac{\partial U}{\partial z} \frac{k_3 k_1}{k^2} \mathrm{d}Z_3(\boldsymbol{k},t) \tag{A.33}$$

is rearranged as

$$\frac{\mathrm{Dd}Z_3(\boldsymbol{k},t)}{\mathrm{d}Z_3(\boldsymbol{k},t)} = 2\frac{k_3 k_1}{k^2} \mathrm{D}\beta = \frac{2k_1(k_{30} - k_1\beta)}{k_1^2\beta^2 - 2k_1 k_{30}\beta + k_0^2} \mathrm{D}\beta. \tag{A.34}$$

Integrating on both side yields

$$\ln\left(\mathrm{d}Z_3(\boldsymbol{k},t)\right) = -\ln\left(k_1^2\beta^2 - 2k_1 k_{30}\beta + k_0^2\right) + C = \ln\left(\frac{\exp(C)}{k^2}\right), \tag{A.35}$$

where C is an arbitrary constant. This implies that $\mathrm{d}Z_3(\boldsymbol{k},t)$ can be obtained from the initial non-sheared state

$$\mathrm{d}Z_3(\boldsymbol{k},t) = \frac{k_0^2}{k^2} Z_3(\boldsymbol{k_0},0). \tag{A.36}$$

Townsend [82] and Mann [32] provided the solutions for the other two velocity components as

$$\mathrm{d}Z_1(\boldsymbol{k},t) = Z_1(\boldsymbol{k_0},0) + \zeta_1 Z_3(\boldsymbol{k_0},0), \tag{A.37}$$

and

$$\mathrm{d}Z_2(\boldsymbol{k},t) = Z_2(\boldsymbol{k_0},0) + \zeta_2 Z_3(\boldsymbol{k_0},0), \tag{A.38}$$

where the definition of ζ_1 and ζ_2 has been provided in Section 2.1.5. Because the stochastic process $\mathrm{d}\boldsymbol{Z}$ (3 by 1 matrix) is related to the spectral tensor by

$$\frac{\langle \mathrm{d}Z_i(\boldsymbol{k},t)\mathrm{d}Z_j^*(\boldsymbol{k},t)\rangle}{\mathrm{d}k_1\mathrm{d}k_2\mathrm{d}k_3} = \Phi_{ij}(\boldsymbol{k},t), \tag{A.39}$$

where "$*$" is the complex conjugate operator, the shear included spectral tensor is then expressed as

$$\boldsymbol{\Phi}(\boldsymbol{k},t) = \begin{bmatrix} 1 & 0 & \zeta_1 \\ 0 & 1 & \zeta_2 \\ 0 & 0 & k_0^2/k^2 \end{bmatrix} \frac{\langle \mathrm{d}Z_i(\boldsymbol{k_0},0)\mathrm{d}Z_j^*(\boldsymbol{k_0},0)\rangle}{\mathrm{d}k_1\mathrm{d}k_2\mathrm{d}k_3} \begin{bmatrix} 1 & 0 & \zeta_1 \\ 0 & 1 & \zeta_2 \\ 0 & 0 & k_0^2/k^2 \end{bmatrix}^* . \tag{A.40}$$

The initial non-sheared process can be expressed as the isotropic von Kámán tensor: [34, 11, 32]

$$\frac{\langle \mathrm{d}Z_i(\boldsymbol{k_0},0)\mathrm{d}Z_j^*(\boldsymbol{k_0},0)\rangle}{\mathrm{d}k_1\mathrm{d}k_2\mathrm{d}k_3} = \Phi_{\mathrm{iso},ij}(\boldsymbol{k_0}) = \frac{E(k_0)}{4\pi k_0^4}(\delta_{ij}k_0^2 - k_i k_j), \tag{A.41}$$

in which $i,j = 1,2$ and 30 (30 is for the initial non-sheared wavenumber). Replacing Equation A.41 in Equation A.40, the solutions for all elements in the sheared spectral tensor $\Phi_{ij}(\boldsymbol{k},t)$ can be obtained, which have been provided in Section 2.1.5.

A.3 Code Availability

(a) The OpenFAST version 3.0 with a lidar simulator integrated can be accessed via: `https://github.com/MSCA-LIKE/OpenFAST3.0_Lidarsim`. Last access: Last access: March 5, 2023.

(b) The *4-D Mann Turbulence Generator* can be found by: `https://github.com/MSCA-LIKE/4D-Mann-Turbulence-Generator`. Last access: March 5, 2023.

(c) The open-access tool *evoTurb* has been published on Github: `https://github.com/SWE-UniStuttgart/evoTurb`. Last access: Last access: March 5, 2023.

(d) The source codes of the wrapper DLL, baseline lidar data processing DLL, pitch feedforward DLL, and the modified ROSCO DLL are all available from

`https://github.com/MSCA-LIKE/Baseline-Lidar-assisted-Controller`. The DLL used in this thesis are modified from the Commit: 458c57b. Last access: March 5, 2023

A.4 Publications not Included in This Thesis

The following research outcomes were completed during the Ph.D. project (Lidar Knowledge Europe), but are not included in this thesis:

(a) F. Guo and D. Schlipf, "Lidar Wind Preview Quality Estimation for Wind Turbine Control", *2021 American Control Conference (ACC)*, 2021, pp. 552-557, doi: 10.23919/ACC50511.2021.9483442.

(b) F. Guo and D. Schlipf, "A Spectral Model of Grid Frequency for Assessing the Impact of Inertia Response on Wind Turbine Dynamics". *Energies* 2021, 14, 2492, https://doi.org/10.3390/en14092492.

(c) D. Schlipf, F. Guo, and S. Raach. "Lidar-based estimation of turbulence intensity for controller scheduling". *Journal of Physics: Conference Series*. Vol. 1618. No. 3. IOP Publishing, 2020. doi: 10.1088/1742-6596/1618/3/032053.

(d) Y.Y. Chen, W. Yu, F, Guo and P.W. Cheng. "Adaptive measuring trajectory for scanning lidars: proof of concept". *Journal of Physics: Conference Series* Vol. 2265, No. 2, p. 022099. IOP Publishing, 2022. doi: 10.1088/1742-6596/2265/2/022099.

(e) I. Miquelez-Madariaga, D. Schlipf, J. Elso, F. Guo and A. Díaz de Corcuera. "LIDAR based multivariable H_∞ feedforward control for load reduction in wind turbines". *Journal of Physics: Conference Series* Vol. 2265, No. 2, p. 022070. IOP Publishing, 2022. doi: 10.1088/1742-6596/2265/2/022070.

(f) F. Guo and D. Schlipf, "Assessing lidar-assisted feedforward and multivariable feedback controls for large floating wind turbines". *Wind Energy Science Discussions*, Vol. 2023, pp. 1-25, 2023. doi: 10.5194/wes-2023-9.

Bibliography

[1] A. Clifton and D. Schlipf, "Wind lidar technology development and transfer," May 2021, Presented at the 2021 Wind Energy Science Conference on 27th May 2021. [Online]. Available: https://doi.org/10.5281/zenodo.4817725

[2] G. I. Taylor, "The spectrum of turbulence," *Proceedings of the Royal Society of London. Series A-Mathematical and Physical Sciences*, vol. 164, no. 919, pp. 476–490, 1938. doi: https://doi.org/10.1098/rspa.1938.0032

[3] R. A. Pielke and H. A. Panofsky, "Turbulence characteristics along several towers," *Boundary-Layer Meteorology*, vol. 1, no. 2, pp. 115–130, 1970. doi: 10.1007/BF00185733

[4] A. G. Davenport, "The spectrum of horizontal gustiness near the ground in high winds," *Quarterly Journal of the Royal Meteorological Society*, vol. 87, no. 372, pp. 194–211, 1961. doi: 10.1002/qj.49708737208

[5] L. Kristensen, "On longitudinal spectral coherence," *Boundary-Layer Meteorology*, vol. 16, no. 2, pp. 145–153, 1979. doi: 10.1007/BF02350508

[6] D. Schlipf, "Lidar-assisted control concepts for wind turbines," Dissertation, University of Stuttgart, 2015. [Online]. Available: http://dx.doi.org/10.18419/opus-8796

[7] E. Simley and L. Pao, "A longitudinal spatial coherence model for wind evolution based on large-eddy simulation," in *2015 American Control Conference (ACC)*. IEEE, 2015. doi: 10.1109/ACC.2015.7171906. ISBN 978-1-4799-8684-2 pp. 3708–3714.

[8] S. Davoust and D. von Terzi, "Analysis of wind coherence in the longitudinal direction using turbine mounted lidar," *Journal of Physics: Conference Series*, vol. 753, p. 072005, sep 2016. doi: 10.1088/1742-6596/753/7/072005. [Online]. Available: https://doi.org/10.1088/1742-6596/753/7/072005

[9] Y. Chen, D. Schlipf, and P. W. Cheng, "Parameterization of wind evolution using lidar," *Wind Energy Science*, vol. 6, no. 1, pp. 61–91, 2021. doi: 10.5194/wes-6-61-2021

[10] M. de Maré and J. Mann, "On the space-time structure of sheared turbulence," *Boundary-Layer Meteorology*, vol. 160, no. 3, pp. 453–474, 2016. doi: 10.1007/s10546-016-0143-z

[11] J. Mann, "The spatial structure of neutral atmospheric surface-layer turbulence," *Journal of fluid mechanics*, vol. 273, pp. 141–168, 1994. doi: doi:10.1017/S0022112094001886

[12] "Wind energy generation systems – part 1: Design requirements," Geneva, Switzerland, Standard, 02 2019. [Online]. Available: https://webstore.iec.ch/publication/26423

[13] J. C. Kaimal, J. C. Wyngaard, Y. Izumi, and O. R. Coté, "Spectral characteristics of surface-layer turbulence," *Quarterly Journal of the Royal Meteorological Society*, vol. 98, no. 417, pp. 563–589, 1972. doi: 10.1002/qj.49709841707

[14] J. Laks, E. Simley, and L. Pao, "A spectral model for evaluating the effect of wind evolution on wind turbine preview control," in *2013 American Control Conference*. IEEE, 2013. doi: 10.1109/ACC.2013.6580400. ISBN 978-1-4799-0178-4 pp. 3673–3679.

[15] D. Schlipf, F. Haizmann, N. Cosack, T. Siebers, and P. W. Cheng, "Detection of wind evolution and lidar trajectory optimization for lidar-assisted wind turbine control," *Meteorologische Zeitschrift*, vol. 24, no. 6, pp. 565–579, 11 2015. doi: 10.1127/metz/2015/0634

[16] E. Simley, *Wind Speed Preview Measurement and Estimation for Feedforward Control of Wind Turbines*. Ann Arbor: ProQuest Dissertations & Theses, 2015. ISBN 9781339036748. [Online]. Available: https://www.proquest.com/docview/1719284807?pq-origsite=gscholar&fromopenview=true

[17] F. Guo and D. Schlipf, "Lidar wind preview quality estimation for wind turbine control," *2021 American Control Conference (ACC)*, pp. 552–557, 2021. doi: 10.23919/ACC50511.2021.9483442. [Online]. Available: https://zenodo.org/record/5625069#.Yz2zAXbP2Uk

[18] D. P. Held and J. Mann, "Lidar estimation of rotor-effective wind speed – an experimental comparison," *Wind Energy Science*, vol. 4, no. 3, pp. 421–438, 2019. doi: 10.5194/wes-4-421-2019. [Online]. Available: https://wes.copernicus.org/articles/4/421/2019/

[19] L. Dong, W. H. Lio, and E. Simley, "On turbulence models and lidar measurements for wind turbine control," *Wind Energy Science*, vol. 6, no. 6, pp. 1491–1500, 2021. doi: 10.5194/wes-6-1491-2021. [Online]. Available: https://wes.copernicus.org/articles/6/1491/2021/

[20] F. Guo, J. Mann, A. Peña, D. Schlipf, and P. W. Cheng, "The space-time structure of turbulence for lidar-assisted wind turbine control," *Renewable Energy*, 2022. doi: https://doi.org/10.1016/j.renene.2022.05.133. [Online]. Available: https://www.sciencedirect.com/science/article/pii/S0960148122007844

[21] E. Bossanyi, "Un-freezing the turbulence: Application to lidar-assisted wind turbine control," *IET Renewable Power Generation*, vol. 7, no. 4, pp. 321–329, 2013. doi: 10.1049/iet-rpg.2012.0260

[22] E. A. Bossanyi, A. Kumar, and O. Hugues-Salas, "Wind turbine control applications of turbine-mounted lidar," *Journal of Physics: Conference Series*, vol. 555, p. 012011, 2014. doi: 10.1088/1742-6596/555/1/012011

[23] F. Meng, W. H. Lio, and G. C. Larsen, "Wind turbine LIDAR-assisted control: Power improvement, wind coherence and loads reduction," *Journal of Physics: Conference*

Series, vol. 2265, no. 2, p. 022060, may 2022. doi: 10.1088/1742-6596/2265/2/022060. [Online]. Available: https://doi.org/10.1088/1742-6596/2265/2/022060

[24] W. H. Lio, F. Meng, and G. C. Larsen, "On LiDAR-assisted wind turbine retrofit control and fatigue load reductions," *Journal of Physics: Conference Series*, vol. 2265, no. 3, p. 032072, may 2022. doi: 10.1088/1742-6596/2265/3/032072. [Online]. Available: https://doi.org/10.1088/1742-6596/2265/3/032072

[25] E. Albert, W. Perrett, and G. Jeffery, "The foundation of the general theory of relativity," *Annalen der Physik*, vol. 354, p. 769, 1916.

[26] E. Hau, *Wind turbines: fundamentals, technologies, application, economics*. Springer Science & Business Media, 2013. ISBN 978-3-540-29284-5

[27] A. Rettenmeier, J. Anger, O. Bischoff, M. Hofsäß, D. Schlipf, and I. Würth, "Nacelle-based lidar systems," *Remote Sensing for Wind Energy, DTU Wind Energy-E-Report-0029 (EN)*, pp. 157–170, 2013. [Online]. Available: http://breeze.colorado.edu/ftp/RSWE/Andreas_Rettenmeier.pdf.

[28] J. Berg, J. Mann, and M. Nielsen, *Notes for DTU course 46100: Introduction to micro meteorology for wind energy*, ser. DTU Wind Energy E. Denmark: DTU Wind Energy, 2013, no. 0009(EN) rev. ed. ISBN 978-87-92898-15-5. [Online]. Available: https://orbit.dtu.dk/files/52392430/Introduction_to_micro_meteorology_for_wind_energy.pdf

[29] R. B. Bird, "Transport phenomena," *Appl. Mech. Rev.*, vol. 55, no. 1, pp. R1–R4, 2002. doi: https://doi.org/10.1115/1.1424298

[30] J. C. Wyngaard, *Turbulence in the Atmosphere*. Cambridge University Press, 2010.

[31] G. Batchelor, "The application of the similarity theory of turbulence to atmospheric diffusion," *Quarterly Journal of the Royal Meteorological Society*, vol. 76, no. 328, pp. 133–146, 1950. doi: https://doi.org/10.1002/qj.49707632804

[32] J. Mann, "Models in micrometeorology," Dissertation, Risø National Laboratory. ISBN 87-550-1950-1 1994. [Online]. Available: https://orbit.dtu.dk/files/254755257/Mann1994PhD.pdf

[33] R. Bos, "Extreme gusts and their role in wind turbine design," Dissertation, Delft University of Technology. ISBN 978-94-92516-60-2 2017.

[34] G. K. Batchelor, *The theory of homogeneous turbulence*. Cambridge university press, 1953. ISBN 978-0521041171. [Online]. Available: https://www.cambridge.org/de/academic/subjects/mathematics/fluid-dynamics-and-solid-mechanics/theory-homogeneous-turbulence?format=PB&isbn=9780521041171

[35] J. Mann, "Wind field simulation," *Probabilistic engineering mechanics*, vol. 13, no. 4, pp. 269–282, 1998. doi: https://doi.org/10.1016/S0266-8920(97)00036-2

[36] A. Peña, J. Mann, and N. Dimitrov, "Turbulence characterization from a forward-looking nacelle lidar," *Wind Energy Science*, vol. 2, no. 1, pp. 133–152, 2017. doi: 10.5194/wes-2-133-2017

[37] T. Mikkelsen, M. Sjöholm, N. Angelou, and J. Mann, "3d windscanner lidar measurements of wind and turbulence around wind turbines, buildings and bridges," in *IOP Conference Series: Materials Science and Engineering*, vol. 276, no. 1. IOP Publishing, 2017. doi: 10.1088/1757-899x/276/1/012004 p. 012004. [Online]. Available: https://doi.org/10.1088/1757-899x/276/1/012004

[38] A. Peña, C. B. Hasager, J. Lange, J. Anger, M. Badger, and F. Bingöl, "Remote sensing for wind energy," Roskilde, Denmark, Tech. Rep. DTU Wind Energy-E-Report-0029(EN), June 2013. [Online]. Available: https://orbit.dtu.dk/files/55501125/Remote_Sensing_for_Wind_Energy.pdf

[39] D. P. Held, "Inflow measurements by nacelle mounted lidars for wind turbine and farm control," Ph.D. dissertation, Ph. D. thesis, 2019. [Online]. Available: https://orbit.dtu.dk/files/171622775/Thesis.pdf

[40] D. Held and J. Mann, "Comparison of methods to derive radial wind speed from a continuous-wave coherent lidar doppler spectrum," *Atmospheric Measurement Techniques*, vol. 11, pp. 6339–6350, 11 2018. doi: 10.5194/amt-11-6339-2018

[41] GWEC, "Gwec global wind report 2021," *Global Wind Energy Council: Brussels, Belgium*, 2021. [Online]. Available: https://gwec.net/wp-content/uploads/2021/03/GWEC-Global-Wind-Report-2021.pdf

[42] M. B. Ageze, Y. Hu, and H. Wu, "Wind turbine aeroelastic modeling: Basics and cutting edge trends," *International Journal of Aerospace Engineering*, vol. 2017, 2017. doi: https://doi.org/10.1155/2017/5263897

[43] M. Buhl and A. Manjock, "A comparison of wind turbine aeroelastic codes used for certification," in *44th AIAA Aerospace Sciences Meeting and Exhibit*, 2006. doi: https://doi.org/10.2514/6.2006-786 p. 786.

[44] D. Kaufer and P. W. Cheng, "Validation of an integrated simulation method with high resolution load measurements of the offshore wind turbine repower 5m at alpha ventus," in *The Twenty-third International Offshore and Polar Engineering Conference*. OnePetro, 2013. [Online]. Available: http://legacy.isope.org/publications/jowe/jowe-01-1/JOWE-01-1-p030-arr01-Kaufer.pdf

[45] B. Jonkman and J. Jonkman, "Fast v8. 16.00 a-bjj," *National Renewable Energy Laboratory*, 2016. [Online]. Available: https://www.nrel.gov/wind/nwtc/assets/downloads/FAST/FASTv8.16/README_FAST8.pdf

[46] J. Jonkman, "FAST: An open-source platform for wind turbine multi-physics engineering modeling," 2017.

[47] J. M. Jonkman, G. Hayman, B. Jonkman, R. Damiani, and R. Murray, "Aerodyn v15 user's guide and theory manual," Tech. Rep., 2015. [Online]. Available: https://www.nrel.gov/wind/nwtc/assets/pdfs/aerodyn-manual.pdf

[48] R. Damiani, J. Jonkman, and G. Hayman, "Subdyn user's guide and theory manual,"

Tech. Rep., 2015. [Online]. Available: https://www.nrel.gov/docs/fy15osti/63062.pdf

[49] DNV-GL, "Bladed theory manual: version 4.8," Bristol, UK, Tech. Rep., 2016.

[50] T. Burton, N. Jenkins, D. Sharpe, and E. Bossanyi, *Wind energy handbook*. John Wiley & Sons, 2011.

[51] N. J. Abbas, D. S. Zalkind, L. Pao, and A. Wright, "A reference open-source controller for fixed and floating offshore wind turbines," *Wind Energy Science*, vol. 7, no. 1, pp. 53–73, 2022. doi: 10.5194/wes-7-53-2022. [Online]. Available: https://wes.copernicus.org/articles/7/53/2022/

[52] D. Schlipf, D. J. Schlipf, and M. Kühn, "Nonlinear model predictive control of wind turbines using lidar," *Wind Energy*, vol. 16, no. 7, pp. 1107–1129, 2013. doi: https://doi.org/10.1002/we.1533. [Online]. Available: https://onlinelibrary.wiley.com/doi/abs/10.1002/we.1533

[53] D. Schlipf, F. Lemmer, and S. Raach, "Multi-Variable Feedforward Control for Floating Wind Turbines Using Lidar," vol. All Days, 10 2020. doi: http://dx.doi.org/10.18419/opus-11067 ISOPE-I-20-1174.

[54] D. Schlipf, N. Hille, S. Raach, A. Scholbrock, and E. Simley, "Iea wind task 32: Best practices for the certification of lidar-assisted control applications," in *Journal of Physics: Conference Series*, vol. 1102. IOP Publishing, 2018. doi: 10.1088/1742-6596/1102/1/012010 p. 012010.

[55] S. Smith, *Digital signal processing: a practical guide for engineers and scientists*. Elsevier, 2013. [Online]. Available: https://www.elsevier.com/books/digital-signal-processing-a-practical-guide-for-engineers-and-scientists/smith/978-0-7506-7444-7

[56] F. Dunne, D. Schlipf, L. Pao, A. Wright, B. Jonkman, N. Kelley, and E. Simley, "Comparison of two independent lidar-based pitch control designs," in *50th AIAA Aerospace Sciences Meeting Including the New Horizons Forum and Aerospace Exposition*, 2012, p. 1151.

[57] B. Sanderse, S. Van der Pijl, and B. Koren, "Review of computational fluid dynamics for wind turbine wake aerodynamics," *Wind energy*, vol. 14, no. 7, pp. 799–819, 2011. doi: https://doi.org/10.1002/we.458

[58] P. S. Veers, "Three-dimensional wind simulation," Tech. Rep., 1988. [Online]. Available: https://www.osti.gov/biblio/6633902

[59] Y. Chen, F. Guo, D. Schlipf, and P. W. Cheng, "Four-dimensional wind field generation for the aeroelastic simulation of wind turbines with lidars," *Wind Energy Science*, vol. 7, no. 2, pp. 539–558, 2022. doi: 10.5194/wes-7-539-2022. [Online]. Available: https://wes.copernicus.org/articles/7/539/2022/

[60] W. H. Press, B. P. Flannery, S. A. Teukolsky, and W. T. Vetterling, *Numerical Recipes*, 2nd ed. Cambridge: Cambridge University Press, 1992. ISBN 0-521-43108-5

[61] D. S. Watkins, *Fundamentals of matrix computations.* John Wiley & Sons, 2004. ISBN 978-0-470-52833-4

[62] N. J. Higham, *Functions of matrices: Theory and computation.* Philadelphia: Society for Industrial and Applied Mathematics, 2008. ISBN 978-0-898716-46-7

[63] M. T. Heideman, D. H. Johnson, and C. S. Burrus, "Gauss and the history of the fast fourier transform," *Archive for history of exact sciences*, vol. 34, no. 3, pp. 265–277, 1985. doi: https://doi.org/10.1007/BF00348431

[64] G. De Cillis, S. Cherubini, O. Semeraro, S. Leonardi, and P. De Palma, "Pod-based analysis of a wind turbine wake under the influence of tower and nacelle," *Wind Energy*, vol. 24, no. 6, pp. 609–633, 2021. doi: https://doi.org/10.1002/we.2592

[65] J. Jonkman and K. Shaler, "Fast.farm user's guide and theory manual," 2021. [Online]. Available: https://openfast.readthedocs.io/en/dev/source/user/fast.farm/index.html

[66] J. Jonkman, P. Doubrawa, N. Hamilton, J. Annoni, and P. Fleming, "Validation of fast. farm against large-eddy simulations," in *Journal of Physics: Conference Series*, vol. 1037, no. 6. IOP Publishing, 2018. doi: 10.1088/1742-6596/1037/6/062005 p. 062005.

[67] M. Kretschmer, J. Jonkman, V. Pettas, and P. W. Cheng, "Fast.farm load validation for single wake situations at alpha ventus," *Wind Energy Science*, vol. 6, no. 5, pp. 1247–1262, 2021. doi: 10.5194/wes-6-1247-2021. [Online]. Available: https://wes.copernicus.org/articles/6/1247/2021/

[68] H. A. Madsen, G. C. Larsen, T. J. Larsen, N. Troldborg, and R. Mikkelsen, "Calibration and Validation of the Dynamic Wake Meandering Model for Implementation in an Aeroelastic Code," *Journal of Solar Energy Engineering*, vol. 132, no. 4, 10 2010. doi: 10.1115/1.4002555 041014. [Online]. Available: https://doi.org/10.1115/1.4002555

[69] G. C. Larsen, H. A. Madsen, K. Thomsen, and T. J. Larsen, "Wake meandering: a pragmatic approach," *Wind Energy: An International Journal for Progress and Applications in Wind Power Conversion Technology*, vol. 11, no. 4, pp. 377–395, 2008. doi: https://doi.org/10.1002/we.267

[70] D. Conti, "Wind turbine load validation under wake conditions using doppler lidar," Ph.D. dissertation, Technical University of Denmark, Denmark, 2020.

[71] F. Guo, D. Schlipf, Z. Zhang, and P. W. Cheng, "Investigation on the wind preview quality for lidar-assisted wind turbine control under wake conditions," in *2022 American Control Conference (ACC)*, 2022. doi: 10.23919/ACC53348.2022.9867301 pp. 3544–3549.

[72] D. Schlipf, P. W. Cheng, and J. Mann, "Model of the correlation between lidar systems and wind turbines for lidar-assisted control," *Journal of Atmospheric and Oceanic Technology*, vol. 30, no. 10, pp. 2233–2240, 2013. doi: 10.1175/JTECH-D-13-00077.1

[73] H. V. Henderson, F. Pukelsheim, and S. R. Searle, "On the history of the kronecker product," *Linear and Multilinear Algebra*, vol. 14, no. 2, pp. 113–120, 1983. doi: https://doi.org/10.1080/03081088308817548

[74] K. Schacke, "On the kronecker product," *Master's thesis, University of Waterloo*, 2004. [Online]. Available: https://www.math.uwaterloo.ca/~hwolkowi/henry/reports/kronthesisschaecke04.pdf

[75] B. J. Jonkman, "Turbsim user's guide: Version 1.50," Golden, CO (United States), Tech. Rep., 2009. [Online]. Available: https://www.nrel.gov/docs/fy09osti/46198.pdf

[76] G. DNV, "Dnv gl-st-0437: Loads and site conditions for wind turbines," *Standard, DNV GL, Høvik, November*, 2016. [Online]. Available: https://documents.dps.ny.gov/public/Common/ViewDoc.aspx?DocRefId={D6B401D1-D842-4E6E-A4DF-7528E7318856}

[77] C. F. Ropelewski, H. Tennekes, and H. Panofsky, "Horizontal coherence of wind fluctuations," *Boundary-Layer Meteorology*, vol. 5, no. 3, pp. 353–363, 1973. doi: https://doi.org/10.1007/BF00155243

[78] A. Peña, "Østerild: A natural laboratory for atmospheric turbulence," *Journal of Renewable and Sustainable Energy*, vol. 11, no. 6, p. 063302, 2019. doi: 10.1063/1.5121486

[79] D. T. Gillespie, "Exact numerical simulation of the ornstein-uhlenbeck process and its integral," *Physical review E*, vol. 54, no. 2, p. 2084, 1996. doi: https://doi.org/10.1103/PhysRevE.54.2084

[80] P. Welch, "The use of fast fourier transform for the estimation of power spectra: a method based on time averaging over short, modified periodograms," *IEEE Transactions on audio and electroacoustics*, vol. 15, no. 2, pp. 70–73, 1967. doi: 10.1109/TAU.1967.1161901

[81] J. Mann, J.-P. Cariou, M. S. Courtney, R. Parmentier, T. Mikkelsen, R. Wagner, P. Lindelow, M. Sjoholm, and K. Enevoldsen, "Comparison of 3d turbulence measurements using three staring wind lidars and a sonic anemometer," *Meteorologische Zeitschrift*, vol. 18, no. 2, p. 135, 2009. doi: 10.1127/0941-2948/2009/0370

[82] A. A. Townsend, *The Structure of Turbulent Shear Flow, Second Edition, Cambridge University Press. 1976.*, 1976, vol. 56, no. 9.

[83] M. Mirzaei and J. Mann, "Lidar configurations for wind turbine control," *Journal of Physics: Conference Series*, vol. 753, p. 032019, sep 2016. doi: 10.1088/1742-6596/753/3/032019. [Online]. Available: https://doi.org/10.1088/1742-6596/753/3/032019

[84] A. Obukhov, "Turbulence in an atmosphere with a non-uniform temperature," *Boundary-layer meteorology*, vol. 2, no. 1, pp. 7–29, 1971. doi: https://doi.org/10.1007/BF00718085

[85] U. Högström, "Non-dimensional wind and temperature profiles in the atmospheric surface layer: A re-evaluation," in *Topics in Micrometeorology. A Festschrift for Arch Dyer.* Springer, 1988, pp. 55–78.

[86] A. Peña, "Sensing the wind profile," Dissertation, Risø National Laboratory, 2009. [Online]. Available: https://orbit.dtu.dk/files/3737370/ris-phd-45.pdf

[87] J. W. Kirchner, "Aliasing in 1/ f α noise spectra: Origins, consequences, and remedies," *Physical Review E*, vol. 71, no. 6, p. 066110, 2005. doi: 10.1103/PhysRevE.71.066110

[88] F. Guo and D. Schlipf, "A spectral model of grid frequency for assessing the impact of inertia response on wind turbine dynamics," *Energies*, vol. 14, no. 9, 2021. doi: 10.3390/en14092492. [Online]. Available: https://www.mdpi.com/1996-1073/14/9/2492

[89] N. Dimitrov, A. Natarajan, and J. Mann, "Effects of normal and extreme turbulence spectral parameters on wind turbine loads," *Renewable Energy*, vol. 101, pp. 1180–1193, 2017. doi: https://doi.org/10.1016/j.renene.2016.10.001. [Online]. Available: https://www.sciencedirect.com/science/article/pii/S0960148116308655

[90] E. Simley, H. Fürst, F. Haizmann, and D. Schlipf, "Optimizing lidars for wind turbine control applications-Results from the IEA wind task 32 workshop," *Remote Sensing*, vol. 10, no. 6, p. 863, 2018. doi: https://doi.org/10.3390/rs10060863

[91] F. Guo, D. Schlipf, H. Zhu, A. Platt, P. W. Cheng, and F. Thomas, "Updates on the OpenFAST lidar simulator," *Journal of Physics: Conference Series*, vol. 2265, no. 4, p. 042030, may 2022. doi: 10.1088/1742-6596/2265/4/042030. [Online]. Available: https://doi.org/10.1088/1742-6596/2265/4/042030

[92] D. Schlipf, H. Fürst, S. Raach, and F. Haizmann, "Systems engineering for lidar-assisted control: A sequential approach," *Journal of Physics: Conference Series*, vol. 1102, p. 012014, oct 2018. doi: 10.1088/1742-6596/1102/1/012014. [Online]. Available: https://doi.org/10.1088/1742-6596/1102/1/012014

[93] E. Simley and L. Pao, "Reducing lidar wind speed measurement error with optimal filtering," in *2013 American Control Conference*, 2013. doi: 10.1109/ACC.2013.6579906 pp. 621–627.

[94] N. Wiener *et al.*, *Extrapolation, interpolation, and smoothing of stationary time series: with engineering applications*. MIT press Cambridge, MA, 1964, vol. 8.

[95] F. Guo, D. Schlipf, and Y. Chen, "The impact of wind evolution and filter design on lidar-assisted wind turbine control," 2021. doi: 10.5281/zenodo.4985412

[96] A. Peña, J. Mann, and G. R. Thorsen, "Spinnerlidar measurements for the ccav52," 2019. [Online]. Available: https://orbit.dtu.dk/files/193377980/Report_with_cover.pdf

[97] A. Borraccino, D. Schlipf, F. Haizmann, and R. Wagner, "Wind field reconstruction from nacelle-mounted lidar short-range measurements," *Wind Energy Science*, vol. 2, no. 1, pp. 269–283, 2017. doi: 10.5194/wes-2-269-2017. [Online]. Available: https://wes.copernicus.org/articles/2/269/2017/

[98] S. Davoust, A. Jehu, M. Bouillet, M. Bardon, B. Vercherin, A. Scholbrock, P. Fleming, and A. Wright, "Assessment and optimization of lidar measurement availability for wind turbine control," Tech. Rep., 2014. [Online]. Available: https://www.osti.gov/biblio/1132171

[99] M. Boquet, P. Royer, J.-P. Cariou, M. Machta, and M. Valla, "Simulation of doppler lidar measurement range and data availability," *Journal of Atmospheric and Oceanic*

Technology, vol. 33, no. 5, pp. 977–987, 2016. doi: https://doi.org/10.1175/JTECH-D-15-0057.1

[100] M. L. Aitken, M. E. Rhodes, and J. K. Lundquist, "Performance of a wind-profiling lidar in the region of wind turbine rotor disks," *Journal of Atmospheric and Oceanic Technology*, vol. 29, no. 3, pp. 347–355, 2012. doi: https://doi.org/10.1175/JTECH-D-11-00033.1

[101] D. Schlipf, S. Raach, and F. Haizmann, "Control system for controlling a turbine, method for controlling a turbine, and wind turbine," Patent EP3717770B1, 2018.

[102] J. M. Jonkman and M. L. Buhl, Jr, "Fast user's guide - updated august 2005," 10 2005. doi: 10.2172/15020796. [Online]. Available: https://www.osti.gov/biblio/15020796

[103] T. Möller and B. Trumbore, "Fast, minimum storage ray-triangle intersection," *Journal of graphics tools*, vol. 2, no. 1, pp. 21–28, 1997. doi: https://doi.org/10.1145/1198555.1198746

[104] J. S. Bendat and A. G. Piersol, *Random data; analysis and measurement procedures*. New York, USA: John Wiley & Sons, 1971. ISBN 978-0-470-24877-5

[105] F. Guo, D. Schlipf, and P. W. Cheng, "Evaluation of lidar-assisted wind turbine control under various turbulence characteristics," *Wind Energy Science*, vol. 8, no. 2, pp. 149–171, 2023. doi: 10.5194/wes-8-149-2023. [Online]. Available: https://wes.copernicus.org/articles/8/149/2023/

[106] S. J. Julier and J. K. Uhlmann, "Unscented filtering and nonlinear estimation," *Proceedings of the IEEE*, vol. 92, no. 3, pp. 401–422, 2004. doi: 10.1109/JPROC.2003.823141

[107] M. Matsuishi and T. Endo, "Fatigue of metals subjected to varying stress," *Japan Society of Mechanical Engineers, Fukuoka, Japan*, vol. 68, no. 2, pp. 37–40, 1968.

[108] M. Shan, "Load reducing control for wind turbines: Load estimation and higher level controller tuning based on disturbance spectra and linear models," Ph.D. dissertation, Kassel, Universität Kassel, Fachbereich Elektrotechnik / Informatik, 05 2017. [Online]. Available: https://kobra.uni-kassel.de/handle/123456789/2017050852519

[109] M. Stammler, F. Schwack, N. Bader, A. Reuter, and G. Poll, "Friction torque of wind-turbine pitch bearings – comparison of experimental results with available models," *Wind Energy Science*, vol. 3, no. 1, pp. 97–105, 2018. doi: 10.5194/wes-3-97-2018. [Online]. Available: https://wes.copernicus.org/articles/3/97/2018/

[110] Z. J. Chen and K. A. Stol, "An assessment of the effectiveness of individual pitch control on upscaled wind turbines," vol. 524. IOP Publishing, jun 2014. doi: 10.1088/1742-6596/524/1/012045 p. 012045. [Online]. Available: https://doi.org/10.1088/1742-6596/524/1/012045

[111] B. L. Jones, W. Lio, and J. Rossiter, "Overcoming fundamental limitations of wind turbine individual blade pitch control with inflow sensors," *Wind Energy*, vol. 21, no. 10, pp. 922–936, 2018. doi: 10.1002/we.2205

Curriculum Vitae

Feng Guo was born on March 6, 1993, in Kunming, China.

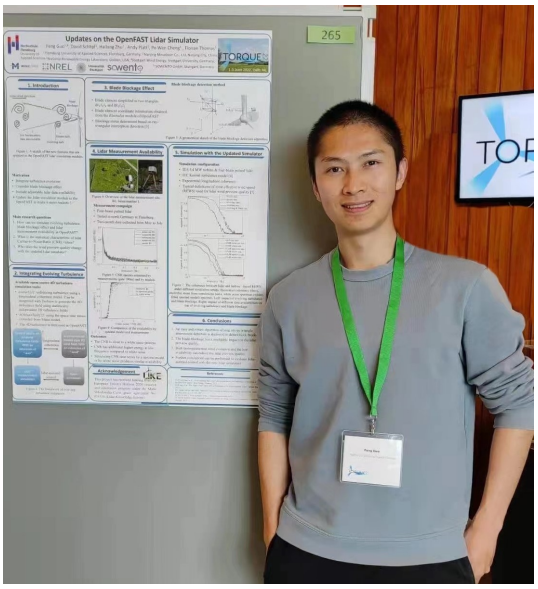

In 2015, he obtained a bachelor's degree in Thermal Energy and Power Engineering from Southeast University in China. His bachelor's study focused on the track of thermal energy and the automation of power plants. After that, he joined a Nordic Five Master program named Innovative Sustainable Energy Engineering, studying the track of System Integration of Wind Power. From 2015 to 2017, he was studying at the Norwegian University of Science and Technology and the Technical University of Denmark, through which he received two master's degrees from both universities. His Master thesis was titled as "Security and Stability of High Wind Penetrated Power System during Storm Conditions".

In December 2017, he started his first job at Power China Kunming Engineering Corporation Limited. His responsibility was mainly in wind resource assessment, wind turbine siting, and wind farm feasibility study.

In February 1, 2020, he joined the MSCA-LIKE (Marie Skłodowska-Curie Actions-Lidar Knowledge Europe) project to pursue a Ph.D. degree. He started working as a research assistant at Flensburg University of Applied Sciences in Germany, and he was enrolled as a Ph.D. candidate at the University of Stuttgart. During his Ph.D. project, he had secondments at Leosphere, Technical University of Denmark, and Sowento. Apart from his research activities, he had supervised several master's theses and projects. One of the most important projects is the "Smart Lidar Project", where he contributed to the installation of lidar on a turbine, data collection systems, and smart lidar applications.